Investigating Complex Organic Species on Mineral Surfaces

Belinda Fonseka

Jesus College

University of Cambridge

This dissertation is submitted for the degree of *Doctor of Philosophy*

December 2020

If I have seen further
it is by standing on the shoulders of Giants.

— Isaac Newton

Declaration

This thesis is the result of my own work and includes nothing which is the outcome of work done in collaboration except as declared in the preface and specified in the text. It is not substantially the same as any that I have submitted, or, is being currently submitted for a degree or diploma or other qualification at the University of Cambridge or any other university or similar institution except as declared in the preface and specified in the text.

It does not exceed the prescribed word limit of 60 000 words.

Belinda Fonseka

December 2020

Abstract

Investigating Complex Organic Species on Mineral Surfaces
Belinda Fonseka

The work in this thesis addresses the complex behaviour of organic species on the surfaces of minerals. The goal is to understand what minerals are of importance as well as the quantity and chemical nature of the adsorbed organics under real/commercial ageing conditions. The work has interest in improving oil recovery and understanding of mineral-organic interfaces.

This thesis covers two sections of oil recovery: (1) characterisation of real rock and (2) understanding the ageing process, before investigating a model system.

Firstly, in Chapter 4, characterisation of a supplied outcrop and reservoir rock via a wide range of state of the art techniques is conducted. The aim is to identify and characterise the key minerals that control the adsorption. It is demonstrated that despite the silicate rock being dominated by silicates, the exposed surface of the rock is not reflected by the bulk composition. To assess the difference, a number of novel experimental methods have been exploited as well as developing script to quantitatively assess this. This code has been taken up by the industrial collaborators.

The work turns to addressing the chemical nature of the organics on real reservoir rock and outcrop samples, where an extensive range of state of the art methods have been employed to assess this challenging problem. It is particularly challenging as the focus is on the species that cannot be removed by a number of solvent combinations and remain irreversibly bound. However, it is these species that might be attributed to the sticking of other molecules and possibly the ultimate determining factor for 'wettability'. Several methods that were anticipated to provide new insight were unsuccessful. However, TOF-SIMS is shown to be the most useful in identifying species. It is concluded that the study of the irreversibly bound species is inherently difficult as in situ measurements failed and removal of

species will change the bound species.

The second part of the work in Chapter 5 and 6 considers ageing of model minerals in a complex organic mixture of crude oil. Guided by the mineralogy determined from the first part of the project, the quantity and chemical nature of organic species adsorbed on selected minerals is assessed. It is found that different species from crude oil adsorbed onto certain minerals to a varying extent. The role of pre-added water with high and low salinities is also discussed. Both powdered substrates (Chapter 5) and flat substrates (Chapter 6) were employed to exploit a wider range of techniques. Key findings include: the asphaltene component of crude oils are implicated as contributing to larger quantities of organic species adsorbed. However, it is identified in Chapter 6 that this is not the case for muscovite mica (clay), where the contact angle determining layer can be removed and identified by a novel high resolution mass spectrometry method.

Finally, to facilitate the detailed understanding of complex systems, a model system was investigated using state of the art techniques to showcase the level of detail that is possible to achieve when investigating an interface. Chapter 7 describes the adsorption of stearic acid on the calcite surface as a representative adsorption study of a model mineral with a model additive. A combination of depletion isotherms, neutron reflectometry, sum-frequency generation spectroscopy and X-ray reflectivity have been used. Stearic acid is shown to adsorb onto calcite from toluene, to a much greater extent than equivalent studies in water. The adsorbed layer is found to be removable and can be reapplied repeatedly. In the presence of toluene saturated with water, the adsorption is not greatly affected. However, in the presence of excess water, the stearic acid can be removed from the surface to form calcium stearate.

Acknowledgments

First and foremost I would like to thank my supervisor, Stuart Clarke. Without your guidance, encouragement and support throughout my time at Cambridge I would not be where I am today. You have taught me not only how to succeed as a scientist but also shown me what a great leader and educator can do for the world. I am grateful for my Durham-supervisor, H. Chris Greenwell for opening my eyes to a wide range of analytical techniques across several scientific fields.

I am thankful to BP plc and EPSRC for providing funding. A big thank you to my industrial contact Stephanie Houston for your advice and support. A special thank you to Huang Zeng and Nathalia Tessarolo for swift assistance and discussions on HRMS.

Thank you to the Clarke group, especially the support from postdocs past and present: Mike Casford, David Madden, Ibrahim Salama and Chris Truscott. In particular, Mary Wood, who had to endure sharing an office with me for almost a year and suffered my grammar when proof-reading. I am forever grateful!

I am indebted to the support staff in the departments/institutes/facilities: Nigel Howard and Stephen Young for elemental analysis, Patrick Welche for software and programming help, Becky Welbourn for all things neutron-related, Iris Buisman for QEMSCAN and Sarah Fearn for TOF-SIMS.

Outside of the PhD work I would like to thank my friends at Jesus College, BPI, Department of Chemistry and other miscellaneous departments/institutes that I have spent time in at Cambridge and across the UK (there are too many to name, you know who you are!) for always being there for a cuppa (...and cake). Thank you Aimee, Sæþór, Keishi and Celia. Most importantly, thank you to AJ and Brett. Your continued support and belief in me means the world.

Thank you for letting me stand on your shoulders.

Abbreviations

ATR	Attenuated total reflection
AMU	Atomic mass unit
BET	Brunauer-Emmett-Teller
BSE	Back-scattered electrons
CaAOT	Calcium bis(2-ethylhexyl)sulfosuccinate
CHN	Carbon, hydrogen and nitrogen
CTAB	Cetyl trimethyl ammonium bromide
DBE	Double bond equivalent
DCM	Dichloromethane
DDAB	Dimethyldioctadecylammonium bromide
DI	Deionised (water)
EDX	Energy dispersive X-rays
EOR	Enhanced oil recovery
ESI	Electrospray ionisation
FTIR	Fourier-transform infrared spectroscopy
GC	Gas chromatography
HA	High asphaltene
HRMS	High resolution mass spectrometry
IC	Inorganic carbon
ICP-OES	Inductively coupled plasma optical emission spectroscopy
IEP	Isoelectric Point
IR	Infrared

LA	Low asphaltene
LSEOR	Low salinity enhanced oil recovery
MeOH	Methanol
Micro-CT	Micro computed tomography
MS	Mass spectrometry
NaAOT	Sodium bis(2-ethylhexyl)sulfosuccinate
NMR	Nuclear magnetic resonance
NR	Neutron reflectometry
PCC	Precipitated calcium carbonate
PDB	Pee Dee Belemnite
PPP	parallel, parallel, parallel component
PTFE	Polytetrafluoroethylene
PXRD	Powder X-ray diffraction
Py-GCMS	Pyrolysis gas chromatography mass spectrometry
QCM	Quratz crystal microbalance
QEMSCAN	Qualitative evaluation of minerals with scanning electron microscopy
RGB	Red, green and blue
SARA	Saturates, aromatics, resins and asphaltenes
SEM	Scanning electron microscopy
SFG	Sum-frequency generation
SLD	Scattering length density
SSP	perpendicular, perpendicular, parallel component
TAN	Total acid number
TC	Total carbon
TGA-MS	Thermogravimetric analysis mass spectrometry
THF	Tetrahydrofuran
TMS	Tetramethyl silane
TOC	Total organic carbon
TOF-SIMS	Time of flight secondary ion mass spectrometry

UV-vis	Ultraviolet-visible
XPS	X-ray photoelectron spectroscopy
XRF	X-ray fluorescence
XRR	X-ray reflectivity

Contents

1 Introduction **1**
1.1 Motivation . . . 1
1.2 Thesis Structure . . . 2

2 Background **3**
2.1 Oil Recovery Review . . . 3
2.1.1 The Importance of Wettability . . . 4
2.1.2 Understanding Rock . . . 5
2.1.3 Crude Oil . . . 6
2.1.4 Asphaltenes . . . 8
2.1.5 Bound Organics . . . 9
2.1.6 Water . . . 10
2.2 Wettability Fundamentals . . . 11
2.2.1 Contact Angle . . . 11
2.2.2 Young-Laplace Equation . . . 12
2.2.3 Washburn Method . . . 14
2.3 Substrates Studied . . . 16
2.3.1 Reservoir and Outcrop Rock . . . 16
2.3.2 Quartz . . . 17
2.3.3 Calcite . . . 19
2.3.4 Clay Minerals . . . 21
2.4 Surface Charge . . . 24

3 Experimental Methods **29**
3.1 Adsorption Isotherms . . . 29
3.1.1 Langmuir Isotherm . . . 31
3.1.2 BET Isotherm . . . 31
3.1.3 Freundlich Isotherm . . . 32

3.1.4 Experimental 32
3.2 Drop Shape Analysis 33
3.3 Tensiometer 33
3.4 Soxhlet Extraction 34
3.5 Micro Computed Tomography (Micro-CT) 35
3.6 Energy Dispersive X-rays and Back-Scattered Electrons 37
3.7 X-Ray Fluorescence 39
3.8 Qualitative Evaluation of Minerals with Scanning Electron Microscopy 40
3.8.1 QEMSCAN Data Analysis 40
3.9 Solution ^{1}H and ^{13}C Nuclear Magnetic Resonance 44
3.10 CHN Elemental Analysis 44
3.11 Thermogravimetric Analysis Mass Spectrometry 45
3.12 Stable Isotope Analysis 46
3.13 Pyrolysis Gas Chromatography Mass Spectrometry 47
3.14 Time of Flight Secondary Ion Mass Spectrometry 51
3.15 High Resolution Mass Spectrometry 52
3.16 X-Ray Reflectivity 53
3.17 Neutron Reflectometry 54
3.17.1 Neutron Refractive Index 54
3.17.2 The Critical Angle 54
3.17.3 Reflection from a Surface and Thin Layer 56
3.17.4 Layer Roughness 58
3.17.5 Matrix Method 59
3.17.6 Reflectivity Calculations for Rough Surfaces 60
3.17.7 ISIS TS2 Reflectometer 62
3.17.8 Data Analysis 62
3.17.9 Neutron Cells 63
3.17.10 Substrate Preparation 63
3.18 Sum-Frequency Generation 65
3.18.1 Selection Rules 65

4 Characterisation of Outcrop and Reservoir Rock 68
4.1 Background 68
4.2 Porosity Measurements 69
4.2.1 Micro-CT 69
4.2.2 Mercury Porosimetry 70
4.3 QEMSCAN 72
4.3.1 Intact Fragment 72

4.3.2 Crushed Sample . . . 78
4.3.3 Solvent Washed Crushed Sample . . . 81
4.3.4 Discussion . . . 83
4.3.5 Impact of QEMSCAN Resolution . . . 85
4.3.6 Conclusions . . . 88
4.4 XRF . . . 89
4.4.1 Irremovable Compounds . . . 92
4.5 Solution NMR . . . 93
4.6 TGA-MS . . . 98
4.7 Elemental Analysis . . . 101
4.7.1 Carbon Analysis . . . 101
4.7.2 Stable Isotope Analysis . . . 104
4.8 TOF-SIMS . . . 106
4.9 Py-GCMS . . . 115
4.10 TGA and Py-GCMS of Model Adsorbed Systems . . . 118
4.10.1 Results and Discussion . . . 118
4.11 Conclusions . . . 126
4.12 Future Work . . . 131

5 Understanding the Ageing Process: Powders 133
5.1 Background . . . 133
5.2 Crude Oil Characterisation . . . 134
5.2.1 SARA Analysis . . . 134
5.2.2 Vanadium and Nickel Content . . . 138
5.2.3 Elemental Analysis . . . 140
5.2.4 High Resolution Mass spectrometry . . . 144
5.3 The Ageing Process . . . 145
5.4 Ageing Particles . . . 147
5.4.1 Bare Particle Characterisation . . . 147
5.4.2 Ageing Quartz . . . 150
5.4.3 Ageing Calcite . . . 163
5.4.4 Ageing Kaolinite . . . 176
5.4.5 Ageing Mica . . . 181
5.4.6 Py-GCMS . . . 184
5.4.7 Removing Bulk Calcite . . . 185
5.4.8 What if the Oil is not Refreshed? . . . 191
5.4.9 Summary: Powder Substrates . . . 196
5.5 Washburn Method . . . 197

5.5.1 Washing Aged Outcrop and Reservoir . . . 197
5.5.2 Experimental . . . 197
5.5.3 Reference Compounds . . . 199
5.5.4 Results . . . 199
5.5.5 Summary . . . 202
5.6 Conclusions . . . 204
5.7 Future Work . . . 206

6 Understanding the Ageing Process: Flat Substrates 207
6.1 Background . . . 207
6.2 Silicon wafers . . . 207
6.2.1 DSA . . . 207
6.3 Mica Discs . . . 218
6.3.1 DSA . . . 218
6.3.2 Heated Brine Pretreatment . . . 226
6.3.3 HRMS . . . 229
6.4 Conclusions . . . 243

7 Effect of Stearic Acid on the Calcite Surface 245
7.1 Background . . . 245
7.2 Materials . . . 247
7.3 Depletion Isotherms . . . 248
7.3.1 Results . . . 248
7.4 Neutron Reflectometry . . . 252
7.4.1 Adsorption of a stearic acid monolayer . . . 252
7.4.2 Reversible adsorption of a stearic acid monolayer . . . 254
7.4.3 Influence of addition of water . . . 254
7.5 XRR and PXRD . . . 257
7.6 SFG . . . 258
7.7 Conclusions . . . 262

8 Conclusions 263

Appendix A QEMSCAN code 266

References 272

List of Tables

2.1 Complexity of components in reservoir well. 5

3.1 Details of chemicals used for Soxhlet extraction. 35
3.2 Parameters used for pyrolysis gas chromatography mass spectrometry. 50

4.1 Components of outcrop and reservoir rock soxhlet extraction detected by ^{1}H and ^{13}C NMR. 96
4.2 ^{1}H solution NMR results for outcrop and reservoir rock 96
4.3 ^{13}C solution NMR results for outcrop and reservoir rock 97
4.4 BET surface area analysis of reservoir rock as received, after a solvent wash, and after a solvent and HCl wash. 103
4.5 Compilation of results from all techniques used with a key stating whether the technique will be used for analysis of isolated minerals. . 128
4.6 Table of findings in thesis and respective comparisons in literature. . 130

5.1 DBE and DoS values for crude oil, assuming CHN results produce one fragment. 142
5.2 DoS and DBE of common molecules. 143
5.3 Composition of brine. 145
5.4 BET surface area of quartz, calcite, kaolinite and mica. 149
5.5 Degree of saturation and double bond equivalent for outcrop and reservoir rock in Chapter 4 normalised to take into account hydrogen-containing minerals. 158
5.6 Nitrogen comparison in crude and adsorbed onto quartz. 162
5.7 Py-GCMS results for all minerals aged in HA oil after 6 weeks. 184
5.8 Results from ageing powdered minerals in crude oil. 196
5.9 Brine compositions and densities. 198

6.1 Key classes for the negative electrospray ionisation are acidic and compound suggestions are above. 230

6.2 O_2 and O_5 class suggested molecules. 235
6.3 O_3S_1 class suggested molecules. 237
6.4 O_4S_1 class suggested molecules. 239
6.5 O_5S_x class suggested molecules. 240

7.1 SLDs of materials used in stearic acid on calcite study. 252
7.2 Summary of SFG peaks in the C−H stretching region. 259

List of Figures

2.1 Crude oil SARA analysis flowchart. 7
2.2 Asphaltene structure examples. 8
2.3 Contact angle of water on a solid in air. 11
2.4 Diagram of a spherical drop. 13
2.5 Cylindrical pore with finite contact angle. 14
2.6 Washburn schematic. 15
2.7 Outcrop and Reservoir plug. 17
2.8 Crystal structure of quartz. 18
2.9 Crystal structure of calcite. 19
2.10 Calcite block used for NR. 20
2.11 Crystal structure of kaolinite. 22
2.12 Structure of kaolinite aggregation modes. 23
2.13 Crystal structure of muscovite mica. 24
2.14 Electric double layer. 26
2.15 Zeta-potential diagram. 27

3.1 Depletion Method for Isotherms. 30
3.2 Example isotherms. 30
3.3 Diagram of Soxhlet apparatus. 34
3.4 Micro-CT sample preparation schematic. 36
3.5 BSE Diagram. 37
3.6 Generation of a QEMSCAN image. 40
3.7 QEMSCAN analysis example input image. 41
3.8 QEMSCAN analysis code flowchart 43
3.9 TGA schematic. 45
3.10 Py-GCMS schematic. 48
3.11 TOF-SIMS schematic. 51
3.12 Neutron Reflectometry angles. 55
3.13 Neutron Reflectometry reflection and transmission. 57

3.14 Simulated Neutron Reflectometry data. 59
3.15 SLD roughness profile. 60
3.16 Neutron Reflectometry rough surface example. 61
3.17 Neutron Reflectometry rough surface example SLDs. 61
3.18 Neutron Reflectometry cell. 64
3.19 Photograph of SFG spectrometer with calcite crystal. 67

4.1 Micro-CT of outcrop and reservoir rock. 70
4.2 Micro-CT defects. 71
4.3 QEMSCAN of reservoir rock fragment zoomed in. 73
4.4 QEMSCAN of outcrop and reservoir rock intact fragments. 73
4.5 Example of QEMSCAN analysis output images. 74
4.6 Raw QEMSCAN analysis edges versus bulk. 75
4.7 QEMSCAN analysis edges versus bulk. 77
4.8 Example of QEMSCAN images of crushed outcrop and reservoir rock. 78
4.9 QEMSCAN analysis crushed outcrop and reservoir rock edges versus bulk difference. 79
4.10 SEM image with EDX analysis of kaolinite booklet on outcrop and reservoir rock. 80
4.11 Example of QEMSCAN images of crushed and solvent washed outcrop and reservoir rock. 81
4.12 QEMSCAN analysis crushed outcrop and reservoir rock edges versus bulk difference. 82
4.13 QEMSCAN analysis of all outcrop and reservoir rock sample edges. . 84
4.14 QEMSCAN high and low resolution image extraction. 86
4.15 QEMSCAN analysis of high- and low-resolution images. 87
4.16 XRF of outcrop and reservoir rock major element oxides. 89
4.17 XRF of outcrop and reservoir rock minor elements. 91
4.18 Proton NMR for outcrop and reservoir solvent extracts. 94
4.19 Carbon NMR for outcrop and reservoir solvent extracts. 95
4.20 TGA-MS of outcrop and reservoir rock fragment. 99
4.21 TGA-MS of outcrop and reservoir rock fragment; MS data. 100
4.22 Carbon content of outcrop and reservoir rock samples. 102
4.23 Stable isotope analysis data for outcrop and reservoir rock. 105
4.24 TOF-SIMS mass spectrometer data. 108
4.25 TOF-SIMS aliphatic hydrocarbon data. 109
4.26 TOF-SIMS siloxane data. 110
4.27 TOF-SIMS serine and threonine data. 112

4.28 TOF-SIMS poly(2-vinylpyridin) data. 113
4.29 Py-GCMS of outcrop and reservoir rock. 116
4.30 Carbamic acid. 116
4.31 TGA of functionalised silica. 119
4.32 MS of pure materials and functionalised silica. 121
4.33 Py-GCMS of octadecyl functionalised silica. 123
4.34 Py-GCMS of CTAB on silica. 124
4.35 Py-GCMS of NaAOT on silica. 125
4.36 Py-GCMS of CaAOT on silica. 125

5.1 SARA analysis of all crude oils. 135
5.2 Difference map of SARA analysis for HA and LA crude oil. 136
5.3 Nickel and vanadium content of crude oils. 139
5.4 C, H and N content of crude oils. 140
5.5 Ageing process diagram. 145
5.6 CHN of particles used for crude oil ageing. 148
5.7 Carbon content of aged quartz in HA oil. 151
5.8 Water binding onto quartz schematic. 152
5.9 Carbon content of aged quartz in HA and LA oil. 153
5.10 Molecules from crude oil binding onto quartz surface. 155
5.11 Carbon content of aged quartz in HA, LA and LA-carb oil. 156
5.12 Degree of saturation for quartz in HA, LA and LA-carb oil. 157
5.13 Double bond equivalent for quartz in HA, LA and LA-carb oil. 159
5.14 Nitrogen content of aged quartz in HA, LA and LA-carb oil. 161
5.15 Total carbon content of aged calcite in HA oil. 164
5.16 Schematic of TGA calcite decomposition. 165
5.17 Organic carbon content of aged calcite in HA oil. 166
5.18 Water binding onto calcite schematic. 167
5.19 Total and organic carbon content of aged calcite in HA or LA oil. . . 168
5.20 Total and organic carbon content of aged calcite in HA or LA or LA-carb oil. 170
5.21 PXRD of LA-carb aged calcite. 171
5.22 Degree of saturation for untreated calcite in HA, LA and LA-carb oil. 172
5.23 Double bond equivalent for quartz in HA, LA and LA-carb oil. 173
5.24 Degree of saturation for untreated calcite in HA, LA and LA-carb oil. 174
5.25 CHN elemental analysis of aged kaolinite powder. 177
5.26 Degree of saturation and double bond equivalent of aged kaolinite. . . 179
5.27 CHN elemental analysis of aged mica powder. 182

5.28 Ageing process diagram with removal of calcite. 186
5.29 CHN results for irreversibly bound organics on calcite. 188
5.30 DoS and DBE results for irreversibly bound organics on calcite. . . . 189
5.31 SARA results for irreversibly bound organics on calcite. 190
5.32 CHN, DoS and DBE for aged quartz without an oil refresh. 192
5.33 CHN, DoS and DBE for aged calcite without an oil refresh. 193
5.34 CHN, DoS and DBE for aged kaolinite without an oil refresh. 194
5.35 CHN and DoS for aged mica without an oil refresh. 195
5.36 Diagram for washing substrates for Washburn Method 198
5.37 Washburn Reference Compounds 200
5.38 Effect of brine on Castlegate and Berea 201
5.39 Effect of ageing and washing on Castlegate and Berea by Washburn Method 202

6.1 DSA of bare silicon wafer. 210
6.2 Contact angles of aged silicon wafers. 213
6.3 DSA of bare mica discs. 219
6.4 Contact angle of aged mica discs. 222
6.5 Comparison between two studies mica ageing in crude with brine. . . 227
6.6 HRMS classes for HA oil, toluene extract and methanol extract. . . . 231
6.7 HRMS DBE versus carbon number for O_2 class. 234
6.8 HRMS DBE versus carbon number for O_2 class. 236
6.9 Toluene washing from aged mica. 237
6.10 HRMS DBE versus carbon number for O_4S_1 class. 238
6.11 HRMS DBE versus carbon number for O_5S_{1-2} class. 240

7.1 Structure of stearic acid 246
7.2 Isotherm of stearic acid on calcite 249
7.3 Karl Fischer titration values of solvents 250
7.4 Isotherm of stearic acid on calcite with added water 251
7.5 Neutron Reflectometry data from calcite with D-toluene, H-toluene, and H-stearic acid in D-toluene. 253
7.6 Neutron Reflectometry data showing reversible adsorption of H-stearic acid in D-toluene. 255
7.7 Neutron Reflectometry data showing adsorption of H-stearic acid in D-toluene with bulk D_2O. 256
7.8 Neutron Reflectometry data showing adsorption of D-stearic acid in D-toluene with bulk H_2O. 257

7.9 X-ray reflectivity measurements of calcite before and after neutron reflectometry. 258
7.10 Powder X-ray diffraction of calcium stearate. 258
7.11 SFG of stearic acid on calcite at room temperature and 60 °C. 260
7.12 SFG of stearic acid on calcite as a function of rotation. 261
7.13 Suggested mechanism for dissolution of calcite in the presence of stearic acid. 262

Chapter 1

Introduction

1.1 Motivation

We are in a climate crisis. Carbon emissions and other greenhouse gases, predominantly methane, have led to a global warming through the greenhouse effect, changing the climate of the Earth. The transition to greener sources of renewable energy and achieve a net zero (no net emission of CO_2) has become more pressing in the recent years. A transition away from oil, gas and coal towards carbon-free sources such as wind and solar power has started to occur. However, the technology required to make a full transition is not yet available. Oil will continue to be needed until sustainable transitions can be made.

One way to limit emissions from oil recovery is to maximise extraction from oil wells that are already geologically mapped and have infrastructure deployed. Currently, after three stages of oil recovery, only 40 % of crude oil is extracted from the wells. Increasing extraction efficiency of a well by 0.55 % would save the total CO_2 emissions that the United Kingdom generates in a year.[1,2]

Considerable screening needs to occur to assess a method for enhanced oil recovery to maximise extraction. A new surfactant or polymer to enhance recovery cannot be input into the well without screening its efficiency: the scale of deployment is so large that a mistake could be costly. When a possible new recovery method is found, rock samples are needed to test the oil recovery of the method. The rock samples are acquired by drilling thousands of feet into the oil reservoir, which is very costly, or can be acquired by an outcrop that is of similar mineralogy to the reservoir well of interest. For example, a silicate well will be matched with a silicate outcrop. Once the rock has been acquired, the rock must be aged in the laboratory

at reservoir temperature and pressure to mimic the environment. After an ageing duration (usually weeks), the new recovery method can be tested and assessed for oil recovery.

It is currently unclear which minerals are most useful to promote effective ageing; matching an outcrop rock mineralogy has not always produced the same results as a real reservoir rock.

This thesis covers two sections of oil recovery: (1) characterisation of real rock and (2) understanding the ageing process.

1.2 Thesis Structure

This thesis contains seven chapters: Chapter 2 is a background literature review; Chapter 3 discusses the experimental techniques used in subsequent chapters. In Chapter 4, the characterisation and comparison of outcrop and reservoir rock was achieved by a range of analytical methods, with electron microscopy proving the most revealing with regards to pore surface mineralogy. This is of great importance as this surface defines the chemistry that causes adsorbed oil to remain within an oil well.

After discussing minerals at the pore surface, these ideal minerals are investigated in powdered and flat forms in Chapter 5 and 6 respectively. This is advantageous as some novel analytical techniques are only feasible with flat surfaces. These chapters showcase the different atomic contents and quantities of organic species that adsorb on individual ideal minerals. The most interesting finding is the identification of sulfur containing species that alter contact angle on muscovite mica, analysed via high resolution mass spectrometry and drop shape analysis.

Finally, to highlight the power of more recent novel techniques in structure determination at the surface and interface of simple systems, the effect of stearic acid at the calcite surface is investigated in Chapter 7. Here, adsorption isotherms, neutron reflectometry, X-ray reflectometry and sum-frequency generation spectroscopy show the adsorption of stearic acid as a monolayer on calcite in toluene. The monolayer is removable and reapplied in toluene, yet can be removed upon the addition of excess water to form calcium stearate.

Chapter 2

Background

This chapter considers the origin of an oil well and the chemical considerations when understanding the system. These include mineralogy, chemical composition of crude oil and the role of water. After the basis of oil well contents are covered, two fundamentals that are critical to mineral-oil interaction (and therefore, this thesis) are discussed: wettability and surface charge.

2.1 Oil Recovery Review

Oil is produced from decaying plants and animals that have fallen to the bottom of bodies of water. They are subsequently buried by rocks and mineral. Increasing depth of burial leads to larger pressures and temperatures, speeding up decay and forming hydrocarbons.[3] The oil formed will float above any water and rise through the strata and continue to rise if not entrapped by a caprock, typically an impermeable rock layer of clay, deformed into a suitable dome-shaped trap formed by the tectonic movement of the Earth's mantle, where the oil will collect. An important consequence for this work is that the oil is considered to displace water from the initially water wet porous rock that will form the oil reservoir. In this way, the reservoir rock may end up with a variety of complex organic species bound to the mineral surfaces. This is significant as it may lead to a change in wettability and greatly change the ease that oil can be removed from the rock. In simple terms, if the rocks are covered in oil-like molecules, the oil tends to stick to the rock, making it hard to remove the oil.

Oil recovery is generally performed in three stages: (1) primary oil recovery, where the caprock is pierced and crude oil is allowed to flow under its natural pressure,

which will diminish over time; (2) secondary oil recovery, usually involving pumping water through the well to push the oil out; finally, (3) enhanced oil recovery, where additives such as polymers or surfactants are added that are intended to aid oil recovery in a number of ways, such as overcoming capillary forces and preventing flow bypass to release trapped oil.[4–6] It is desirable to experimentally test difference additives and fluids in representative rocks prior to deployment in the field. However, this can be challenging. There is an increased need for model reservoir rocks and organic systems to capture key aspects of the recovery process for lab-based testing. This is particularly true in this commercial area as acquisition of reservoir plugs in large quantities for full studies is very expensive.[7,8]

One important method exploited commercially is generation of representative cores via outcrop rock that is accessible from the surface of the Earth and treating it in various ways to recover an appropriate covering of organic species and attain the correct wettability. This can include an ageing process, where the crude oil from a particular reservoir is exposed to an outcrop for an extended period to capture the key chemistry of the real reservoir.

The literature review below covers the importance of wettability, the three main components to consider with oil recovery (rock, oil and water) and research into enhancing oil recovery.

2.1.1 The Importance of Wettability

After three stages of oil recovery, 60% of the oil remains stuck in the well. The oil is located within pores of the rock and can be unmovable for a variety of reasons such as wettability of surrounding rock, capillary pressure, pore geometry and permeability.[9–13] During waterflooding, the water and oil will flow simultaneously but not necessarily in the same pore network. However, both may be found in small crevices or where one is adsorbed onto rock in molecular layers.[5]

Reviews by Anderson have suggested that changes in wettability affect the physical parameters that cause oil to be stuck in the well.[11,14–18] Anderson suggests that any attempts to return a solvent cleaned core to its native wettability should undergo the following procedure: saturate the core with brine, flood the core with oil and then age the core at reservoir conditions for 1000 hours (6 weeks).[11] This procedure of core ageing has been used for the decades since the review was published, sometimes with a lower ageing duration but still within the ageing magnitude of weeks.[19–24]

Both the rock and the crude oil contain several components that are incredibly

complicated to investigate in-situ. Therefore, the rock, brine and crude oil system can be broken down in complexity:

Substrate	**Oil**	**Water**	Decreasing
Real rock	Crude oil	Connate brine	complexity
Individual minerals	Extracted asphaltenes	Brine with 1 or 2 salts	of system
	Model asphaltenes	DI water	↓

Table 2.1: Complexity of components in reservoir well.

When characterising the system containing rock, oil and water, there are two parts to consider: the solid and the liquid. The sections below discuss literature regarding characterisation of the rock, crude oil (including a brief look at asphaltene research) and the role of brine.

2.1.2 Understanding Rock

The first part of the puzzle is characterisation of solid multimineral rock. Studies have focussed on the bulk mineralogy with porosity/permeability as well as wettability. Here, utilisation of electron microscopy coupled with micro computerised tomography and nuclear magnetic resonance can be used to map porous networks within the rock core, sometimes based on where the clay lies within the rock.[25–29] This is especially important for investigating formation damage in reservoirs where a non-destructive technique is required.[30] A review by Barclay summarises efforts to determine rock wettability that include measurements of: contact angle, pressure displacement, spontaneous imbibition and dye adsorption.[25] It is emphasised here that results obtained from analysis of single minerals should be taken with caution due to the polymineralic nature of real reservoir rocks.[11,31]

Investigation into the role of individual minerals is important due to the complexity of investigating a heterogenous and uncontrollable real rock sample. Common individual minerals investigated in terms of oil recovery are: quartz, calcite, kaolinite and mica. Quartz and calcite are the bulk mineralogy of the two major types of oil wells.[32–36]

Flat quartz surfaces have been investigated using contact angle measurements of a crude oil drop whilst the substrate is submerged in water. Treatment shows the quartz moving from water-wet to oil-wet.[37] Quartz has also been doped with anionic, cationic and nonionic surfactants to test wettability alteration of the substrate when a known chemical functionality is present.[38] This is an example of a very simplified oil-well system.

Rao *et al.* found that ageing calcite crystals to brine and crude oil leads to aromatic and polar hydrocarbons not only depositing on the surface but also embedding in the mineral, leading to an oil-wet calcite system.[32] Work by Abdallah *et al.* found that the inclusion of magnesium ions in brine was needed to alter calcite wettability.[39]

Kaolinite is a clay with low surface charge that is believed to adsorb polar organic base molecules that influence reservoir wettability.[40–43] Counterions from water are believed to form a double layer between kaolinite and oil.[44] Mica is of most interest due to its surface charge tunability and possibility for cation bridging, which is believed to be the mechanism behind low salinity enhanced oil recovery (LSEOR), explained more below in Section 2.1.6.[20,45,46] Mica has the advantage that it can be cleaved to an atomically flat surface. Therefore, modern surface science techniques (contact angle, neutron reflectometry and atomic force microscopy) can be used to analyse the binding of oil on the mica surface.[47–50]

The ideal surfaces are generated from a range of methods, from spin-coating powders to compressed pellets. It is difficult to replicate the real rock system including pore network to investigate the interactions between minerals and crude oil. Techniques used to investigate these ideal surfaces include: stable isotope analysis, TOC, thermal analysis such as pyrolysis mass spectrometry, contact angle (both sessile, Washburn and in some cases via image analysis).[34,51–54]

2.1.3 Crude Oil

Understanding of the second part of the oil recovery puzzle lies within the composition of the liquid extracted, which has been exceptionally difficult due to the complex nature of crude oil. Crude oil is a term for the naturally occurring, unrefined product of petroleum present in an oil reservoir and is composed of a complex variety of hydrocarbon and organic components.[55–57] It is extremely difficult to determine exact structures of molecules from the crude oil. Therefore, the components of crude oil can be broadly classed into four categories: saturates, aromatics, resins, and asphaltenes (SARA) and there are standard analyses based on these fractions. Fractionation is based on the solubility of hydrocarbons in various solvents (Figure 2.1); each solubility class contains a very wide range of species of different molecular weight and chemical groups.

The first stage of separation is to dilute the crude oil with an n-alkane, usually n-heptane. Here, the asphaltenes—which are the heaviest and most polar components of crude oil—will crash out of solution as a precipitate, leaving a solution

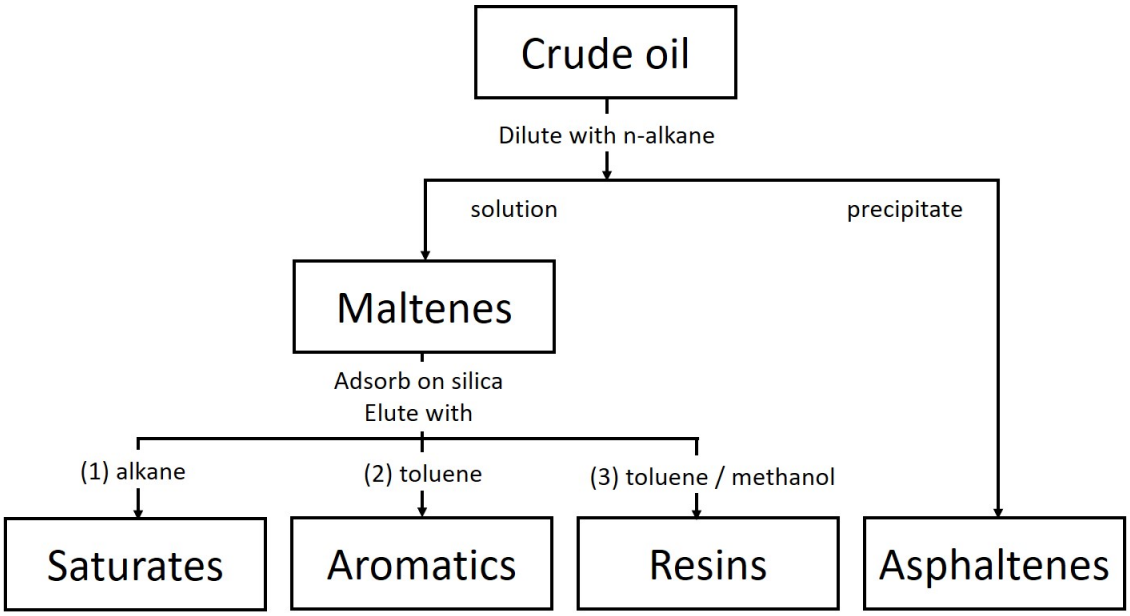

Figure 2.1: SARA analysis schematic showing the separation of crude oil into saturates, aromatics, resins, and asphaltenes.

of the remaining components, broadly referred to as maltenes. The maltenes are adsorbed onto silica and eluted with a range of solvents. The saturates are the least polar component followed by the aromatic hydrocarbons, before finally leading to the final fraction which is resins. Resins contain a small percent of polar heteroatoms (oxygen, nitrogen, and sulfur).

If an oil is composed of only saturates and aromatics, it will not be water wetting on most mineral surfaces. In contrast, resins and asphaltenes are reported to lead to minerals that are more water wet.[58] For this reason, resins and asphaltenes are considered most important for wettability alteration on minerals to the more water wet state. Both asphaltenes and resins are reported to have high molecular weight polar components that adsorb onto silica and mineral surfaces.[59] These are very complicated species with a chemical composition that will depend on where the oil has originated from: the animals and plants that decomposed and sedimented over time will vary according to location, which results in a variety of molecular weights being produced. The method of fraction separation will also impact chemical composition.

Although broadly standardised, it is important to note that SARA analysis can vary across different laboratories and there are reports of cross-contamination, raising a question of reliability.[60] The method of precipitation is also critical, as a different solvent will lead to a different elemental composition and other

properties of molecules precipitated, especially when considering investigation of asphaltenes.[61–63]

2.1.4 Asphaltenes

As mentioned above, asphaltenes are formally a solubility class of polar organic compounds that are essentially defined as the fraction that will precipitate out of crude oil upon the addition of an n-alkane or other aliphatic solvents (conventionally taken to be 40 volumes of heptane).[64] It is worth noting that different asphaltenes are extracted with different solvents.[65] The molecular weight of asphaltenes typically range from 400–1500 g mol^{-1} and will contain heteroatoms such as O, N, S, as well as co-ordinated metal ions and can be characterised via XPS, pyrolysis techniques, ultra violet spectroscopy, quartz crystal microbalance, infrared spectroscopy and nuclear magnetic resonance spectroscopy.[65–68] They can also form large associates and these can be hard to distinguish from the monomers. Asphaltenes can cause several problems in the recovery process, from precipitating out within the piping that can cause pressure changes and damaging equipment to being immiscible with extraction solvents.[58,63,69]

It is widely accepted that there are broadly two categories of asphaltene: archipelago and island. Archipelago asphaltenes contain small polyaromatic groups linked by aliphatic and/or naphthenic groups. Island asphaltenes comprise a single polyaromatic ring with aliphatic and/or naphthenic chains. Example structures are shown below in Figure 2.2.

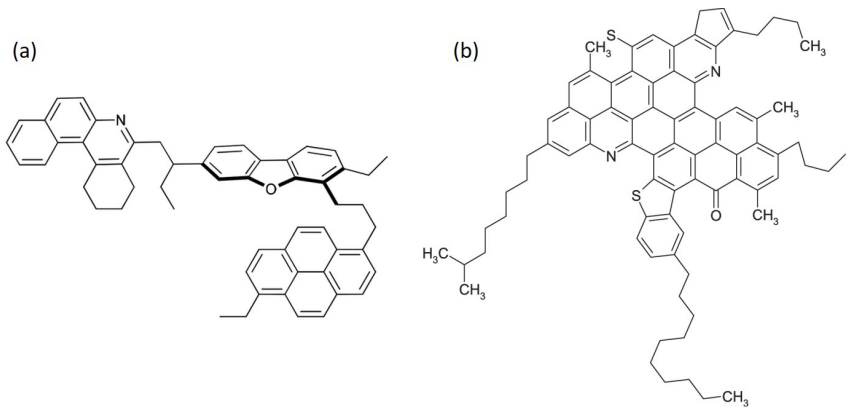

Figure 2.2: Example of (a) archipelago and (b) island asphaltenes.

Asphaltenes are believed to be surface active and alter the wettability of reservoir rocks and hence are considered to be very important in oil recovery.[11,70] However, between different reservoirs, asphaltenes will vary in molecular weight, structure

and degree of aggregation, hence their broad definition. The molecules also exhibit a range of solution physical chemistry, particularly association and aggregation that depends on solvent quality and concentration. Aggregation of archipelago asphaltenes is reported to be promoted via π–π stacking of aromatic groups and hydrogen bonding; Island asphaltene aggregation is thought to be through π–π bonding.[71] Importantly, in this thesis several crude oils with different asphaltene contents were exploited to assess the importance of their contribution to adsorption.

Model asphaltenes are simpler to use because the exact chemical functionalities are known. However, what exact molecules should be used as models is still highly debated, from derivatives of pyrenes to branched alkyl chains attached to polyaromatic cores.[72–75] Asphaltenes are notoriously heterogeneous and have fundamental properties, such as emulsion stabilisation and self-association that will need to be matched in the modelling process.[76–79]

2.1.5 Bound Organics

Along with the mineralogy lining the pores of rocks, the organics bound on the mineral will play a role in wettability alteration. It is common to use a Soxhlet extraction to fully extract residual crude oil from rocks that have not been recovered in efficiency tests.[34,80–87] Identification of crude oil before and after extraction from the rock can be achieved via elemental analysis of C, H, N, O and S components via XPS or pyrolysis techniques and chromatography coupled with mass spectrometry to elute fractions.[34,88] A study by Pan *et al.* showed bulk oil was predominantly saturated in hydrocarbons but upon extraction of the organic within the reservoir core via Soxhlet extraction, the adsorbed oil contained mostly resin and asphaltenes with a low hydrocarbon content.[34] A more modern technique is high resolution mass spectrometry, where washings of the crude oil and rock are analysed and can be groups into classifications depending on combination of heteroatoms present as a function of double bond equivalence and number of carbons.[55–57] Studies by Zeng, Wicking and Tessarolo at BP plc have shown possible layered structures of types of molecules present on real sandstone and carbonate rock, suggesting a ‘double-sided sticky tape’ scenario where a molecular layer (the ‘sticky tape’ layer) is between the rock and asphaltenes.

The above studies investigate what is removed from the rock via solvent. What is of more interest is the insoluble organics that remain stuck to the rock. These are inherently harder to investigate in-situ as removing organic may alter the nature of

the chemical functionalities present. For example, a bound ester could be released and quickly form a carboxylic acid due to oxidation. Subramanian *et al.* investigated crude oil extracted asphaltene adsorption on powdered ideal calcium carbonate.[89] They identified three types of organic: bulk, adsorbed and irreversibly adsorbed. Here, the irreversibly adsorbed organics are only obtained after dissolving away the calcium carbonate with hydrochloric acid. The irreversibly bound fraction is found to contain more carbonyl and carboxylic acid groups as well as increased aggregation between molecules. Ganeeva *et al.* assessed 18 cores using thermal analysis for organic matter and insoluble organic matter and suggest the insoluble organics are lighter hydrocarbons as opposed to heavier asphaltenics.[90] This aligns with the suggestion of the 'sticky tape' model by Zeng discussed above.[55]

Nitrogen is of interest because it is a heteroatom that can be in the wettability altering asphaltenes as well as porphyrins. Neutral pyrrolic structures have been suggested to be more favourable than the basic pyridinic form found in asphaltenes.[66,91,92] Understanding how much nitrogen is present and under what conditions it is removed in (e.g. acidic or basic conditions) could allude to what type of molecule the nitrogen comes from.[93] Sulfur detection can suggest asphaltenic presence, similar to nitrogen mentioned above as sulfur is only expected to be found in aromatic rings native to the asphaltene structure.[94] Detection is usually via organic inductively coupled plasma, resulting in the sulfur needing to be soluble in an organic solvent. The area of characterisation of irreversibly bound organics is the main knowledge gap that is preventing a full picture of how oil binds to rocks and changes wettability. Chapter 4 aims to try to address this further by using modern techniques to investigate irreversibly bound organics in-situ.

2.1.6 Water

Water is trapped within the porous rock before oil is deposited. This water is referred to as connate water and is deposited at the same time as the rock, usually dense and with a high salinity but can change chemical composition throughout the history of the rock. It is common to utilise water surrounding the oil well as it is readily available and cheap. However, research has shown low salinity water (salinities $<$ 5000 ppm) is more effective for oil recovery than high salinity water.[95–99]

The mechanism of how low salinity enhanced oil recovery (LSEOR) is still debated but some of the most important factors appear to be the composition of crude oil coupled with a clay-rich sandstone reservoir: polar components (resins and asphaltenes) are more favourable to adsorb onto mineral surfaces.[11,19,100–102] Here,

it is suggested that the substitution of divalent cations that bridge between anionic oil and anionic clay with monovalent cations that do not bridge in this method.[103] This method releases the adsorbed polar molecules and convert the system from oil-wet to water-wet. Crucially, Zhang *et al.* found that refined oil that does not contain polar fractions, does not respond to LSEOR, which supports the importance of polar molecules.[104]

The role of water will be investigated in Chapters 5 and 6, where ideal minerals are pre-treated in deionised water or brine (or untreated) and aged in crude oil before washed in solvent and analysed for irreversibly bound organics.

2.2 Wettability Fundamentals

The adhesion of oil onto the rock can be characterised using the concept of wettability and particularly expressed by the contact angle of the system, which is a readily experimentally assessable parameter. These concepts are introduced in the section below.

2.2.1 Contact Angle

Wettability is a solid's preference to be in contact with a fluid phase as opposed to another, often expressed by measuring the three-phase contact angle. Considering a simplified system where a droplet of water is brought into contact with a flat solid surface, the water droplet will adopt a shape to minimise the total surface energy. Gravity is neglected as a small droplet is assumed. The resulting force balance gives a contact angle that is defined as the angle between the tangents of the water droplet / air and water / solid surface (Figure 2.3). The contact angle is conventionally measured through the water phase. The three interfacial energies are related by Young's equation (Equation 2.1).[105,106]

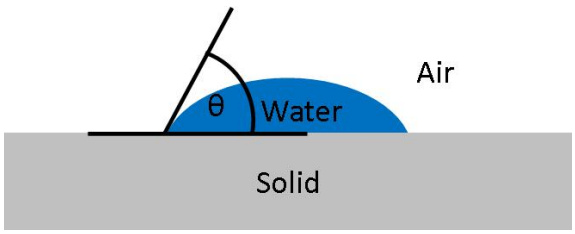

Figure 2.3: Water droplet deformed on a solid surface, surrounded by air with a contact angle of θ.

$$cos\theta = \frac{\gamma_{SA} - \gamma_{SW}}{\gamma_{WA}} \tag{2.1}$$

Where θ is the contact angle, and γ_{SA}, γ_{SW}, γ_{WA} are the interfacial tensions at the solid-air, solid-water, and water-air interfaces respectively. The surface tension for an air-water interface at 25 °C is 0.072 Nm^{-1}.[107] Considering a more complex system of an oil droplet on a solid surface surrounded by water, Young's equation (Equation 2.1) becomes:

$$cos\theta = \frac{\gamma_{SO} - \gamma_{SW}}{\gamma_{WO}} \tag{2.2}$$

Where γ_{SO}, γ_{SW}, γ_{OW} are the interfacial tensions at the solid-oil, solid-water, and oil-water interfaces respectively. When the contact angle is 0° it is said the system is completely wetting where the water will completely spread across the solid surface. A small contact angle ($90° > \theta > 0°$) means the surface has incomplete wettability; a large contact angle between $90° < \theta < 180°$ means the surface is said to be incompletely dry, and complete drying occurs when the contact angle is 180°.[108] Values of 180° are very rare and usually arise from other effects, such as roughness and super hydrophobic materials.[109]

2.2.2 Young-Laplace Equation

Secondary and enhanced oil recovery involve the flow of fluid through a porous medium where one phase is used to displace another: it is often the case that it is inconvenient to try and displace oil by water. This is a two-phase flow through porous media. In the two-phase system, there are three key 'forces' causing trapping and/or displacement of one phase by another: capillary, viscous, and gravity drainage forces.

It is believed that residual oil in the reservoir is trapped by capillary forces that arise from the curvature of the oil-water interface. The capillary force can be discussed in terms of the Young-Laplace equation which concerns the pressure difference across a curved surface caused by surface energy costs (Equation 2.3).[110] The pressure inside the curve is a larger pressure than outside (Figure 2.4).

A drop on a single surface is illustrated in Figure 2.4. ΔP_L is the pressure difference, P_{inside} is the pressure inside the drop, $P_{outside}$ is the pressure out of the drop. The radius, R, is taken as positive if the corresponding centre of curvature lies in the phase in which P_{inside} is measured and negative in the converse case. For a sphere,

the two radii, R_1 and R_2 of a surface at the point X are the same.

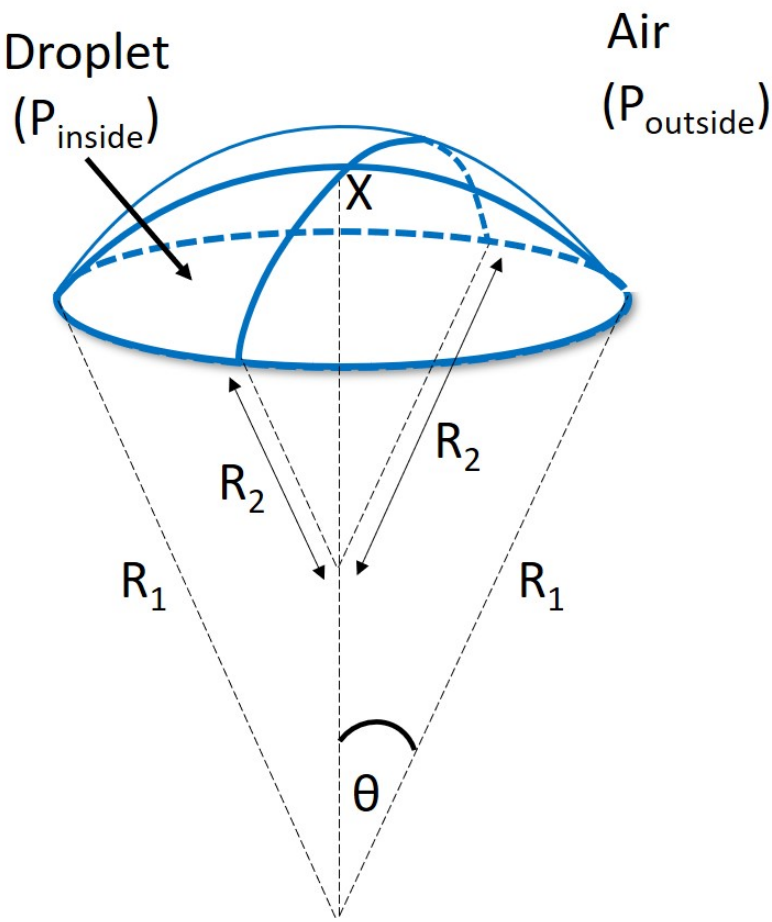

Figure 2.4: A droplet system showing large pressure inside the curvature and smaller pressure outside the curvature. For a sphere, the two radii, R_1 and R_2 of a surface at the point X are the same.

$$\Delta P_L = P_{inside} - P_{outside} = \gamma_{aw}(\frac{1}{R_1} + \frac{1}{R_2}) \tag{2.3}$$

If the contact angle in a cylindrical pore is finite (non-zero), the radius of the spherical meniscus formed at the oil-water interface is a function of the three-phase contact angle (Figure 2.5).

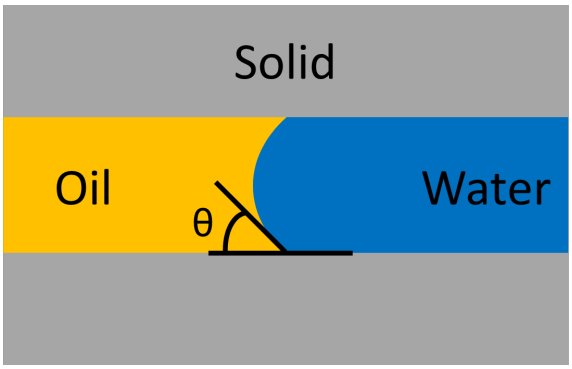

Figure 2.5: Cylindrical pore with finite contact angle.

$$R = \frac{a}{cos\theta} \tag{2.4}$$

Where 'a' is half the diameter of the pore. The pressure difference can now be written as:

$$\Delta P_L = \frac{2\,\gamma_{OW}\,cos\theta}{r_{pore}} \tag{2.5}$$

Where r_{pore} is the radius of the pore, θ is the contact angle, γ_{OW} is the interfacial energy and ΔP is the pressure difference.[111]

2.2.3 Washburn Method

Contact angle is a standard measurement when dealing with flat or cylindrical substrates, where the Young equation is employed. However, such a direct approach cannot be used for the contact angle of powdered materials where the contact angle of the material that makes up the lining of the pores between particles are of interest, especially within the work in this thesis. To determine the contact angle of porous materials one may use the Washburn equation, which describes capillary flow as a bundle of parallel cylindrical tubes of constant radius. The approach is based on the Laplace equation for capillary rise in a tube, given by Figure 2.6 and Equation 2.6:[112–114]

$$P_{capillary} = h\Delta\rho g = \frac{2\gamma cos\theta}{r} \tag{2.6}$$

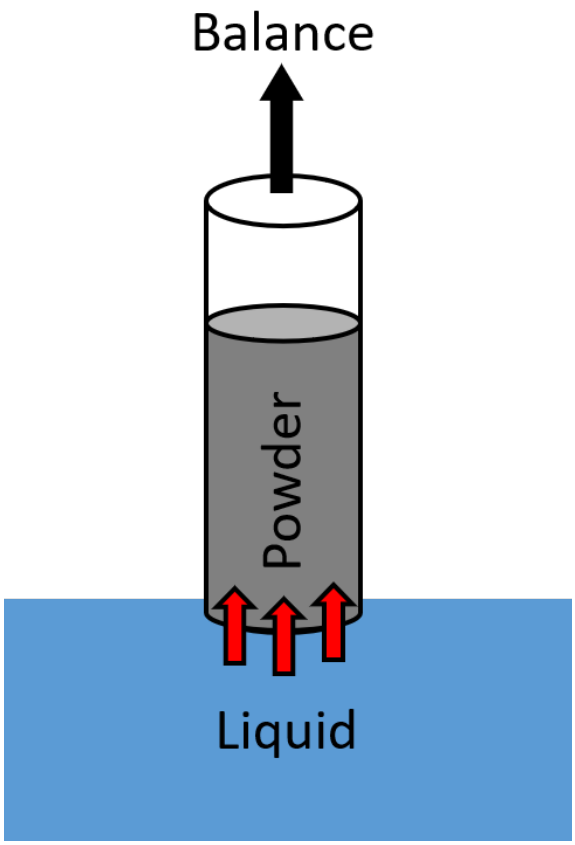

Figure 2.6: Schematic diagram of Washburn wettability apparatus.

Where $P_{capillary}$ is the pressure due to capillary forces acting on a tube of radius r, producing an interfacial tension (γ) and contact angle (θ). The contact angle of the liquid on the solid capillary wall can be determined by measuring the final height (h) of a liquid of known density contrast with the surroundings, usually air ($\Delta\rho$) and surface tension (γ). However, this method requires knowing the radius of the pores, which are generally unknown. The larger and more uniform a particle, the larger the pore size, which is inversely proportional to the capillary rise height. When a porous solid is brought into contact with a liquid, and the liquid undergoes capillary rise, the height of the fluid is governed by the time after contact (t) and the square of the mass of liquid uptake and a constant (A) (Equation 2.7).

If the parameters in constant A (Equation 2.8) are known (where η is liquid viscosity, ρ is liquid density, θ is surface tension, c is the capillary constant which is dependent on the porosity of the solid and thus packing reproducibility), then the contact angle can be calculated using Equation 2.9.[112,115,116]

$$t = Am^2 \tag{2.7}$$

$$A = \frac{\eta}{c\rho^2\gamma cos\theta} \tag{2.8}$$

$$cos\theta = \frac{m^2\eta}{t\rho^2\gamma c} \tag{2.9}$$

The Washburn method is used when a large amount of solid is available, and a liquid of known density, viscosity and surface tension is available. A cylindrical tube is prepared with a support that allows liquid to penetrate the solid and allows a packed powder bed to be prepared without dropping into the liquid. The powder is packed into the tube via a repeatable tapping method.

Importantly, the true radius of the pores is unknown; therefore, a repeatable packing method is required so that the same material can be exposed to two fluids. The first fluid has a known contact angle because it is completely wetting. This allows determination of the effective pore size. The fluid of interest can then be used, where the contact angle is unknown.

The mass of the liquid rising through the tube is measured as a function of time, leaving two unknowns in Equation 2.9: the contact angle and the capillary constant. When using a powder of unknown capillary constant, a completely wetting liquid (n-hexane or n-heptane) is used—such that $\theta = 0°$ ($\cos\theta = 1$) and the capillary constant can be deduced. Once the capillary constant for a specific solid has been determined using the completely wetting liquid, a non-completely wetting liquid of interest can be used to determine contact angle.

Contact angles that are greater than 90° cannot be measured using the Washburn method as no wetting of the powder via imbibition or capillary rise will occur.

2.3 Substrates Studied

Naturally Occurring Substrates

2.3.1 Reservoir and Outcrop Rock

The cylindrical outcrop plug supplied is a Castlegate sandstone (Figure 2.7, left), preserved in brine. The cylindrical reservoir plug (Figure 2.7, right) was supplied from a silicate well, preserved in kerosene. The kerosene used for preservation has a hydrocarbon content consisting of alkanes with between 6 and 16 carbon atoms per molecule. The experimental work described below will involve characterising

the mineralogy and organic contents of these minerals.

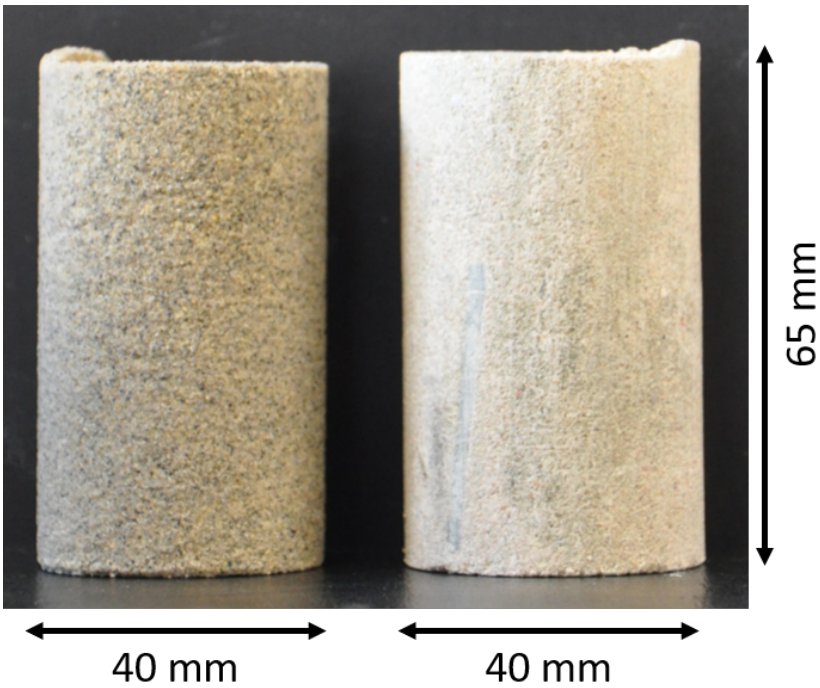

Figure 2.7: Photograph of Castlegate outcrop rock plug (left) and reservoir rock plug (right) used in this study.

Supplied reservoir and outcrop rocks were ground up in an inert agate mortar and pestle. Ground up rock was used in Soxhlet extraction (Section 3.4) to remove the maximum amount of organic.

Ideal Substrates

2.3.2 Quartz

Silicates are the largest group of rock forming minerals forming 90 % of the Earth's crust, of which 12 % is quartz.[117] Most significant for this work is that quartz is a large component of oil-containing reservoirs from sedimentary rock formations, which is one of the two dominant reservoir types. The mechanism of adsorption and release of organic material from the quartz surface is of great interest for enhanced oil recovery.

The crystal structure of quartz is shown in Figure 2.8.

The quartz surface has a number of Si−OH groups that exhibit a pH-dependent dissociation. The extent of dissociation can be characterised by an equilibrium

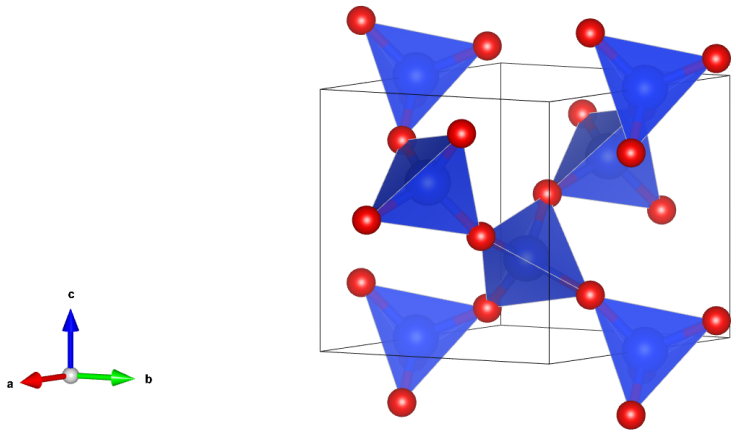

Figure 2.8: Crystal structure of quartz (blue = silicon and red = oxygen. Black lines represent the unit cell).

constant that depends on the relative concentrations of SiO^- and $SiOH_2{}^+$ shown below:

$$\mathrm{SiOH} \overset{K_1}{\rightleftharpoons} \mathrm{SiO^-} + \mathrm{H^+}$$
$$\mathrm{SiOH_2{}^+} \overset{K_2}{\rightleftharpoons} \mathrm{SiOH} + \mathrm{H^+}$$

The top reaction involves dissociation, giving rise to a negative quartz surface at neutral pH. Reduction of pH can force re-protonation of the surface leading to a neutral surface and isoelectric point (IEP) at pH 2–3.5.[118] This negatively charged surface is formed of Si^--O^- groups. At very low pH it has been suggested that $SiOH_2{}^+$ may occur as shown above; however this is complicated by significant dissolution of the solid at these very low pH conditions.

In this thesis, powdered quartz and flat silicon wafers are used. The silicon wafers have a native oxide that rapidly forms in air and is also reasonably representative of a quartz surface.

Details of the Si−OH surfaces can be complex.[118] The key point is the number density of the surface −OH groups and how they interact with each other.[119] There is evidence that some hydroxide groups can be lost on heating and some recovered on re-exposure to moist air.[120] Interestingly, the surface charge arising from −OH dissociation is not necessarily increased with more −OH. Some literature

report adjacent −OH groups hydrogen bond and make dissociation of protons more difficult.[121]

2.3.3 Calcite

Calcium carbonate occurs in three major crystallographic structures: calcite, aragonite, and vaterite. Sedimentary rocks recrystallise over geological timescales of time and will form the most stable polymorph, calcite; aragonite and valerite are less stable respectively.[122] When precipitated, the calcium carbonate can form optically clear single crystals, or polycrystalline, optically white samples. The crystal structure of calcite is shown below in Figure 2.9

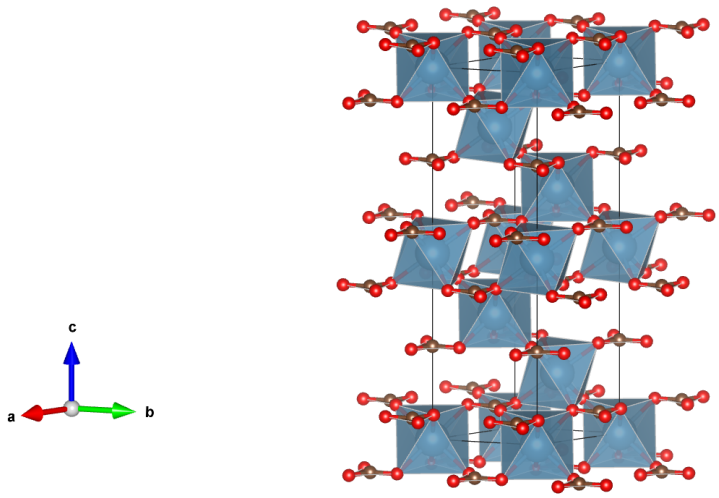

Figure 2.9: Crystal structure of calcite (light blue = calcium, brown = carbon, red = oxygen, black lines represent the unit cell).

Figure 2.9 shows that calcite is a hexagonal structure with a three-fold rotational and six-fold screw axis about the c-axis as well as a two-fold rotational axis perpendicular to the c-axis, overall described as a R3c symmetry.[122] Calcite is composed of alternating layers of carbonate groups and calcium ions that make the structure a closed-packed structure with respect to the carbonate groups, with calcium ions in the octahedral interstices. Calcite is referred to as a hexagonal unit cell, containing six $CaCO_3$ molecules, and will fracture into a rhombohedron shape as this is the most stable, with no C-O bonds needing to be broken and the least number of weak Ca-O bonds.

Optically, calcite is highly anisotropic, which produces a birefringence (Figure 2.10). This turns out to be important in this work when novel optical methods are used to characterise the material and adsorbed layers. The alternating layers of calcium

and carbonate ions in the calcite crystal lattice produce a high electron density within the crystal plane containing the carbonate groups, but only little electron density normal to this plane. Hence, the refraction of the incident light ray will be orientation-dependent, and it will split into two rays. The refractive indices parallel to the c-axis (n_e) and normal to it (n_o) are 1.658 and 1.486 respectively.[123] The difference between the refractive indices is called birefringence and has a value of –0.278. A light beam travelling along the optical axis of the crystal does not become polarised. Hence, no birefringence occurs if light travels through the crystal at an orientation exactly parallel to the c-axis.

Figure 2.10: Image of a calcite crystal, used for Neutron Reflectometry, on top of a piece of paper displaying the crest of Jesus College, Cambridge. The anisotropy of the crystal structure leads to two refractions of light, producing two images, referred to as birefringence.

The native crystal habit of the calcite exposes the 104 faces as a characteristic rhombohedral. Typically, the crystal will fracture at the cleavage planes terminated by the $10\bar{1}4$, $0\bar{1}14$ and $\bar{1}104$ planes. These are the most stable as they contain the lowest quantity of weak Ca−O bonds. Therefore, no strong C−O bonds are broken along these planes.

Calcium Carbonate in Solution

The calcite surface is a challenging system because the complex solution chemistry is dependent upon several coupled equilibria, including dissolved CO_2. The solubility product, K_{sp}, of calcium carbonate is 3.7 x 10^{-9} mol dm^{-3} at room temperature.[123,124] This corresponds to a solubility of 61 μg $CaCO_3$ per litre of water. For comparison, rock salt, NaCl, has a 1010 times higher solubility product of 37.7 mol dm^{-3}, corresponding to a solubility of 359 g NaCl per litre of water.[123] All constants below are given at standard temperature and pressure.[123–125]

$$CaCO_3 \rightleftharpoons Ca_2{}^+ + CO_3{}^{2-} \quad K_{sp}=3.7x10^{-9}\ mol\ dm^{-3}$$
$$H_2CO_3 \rightleftharpoons H^+ + HCO_3{}^- \quad K_{a1}=2.5x10^{-4}\ mol\ dm^{-3}$$
$$HCO_3{}^- \rightleftharpoons H^+ = CO_3{}^{2-} \quad K_{a2}=5.6x10^{-11}\ mol\ dm^{-3}$$
$$H_2O + CO_2 \rightleftharpoons H_2CO_3 \quad K_h=1.7x10^{-4}\ mol\ dm^{-3}$$
$$CO_{2(}g) \rightleftharpoons CO_{2(}aq) \quad K_H=29.76\ atm\ \ mol^{-1}\ dm^3$$
$$H_2O \rightleftharpoons H^+ + OH^- \quad K_w=1.0x10^{-14}\ mol\ dm^{-3}$$

The value of K_H is referred to as Henry's law constant. Henry's law states that the amount of dissolved gas is proportional to its partial pressure in the gas phase; therefore the Henry's law constant is the proportionality factor.

Surface Charge of Calcite

The surface charge of calcite has been widely researched, but still remains a matter of debate.[126–131] From the equilibrium of $CaCO_3$ in water at varying conditions, the following factors can be considered to influence surface charge: pH, pressure and ionic strength.[126] Furthermore, physical parameters of the substrate have been reported to manipulate the charge, such as particle size, surface area and even stirring rate.[132] If using natural crystals, then the location the substrate originated from might also be important: calcite that has been in contact with organic species may contain organic material within the substrate.[132,133] In addition to organics, a variety of inorganics may have been in contact with the calcite, such as metal ions in trace amounts.[134]

It is largely accepted that calcite is positively charged at ambient conditions with an isoelectric point at pH = 8.3. Ca^{2+} and CO^{3-} are expected to be potential determining ions in a calcite-water system.[126,128,130,135,136]

2.3.4 Clay Minerals

Mineral Structure

Clay minerals are hydrous aluminium phyllosilicates and have two main structural elements: tetrahedral and octahedral sheets.[137]

Tetrahedral sheets consist of silicon atoms tetrahedrally coordinated by oxygen atoms. Octahedral sheets consist of close-packed planes of oxygen atoms with either di- or trivalent ions such as Al^{3+} or Mg^{2+} held between them. The occupancy of octahedral sites is determined by the requirement to satisfy electroneutrality.

Tetrahedral and octahedral sheets join together to form compound layers, where each octahedral sheet may combine with one or two tetrahedral sheets to form a repeating unit of octahedral-tetrahedral (OT motif) or tetrahedral-octahedral-tetrahedral (TOT motif) structure. This is the distinction between a 1:1 or 2:1 clays. When oxygen atoms from the octahedral sheet are not shared with the tetrahedral sheet, they form terminating hydroxyl groups.

The layers described above are neutral overall and are representative of clays such as talc. Due to the unchanged nature of the sheets that are held together by only Van der Waals forces, they can easily be cleaved apart.

Kaolinite

Kaolinite, $Al_2Si_2O_5(OH)_4$, is the most common type of clay mineral in sandstones.[138,139] Kaolinite is comprised of one tetrahedral layer linked to one octahedral layer (OT motif outlined above) a 1:1 type structure (Figure 2.11). Silica tetrahedra are arranged in a hexagonal pattern in the silica sheet; three oxygens of each tetrahedron are shared with three other tetrahedra, and the fourth oxygen is shared with two alumina octahedra in the alumina sheet. In the alumina sheet, an aluminum atom is bonded to four hydroxyls (OH) groups and two oxygens from the tetrahedral sheet. Layers are joined by hydrogen bonds between adjacent silica and alumina sheets.[140]

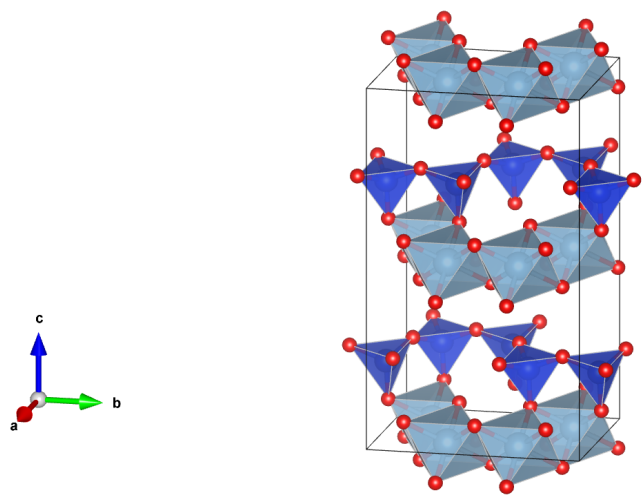

Figure 2.11: Crystallographic structure of kaolinite. Silicon in dark blue, aluminium in light blue, oxygen in red. Black lines represent the unit cell.

Kaolinite has a small amount of isomorphic substitution, resulting in a permanent charge in the siloxane surface. Furthermore, the charge on the aluminol face is

pH dependent, as it is controlled by protonation and deprotonation of hydroxyl groups.[47,50,141–143] In addition, the edges of kaolinite particles are composed of broken bonds whose charge will also depend on protonation and deprotonation equilibrium and therefore, will be pH dependent.[142,144] Kaolinite's morphology is commonly described as pseudohexagonal plates that aggregate in a book or worm-like fashion (Figure 2.12).

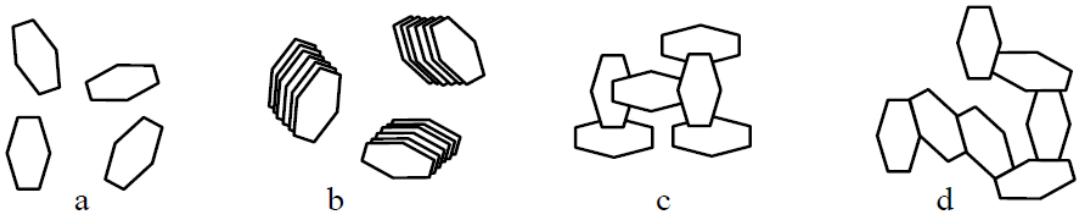

Figure 2.12: A range of aggregation types of kaolinite particles: a) dispersed, b) face-face, c) edge-face and d) edge-edge.

Kaolinite aggregation is reported to be dependent on pH, electrical double layer thickness, sample crystallinity and particle aspect ratio.[141,145–147] In a reservoir, kaolinite has been reported to cause severe plugging of pore throats and loss of permeability near near-wellbore if the particles mobilised by liquid flow and/or appropriate changes in surface charge.[138,139,148]

Muscovite Mica

Muscovite mica, $KAl_2(Si_3Al)O_{10}(OH,F)_2$, shown in Figure 2.13 has one quarter of the silicon atoms substituted in the tetrahedral sheets for an aluminium atom. This leads to a very high structural surface charge that is one of the highest of all clays. In the native mineral, the layer charge is compensated for by potassium ions between the sheets.[149]

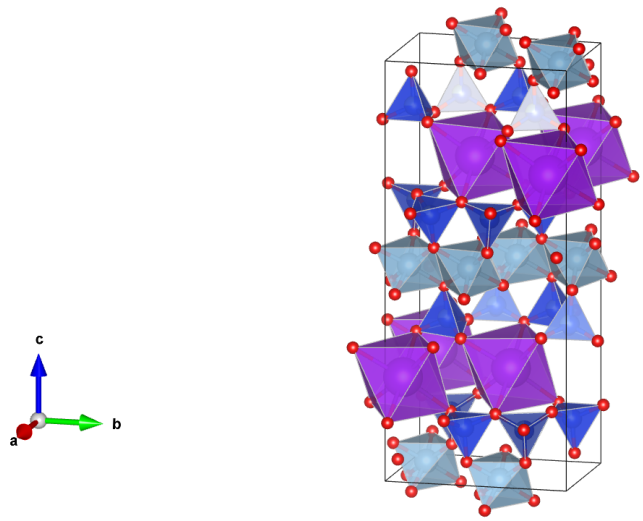

Figure 2.13: Crystallographic structure of muscovite mica. Potassium in purple, silicon in dark blue, aluminium in light blue, oxygen in red. Black lines represent the unit cell.

This high layer charge holds the layers together very strongly and as such, water cannot intrude and swell the clay. However, muscovite mica is easily cleaved between layers to expose the basal plane, which consists of a hexagonal array of oxygen atoms. Once cleaved, half the potassium ions will remain with each associated layer and then may be exchanged with other ions or surfactants when exposed to a solution. The mica has a high surface charge density (1 charge per $\sim$47 Å^2) and large zeta potentials.[137,150–152] This charge is mainly structural and hence the surface charge of the mica basal plane is largely pH independent. However, broken edges of the mica sheets will expose $-$OH groups like kaolinite and other clays mentioned above. Unless only the basal plane is examined, the net surface charge will be a complex mixture of faces and edges.

2.4 Surface Charge

Many metals and metal oxides have surface groups that can be ionised at differing pHs. For example, silica's Si$-$OH bonds and iron oxides Fe$-$OH. At high pH these

are deprotonated to give SiO^-. At low pH ($\sim$ pH 2) they will be protonated. At very low pH they may be positively charged due to another bound proton. However, for silica, this usually combines with dissolution.

Other systems where surface charge occurs include an ion preferentially dissolving and causing an excess of opposite charge at the surface. This is exmplified by AgI, where the Ag ion preferentially dissolves.

In clays, the charge will arise from isomorphic substitution, where an ion of one valency (e.g. Si, which has a formal charge of +4) is replaced with a species with a lower or higher valency (such as aluminium with a formal charge of +3) without any further change to the structure. This results in a net negative charge in the surface of the clay sheets. This charge is compensated, for example in mica, by the potassium counter ions at the mineral surface. This is discussed in Section 2.3.4.

Focussing on the effect of pH, at a certain pH there is no charge across the surface; this is known at the point of zero charge, or isoelectric point. The isoelectric point is different from the point of zero charge when ions that can adsorb strongly are present (referred to as potential determining ions) as they can change the surface charge. Ions that adsorb and do not change the surface charge directly can still influence overall surface charge behaviour by changing the distribution of the ions in the electrical double layer.

The electrical double layer is the ionic structre around a charged surface in solution. This ionic distribution can be described by the Stern model (Figure 2.14), where the counter ions are in a layer that is immediately next to the surface.[153] However, in some cases the elctrostatic attraction of the counter ions to the surface is overcome by the entropy of forming a disordered layer adjacent to the charged solid surface. This 'diffuse layer' of counterions reaches out into the solution. Overall, the combination of the Stern layer and diffuse layer cause the surface to appear electrically neutral from a sufficient distance where the ionic distribution has reached the bulk concentration level and the electrostatic potential has decayed to zero.

Potential determining ions are usually ions that are a part of the crystal lattice or have similar sizes and charge densities; for quartz these are H^+ and OH^- and for calcite they are Ca^{2+} and CO_3^{2-}. The calcite surface charge is not directly impacted by H^+ and OH^- ions, which most oxides are directly controlled by H^+ and OH^-. However, these ions are examples of ones that can affect the equilibrium concentrations of other species in the calcite system by selective dissolution of either Ca^{2+} or CO_3^{2-}.

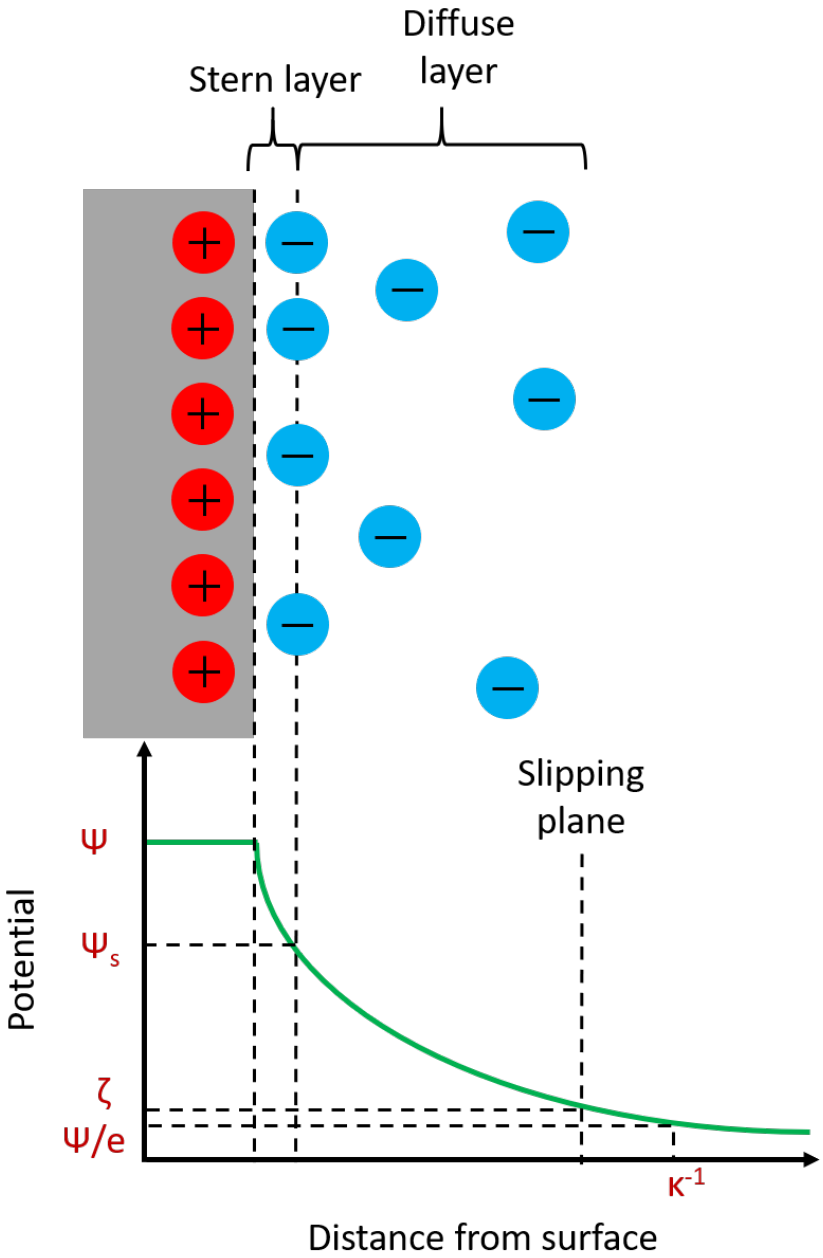

Figure 2.14: The electrical double layer, according to the Stern model. A layer of counterions adsorb within the Stern layer, causing the surface potential to drop off steeply up to the Stern plane before decreasing more gradually in the diffuse layer up to the slipping plane where the zeta-potential is measured.

One of the key characteristics of this ionic structure is the 'Debye length' (κ^{-1} in Figure 2.14). This is where the electrostatic potential has dropped to e^{-1} of its initial value at the surface and is the separation up to which two like charged particles can approach each other before the overlap of their double layers leads to significant electrostatic interaction. As the ionic strength of a solution is increased by increasing the number and/or valency of ions in solution, the Debye length decreases

and therefore particles will be able to approach each other more closely without interacting.

Determining this electrostatic surface potential is challenging. In practice it can be measured at a 'slipping plane'. This is where a solid particle is moving in solution and carrying a certain number of ions that depends on the surface charge and the solution ionic strength. The potential at this slipping surface is known as the zeta potential. The zeta potential will generally have a lower value than the surface potential but is reasonably straight forward to experimentally measure. By determining how zeta potential varies with pH, as shown in Figure 2.15, the isoelectric point of a surface may be found: this is when the zeta potential is 0 mV as overall surface charge is zero.

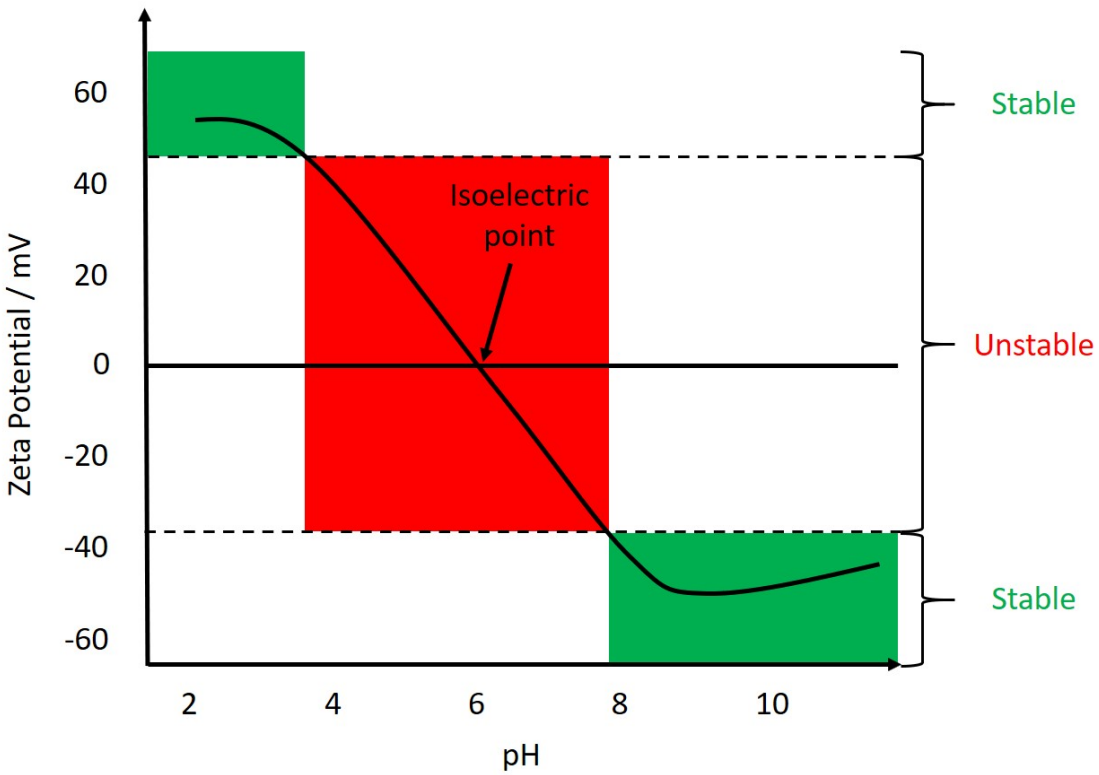

Figure 2.15: Schematic of possible zeta-potential diagram. The isoelectric point corresponds to the pH at which the overall surface charge is zero. At low pH the surface is positively charged; at high pH the surface is negatively charged.

Overall, when studying adsorption of a species in aqueous solution, considering charge effects arising from potentially determining ions, electrolytes and additives that will impact charge distribution are critical to consider.

In this work, several minerals that have a surface charge in water are considered. This means a change in behaviour in the presence of different dissolved ions is

expected. This is relevant in Chapter 5 and 6 when ageing of minerals is explored with and without pre-exposure to water and/or ionic solutions. Significant changes in non-aqueous systems are not expected as these fluids usually have low dielectric constant. This results in charged groups becoming strongly attracted to each other and do not survive long, in contrast to water.

Chapter 3

Experimental Methods

A very wide range of experimental methods have been employed to try and characterise these complex systems. This is because no one technique, even if it worked perfectly, would be able to reveal all information about a system. A range of novel methods that have not previously been used on these systems were used to hopefully bring new insight.

There are key distinctions between the methods used and what part of the system they analyse. Some techniques will investigate molecules that **can** be removed from a surface with a solvent (removable molecules). Other techniques will investigate molecules that **cannot** be removed from a surface (irreversibly bound molecules). The ideal technique will analyse a surface and molecular deposition in a non-invasive manner. However, many methods can only probe the surface by ripping bound species off, sometimes chemically altering the species in the process.

3.1 Adsorption Isotherms

Solution isotherms are one of the most common starting points for adsorption studies of simple systems. Adsorption isotherms were collected using the 'depletion method' (Figure 3.1). A solution of known initial concentration is tumbled with a high surface area powder and allowed to reach equilibrium. The change in solution composition, determined using an appropriate analytical method, can then be measured to determine the molar adsorption per unit surface area or per unit mass as a function of final solution concentration.

Various models have been developed to describe isotherms of a variety of systems. Usually the theoretical models are used to investigate gas-solid adsorption; however,

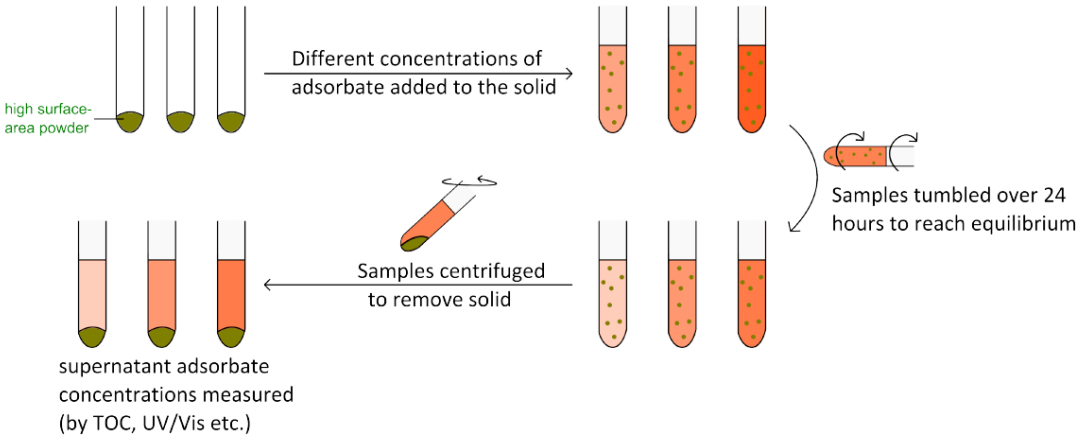

Figure 3.1: Standard procedure for depletion isotherm method.[154]

they are still helpful when considering the solid-liquid interface. By fitting the measured data with a model, an understanding of the physical system can be obtained and in favourable circumstances and important quantitative and qualitative parameters such as monolayer vs multilayer formation, or area occupied by a molecule and thus whether a molecule is 'stood up' or 'laying down' on a surface, can be determined.

Literature cites numerous types of isotherms.[155,156] This work will discuss three potential isotherm systems: Langmuir, Freundlich and Brunauer-Emmett-Teller (BET) isotherm. Examples of the generic shapes for the isotherms are shown in Figure 3.2.

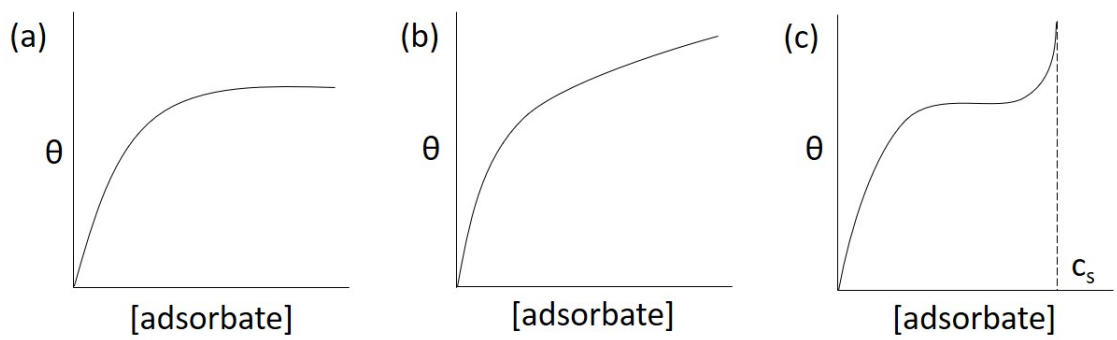

Figure 3.2: Generic curve shapes for (a) Langmuir isotherm, (b) BET isotherm and (c) Freundlich isotherm.

3.1.1 Langmuir Isotherm

Possibly the most common isotherm, the Langmuir isotherm (Figure 3.2 (a)) is used to fit many experimental datasets. There are several assumptions fo the isotherm:

1. The surface containing the adsorbing species is atomically flat
2. All sites are energetically equivalent
3. One site holds one adsorbate (monolayer coverage)
4. No interactions between neighbouring adsorbates

The Langmuir isotherm is described by the following equation:

$$\nu = \frac{\nu_{max} K_L c}{1 + K_L c} \tag{3.1}$$

where ν is the adsorbed amount, ν_{max} is the maximum adsorbed amount, c is the equilibrium concentration and $\mathrm{K_L}$ is the Langmuir constant. The equation above can be rearranged:

$$\frac{c}{\nu} = \frac{1}{K_L \nu_{max}} + \frac{c}{\nu_{max}} \tag{3.2}$$

A linear relationship between (c/ν) and c is observed for a system with Langmuir behaviour.

3.1.2 BET Isotherm

Figure 3.2 (b) shows the BET isotherm. It is similar to the Langmuir isotherm but includes the possibility of multilayer adsorption and interactions between adsorbed layers are permitted. However, lateral interactions are ignored.

BET isotherms are used to calculate the specific surface area of a solid powder by measuring nitrogen gas adsorption onto the solid surface. Nitrogen gas is used as it has a well defined surface area of 16.2 $Å^2$.[157] Equation 3.3 shows the BET equation, where P is the adsorbate equilibrium pressure, $\mathrm{P_0}$ is the adsorbate saturation pressure, ν is the adsorbed gas' equilibrium volume, ν_{m} is the volume of gas required to cover a monolayer, and $\mathrm{K_B}$ is the BET constant.

$$\frac{P}{\nu P_0} = \left(\frac{1}{\nu_m K_B}\right) + \left(\frac{K_B - 1}{\nu_m K_B}\right)\left(\frac{P}{P_0}\right) \tag{3.3}$$

A plot of $\frac{P}{P_0}$ by $\frac{1}{\left[\nu\left(\frac{P_0}{P}-1\right)\right]}$ where the slope and y-intercept can be used to calculate ν_{m} and $\mathrm{K_B}$.

For solution isotherms, the equation is written in linear form:

$$\frac{c}{\nu(c_s - c)} = \frac{1}{K_B \nu_{max}} + \left(\frac{K_B - 1}{K_B \nu_{max}}\right)\left(\frac{c}{c_s}\right) \tag{3.4}$$

where c_s is the saturation concentration. Plotting $\frac{c}{\nu(c_s-c)}$ versus $\frac{c}{c_s}$ will give an intercept of $\frac{1}{K_B \nu_{max}}$ and gradient of $\frac{K_B-1}{K_B \nu_{max}}$.

3.1.3 Freundlich Isotherm

Figure 3.2 (c) shows the Freundlich isotherm. This model considers interactions between adsorbed molecules, where one molecule will increase or decrease the chance of further adsorption. The Freundlich is shown below:

$$\nu = \nu_{max} K_F c^{\frac{1}{n}} \tag{3.5}$$

where $\mathrm{K_F}$ is the Freundlich constant and n is a dimensionless constant greater than 1. By plotting log(ν) versus log(c), an intercept of log($\nu_{\mathrm{max}}\mathrm{K_F}$) and gradient of 1/n are obtained. This model is empirical as opposed to theoretical. Therefore, it should only be used when Langmuir and BET isotherms are not suitable.

3.1.4 Experimental

In this work, isotherms were used when investigating stearic acid on the calcite surface (Chapter 7). Depletion isotherm samples were prepared using a batch method: Stearic acid solutions with concentrations between 0.1 and 120 mM in 10 ml of dried toluene were added to 2.7 g of calcite powder. The samples were tumbled for 72 hours, before centrifugation and extraction of the supernatant, analysed using IR spectroscopy. Data were obtained with a Bruker VERTEX 70v FTIR spectrometer, Specac PearlTM liquid transmission accessory and liquid nitrogen-cooled mercury cadmium telluride detector with a path length of 50 micron and spectral resolution of 4 $\mathrm{cm^{-1}}$ and 50 acquisitions. For each sample, the equilibrium solution concentration was determined from the intensity of the IR absorbance due to stearic acid at 1709–1713 $\mathrm{cm^{-1}}$ using a calibration data set.

The difference between the initial and equilibrium solution concentrations was attributed to adsorption of the stearic acid on the calcite powder. The experiment

was repeated with toluene saturated with water, which itself was pre-saturated with calcium carbonate (to minimise dissolution of the powdered substrate).

BET surface areas were used to calculate surface adsorption of organics and BET measurements were determined by N_2 adsorption at the Department of Materials and Institute for Manufacturing in Cambridge.

3.2 Drop Shape Analysis

Shape analysis of a liquid drop on a solid surface is referred to as the sessile drop method. A high resolution camera captures an image of the liquid droplet sat on the solid surface, and through image analysis applies a baseline (characterising the liquid-solid interface) and an outline of the droplet can be used to determine the contact angle.

A Krüss DSA100 was used to determine the contact angle of water on crude-oil-functionalised substrates. The method generally requires large, flat substrates and roughness of the substrate can lead to incorrect interpretation of data.

3.3 Tensiometer

A tensiometer (a delicate force transducer) was used to investigate wettability of solids using the Washburn method. An explanation of the Washburn method is given in Section 2.2.3. Considering the background literature regarding the Washburn method and its comparison with other contact angle measurements, the Washburn method will be used to rank substrates relatively, rather than taking their absolute values.

Washburn method experiments were conducted with a Krüss K100 Force Tensiometer at the BP Sunbury laboratories.[158] All measurements were taken at room temperature and atmospheric pressure. Analysis was via Krüss ADVANCE software.

3.4 Soxhlet Extraction

Soxhlet extractions were used in this study to extract 'removable' compounds from the surface of the rock samples, removing fractions of different types of adsorbed organic species, ultimately leaving the 'irremovable' compounds at the substrate surface, which could then be investigated. The nature of the removable material is interesting as it also provides some clue to the nature of the bound material. The functional groups present in the removed material may be used to infer the nature of the remaining bound material. The chemical composition of the solvent selected for the washes were based on reservoir core cleaning procedures. [87]

Soxhlet extraction is an effective and convenient method for organic removal where a distilling solvent is allowed to condense above the sample of interest, held in a porous thimble (Figure 3.3). As the condensing solvent runs down to the sample dissolution can occur. More solvent will distil until a critical level of fluid is reached and a syphon is triggered that removes all the solvent fluid that contains dissolved species. This process can continue indefinitely, bathing the sample in clean solvent to facilitate dissolution.

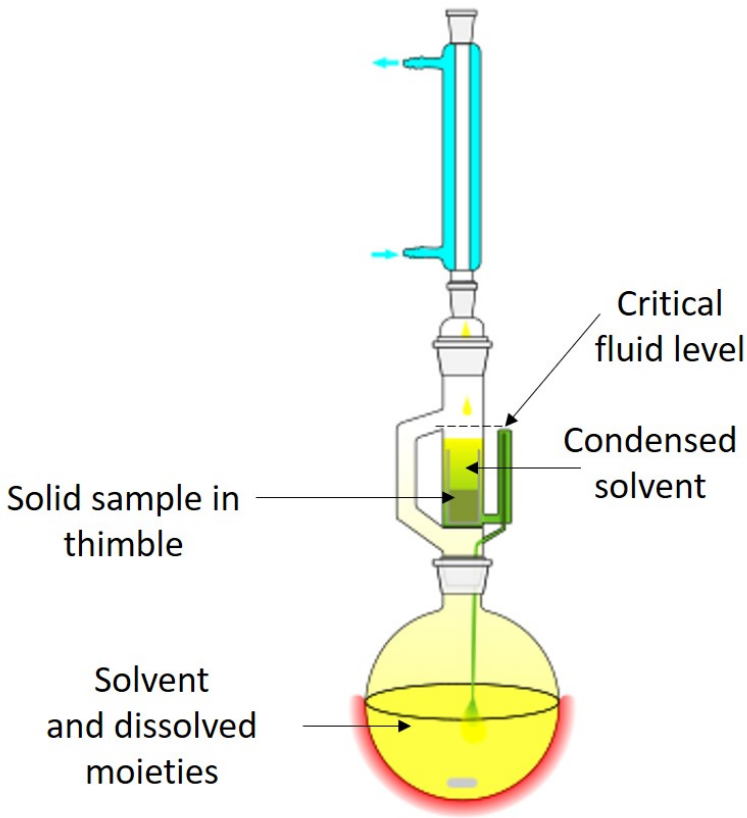

Figure 3.3: Diagram of Soxhlet apparatus.

The sequence of solvent extractions used for washing of 30 g of ground reservoir rock was: 40 mL of dichloromethane (DCM) and methanol (93:7), 40 mL DCM/MeOH (93:7), 40 mL tetrahydrofuran (THF) / acetone / MeOH (50:25:25), 40 mL THF/acetone/MeOH (50:25:25), and finally 40 mL THF/acetone/MeOH (50:25:25).[34,87]

For 30 g of ground outcrop rock, a large quantity of organics is not expected to be extracted and therefore less solvent was needed. Thus, only the last extraction of 40 mL THF/acetone/MeOH (50:25:25) was used. Details of chemicals and suppliers and extraction processes are listed in Table 3.1.

Chemical	**Supplier**	**Purity / %**	**Batch Number**
Dichloromethane	Sigma Aldrich	$\geq$ 99.5	BCBQ1661V
Methanol	Sigma Aldrich	$\geq$ 99.9	SZBF166FV
Tetrahydrofuran	Sigma Aldrich	$\geq$ 99.5	BCBN5103V
Acetone	Sigma Aldrich	$\geq$ 99.9	MKBK0156V

Soxhlet Extraction of Reservoir Rock

	Chemicals	**Volume / mL**	**Ratio**
Extraction 1	DCM and MeOH	40	93:7
Extraction 2	DCM and MeOH	40	93:7
Extraction 3	THF, acetone and MeOH	40	50:25:25
Extraction 4	THF, acetone and MeOH	40	50:25:25
Extraction 5	THF, acetone and MeOH	40	50:25:25

Soxhlet Extraction of Outcrop Rock

	Chemicals	**Volume / mL**	**Ratio**
Extraction 1	THF, acetone and MeOH	40	50:25:25

Table 3.1: Details of chemicals used for Soxhlet extraction.

3.5 Micro Computed Tomography (Micro-CT)

Micro computed tomography (Micro-CT) is a non-destructive technique which uses X-rays which are partially absorbed by the sample and can be used to determine the spatial distribution of material in the sample (Figure 3.4). The attenuation of a beam passing through a sample is given by the Beer-Lambert law in Equation 3.6, where I_0 is the X-ray intensity initially, I is the X-ray intensity after passing through the object, μ is the X-ray attenuation co-efficient, and t is thickness of absorbing material. The transmitted X-rays fall on a 2D detector to create a projection image

of an object. Generally, because the electron density of an atom determines its X-ray absorption, the denser the material, the more X-rays are absorbed and the darker the area produced in the image. Materials with a high atomic number, such as lead, may absorb X-rays too much and therefore cannot be readily imaged. Conversely, low atomic number elements such as beryllium are difficult to image due to low attenuation rates. [26]

The object of interest is rotated in 0.5° intervals and another projection image is taken. This is repeated until 360° rotation of the sample is reached. Careful analysis of this group of transmitted images can be used to produce a 3D model of the sample. The reconstruction requires significant computational power.

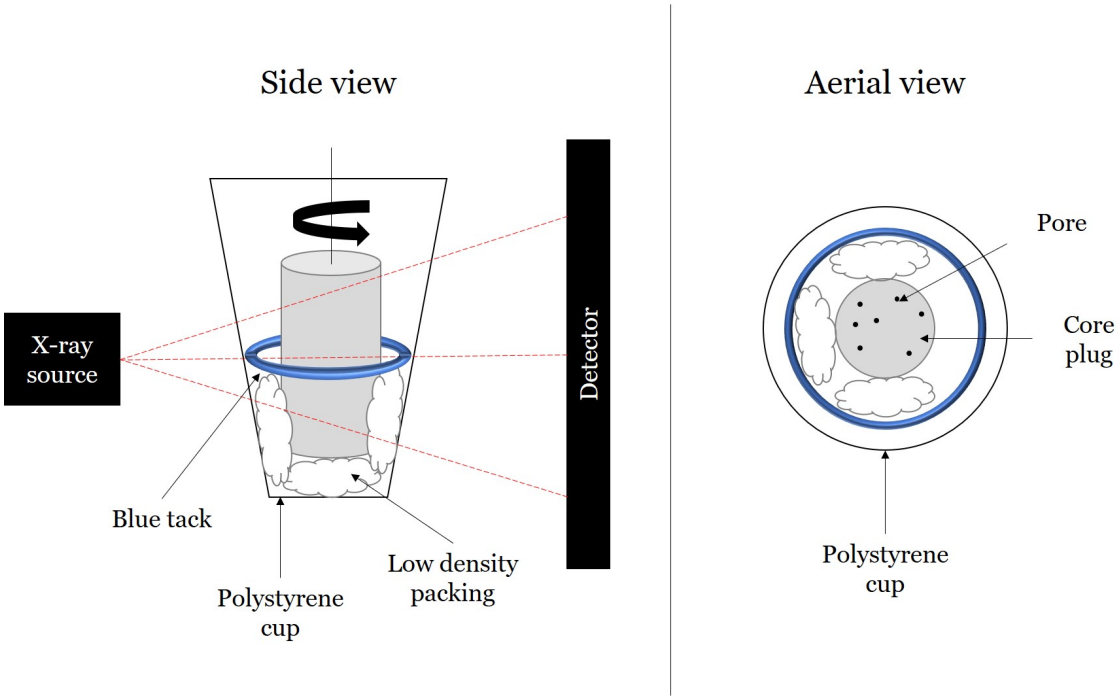

Figure 3.4: Micro-CT scan sample preparation. Low density packing material used to differentiate sample and background. A high density source is used to differentiate between top and bottom segments. Side (left) and aerial (right) view shown.

$$I = I_0 exp^{-\mu t} \tag{3.6}$$

Micro-CT was conducted with Mr Jaap Saers at The Cambridge Biotomography Centre on a Nikon XT H 225 ST industrial scanner. Figure 3.4 shows the sample preparation. A high-density material (blue tack) was placed on-top of the packing material, providing spatial reference. The boundary between density of 'dividing' material can be observed on the images; thus allowing 'stitching' of images to create a full stack.

3.6 Energy Dispersive X-rays and Back-Scattered Electrons

Energy dispersive X-rays (EDX) is an analytical technique where an excitation source (electron or X-ray beam) is focussed onto the sample. The beam interacts with the low energy level electrons of the elements present in the sample and eject a low energy electron, causing a vacancy that is subsequently filled by a higher energy electron to stabilise the atom. When the higher energy electron fills the lower energy vacancy, excess energy is emitted in the form of X-rays. The X-rays are element specific allowing the identification of the atom. EDX is a common feature of many electron microscopes.

Back-scattered electrons (BSE) are formed when an electron beam is focussed onto the sample, and electrons from the specimen atoms are scattered back, essentially along the incident beam direction, into a detector (Figure 3.5). As heavy elements with higher atomic numbers will backscatter electrons more strongly than lower atomic number elements, the BSE map will show heavier elements as brighter, and lighter elements as darker areas.

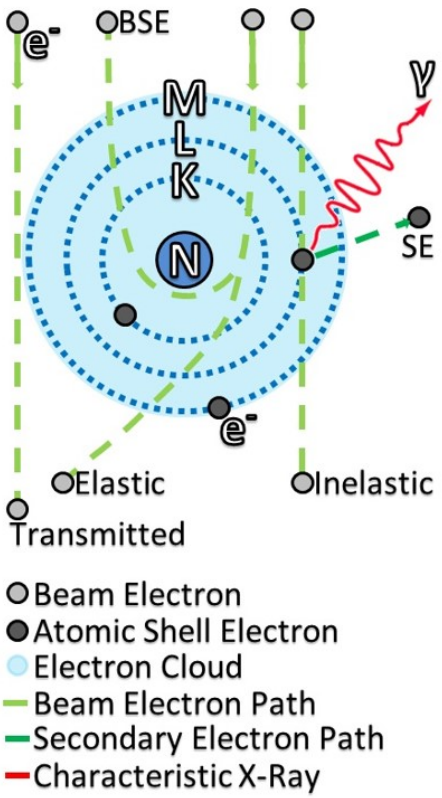

Figure 3.5: Generation of backscattered electrons and X-rays that are characteristic of each element.

Both EDX and BSE are used in scanning electron microscopy (SEM) methods as analytical 'add-ons' to identify the elements present in a sample and couple it to an electron microscopy image of a sample.

3.7 X-Ray Fluorescence

X-ray fluorescence (XRF) is a technique which utilises X-rays for elemental analysis of a bulk material. X-rays are generated from a suitable X-ray source and directed at the sample (Figure 3.5). The X-rays interact with the low energy level electrons of elements present and eject a low energy electron, causing a vacancy which is subsequently filled by a higher energy electron to stabilise the atom. When the higher energy electron fills the lower energy vacancy, excess energy is emitted in the form of secondary X-rays. The secondary X-rays wavelength are element specific, allowing the identification of the atom.[159] The difference between XRF and EDX (via an electron microscope)is the excitation source: XRF uses an X-ray beam whereas electron microscopes use an electron beam excitation source, but essentially reveal similar element specific information.

Sample preparation to identify the major elements (most abundant in the sample) requires a fused bead of the sample to be produced. Results are typically reported in wt %. Sample preparation for trace element analysis is via production of pressed powder briquettes, with results reported in ppm. Fused beads give a homogeneous sample and minimal matrix effect (X-rays produced from lighter elements are absorbed by heavier elements in the sample, thus lowering their observed intensity; heavier elements can enhance lighter elements' intensity by secondary fluorescence), buffered by the melting reagent, and no correction is required: the intensity of emitted X-rays is directly proportional to the concentration of element in the fused bead. Pellets are used when the trace element is incompatible with the fused bead production.[160,161]

XRF was conducted using the PANalytical Axios Advanced X-Ray Fluorescence spectrometer which runs a 4 kW rhodium anode end window super charp ceramic technology X-ray tube at the University of Leicester. Samples were created for reservoir core as received, outcrop core as received, solvent-washed reservoir core, and solvent-washed outcrop core.

3.8 Qualitative Evaluation of Minerals with Scanning Electron Microscopy

Quantitative evaluation of minerals by scanning electron microscopy (QEMSCAN) is a fully automated technique that involves a scanning electron microscopy (SEM) platform to establish the mineralogy of a sample. The approach utilises an electron beam source, with a combination of four energy-dispersive spectrometers to generate EDX spectra. BSE that are measured are coupled with the electron-induced secondary X-ray emission spectra that can classify sample mineralogy. Figure 3.6 shows the QEMSCAN image analysis of a sample.[162,163] QEMSCAN allows determination of mineralogy, grain size, shape, and porosity (that aids understanding of fluid flow through the rock, although not the focus of this work). Analyses were performed by conducting scans which provide a chemical spectrum of the sample (Figure 3.6 b). An EDX spectrum for each pixel was generated and processed using species identification protocol (SIP, Figure 3.6 c) files that compares the peak positions against a database of known mineral species to identify the minerals present at each point based on their characteristic X-ray and backscatter intensities from an ideal mineral in the database. (Figure 3.6).[162,163]

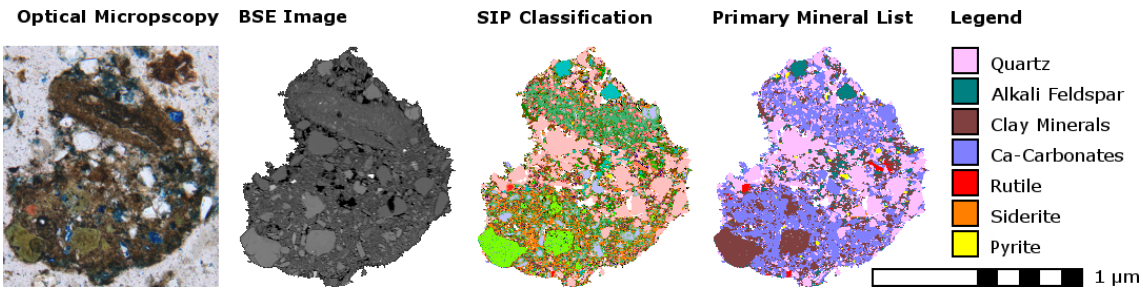

Figure 3.6: Generation of a QEMSCAN image. (a) under optical microscopy, (b) using back scattered electrons from SEM, (c) shows sample identification procedure (SIP) where energy dispersive X-rays characterise elements, and (d) shows the final mineral map.

QEMSCAN was conducted in the University of Cambridge, Department of Earth Sciences with Dr Iris Buisman on a Quanta 650F SEM. Samples were prepared by stabilising particles of the ground rock in resin blocks and sputtering with carbon to prevent charge build-up during detection.

3.8.1 QEMSCAN Data Analysis

Mineralogy was determined using iDiscover software and the database of known minerals and matching each pixel to a mineral, which uses the identification

approaches outlined above. This software has a range of image analysis options available; however, it is unable to determine minerals that line the pore boundaries, which is the focus of this work. To determine which minerals coat the pores, the mineral-pore boundary composition was determined using a script written with the help of Patrick Welch (Computer officer at BPI, University of Cambridge) in C++ (Appendix A). In addition, new images were specifically created to assess the interpretation and likely errors from the code.

Figure 3.7 shows proof-of-concept images for the (a) input and (b) output for mineral-pore boundary determination. Figure 3.7 (a) shows the input with two different minerals, 33 % quartz (pink) and 66 % kaolinite (purple), lining pores (white).

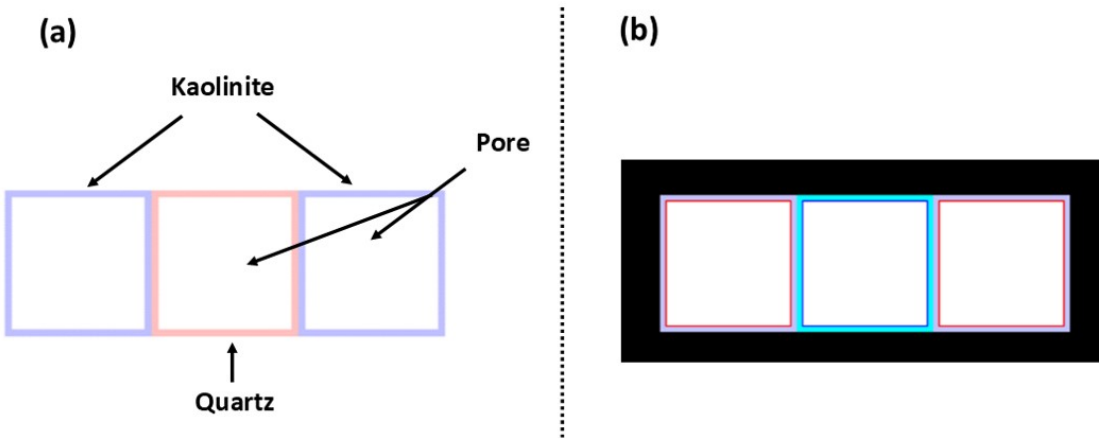

Figure 3.7: Test images of (a) input and (b) output for image analysis of QEMSCAN data to determine mineral-pore boundaries.

Before the script is run, the areas of interest need to be assigned. Colour #1 should be the pore colour (e.g. white, RGB value 0, 0, 0), colour #2 should be the mineral of interest (in the case of the test image, kaolinite purple, RGB value 192, 63, 0). Any other minerals that are not the colour of colour #2 will be assigned a light blue.

When the script begins, it determines whether the input image has a white border, which is highlighted as a black border on the output image: this is to differentiate the white image border from a white pore space.

The script starts at the first pixel, analysing in a clockwise loop for contact with a white space (pore) that is not the boundary and will assign each edge of the pixel with a 1 (yes, the edge is in contact with a pore) or 0 (no, the edge is not in contact with a pore). The output image visually depicts a '1' as a red line, and a '0' as a blue line, so the output pore-mineral edge can be easily observed. Once all four

edges of a pixel are assigned, the script moves left to right, top to bottom, onto the next pixel.

Figure 3.7 (b) shows the output image for the test image in Figure 3.7 (a). Kaolinite is the focus of the image as it has retained its original colour and quartz has been labelled as 'other' mineral, depicted by a light blue. The edges of the kaolinite that are in contact with a white space (assigned as a pore) are highlighted in red, whereas the non-kaolinite 'other' mineral-pore boundaries are highlighted in dark blue. A ratio of the total pore-edge of the mineral of interest and the total pore-edge of all minerals is then calculated, shown in Equation 3.7

$$pore\text{-}mineral\ edge\ \%coverage = \frac{total\ pore\text{-}edges\ of\ mineral}{total\ pore\text{-}edges\ of\ all\ minerals} \times 100 \tag{3.7}$$

A flowchart in Figure 3.8 goes through the process of pore-edge identification and assignment and the percentage pore-edge coverage determination.

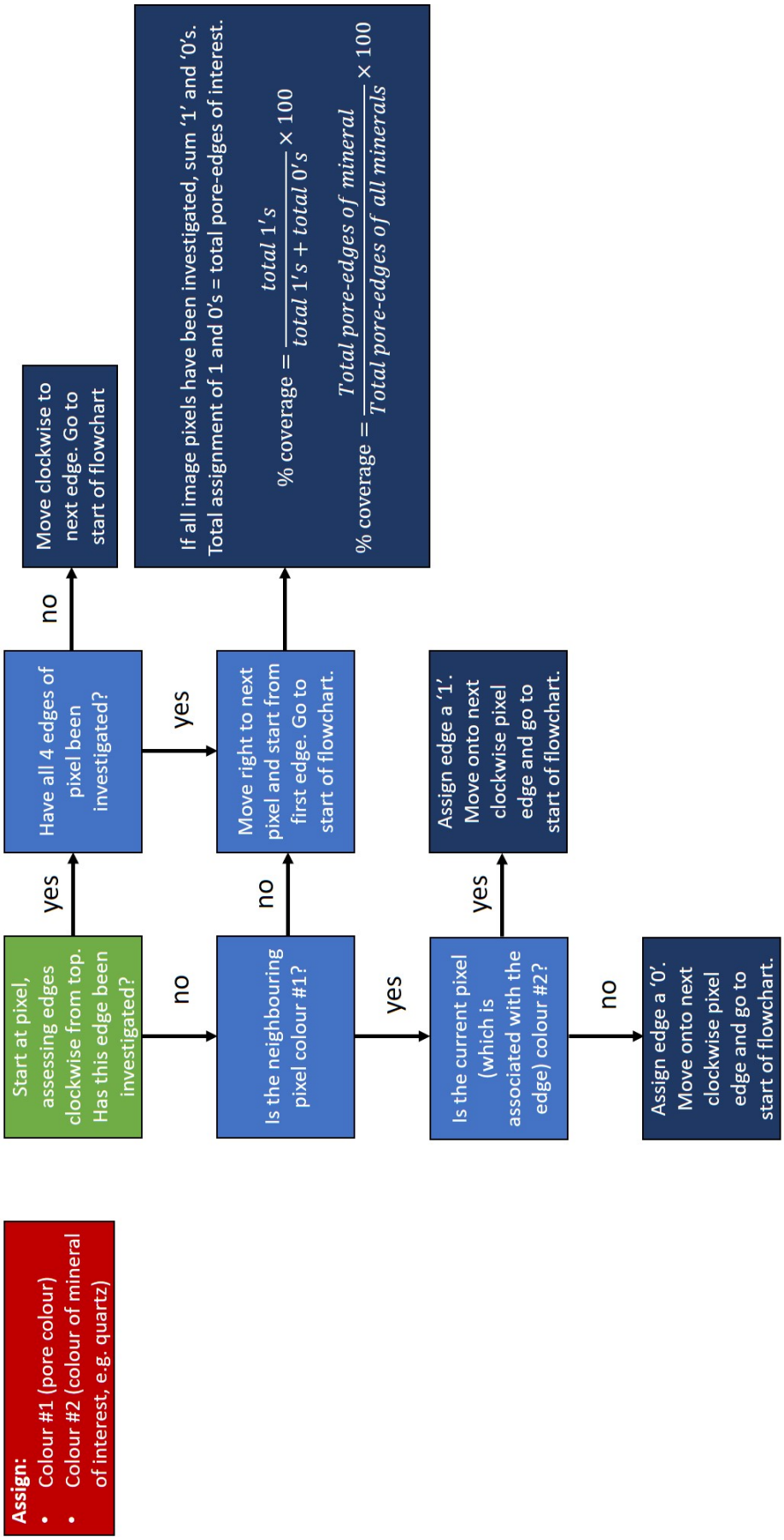

Figure 3.8: Flowchart showing the process of calculating pore-mineral edges from QEMSCAN images.

3.9 Solution ^{1}H and ^{13}C Nuclear Magnetic Resonance

Solution phase nuclear magnetic resonance (NMR) was evaluated as a method to determine the chemical composition of organics washed off the mineral samples.

NMR considers the behaviour of a sample nuclei in a magnetic field. The classical model relies on non-coupled nuclei that possess a spin of ± ½. When no magnetic field is applied, the ^{1}H (or ^{13}C) nuclei are orientationally disordered. Upon application of the magnetic field, the magnetic moments of the nuclei are aligned with or against the applied field and the energies of the up and down spin states are now different. The field experienced at the nuclei also depends on the local electron distribution.

An electronegative group attached to a proton will cause the electrons to be removed from the hydrogen nucleus and the field experienced will be larger than one where the electrons shield the proton of interest. This behaviour results in protons in different chemical environments experiencing different external magnetic fields and hence the nuclear energy levels have different separations. This means different energies are required to excite the nucleus. This behaviour is visualised in NMR spectra as a chemical shift downfield from a standard (usually tetramethyl silane – TMS). The chemical shifts for different functionalities are tabulated. In addition, the proton NMR spectra allows quantification of amount of protons in these different environments from the peak height and area.

Solution NMR was conducted at the University of Cambridge Department of Chemistry with MeOH-d4 on a Bruker 500 MHz DCH Cryoprobe Spectrometer. Samples used for analysis were taken from the solvent extractions of organics recovered from the reservoir and outcrop rock samples, as discussed above.

3.10 CHN Elemental Analysis

A CHN analyzer (carbon, hydrogen and nitrogen) allows for determination of C, H and N levels in a small amount of sample via flash combustion. The sample ($\sim$ 5 mg) is rapidly heated to 900 °C in oxygen to promote complete combustion, producing carbon dioxide, water, and nitrogen. The gases are passed over columns, which measure thermal conductivity. The first column absorbs carbon dioxide and water. A second column separates nitrogen from residual carbon dioxide and water. C, H

and N content are determined by conductivity relative to a calibration standard of known C, H and N levels. The precision is typically 0.1 % of the initial sample mass. It is important to note that this method cannot determine the amount of oxygen in a sample.

CHN analysis is a destructive technique used for both powders and liquids and was conducted at the Department of Chemistry by Stephen Young and Dr Nigel Howard.

3.11 Thermogravimetric Analysis Mass Spectrometry

Thermogravimetric analysis (TGA) provides information about mass loss of a sample over time upon the application of heat to a sample (Figure 3.9). In this work the main interest was the amount and chemical nature of the evolved components, representing the organics on the reservoir and outcrop rocks.

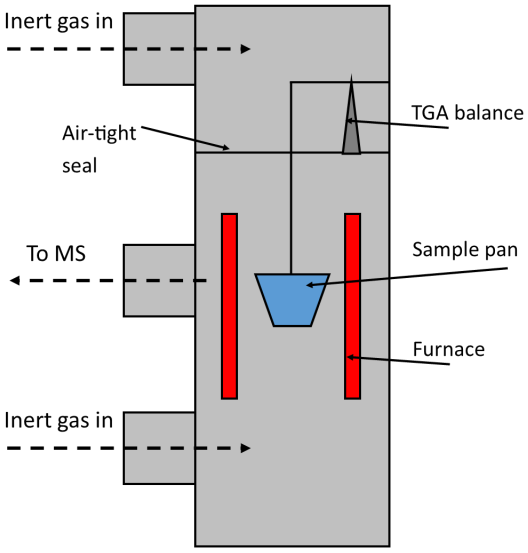

Figure 3.9: Simple schematic of a TGA-MS showing gas entry, sample pan in furnace, port to the mass spectrometer, and TGA balance.

The sample (minimum 30 mg) is loaded onto a sample pan—usually ceramic or platinum metal—before being loaded into the furnace and purged with nitrogen or air, ready to begin heating at a predetermined rate. The high precision balance accurately measures any mass loss over time (temperature) and the purging gas sweeps volatile compounds from the balance and sample. Therefore, loss of material is captured by a loss of mass. On some rare occasions the sample mass can increase, for example, metals forming oxides by picking up oxygen from the air.

The TGA used in this study was coupled with a mass spectrometer (TGA-MS) so any volatile compounds were swept into the MS for fragmentation detection and identification. After reaching the target temperature, the furnace is allowed to cool to room temperature before removal of remaining 'char'. If desired, the char can be analysed via PXRD for a complete picture of what is lost and what is left after thermolysis.

3.12 Stable Isotope Analysis

Stable isotope analysis is used to determine the distribution of specific stable isotopes of an element in the sample. This study focuses on the two stable and naturally occurring isotopes of carbon: ^{12}C and ^{13}C (naturally occurring in a 98.89 % and 1.11 % abundance respectively). Firstly, there are two fractionation mechanism's to consider that might lead to a change in this natural abundance ratio: kinetic and equilibrium. Kinetic fractionation is the process which separates stable isotopes during particular processes. An example is assimilation of atmospheric CO_2 during photosynthesis preferentially takes up ^{12}C, thus making plant material depleted in ^{13}C relative to other inorganic carbon on Earth.[164] Equilibrium isotope fractionation is the partial separation of isotopes from processes that are in equilibrium; the effect is greatest at low temperatures. An example of equilibrium fractionation is water vapour condensation. The heavier water isotopes ($H_2{}^{18}O$ and D_2O) stay in the liquid phase, whereas the lighter isotopes remain in the vapour phase.[165,166] As both the kinetic and equilibrium fractionation effects are very small, they are reported in per mil (‰) and represented as a ratio of heavy to light isotope in the sample, over the ratio of a standard (Equation 3.8):

$$\delta^{13}C = \left(\frac{\left(\frac{^{13}C}{^{12}C}\right)_{sample}}{\left(\frac{^{13}C}{^{12}C}\right)_{standard}} - 1 \right) \times 1000‰ \tag{3.8}$$

The standard used for δ^{13}C was a marine fossil from the Pee Dee Formation in South Carolina. It has a high ^{13}C:^{12}C ratio of 0.0112372 and was assigned to be the δ^{13}C zero value. Using this standard, known as the Pee Dee Belemnite (PDB), a sample will usually yield a negative δ^{13}C. As all of the original fossil was used up, a new reference standard is used, known as the Vienna PDB (VPDB) and calibrated to the PDB to indicate normalised values to the PDB.[165–167] According to Equation 3.8, assuming kinetics/photosynthesis is the main mechanism in determination of δ^{13}C, a sample that is based on plant based sources (photosynthesis) results in more

atmospheric ^{13}C being captured in the sample, leading to a higher ratio and thus more positive value of δ^{13}C, compared less photosynthesising plant content. The greater the atmospheric ^{13}C content means more is absorbed by the ocean during its carbon cycle. From this, marine sediments will be expected to have a small negative or small positive δ^{13}C relative to terrestrial sediments, which will have a more negative δ^{13}C.[168–170]

Stable isotope analysis was also used to determine the total organic carbon (TOC) content of samples. This is achieved by measuring the total carbon content, then measuring inorganic carbon (through degradation of the carbonates) from an acidified aliquot of sample. Total organic carbon is the difference between the total carbon measurement and the total inorganic carbon measurement (equation below).

$$Total\,carbon = (inorganic\,carbon) + (organic\,carbon) \tag{3.9}$$

Carbon isotope analysis was performed using a Costech Elemental Analyser (ECS 4010) connected to a Thermo Scientific Delta V Advantage isotope ratio mass spectrometer, at the University of Durham. Carbon isotope ratios were corrected for 17O contribution and reported in standard delta (δ) notation in per mil (‰) relative to Vienna Pee Dee Belemnite (VPDB), as discussed above. Analytical uncertainty in δ^{13}C was ±0.1 ‰ or better for replicate analyses of the international standards. Total organic carbon was obtained as part of the isotopic analysis using an internal standard (Glutamic Acid, 40.82 % C).[171]

3.13 Pyrolysis Gas Chromatography Mass Spectrometry

Pyrolysis gas chromatography mass spectrometry (Py-GCMS) is similar to TGA-MS (Section 3.11) as heat is applied to the sample, material is lost and MS detects fragments. The main difference is the rate of heating: Py-GCMS is flash heating; the rate of heating is very high—typically 120 000 times quicker than TGA. Rapid/flash heating versus the slower rate of heating of the TGA is considered to avoid any chance of fragments reacting with each other and/or exposed surfaces in a TGA environment. This means that the fragments detected may be more representative of the species on the surface. Py-GCMS is used to investigate molecules that will not come off the surface after a solvent wash (irreversibly bound molecules).

Figure 3.10 shows a schematic of Py-GCMS. 0.5 mg of sample is packed in a quartz tube between two pieces of quartz wool. The quartz tube with the sample is loaded into the heating element of a pyroprobe. The pyroprobe is inserted into an airtight chamber where helium purges the system and it is brought to a thermal equilibrium. After 10 minutes, power is supplied to the heating element and heats the sample to a pre-defined temperature, which is held for a short period of time whilst pyrolysis occurs. Any volatile molecules are moved from the chamber to a trap by the purging carrier gas. The trap contains a material which has an affinity for several functional groups and is maintained at a low temperature to promote condensation. Any fixed gases such as CO_2, CO, H_2 and N_2 which are not absorbed will go directly to a fixed gas analyser (a GC coupled with a thermal conductivity detector).

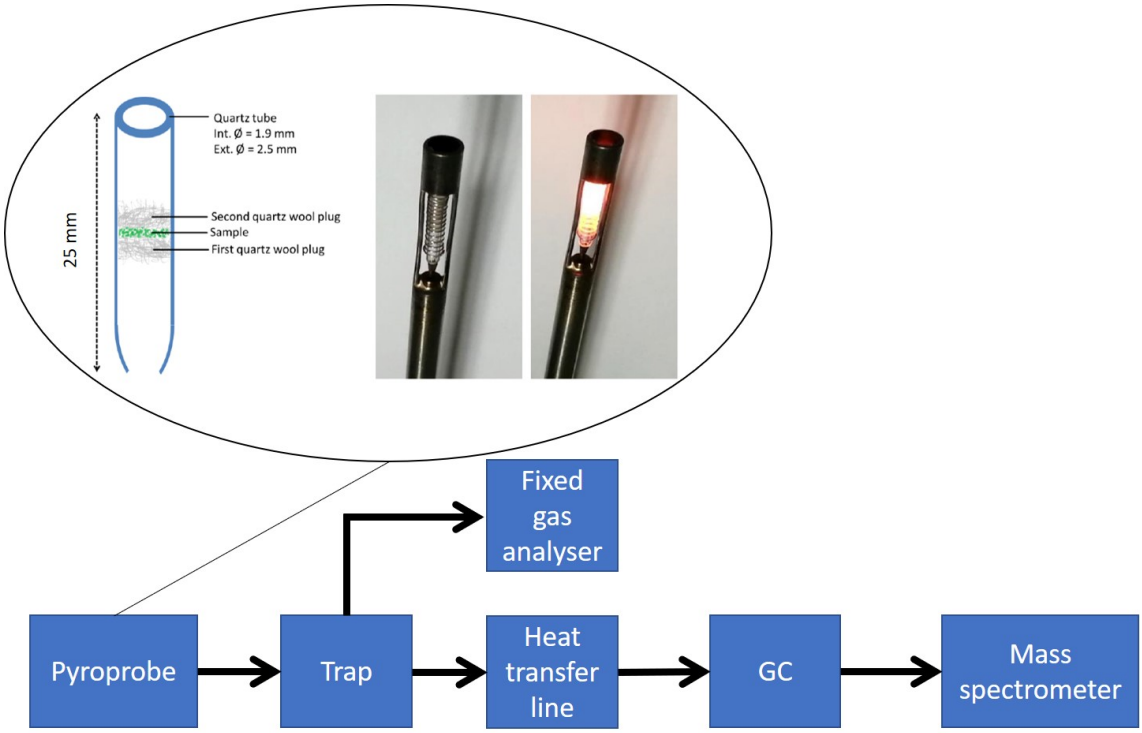

Figure 3.10: Py-GCMS schematic.

After pyrolysis has completed, products collected on the trap are allowed to desorb upon application of heat to the trap, and the carrier gas is redirected to the GC causing a small amount of material to be sent for analysis. The complex material is swept along a GC column and retained depending on its affinity to the column stationary phase. Further enhancement of separation is achieved via method development of the gas flow rate and GC oven temperature. After the compounds have eluted from the GC column, they are detected by a mass spectrometer: high energy electrons bombard the eluted molecules. The positively charged ions are

accelerated and deflected in a magnetic field before being detected (separation occurring based on their mass-to-charge ratio m/z). The GCMS results are a presented as a plot of the ion fragments detected over time and are assigned via a library of known compounds. The char after pyrolysis can be weighed and accurate losses calculated from integration of GCMS peaks.

Standard pyrolysis procedure will flash heat a sample to a single temperature, but it is possible to use two or more temperatures: A method for producing fractionations of biomass components, such as sugars and lignins, has been developed, known as a 'two-step' process. The first stage in the process heats the sample to a 'low' temperature (usually 300–350 °C), which usually pyrolyses low molecular weight oxygenated compounds (organic acids, aldehydes, ketones). The second stage heats the sample at 400 °C and pyrolyses lignin biomass.[172–174] The benefit of the two-step process is the first heating step 'pre-treatment' where lignin-derived intermediates are not pyrolysed, and remain for the higher pyrolysis temperature, resulting in a clearer spectrum of smaller molecular weight compounds (from the first step) and lignin-derived intermediates (second step).

When conducting Py-GCMS, the one step process of heating to a single temperature was used. Settings used for this study are shown in Table 3.2:

Parameter	Setting	Comment
Pyroprobe (CDS 5200)		
Pyroprobe heating	Heating at 10 °C ms^{-1} to temperature and held for time	
Trap	Tenax®TA (poly(2,6-diphenylphenylene oxide))	150 mg, 20–35 mesh
Trap absorb / desorb	50 °C (2 minutes) / 280 °C (2 minutes)	
Purge gas flow	Helium, 15.0 ± 0.5 ml min^{-1}	By Ellutia 7000 Flowmeter
Transfer line temperature	300 °C	
Quartz sample tube	CDS (L = 25, ID = 1.9, OD = 2.5 mm)	Cleaned at 1000 °C in air
Quartz wool	H. Baumbach, 4 /mum diameter	Cleaned at 1000 °C in air
Sample size	0.2–0.5 mg	Weighed on a Sartorius SE2 microbalance
Gas Chromatograph (Agilent 7820A GC)		
Column	Thermo Scientific TraceGold: capillary TG-1701MS (60 m X 250 /mum X 0.25 /mum)	14% cyanopropylphenyl 86% dimethyl polysiloxane
Inlet temperature	300 °C	
Septum	Agilent CrossLab 9.5 mm inlet septum	
Oven program	40 °C (hold 2 mins), heat at 10 °C min^{-1} to 250 °C (hold 10 mins). Total = 33 mins	
Column head pressure	Initial = 10.7 psi (40 °C) Final = 24.36 psi (250 °C)	
Column flow rate	Constant flow = 0.68 mL min^{-1}	
Mass Spectrometer Detector (Agilent 5977E MSD)		
MS source temperature	230 °C	
MS quad temperature	150 °C	
Electron ionisation (EI)	70 eV	
Mass detection range	1.6–300 amu	0.1 amu incements
Analysis	Agilent MassHunter B.06.00	NIST 11.L (MS library)
Fixed Gas Analyser (TCD CDS 5500)		
Oven parameters	35 °C (hold 5 mins), heat at 20 °C min^{-1} to 250 °C (hold until end of GCMS run)	
Column	Carboxen 1000 (60–80 mesh): packed	I.D. = 1/8”, L = 9’
TCD bridge current	150 mA	
Carrier gas flow	Helium (CP grade, BOC), 15.0 ± 0.5 mL min^{-1}	By Ellutia 7000 Flowmeter
Analysis	ChromPerfect 6.0.10	

Table 3.2: Parameters used for pyrolysis gas chromatography mass spectrometry.

3.14 Time of Flight Secondary Ion Mass Spectrometry

Time of flight secondary ion mass spectrometry (TOF SIMS) is a surface sensitive analytical technique used to analyse composition of a surface. The method uses an ultra-high vacuum chamber where the sample is bombarded by ions from a primary beam. The primary ion beam produces several sputtered fragments from the molecules at the sample surface such as mono- and polyatomic species. There may also be re-sputtering from the primary ions. Secondary ions formed from the sample can be positive or negative and will be detected by a mass spectrometer. Peak assignment is then conducted to determine which ions / fragments are produced from the surface. TOF-SIMS is ideal to investigate irreversibly bound organics. However, it may rip molecules to pieces and could yield a false positive.

TOF-SIMS also has the capability to depth profile a sample: a primary ion beam generates secondary ions from the sample as discussed above, whilst a secondary ion beam is used to etch away at the sample surface, enabling the primary ion beam to simultaneously aid production of secondary ions from the new surface (Figure 3.11). This is destructive as it removes layers from the surface. The variation of intensity of a specific m/z ratio peak is measured as a function of 'sputter time'. Theoretically, the more time spent sputtering the sample, the greater the depth in the sample which will be analysed. However, the depth scale requires calibration.[175]

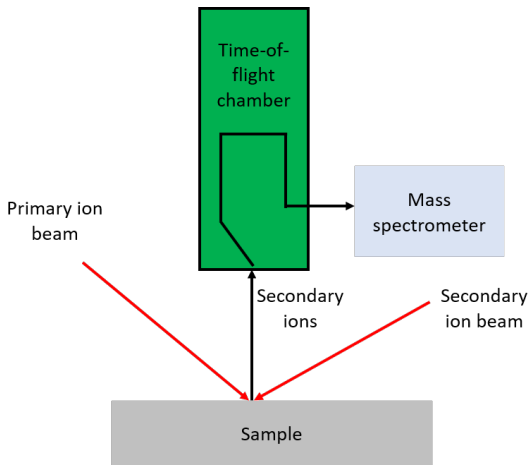

Figure 3.11: TOF SIMS schematic showing the main components of a dual beam setup.

One key problem is the contamination of poly-dimethyl-siloxane (PDMS) in TOF-SIMS which is present in essentially all datasets, even if not consciously in the sample of interest. This is often attributed to use of any tape (i.e. to secure samples when mounting, the procedure utilised here) or ineffective cleaning of silicon wafer

substrates.[176] Cleaning methods conducted in hexane have been found to remove such siloxane contaminations, but can only be used on ceramics, metals, and some polymers.[177] PDMS signals may confuse any signals for silica based compounds, which are of interest here.

TOF-SIMS was conducted at Imperial College London, using the IONTOF TOF-SIMS V instrument in the Department of Materials. Both raw and solvent washed samples were analysed and prepared by adhering the particles to a mounting stub for analysis. The samples were placed under ultra-high vacuum in a field of 2500 V as to minimise sample charging, with a dual beam (Cs^+ sputter beam and bismuth probe beam) arrangement. A sputter time of 0.5 seconds was used when depth profiling.

3.15 High Resolution Mass Spectrometry

High resolution mass spectrometry (HRMS) is a used to detect molecular species to the nearest 0.0001 atomic mass unit. This very high precision enables identification of each component of even very complex multicomponent mixtures. It is a relatively new approach in this area of work. Therefore, data reported using this technique is very important and holds a lot of new information in the field.

It is notably used in electrospray ionisation (ESI) mode as the sample does not separate or undergo esterification leading to successful analysis of organic acids ((−)ESI) and organic bases ((+)ESI).[178] ESI is an electrospray where a high voltage is applied to a liquid to create an aerosol before entering the mass spectrometry chamber.

For ESI experiments, the oil/extract sample is dissolved in toluene-methanol (6:4 v/v solution). The solution was doped with 0.1 wt % ammonium hydroxide prior to the negative electrospray ionization measurement (−)ESI. The high-resolution instrument used for the analysis is a QExactivePlus Orbitrap Mass Spectrometer (from Thermo Scientific) which was operated from m/z range of 133–2000. The ESI conditions were spray voltage of 3 kV, and transfer capillary temperature of 350 °C. Thermo Xcalibur (version 3.0.63, from Thermo Scientific Inc.) and PetroOrg (version 18, from Florida State University) were used for the data processing.

HRMS was run at BP Pangbourne, Reading, by Nathalia Tessarolo with data analysis help from Huang Zeng at BP Houston, Texas.

3.16 X-Ray Reflectivity

X-ray reflectivity (XRR) may be used to determine detailed information concerning surface features including thickness and roughness of thin film layers, following optimisation of theoretical models to fit experimental data. As X-rays interact with electron density, XRR will only detect elements with a significant atomic mass, and thus cannot easily measure the hydrocarbon adsorbed layers of interest in this work, unlike neutron reflectometry. However, it is a useful method to confirm the structure of deposited inorganic films. Furthermore, the instruments used here cannot penetrate a solvent environment, and so measurements are restricted to the solid/air interface.

Experiments at the solid/liquid interface are possible but the pathlength of the X-ray beam must be as short as possible to stop total attenuation of the X-ray beam when passing through the liquid medium. The application of synchrotron radiation to XRR has allowed the study of a wide range of soft matter systems, including surfactants, membranes and proteins.[179–181] However, due to the high brilliance of current synchrotron X-ray sources the study of organic molecules is hampered by radiation damage, which can destroy the sample being analysed.

X-ray reflection experiments were used to characterise the surface of substrates used in neutron reflection before neutron beam time experiments to test for roughness, film thickness and cleanliness. X-ray reflectivity is calculated in a similar way to neutron reflectivity using the Abeles matrix method and classical optics (Section 3.17.5).[182]

$$n = 1 - \sigma + i\beta \tag{3.10}$$

$$\sigma = \frac{\lambda^2}{2\pi} r_{\mathrm{e}} \rho_{\mathrm{e}} \tag{3.11}$$

$$\beta = \frac{\lambda}{4\pi} \mu_{\mathrm{x}} \tag{3.12}$$

The X-ray refractive index (n) is related to the electron density of the material (ρ_{e}) and the classical electron radius ($\mathrm{r_e}$) as shown in Equations 3.10 and 3.11. The imaginary part of the refractive index ($\mathrm{i}\beta$, where β is calculated from Equation 3.12) plays a more significant role in XRR compared to neutron reflectivity, as the X-ray absorption cross-section is much larger.

XRR experiments were carried out in the Materials Characterisation Lab at ISIS using a Rigaku SmartLab X-ray diffractometer in reflectivity mode. Data was fitted using GenX 2.0.0.

3.17 Neutron Reflectometry

Neutron reflectometry (NR) is a powerful surface-specific technique which allows for determination of adsorbed layer composition, thickness, and roughness. Neutrons are subatomic particles that can penetrate most materials because they have no charge, interacting with the nuclei of a sample's atoms, rather than surrounding electrons (in contract to when X-rays are employed). Here the elastic scattering of neutrons is considered. The section below covers a brief description of mathematical and practical considerations of NR data analysis.[183–187]

3.17.1 Neutron Refractive Index

Neutrons have a wave-like nature, which allows neutron reflectometry to be treated similarly to reflection of visible light from a surface, following the laws of classical optics. Although in classical optics the angles are conventionally defined relative to the surface normal (Q_z), the angles in neutron and X-ray reflectometry are traditionally defined with respect to the surface plane (Figure 3.12).

In specular reflectometry, the angle of incidence and the angle of the reflected beam are the same; in this geometry, the scattering reveals the structure perpendicular to the surface. Off-specular scattering can be observed when there is a structure parallel to the interface, and incident and reflected angles are not the same. Off-specular scattering will not be discussed in this thesis.

All materials have a neutron refractive index, n, which dictates the speed and momentum with which a neutron passes through a material, given as a ratio between neutron wavevectors k and k_0, which are wavevectors in the medium and in a vacuum respectively (Equation 3.13):

$$n = \frac{k}{k_0} \tag{3.13}$$

3.17.2 The Critical Angle

When a neutron passes from one medium to another it can either be reflected or transmitted. If the neutron is transmitted, it will speed up or slow down depending

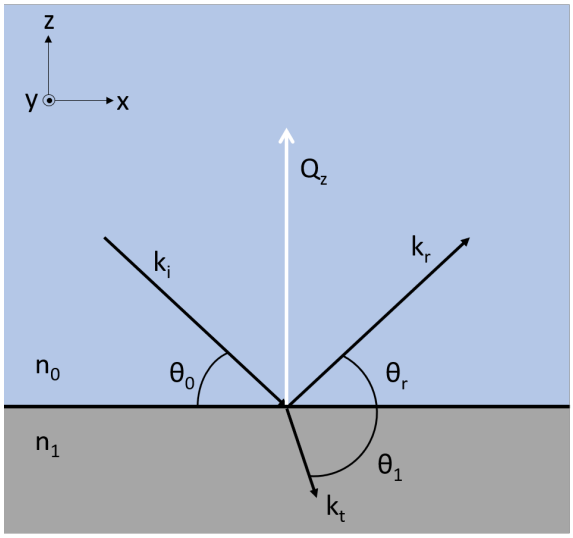

Figure 3.12: Diagram of neutron reflectometry geometry. n_0 and n_1 are the neutron refractive indices of phase 0 and 1. k_i and k_r are the incident and reflected wave vectors. θ_0, θ_r and θ_1 are the angles of incidence, reflection and transmission. Q_z is the momentum transfer normal to the surface, which is the difference of the two wave vectors and leads to the method giving structural information in the z-direction

on the relative refractive index of the new medium. This changes the angle of the transmitted beam, θ_1, resulting in refraction. Snell's Law (Equation 3.14) describes the direction of the neutrons as changed by the different media due to varying indices of refraction:

$$\frac{n_0}{n_1} = \frac{cos\theta_t}{cos\theta_i} \tag{3.14}$$

At a very low angle of incidence, total reflection may occur. The angle below which total reflection occurs is called the critical angle. The critical angle is a bulk material-dependent property (not surface-dependent) and relates to the ratio of scattering length densities (SLD) of the two bulk phases. The SLD of a material is the sum of scattering lengths divided by the volumes and is essentially another representation of the refractive index of the phase.

At the critical angle, θ_t is equal to 0, therefore $\cos\theta_t$ equals 1, hence $\cos\theta_c = n$. Total reflection occurs until a critical value, Q_c, beyond which transmission of neutrons into the layers begins and the reflected intensity starts to decay.

In neutron reflectometry, the reflectivity—defined as the fraction of incident light reflected from a surface—is acquired as a function of the momentum vector Q_z. Using trigonometry, the z-component of momentum transfer from Figure 3.12 can

be calculated:

$$Q_z = \frac{4\pi sin\theta}{\lambda} \tag{3.15}$$

Neutron Wavevectors in a Medium

The neutron refractive index can be expressed as Equation 3.16.

$$n = 1 - \frac{\lambda^2 \rho}{2\pi} \tag{3.16}$$

where λ is the incident wavelength of neutrons and ρ is the SLD of the medium.

For strong neutron-absorbing and thick materials, there is an imaginary component. However, neutrons are generally very penetrating and the imaginary component is considered to be negligible for this work.

There are two key features that impact experimental neutron reflectometry data: the presence of thin (< 100 Å) adsorbed layers and interfacial roughness. A thin adsorbed layer will cause constructive and destructive interference from neutrons reflected from the top and bottom of the layer, resulting in an increase or decrease of the experimental reflectivity. A rougher surface will cause a lower intensity at higher Q_z. In very extreme cases, the roughened surface causes the specular beam to become diffuse. This will be evident in particular examples in data in Chapter 7.

3.17.3 Reflection from a Surface and Thin Layer

The reflectivity, R, from a single interface can be described using Fresnel coefficients, r. These coefficients describe the fraction of reflected and transmitted radiation across the interface, given in Equation 3.17.[188]

$$r_{01} = \frac{n_0 sin\theta_0 - n_1 sin\theta_1}{n_0 sin\theta_0 + n_1 sin\theta_1} \tag{3.17}$$

R will be equal to 1 at values of $\theta_i \leq \theta_c$ as all radiation is reflected. R is found from the squared modulus of Equation 3.17, known as Fresnel's Law. However, the square relation of this expression prevents the inversion of experimental data to give adsorbed layer structures directly because the phase is unknown. Intensities are measured, but this means the calculation cannot go back to amplitudes required for structural solution. Therefore, the structure is usually solved by fitting the

calculated intensity from a model to the experimental data that is discussed later.

$$R_{01} = \left| \frac{n_0 sin\theta_0 - n_1 sin\theta_1}{n_0 sin\theta_0 + n_1 sin\theta_1} \right|^2 \tag{3.18}$$

As illustrated by Figure 3.13 there are lots of rays that will propagate through the system. The incident, reflected and transmitted waves are described by a wave function, Ψ:

$$\Psi = re^{ikr} \tag{3.19}$$

Where r is the amplitude which can be expressed as a combination of reflected (r_{01}) and transmitted (t_{01}) components. ikr is the phase. In Figure 3.13, the wave reflected at the first interface has an amplitude of r_{01}.

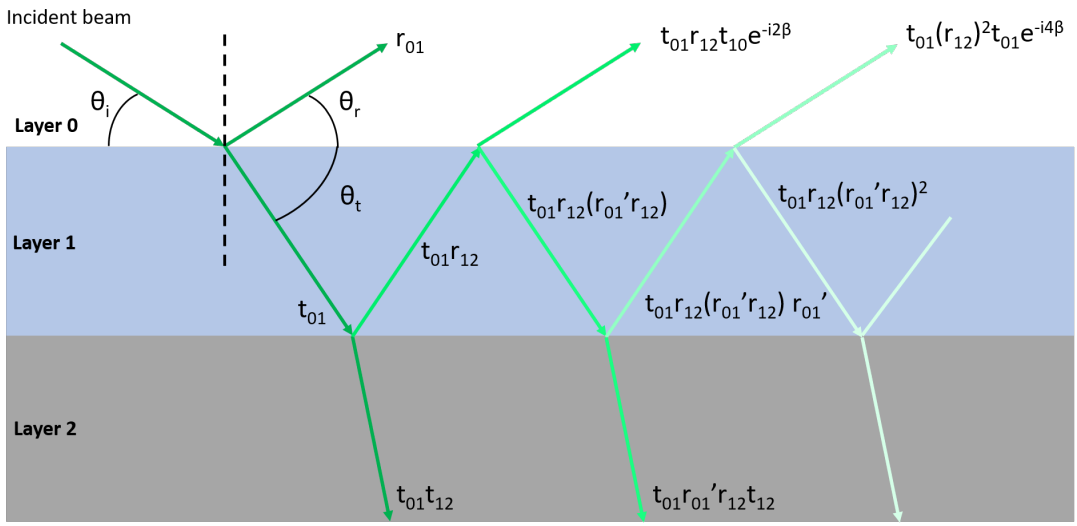

Figure 3.13: Diagram showing reflection and transmission of light by a layer into Layer 0 from Layer 1.

Waves that are reflected more than once will have a phase-lag due to variation of speeds travelling through different media, denoted by β in Equation 3.20:

$$\beta = \left(\frac{2\pi}{\lambda}\right) ndsin\theta \tag{3.20}$$

where d is the layer thickness. The phase-lag causes constructive or destructive fringes known as Kiessig fringes. These are helpful when characterising thicker

films: the spacing of the fringes is equal to $2\pi/d$ and the height of the peaks is related to the difference in SLD between two materials.

By the time a wave is reflected by an interface between a film (Layer 1) and the bulk material (Layer 2) and has arrived back at the original layer, the wave would have travelled across the film twice and therefore the amplitude becomes $t_{01}r_{12}t_{10}e^{-i2\beta}$. The total amplitude for the reflected wave can be expressed as the sum of a geometric progression:

$$r_{total} = r_{01} + t_{01}r_{12}t_{10}e^{-i2\beta} + t_{01}{r_{12}}^2t_{10}e^{-i4\beta} + ... \tag{3.21}$$

Considering $-r_{01} = r_{10}$, the resulting reflected amplitude can be calculated and on squaring results in the reflected intensity R_{012} in Equation 3.22. This notation means the total reflected intensity of a thin layer of material 1 between two bulk phases 0 and 2 where the incident beam is phase 0.

$$R_{012} = \left| \frac{r_{01} + r_{12}e^{-i2\beta}}{1 + r_{01}r_{12}e^{-i2\beta}} \right|^2 \tag{3.22}$$

By expanding Equation 3.22 and using Euler's theorem, the following equation is generated:

$$R_{012} = \frac{r_{01}^2 + r_{12}^2 + 2r_{01}r_{12}cos2\beta}{1 + r_{01}^2 + r_{12}^2 + 2r_{01}r_{12}cos2\beta} \tag{3.23}$$

The trigonometric functions give a periodic oscillation that can be used to find the thickness of the layer (Figure 3.14). Now the thickness of the layer can be determined, d, after assuming the SLD and measuring the reflectivity.

3.17.4 Layer Roughness

Preparing a surface for neutron reflectometry requires it to be polished to ensure minimal roughness on an atomic scale. Roughness introduces a gradual change in the SLD across an interface (Figure 3.15), commonly calculated by applying a Nevot-Croce factor (Equation 3.24) to the Fresnel reflectivity coefficient, where R_0 is the reflectivity for a perfectly smooth surface with no roughness.

Equation 3.24 only holds true when the roughness is less than one-third of the two adjacent layer thicknesses. If that condition is not met, the interface must be constructed from a series of smaller layers with varying SLDs and low roughness.

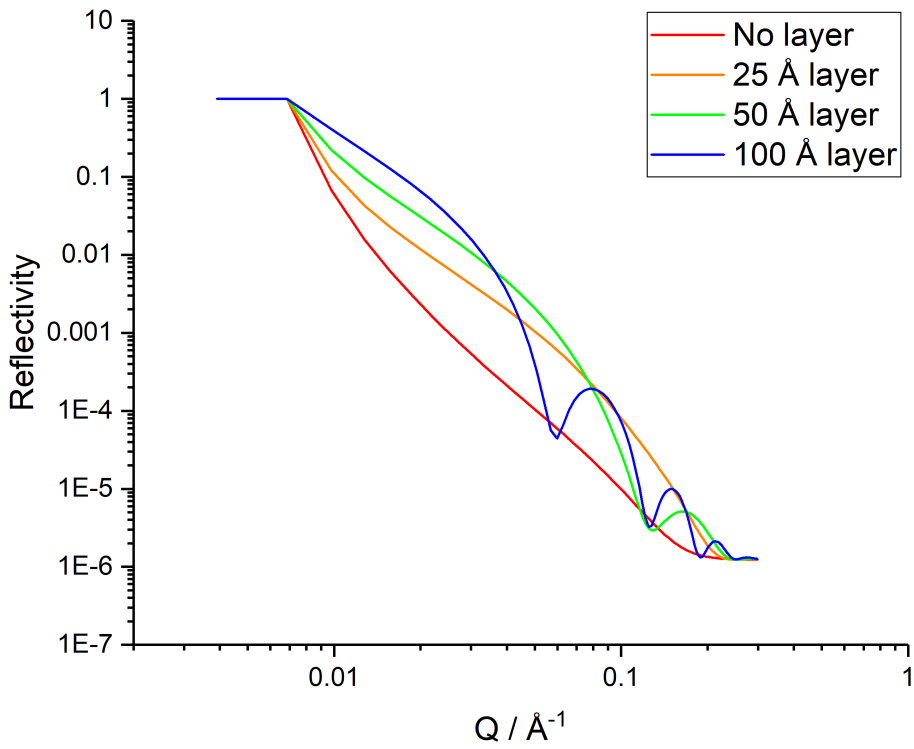

Figure 3.14: Simulated neutron reflectometry data of thin layers at the calcite / d-toluene interface of thickness 25, 50, and 100 Å.

This method is employed later in the thesis because the calcite mineral surface could not be obtained as flat as desired.

$$R = R_0 \exp^{2\sigma j^2 k_j k_{j+1}} \tag{3.24}$$

3.17.5 Matrix Method

To describe reflection from multiple layers, a matrix method is used to solve the reflectivity. This approach is widely available on software such as RasCAL.[189–191]

In the matrix method, each layer is described by a characteristic matrix, C_j, for a layer j, where r_j is the reflected amplitude at the j and $j+1$ interface.

$$C_j = \begin{bmatrix} e^{(i\beta_{j-1})} & r_j e^{(i\beta_{j-1})} \\ r_j e^{(-i\beta_{j-1})} & e^{(-i\beta_{j-1})} \end{bmatrix} \tag{3.25}$$

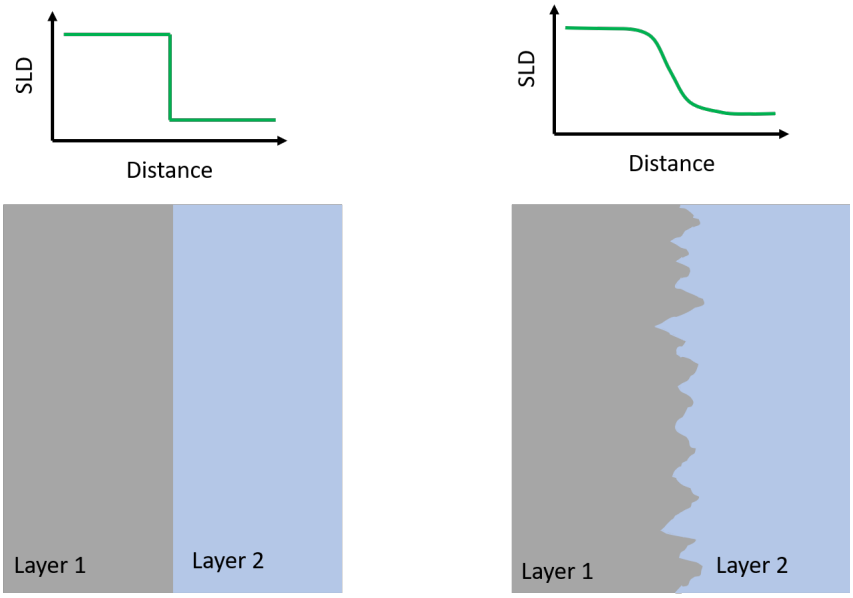

Figure 3.15: Schematic showing the change in SLD for a theoretical flat interface with no roughness and a realistic interface with roughness characteristics.

Multiplying the matrices of each individual layer results in a 2 by 2 matrix which describes the entire system (Equation 3.26):

$$[C_1] \,.\, [C_2] \,.\, [C_3] \ldots [C_{n+1}] = \begin{bmatrix} a & b \\ c & d \end{bmatrix} \tag{3.26}$$

C_1 is the reflectivity of the incident phase and the first layer. C_{n+1} is the reflectivity from the final layer. The reflectivity of the system can then be found (Equation 3.27):

$$R_{tot} = \frac{c.c^*}{a.a^*} \tag{3.27}$$

3.17.6 Reflectivity Calculations for Rough Surfaces

When the roughness of an interface is less than approximately 1/3 of the adjacent layer thicknesses, the Gaussian roughness approximation, coded in RasCAL, can be used. Where the roughness of the interface is comparable to the layer thicknesses, another approach is required. Here, the surface normal profile has been considered as a series of thin slices. Each slice has different amounts of the different materials, depending on the roughness. By combining these contributions the effective SLD of the slices can be determined and the stack of slices used to determine the reflectivity.

The figure below illustrates a substrate (black) with two layers (in shades of blue) and the solvent (in white). The roughness is illustrated by the wavey interfaces. The horizontal grey lines represent the slices. Each slice is used to calculate the contents of the different materials present (ie how much black, dark blue, light blue and white) and hence the effective SLD of that slice

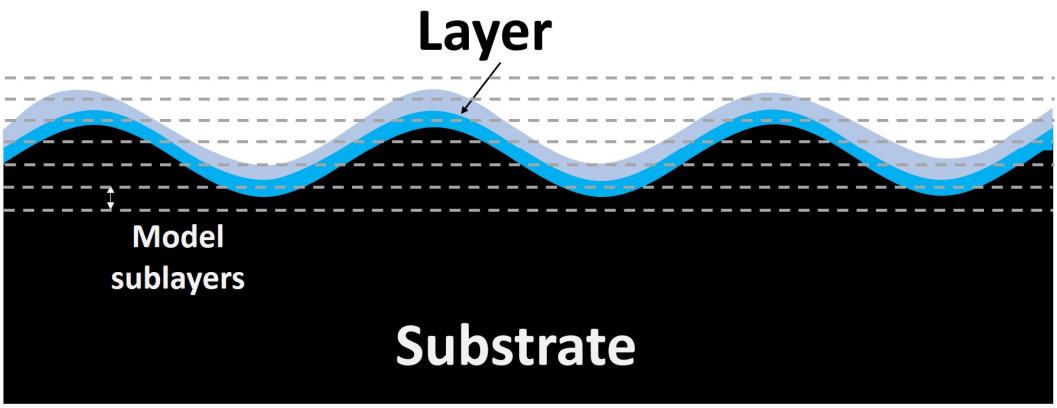

Figure 3.16: Neutron reflectivity calculation using slices when a sample is very rough.

The figures below illustrate the error function profiles used to perform these calculations (left-hand side), the volume fractions of each material with distance (middle) and the SLD profile (right-hand side).

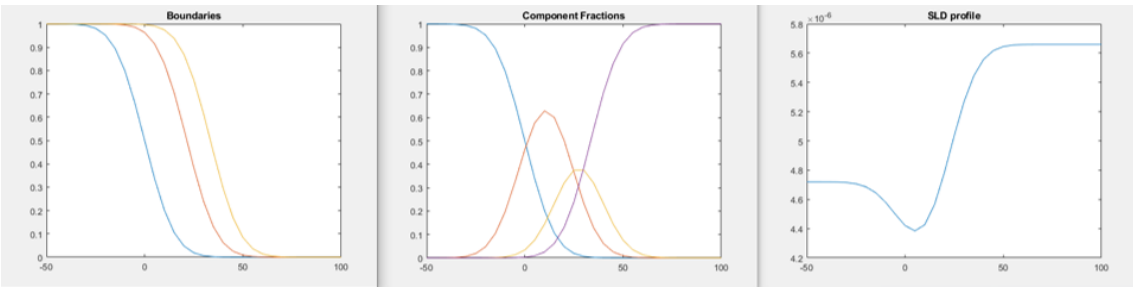

Figure 3.17: SLD of Figure 3.16: the three boundaries of the system (left-hand side), the fraction of each component (middle) and the overall SLD distribution as a function of the z coordinate, the surface normal (right-hand side).

These illustrations have used conformal layers with the roughness at each interface being the same. However, the code is not restricted to this and can use any roughness of each interface, as long as the interface of one boundary does not cross that of another. This approach has been included as a macro in the RasCAL fitting routine based on original code written by Prof. Stuart Clarke for the groups initial studies of adsorption onto calcite for previous group members. Due to the complexity of the code, Prof. Clarke also fitted the experimental data. However, the main

conclusions were found to be in reasonable broad agreement (given the limitations of the model) with the direct RasCAL fitting based on the gaussian roughness approximation.

3.17.7 ISIS TS2 Reflectometer

The neutron reflectometry results recorded in this study were measured at the ISIS facility in Oxford. Neutrons are produced at a spallation source, where a tungsten source is bombarded with high-energy protons to produce a neutron pulse that is resolved via time-of-flight.

Target Station 2 (TS2) reflectometer INTER was used in this study. INTER receives a pulse of neutrons with a long wavelength, and a large range (1–15 Å) accessing a large Q range at low Q required for reflection. The beam enters the INTER sample position at an adjustable angle of 2.3 °and reflects from an essentially horizontal interface before being detected upwards. Sample cells are mounted on an optical board with magnets to easily locate and realign samples. Alignment was carried out to check position of the specular peak before measurement.

INTER uses a point detector, which detect neutrons by bombardment of a ^{3}He gas-filled tube: when a neutron hits a helium atom, it decays to ^{1}H and ^{3}H. This produces an electrical signal, which is recorded as a function of time. The pulsed nature of the beam is used to determine the wavelength based on the time taken between the pulse forming at the source (cut by choppers to give a well defined pulse) and the detector.

3.17.8 Data Analysis

Data is recorded as intensity as a function of neutron wavelength at a given incident angle of the neutron beam at the sample. A transmission run is used to measure beam shape and intensity without reflection by passing the beam through the substrate. The measured reflected signal is divided by that of the transmission run to give the reflectivity.

Data from reflectivity in this study was analysed using the RasCAL fitting program provided by ISIS Spallation Neutron Source, Rutherford Appleton Laboratory. As mentioned above, RasCAL uses the matrix method to build a model of a number of roughened layers and calculates reflected intensity. A best fit to the experimental reflectivity can be found by constraining multiple fitting parameters simultaneously.[182,192]

Each layer is described with the following parameters: SLD, roughness, thickness and hydration (or solvation). The hydration term is calculated as a percentage and changes the SLD of the layer towards that of the solvent subphase, giving an indication of the coverage of adsorbate within a layer.

3.17.9 Neutron Cells

Sample cells were designed specifically for calcite crystals. The sample cells allow a solid-liquid interface to form. Key to forming the interface is to ensure good contact of the liquid on the solid, and minimise organic contaminant from entering the cell. A complete seal is required. The use of a Teflon trough with thin chamfered sides that deform under pressure allows a seal to form against the crystal or block. Teflon is chosen because it is hydrophobic and inert, allowing it to be cleaned with nitric acid without leaching.

For calcite crystals, details of the steel sample holder are given by Stocker *et al.* (Figure 3.18).[193] The updated calcite sample cell has a rectangular o-ring rather than a circular o-ring. The rectangular o-ring on a rectangular crystal allows a more even distribution of pressure on the crystal when clamping the crystal: calcite crystals are very brittle under compression and will crack and cleave to the rhombohedral shape, rendering them unusable. A torque wrench set to 0.2 Nm and calipers were used to ensure the same pressure was applied to each bolt. The torque was slowly increased to 0.35 Nm on each bolt. The clear housing with embedded o-ring was used for a visual guide to observe uniformity of pressure through deformation of the o-ring.

The subphase liquid in the Teflon troughs was exchanged by pipette: an inlet hole and outlet holes are drilled into the side of the trough to remove air bubbles. In-situ exchange via HPLC pump was not possible as this requires many cell volumes of solution and due to the costs of the deuterated solvents, this was not feasible for the non-aqueous solvent of interest here.

3.17.10 Substrate Preparation

Prior to each experiment, any Teflon (troughs and plugs), glassware and silicon block substrates were submerged in nitric acid for a minimum of four hours and soaked overnight in ultrapure water (18.2 MΩ.cm). The items were thoroughly rinsed with more ultrapure water to ensure no nitric acid was remaining, especially in the cavities of the troughs that are used to syringe the liquid phase. The items

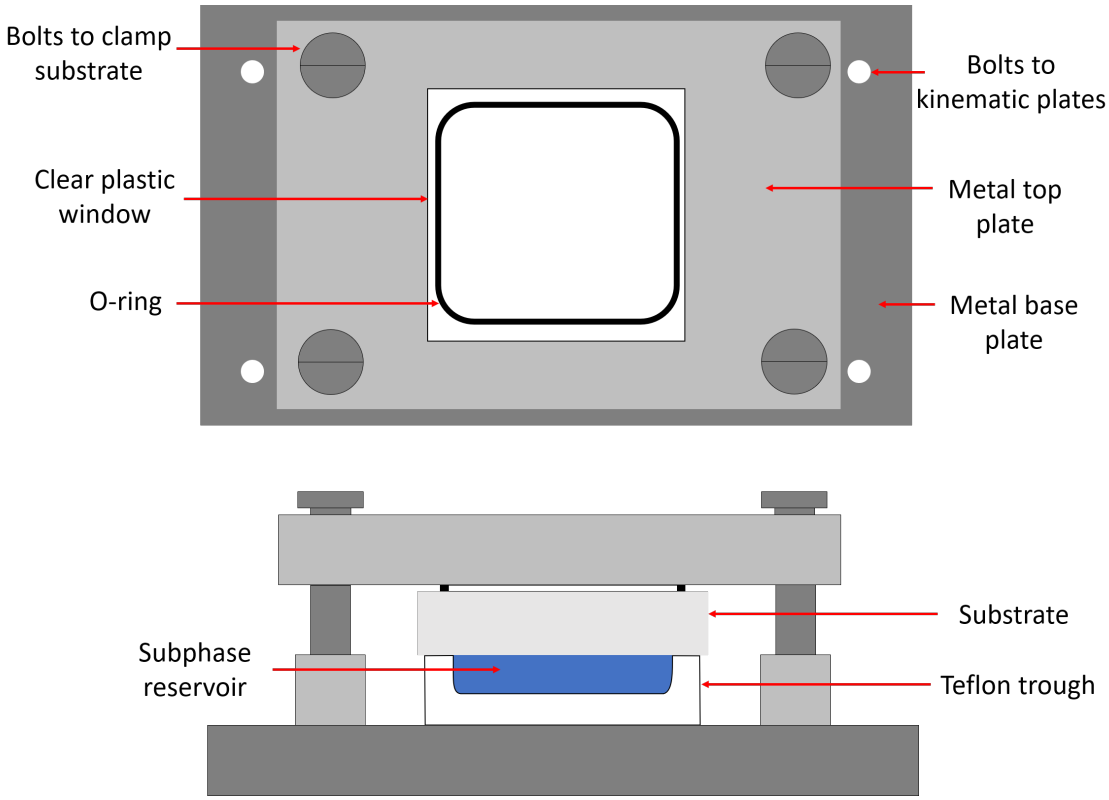

Figure 3.18: Aerial and side view of sample cells used in neutron reflectometry measurements.

were air dried under a beaker and troughs were immediately placed against a clean crystal. The trough inlets were plugged with clean Teflon plugs, cleaned within the method outlined above.

For equipment such as spatulas, pipettes and plastic bottles, which are incompatible with nitric acid, surface active cleaning agent Decon 90 was used. This is a low adhesion surfactant mixture readily removed by rinsing. Items were soaked in 10 % Decon 90 for 2 hours minimum before removing and rinsing in ultrapure water ten times. Items were then air dried under a glass beaker.

Silicon blocks were cleaned using the nitric method mentioned above, dried in air, and finally placed in a UV-ozone cleaner for 10 minutes to remove any remaining surface contamination. Calcite crystals do not undergo a nitric acid treatment, but are simply placed in a UV-ozone cleaner for 20 minutes. Clean substrates were immediately clamped against clean Teflon troughs.

3.18 Sum-Frequency Generation

Sum frequency generation (SFG) is a surface-specific, non-linear, optical technique. To produce an SFG signal, a fixed-frequency visible laser beam and a variable-frequency infrared (IR) laser beam are temporally and spatially overlapped on a surface or interface. In addition to reflection and transmission of the visible and IR lasers, the non-linear process of SFG results in light being emitted at the sum of their frequencies:

$$\omega_{SFG} = \omega_{VIS} + \omega_{IR} \tag{3.28}$$

Where ω is the frequency of the beam. By varying the frequency of the IR beam and measuring the output SFG beam intensity, the SFG response of the molecules at the surface can be obtained through a range of frequencies, producing a vibrational spectrum analogous to that produced by conventional IR spectroscopy. SFG has been used to gain information on the polar orientation, tilt angle and degree of conformational ordering of alkyl chains adsorbed at a surface.

3.18.1 Selection Rules

In the bulk of a substrate or a solvent, the environment is centrosymmetric and there is no SFG signal. However, the isotropic nature of a system is broken at the interface, resulting in SFG being a surface-specific technique.

Observing an SFG signal requires that a molecular vibration is both IR and Raman active and only species that are not centrosymmetric have that capability. C-H vibrational modes fulfil this requirement and therefore can be assessed via SFG spectroscopy. The C-H resonances are often observed and occur between 2800–3000 cm^{-1}. For molecules that contain a long alkyl chain there are two significant groups—the methyl (CH_3) group at the end of the tail and the methylene (CH_2) groups that form the backbone.

SFG spectra were recorded in SSP and PPP polarisation combinations (sum-frequency, visible, infrared). For the methyl group vibrational modes, the selection rules for SSP and PPP polarisations are:

- For the symmetric mode, the SSP intensity is always many times that for PPP.
- For the antisymmetric mode, the PPP is always many times that for SSP, and both peak when the tilt angle of the group is 54.7°.

- In SSP spectra, the antisymmetric and symmetric modes will negatively interfere where their frequencies overlap.

For the CH_2, the relevant selection rules are very similar:

- For the symmetric mode, the SSP intensity is always many times that of PPP.
- For the antisymmetric mode, the PPP is always many times that for SSP. If there are any peaks which are stronger in the SSP than the PPP spectra, it cannot be from the antisymmetric mode.
- In SSP spectra, the antisymmetric and symmetric modes will negatively interfere where their frequencies overlap when their orientations are similar.

SFG spectra were recorded using a picosecond spectrometer (EKSPLA, Vilnius, Lithuania). The second harmonic of a mode-locked Nd:YAG laser (Ekspla PL4431B) provided the visible beam at 532 nm (30 ps pulses at 50 Hz). Tuneable infrared beams in the 1000–1800 and 2700–4000 cm^{-1} regions were produced by an optical parametric generator (Ekspla PG401). The input IR and visible laser beams were overlapped in a copropagating geometry at angles of 53° and 60°, respectively, to the surface normal. Calcite crystals are rotated on the sample stage by increments of 15° (Figure 3.19) about an axis parallel to the surface normal.

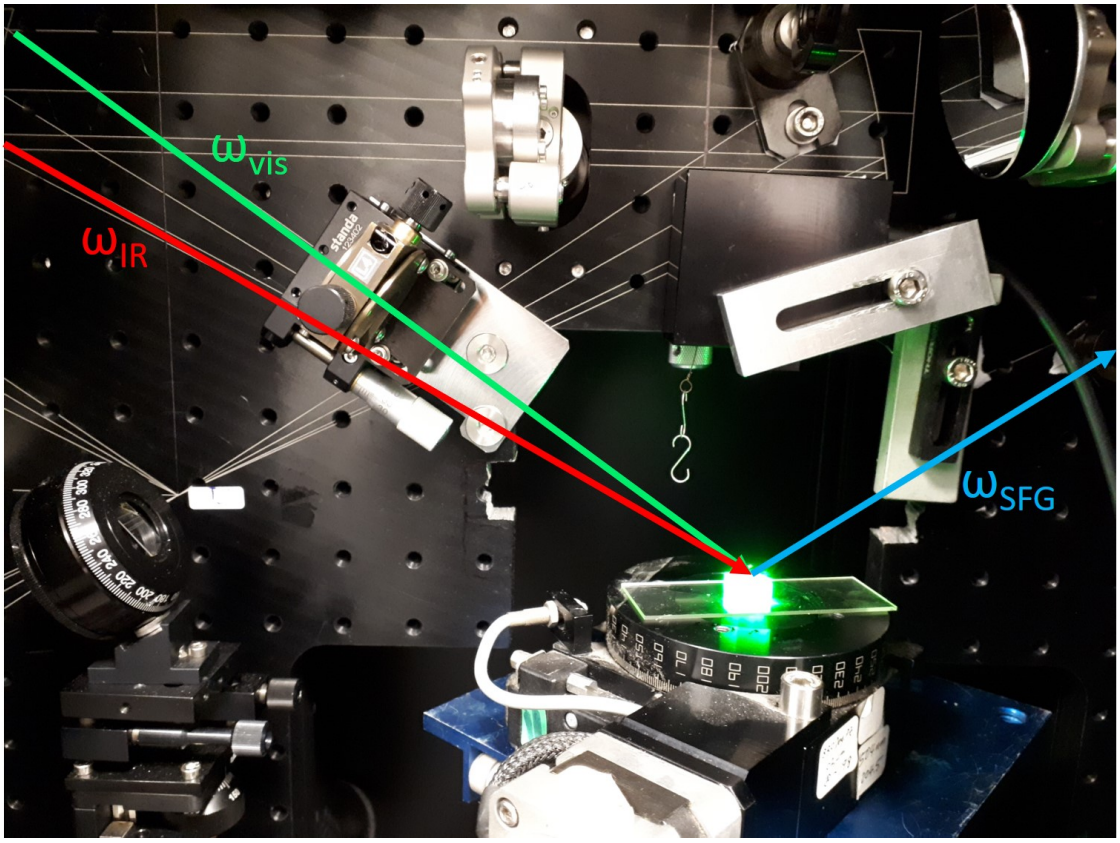

Figure 3.19: Photograph of the SFG spectrometer sample stage with calcite crystal during analysis. The sample is irradiated with visible (green) light. Incident visible (green), IR (red) and resultant SFG (blue) beams are superimposed.

Chapter 4

Characterisation of Outcrop and Reservoir Rock

4.1 Background

In the oil industry, reservoir and outcrop rock are loaded into vessels under the temperature and pressure of a specific oil well and flooded with crude oil for a duration, referred to as 'ageing' the rock. It is intended that in this way a porous matrix with surface chemistry similar to the 'real' reservoir rock can be obtained and used to optimise commercial fluids for recovery. As discussed in Chapter 1, outcrop rocks are used for crude oil ageing as model rocks for reservoir rock—outcrop rocks are usually matched via mineralogy to try and provide similar minerals. However, some evidence in the commercial space has indicated that ageing outcrop rock in this way does not yield the same result as re-ageing of reservoir rock: water flooding of an outcrop and reservoir rock in the same crude oil under the same conditions leads to different amounts of crude oil released under the same methods of oil recovery. It is desirable and commercially important to understand the process and identify what does happen in the ageing process and how to capture key characteristics of the real reservoir rock.

It is generally unknown what minerals of an outcrop sample are most useful to promote effective ageing and recreation of the real rock behaviour. For example, pores may be lined with the most common mineral of the rock (quartz or calcite, depending on well-type). However, if the surface adsorption is significant, then minor minerals that cover pore walls (clay such as mica or kaolinite) may be more significant.

This chapter discusses results from techniques used to characterise and compare the two real rock samples (outcrop and reservoir) with the aim of understanding the key physical and chemical differences. Results from this chapter directly impact the substrates chosen in Chapter 5 and 6 where crude oil ageing studies were conducted to analyse chemistries present on a range of minerals.

4.2 Porosity Measurements

To understand the the physical difference between outcrop and reservoir rocks, the porosity was measured. Two techniques were used to assess porosity of the two rocks provided. Due to the destructive nature of mercury porosimetry, micro-CT of the core were conducted first before the fragments of the same core were analysed by mercury porosimetry.

4.2.1 Micro-CT

For the outcrop plug, a total of 2827 cross-section images were taken from top to bottom of the core. The core height was 79 mm; thus each image covers a slice of thickness 27.9 μm. For the reservoir plug, a total of 3390 images were taken from top to bottom of the core. The core height was 82 mm; thus each image covers a depth of 24.2 μm. The image analysis software ImageJ was used to reconstruct the 3D image from which one can determine empty spaces (porosity) in the sample and solid phase distribution. This is achieved by identification of a threshold intensity, measured relative to the background surrounding the sample, above which represents solid and below which represents void/pore spaces. The same threshold values were used for both images. The total number of solid pixels and void pixels can be used to determine the void fraction/porosity. The porosities of outcrop and reservoir were determined to be 18 $\pm$ 2 and 7 $\pm$ 1 % respectively. These values correlate with the expected values from BP colleagues given their knowledge about the reservoir core and literature values of the outcrop Castlegate (15–20 %).[194]

Figure 4.1 shows cross-section images taken at image number 1345 for two samples, which are 38 and 33 mm from the top of the plug for outcrop and reservoir plugs respectively. The image shows differences in grayscale that can be interpreted as either minerals of different electron density or blends of high contrast minerals with space between them in each voxel. Here the variation in greyscale is a measure of electron density that can be interpreted to arise from different minerals. The black spaces between these light regions were interpreted as void space in the

materials.

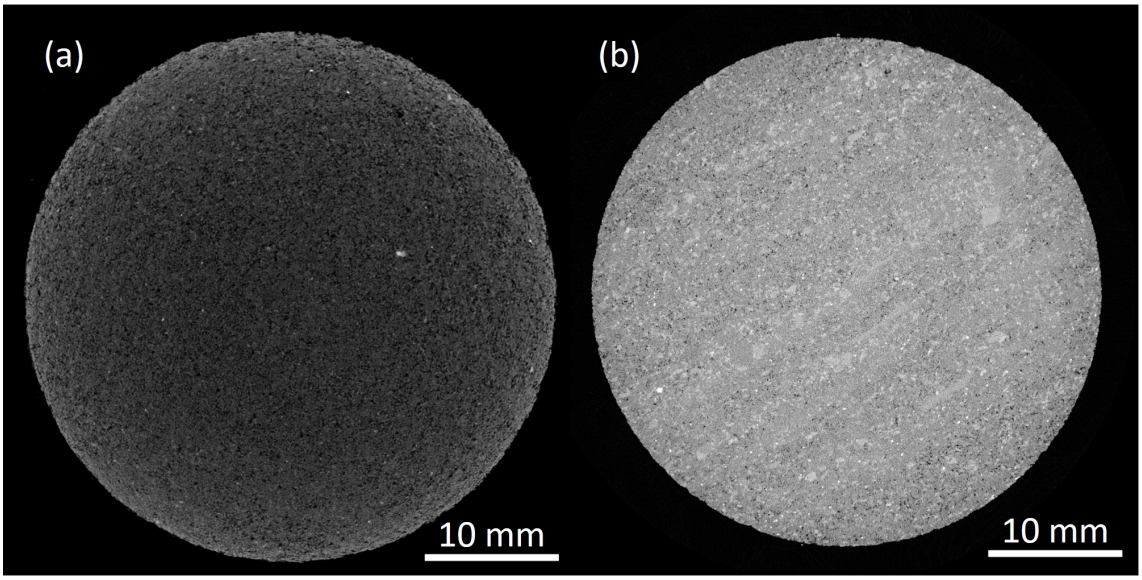

Figure 4.1: Micro-CT images of a segment of (a) outcrop plug and (b) reservoir plug.

Interestingly, defects/fractures can be observed via the micro-CT scan. Figure 4.2 shows two image stacks moving through the reservoir plug where a clay section has a crack defect through it, highlighted by a red circle in the image. During the scan, the crack is not vertical through the 'clay', but at an angle, and tends to penetrate further into the bulk material as the image slices from one end of the sample to the other. How these defects impact porosity needs further investigation from the perspective of fluid flow and nature of the physical factors governing oil recovery, but is not the focus of this work.

4.2.2 Mercury Porosimetry

Mercury porosimetry was run externally due to safety requirements associated with large volumes of mercury. The porosity values for outcrop and reservoir fragments were 24.21 and 10.38 % respectively. For outcrop rock, the value is at the higher end of the literature values. Reservoir rock values are within the range of values anticipated.[194]

The porosity values obtained from micro-CT were approximately 30 % lower than the porosity value that mercury porosimetry yields. This difference could be attributed to a thresholding problem: some pores could be too small and evade micro-CT image analysis. It could also be due to mercury flooding destructively creating a porous network within the rock.[195]

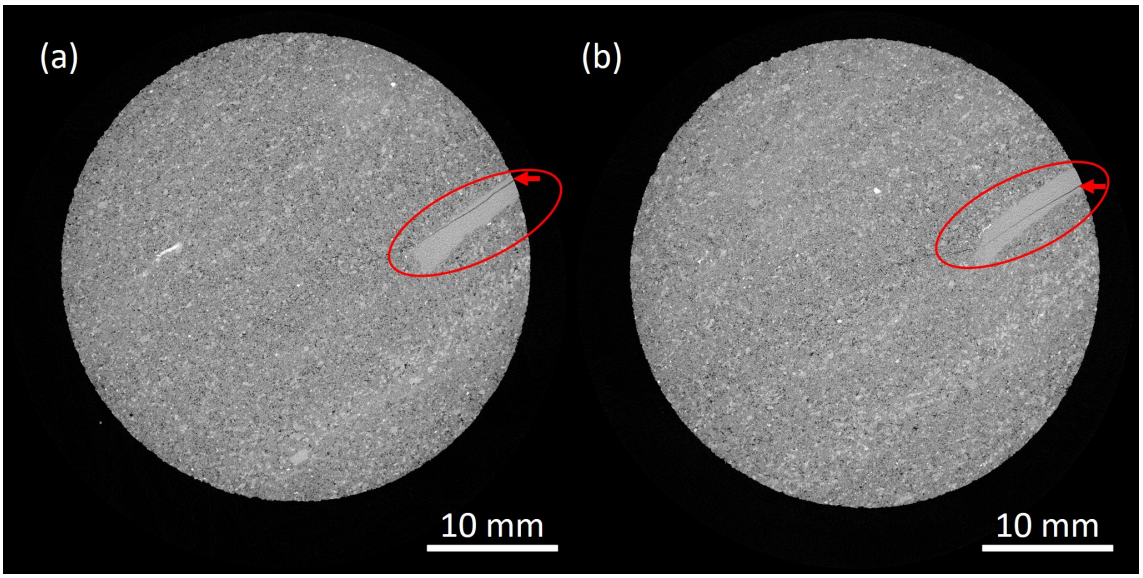

Figure 4.2: Micro-CT defects: Reservoir plug at image (a) 534 and (b) 967 showing movement of a defect (black line) through a clay surface and spreading to the bulk.

Comparing the two rocks, it was immediately obvious there was a difference in physical properties with over double the porosity in the outcrop rock. This is not surprising as they are taken from strata miles apart. If they were from the same strata, there can be differences in porosity within edge versus middle of a reservoir. If the reservoir rock is located to the side of the reservoir it would not be as porous as the main reservoir. Outcrop rock has a higher porosity due to weathering: the rock is exposed to wind and rain and some minerals may dissolve or erode away, such as carbonates. Erosion of minerals will cause an increase in porosity.

The next step was to assess the mineral nature of the surface lining the pores as this is expected to dominate the fluid/rock interactions. This mineralogy govern the possible chemical functionalities that can bind to the rock and provide insight into the binding mechanism of oil/wettability.

4.3 QEMSCAN

There are three samples for each rock which are to be considered in this work:

1. The rock as received (intact fragment).
2. The crushed-up rock.
3. The solvent-washed crushed-up rock.

The sections below will discuss the bulk mineralogy and mineralogy of the pore surfaces of these samples. The pore surfaces are the surfaces of interest in this work because these are the surfaces to which oil will be exposed and to which components may bind. Analysis of the crushed sample and solvent-washed sample is required so we can understand the impact on surfaces exposed when trying to investigate organic irreversibly bound. Only one QEMSCAN image of each sample was taken due to the long scan time (up to 6 hours per scan) and limited access to the facility.

4.3.1 Intact Fragment

Analysis of the intact fragment is of interest because the intact rock is the only sample expected to show the minerals that are in contact with the pores/voids, which are of most interest here (however, crushed-up rock is still of interest as a 'powder' is required for some techniques later, and the difference in minerals exposed was analysed using QEMSCAN to verify which surfaces were being investigated). The mineral-pore interface is where the mineral-organic interaction will occur and thus the organic species to contact the rock/mineral will line the pores. Other organics may also form on top of this initially adsorbed organic layer. Figure 4.3 shows the degree of resolution possible with QEMSCAN.

Figure 4.4 shows the QEMSCAN of the outcrop and reservoir rock fragments. The white regions are pores.

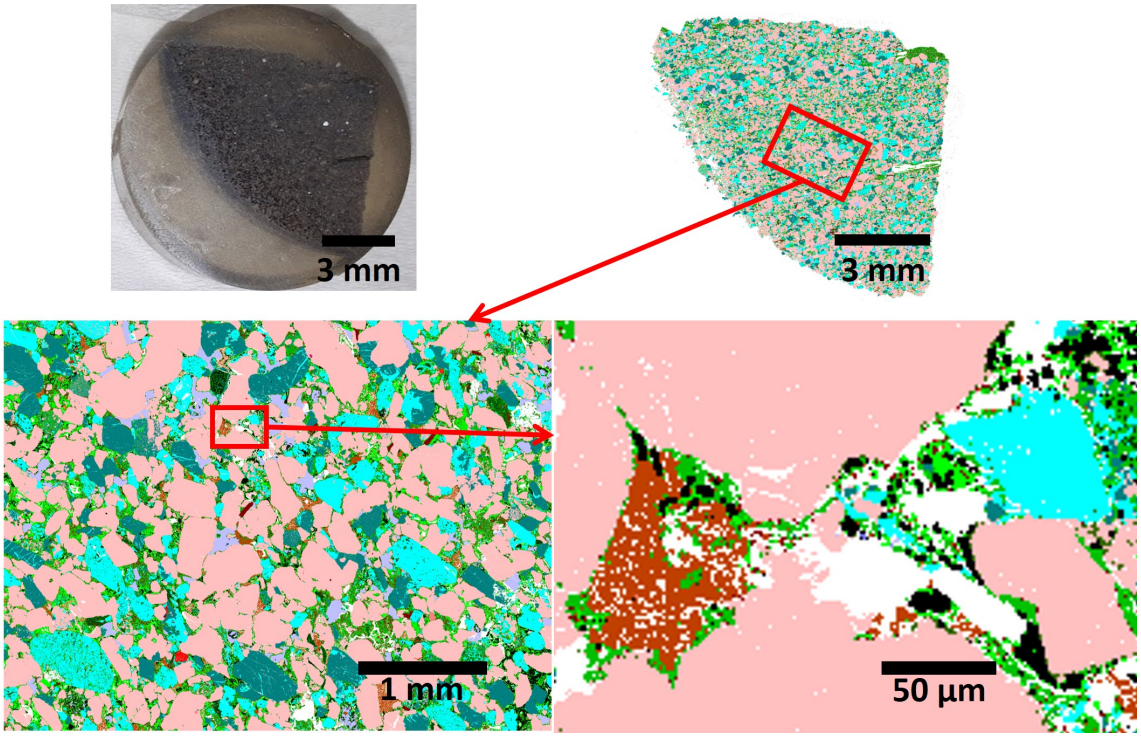

Figure 4.3: QEMSCAN of reservoir rock fragment zoomed in to showcase the resolution achieved. The top left hand image shows the rock stabilised in resin prior to the scan.

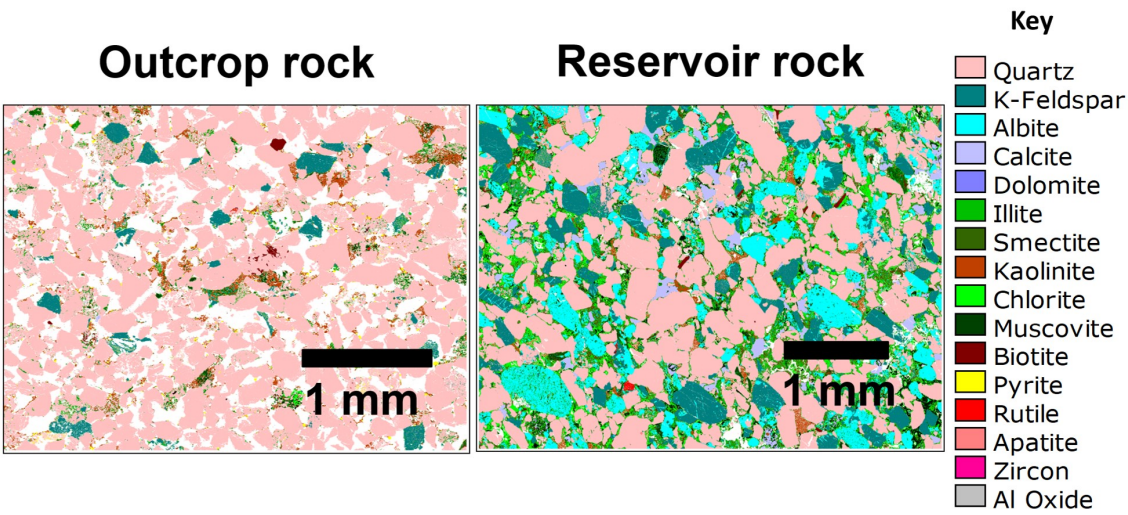

Figure 4.4: QEMSCAN of outcrop and reservoir rock intact fragments.

Through image analysis (as described in Section 3.8.1) the different mineralogy of the bulk and pore lining materials can be identified. Figure 4.5 shows examples of the output images that are generated from the pore lining calculation described in Section 3.8.1. As an example, analysis for four minerals of particular interest in an outcrop rock sample are shown. However, all minerals on both outcrop and reservoir

rock were investigated. The pore-mineral-boundary of interest is highlighted in red, with the mineral of interest coloured as shown in the key; other minerals that are not the focus are highlighted in bright blue, with the pore-'other-mineral' boundary in dark blue.

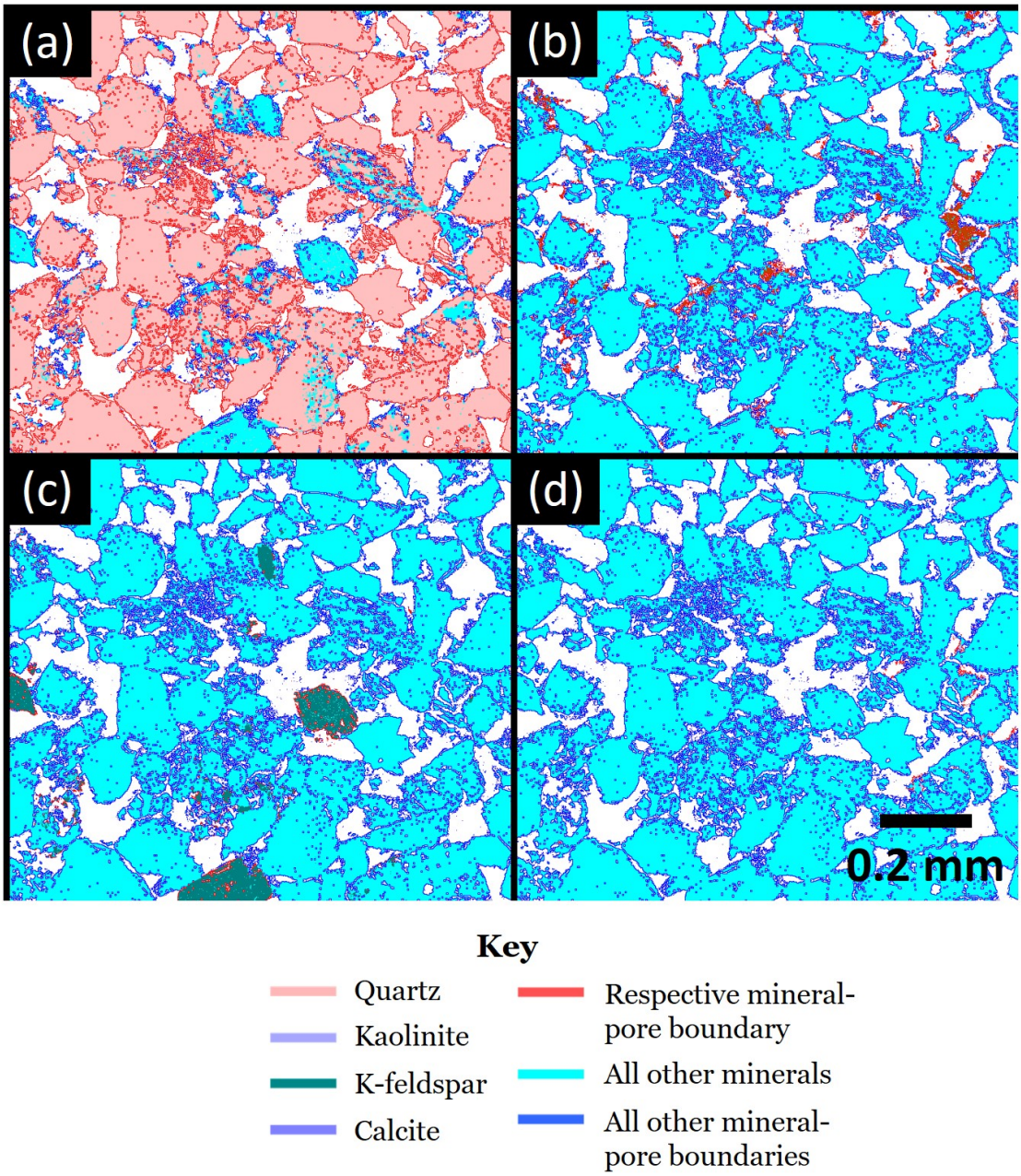

Figure 4.5: Examples of images output from image analysis of QEMSCAN data, showing the outcrop rock with mineral and pore mapping. Each image shows an individual mineral under analysis: (a) quartz, (b) kaolinite, (c) K-feldspar, and (d) calcite.

Data shown in Figure 4.6 are generated by the QEMSCAN data analysis. These numbers are used in Figure 4.7 to highlight differences in the bulk sample composition versus the mineral-pore boundary mineralogy.

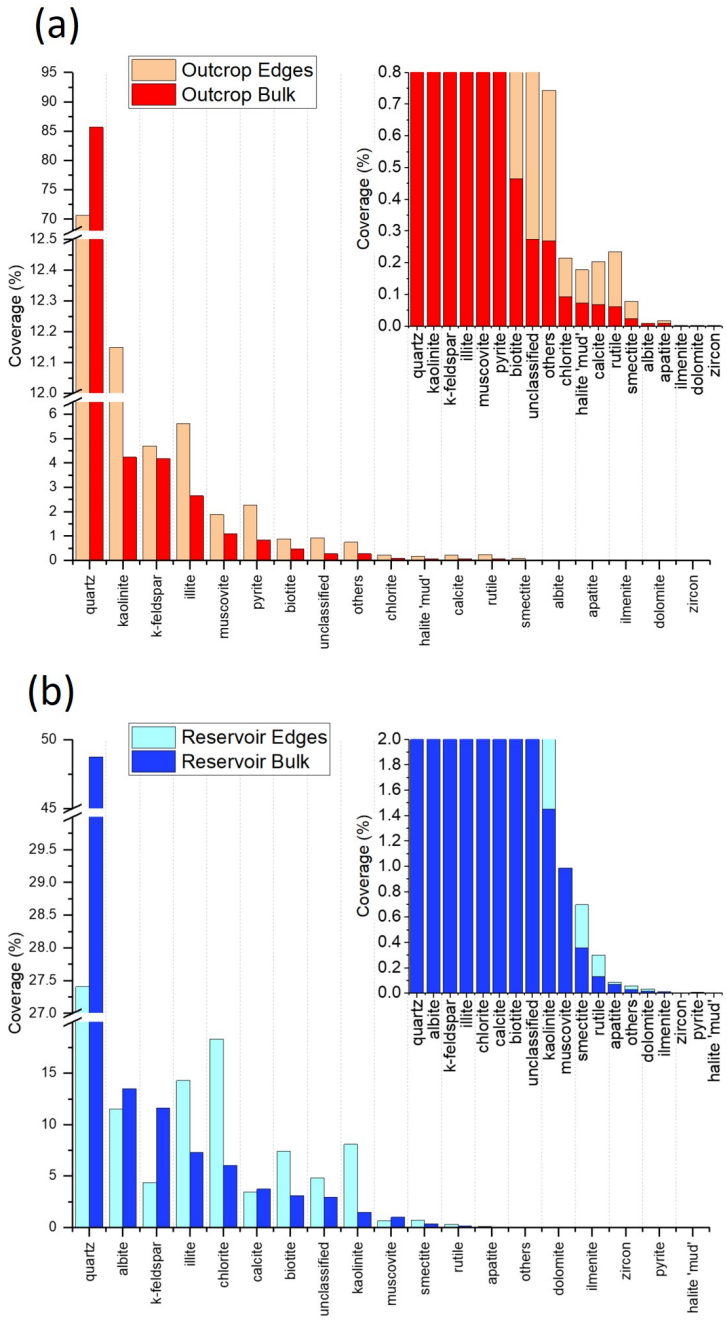

Figure 4.6: QEMSCAN data analysis of (a) outcrop and (b) reservoir fragments, showing the difference between bulk mineralogy and pore-coated 'edge' mineralogy.

Figure 4.7 presents the mineralogy determined from the QEMSCAN as a difference of the pore lining minerals, relative to the bulk composition. This highlights how the pore linings are very different to the bulk. It is noted that the data for the quartz (far left of the chart) shows that there is significantly less quartz coating the pores in both outcrop and reservoir rock than there is quartz in the bulk by 15 and 21 % respectively.

For reservoir rock, the remaining minerals identified by QEMSCAN that are also less abundant around pores than in the bulk are K-feldspar and albite, evident by the blue bars **below** the horizontal axis. Possibly of more significance here are the minerals that occur around pores more abundantly than in the bulk for reservoir rock that are evident in this figure as blue bars **above** the horizontal line. These are: illite (7.0 %), biotite (4.3 %), kaolinite (6.6 %), and chlorite (12.3 %).

For outcrop rock, Figure 4.7 shows only one mineral has a red negative bar. Therefore, it can be concluded that there are no minerals other than quartz that occur significantly less in pores than in the bulk. The main interest are the minerals that occur around pores more abundantly than in the bulk. For outcrop these are: illite (3.0 %), kaolinite (7.9 %), and pyrite (1.5 %).

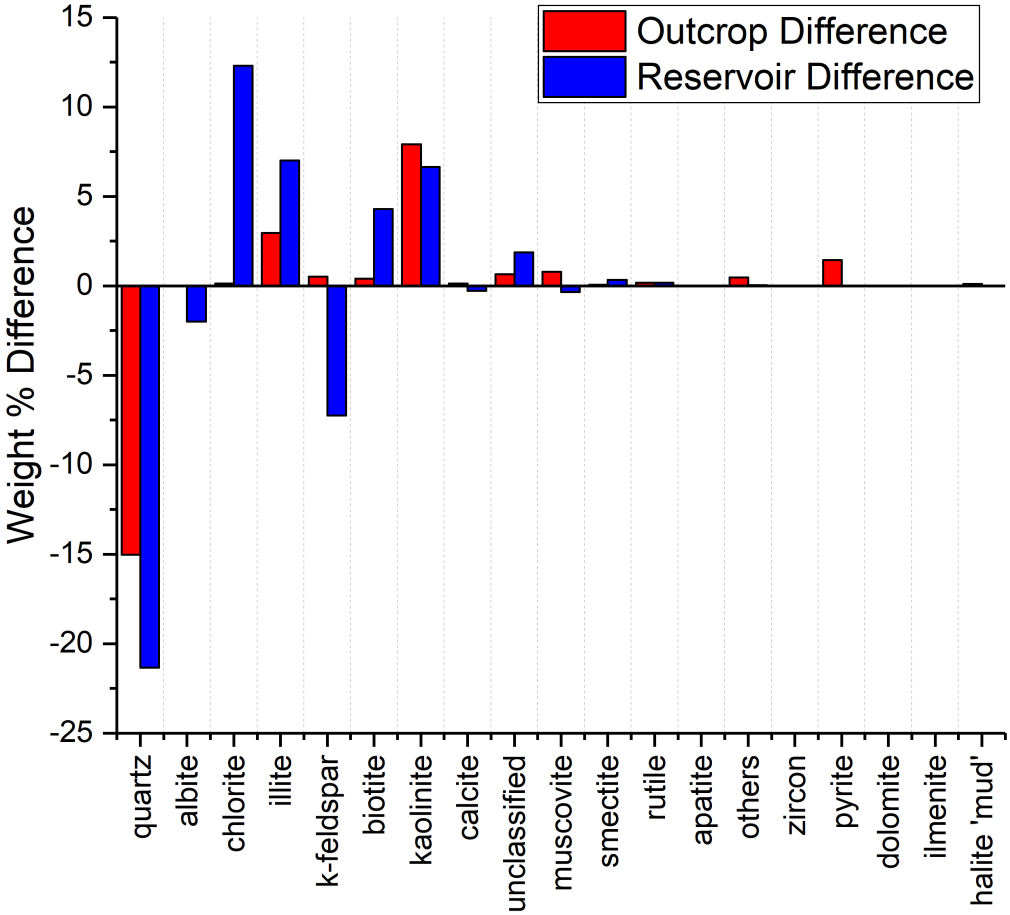

Figure 4.7: QEMSCAN analysis of outcrop and reservoir fragments, showing the weight percentage difference between total mineral present in bulk and total mineral lining pores. Negative values show less mineral around pore than in bulk. Positive values represent mineral that are present around pores more than it is present in the bulk.

Summary:

From the QEMSCAN analysis of the intact rock fragments, the minerals of interest that line the pores are: a) for outcrop rock: quartz, kaolinite, K-feldspar, illite, muscovite and pyrite, and b) for reservoir rock: the minerals of interest are quartz, albite, illite, chlorite, kaolinite, biotite, and K-feldspar.

Hence, it will be interesting to determine if organics interact similarly or differently with these classes of minerals due to the range of chemical natures of each mineral. For example, the interaction between oil on mica or kaolinite is interesting due to the surface charge of each system: at neutral pH mica has a net negative surface charge. Research that considers the interaction of each mineral individually with crude oil will be presented in Chapter 5 and 6.

4.3.2 Crushed Sample

The crushed rock samples are of interest as the outcrop and reservoir rocks will be crushed to maximise extraction from their surfaces with subsequent analysis of any organic on the rock; it is difficult to analyse small amounts of organic within pores of rock whilst a rock is intact. Analysis of the crushed sample is intended to show the amount of minerals exposed during the crushing procedure and can be compared to the intact rock.

Figure 4.8 shows the QEMSCAN images for crushed outcrop and reservoir rock.

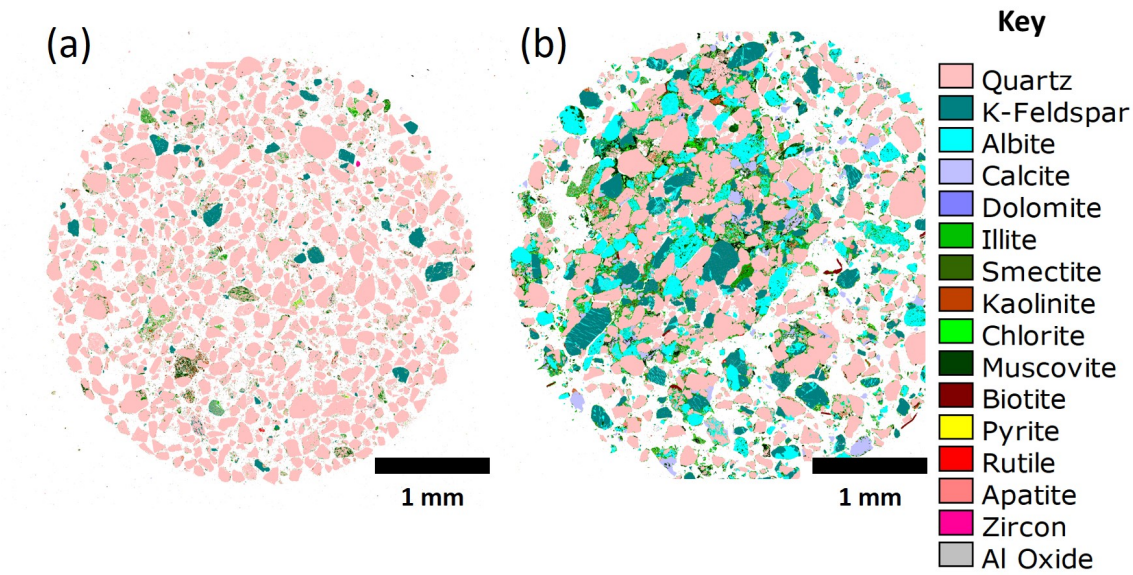

Figure 4.8: QEMSCAN of (a) outcrop and (b) reservoir rock. Ground particles were stabilised in a resin block and carbon coated before scanned. Scale bar shows 1 mm.

Figure 4.8 presents the mineral composition of the crushed outcrop and reservoir rock samples. The figures are dominated by the salmon colour, showing that both samples are dominated by quartz, as expected and in good agreement with the intact fragments above. The mineralogical composition of the bulk crushed reservoir rock shows a lower amount of quartz and thus greater percentage content of the different minerals compared to the outcrop rock, which is mainly quartz with smaller pieces of different minerals—as pictured by the micro-CT scan images (Section 4.2.1). The reservoir rock contains significantly more calcite and albite. There is double the amount of kaolinite in outcrop compared to the reservoir sample; this could be due to location differences: the outcrop rock is not geologically linked to the reservoir rock and will therefore have different minor-mineralogies.

The same method of image analysis (Section 3.8.1) was used to determine the pore

coverage. Figure 4.9 shows the difference between outcrop and reservoir bulk and pore edges. As above, negative values in Figure 4.9 identify less mineral around the pore than in the bulk. Both reservoir and outcrop crushed edges contain significantly more illite, kaolinite, and Feldspar-mixtures (labelled as 'unclassified'). Crushed reservoir rock edges contain more chlorite and pyrite, whereas the bulk contains more apatite than the pore edges. Crushed outcrop rock edges contain significantly more muscovite and pyrite.

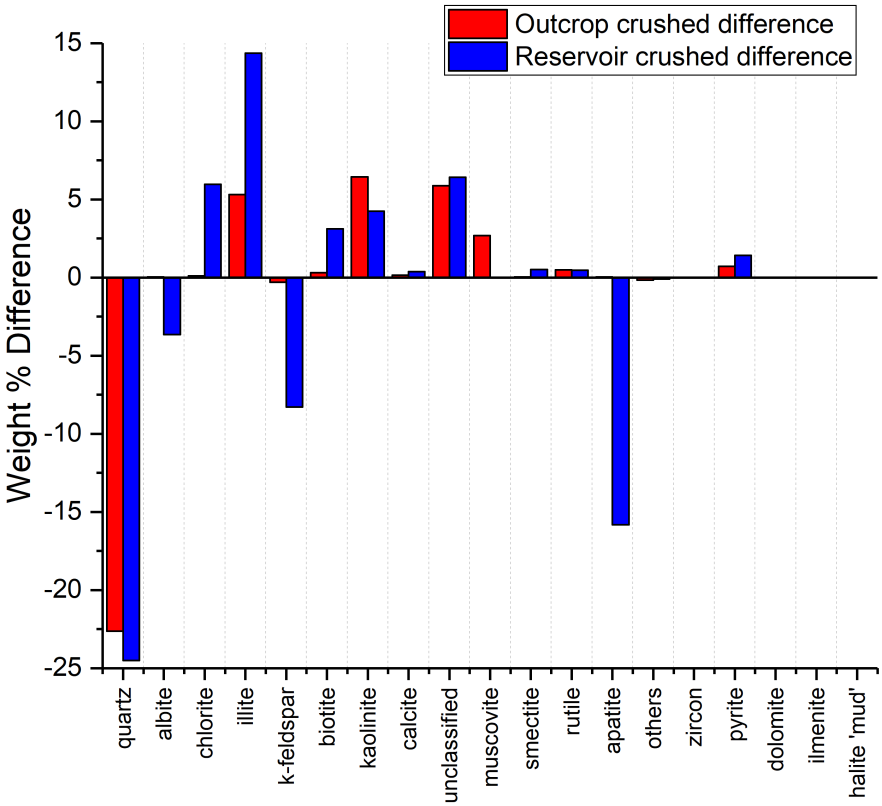

Figure 4.9: QEMSCAN analysis of crushed outcrop and reservoir rock, showing the weight percentage difference between total mineral present in bulk and total mineral lining pores. Negative values show less mineral around the pores than in the bulk. Positive values represent mineral that are present around pores more than it is present in the bulk.

Wettability Discussion

The presence of different minerals in outcrop and reservoir rocks matters to this study as discussed in Section 4.1. The key data is that the rocks, although broadly classed as silicates, might have been expected to behave similarly in terms of wettability. **However, minor minerals have been shown to line the pore walls of the rocks and these are different to the bulk silicate composition. These are expected to be the dominant materials interacting with the**

pore fluids. It may be that these minerals all behave the same with the pore fluids. However, it is know that these different minerals interact with fluids differently and lead to different adsorption behaviour.

There is evidence for this in the literature. It is reported that kaolinite booklets have been implicated in making a water wet system.[196] These booklets' are confirmed in this work visually and elementally from SEM images coupled with EDX of outcrop and reservoir rock samples (Figure 4.10). Compared to the outcrop rock, the reservoir rock contains significantly more albite, chlorite and biotite which are reported to be minerals that tend to be oil-wet driving minerals. The reservoir rock also contains significantly more feldspar and illite, which are considered 'water-wet' minerals.

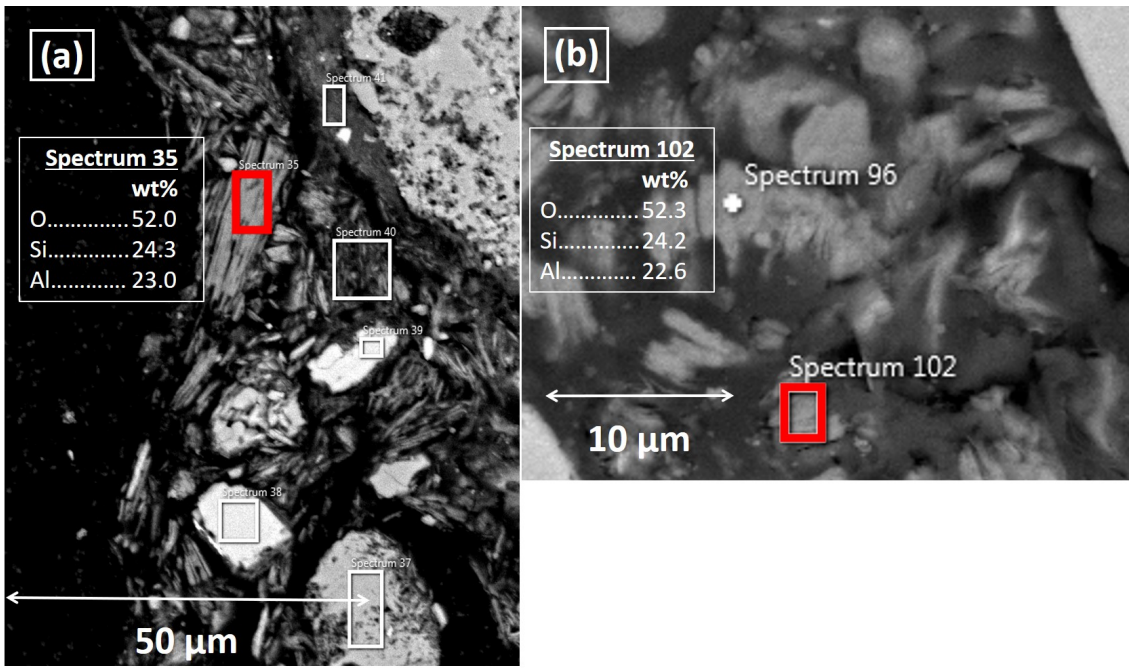

Figure 4.10: SEM image with EDX analysis of kaolinite booklet on (a) outcrop and (b) reservoir rock.

Hence, using the quantitative nature of the mineral analysis given above it can be concluded that there is a similar mineral wt % of both water-wet and oil-wet mineralogy within the reservoir rock. Although there are equal amounts of oil-wet and water-wet minerals present, this does not mean that the wettability of the reservoir rock will be approximately neutral. There could be heterogeneous regions of strongly water-wet and strongly oil-wet minerals, which is not the same as a uniform neutrally wet system.

Summary:

As expected in the crushed rock, bulk and pore lining materials are very similar to the fragments discussed above (Section 4.3.1). There are some modest differences. This may be attributed to the process of crushing, which will break weakly bound mineral bonds, whereas the more strongly bound minerals will remain in place.

4.3.3 Solvent Washed Crushed Sample

The outcrop and reservoir rock undergo a Soxhlet extraction (Section 3.4) to remove as much organic as possible. In this section the exposed mineralogy is assessed for comparison between the intact and crushed samples. The solvent washed sample mineralogy is of interest to see whether different minerals are exposed (for example, if they become separate particles) as a result of solvent washing.

Figure 4.11 shows the QEMSCAN images for crushed and solvent washed (a) outcrop and (b) reservoir rock. Figure 4.12 shows the difference between mineralogy around pores compared to the bulk.

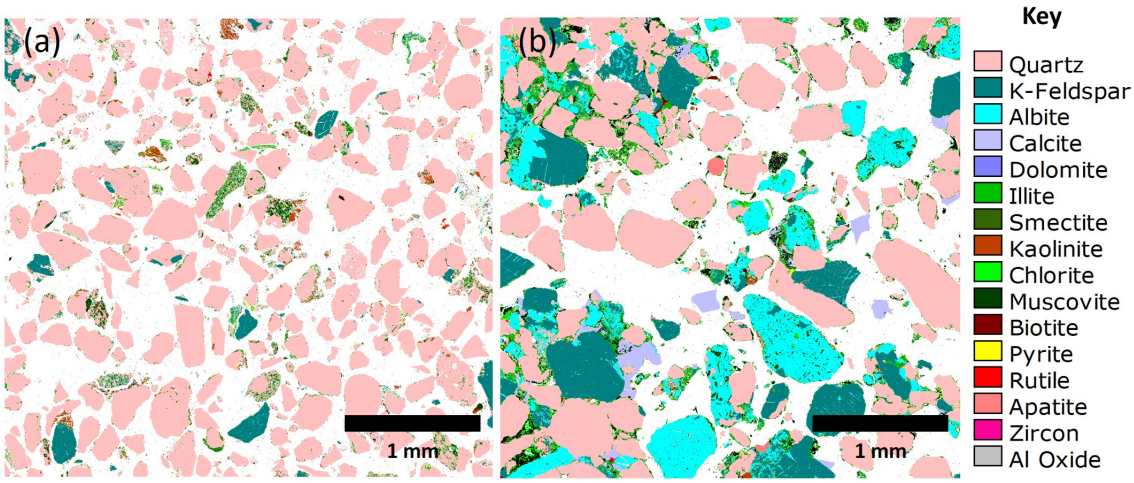

Figure 4.11: QEMSCAN of crushed and solvent washed (a) outcrop and (b) reservoir rock. Ground particles were stabilised in a resin block and carbon coated before scanned. Scale bar shows 1 mm.

The solvent washed reservoir rock, shows 50 % less quartz around the pore-edges compared to the bulk; as well as significantly less K-Feldspar. There are also greater amounts of illite, chlorite, biotite, mixed-feldspars, kaolinite and pyrite around the edges than in the solvent washed bulk.

The crushed and solvent washed outcrop rock shows less quartz around the pore-edges than in the solvent washed bulk, as seen for both the intact fragment and crushed up sample (Figure 4.9). There are greater amounts of illite, mixed-Feldspars,

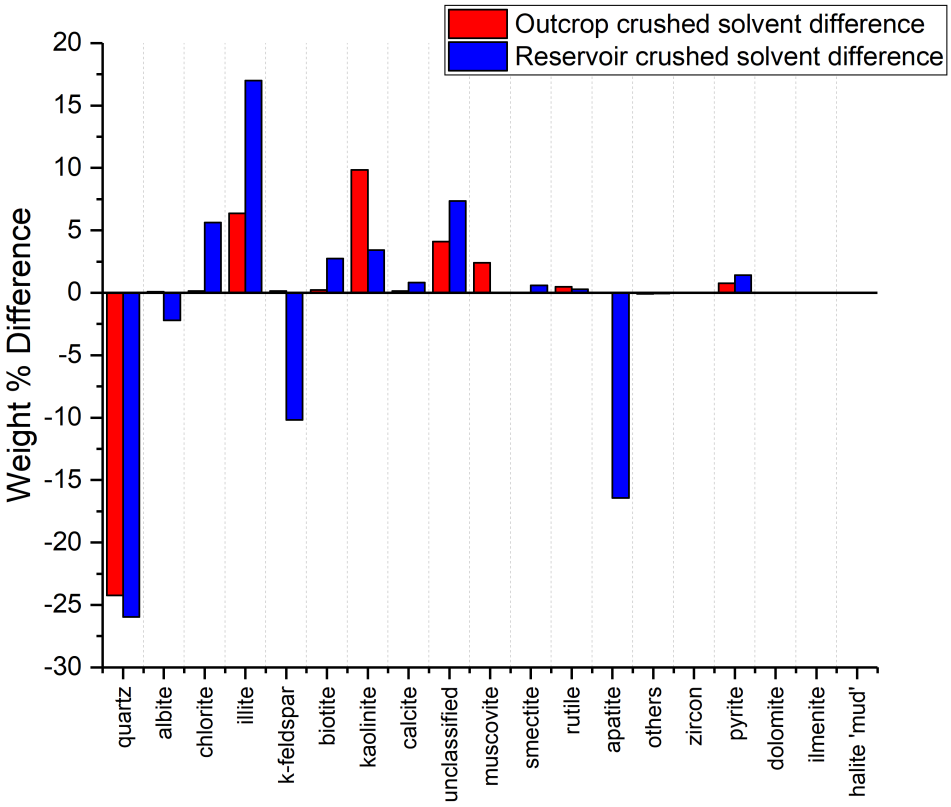

Figure 4.12: QEMSCAN analysis of crushed and solvent washed outcrop and reservoir rock, showing the weight percentage difference between total mineral present in bulk and total mineral lining pores. Negative values show less mineral around the pore than in the bulk. Positive values represent minerals that are present around pores more than present in the bulk.

kaolinite, muscovite, rutile and pyrite around the edges than in the bulk, which is also observed in the sample of outcrop rock that is only crushed.

The solvent extraction is believed to only enable movement or release of 'fines' type particles. Fines are particles with diameters in the range of 5 to 50 μm and include quartz and fine clays such as kaolinite and illite. The migration of fines inside a porous system can lead to blocking of pore throats and reduce oil recovery. Due to the nature of the solvent extraction via a Soxhlet extraction, the fines particles are not lost, and will be retained with the bulk of the sample, unless dissolved in the solvent. **The solvent wash releases fines in the outcrop and reservoir rock.**

4.3.4 Discussion

This work has exploited QEMSCAN to determine the types of minerals coating the pores of the rock. A new code has been used to identify these minerals.

In this respect the as received large rock fragments should be expected to be most representative of an oil reservoir. However, there are also some modest changes to mineralogy after crushing and solvent washing the samples, which may capture changes following pre-treatment of samples prior to core-flood tests. If undetected, these changes may lead to different behaviour and hence incorrect conclusions.

Comparison of pore edge mineral composition exposed in an intact rock and after crushing and solvent washing

Figure 4.13 shows the comparison of mineral-pore coverage for intact rock, after crushing and solvent washing for reservoir and outcrop rock respectively. An initial assumption is that all three samples show the same minerals lining the pores.

Changes in exposed minerals upon crushing may be expected as some minerals may be mobilised. However, it is not expected to see significant changes between a crushed sample and a solvent washed sample because the only loss from the system when crushing the rock is believed to be organics, with essentially no dissolution of the minerals and any mineral losses being only physical detachment; these minimal variations were observed in the data for the reservoir rock treatment progression (Figure 4.13 b).

Focussing firstly on the reservoir rock, the treatments show a loss in quartz at the pore edges when the intact fragment is crushed, which does not change further upon solvent wash. There is also a loss in chlorite, biotite, and kaolinite pore-edges upon crushing, and a similar pore edge coverage present in the solvent washed sample. An increase in material appearing at pore edges after crushing and solvent wash is seen for albite, K-feldspar, illite, mixed-feldspars, and pyrite. From the data it can be concluded that albite, illite, feldspars and pyrite might be loosely bound to the overall rock structure and are freed during the crushing of the rock.

The outcrop rock progression in Figure 4.13 (a) is a bit more complex. A loss from the pored edges of quartz, biotite and pyrite is observed. There is an increase in pore lining for illite, mixed-feldspars (labelled as unclassified) and muscovite. However, for kaolinite there is a loss in pore lining edges of almost 10 % after crushing, but the solvent washed sample shows an increase of 10 % coverage, returning the coverage back to the intact fragment coverage of kaolinite edges.

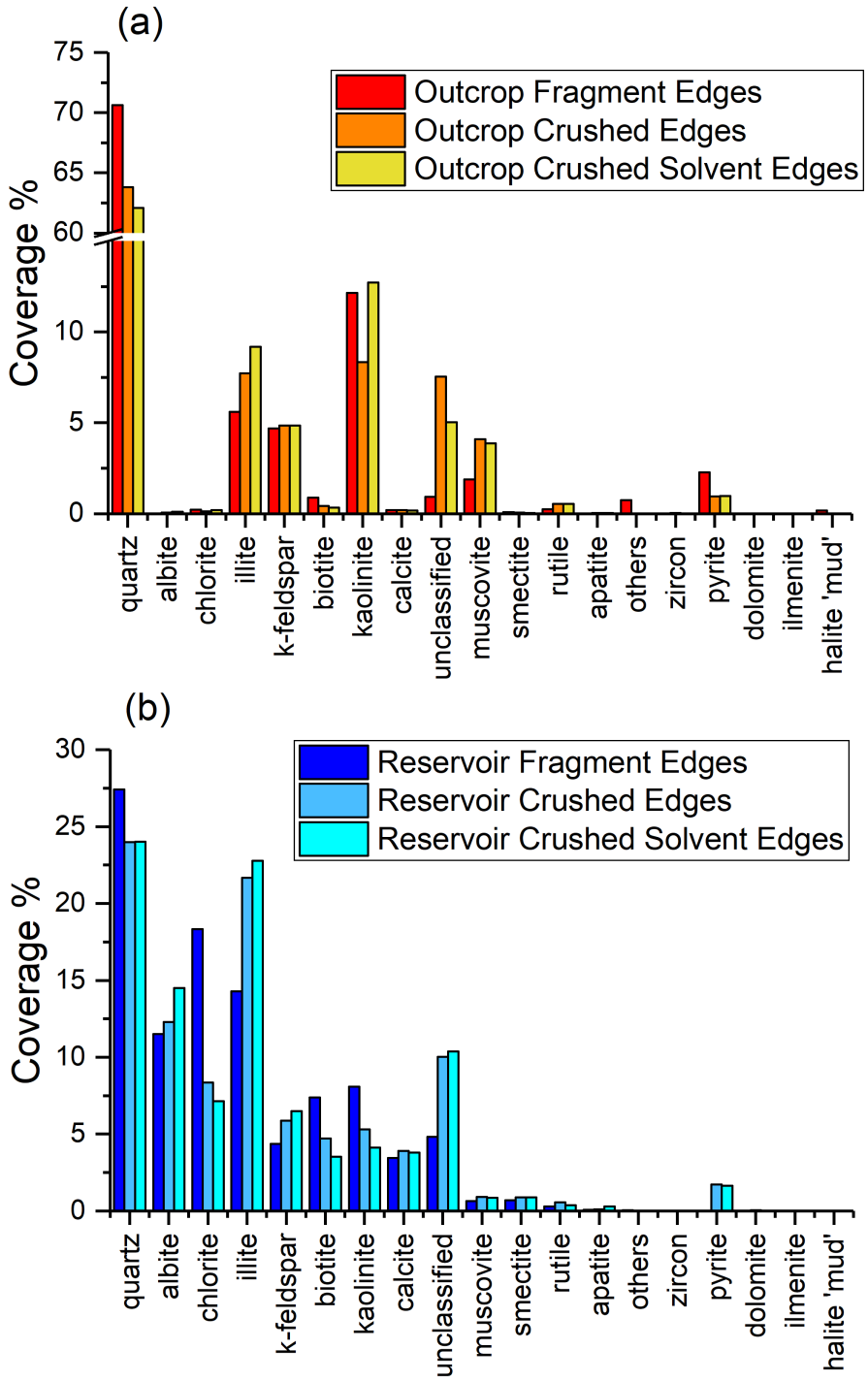

Figure 4.13: QEMSCAN analysis of intact fragment, crushed, and crushed and solvent washed (a) outcrop and (b) reservoir rock.

Throughout this analysis, it must be recalled that analysis of more samples was not possible. Only one image was taken for each sample and other sections of the crushed rock could contain more/less of other mineralogy. However, there are no other minerals that exhibit this change in coverage, suggesting a single image is a

reasonable representation. A second explanation could be the release of fines from the solvent wash as kaolinite and other clays, are often referred to as fines, have been reported to be mobilised under certain conditions. From the data it can be concluded that illite, mixed feldspars and muscovite are loosely bound and able to be freed during crushing of the rock.

4.3.5 Impact of QEMSCAN Resolution

A higher resolution QEMSCAN image is produced when a longer time is spent scanning the sample. There is concern that a coarse (low resolution) image may not be able to resolve small mineral particles liming the pore spaces. Hence, one might incorrectly deduce the wrong minerals are lining the pores. In the limit of a very high-resolution image we should be able to 'see' all the mineral particles and correctly deduce the pore lining composition. However, at lower resolution, small mineral lumps may not be identified and the lining of the pore might be incorrectly taken to be the bulk mineral, such as quartz in this work. Hence, in this section reassurance is given that our deductions about the pore lining minerals are correct by considering manufactured and real images at different spatial resolutions.

Finding the optimum resolution where minerals of interest are still correctly represented will increase throughput for QEMSCAN analysis. Here we look at the reservoir and outcrop complete untreated fragments with a 2 μm per pixel resolution versus a 15 μm per pixel resolution. Figure 4.14 shows the area of the 15 μm per pixel image that was extracted for characterisation and comparison to the higher resolution image.

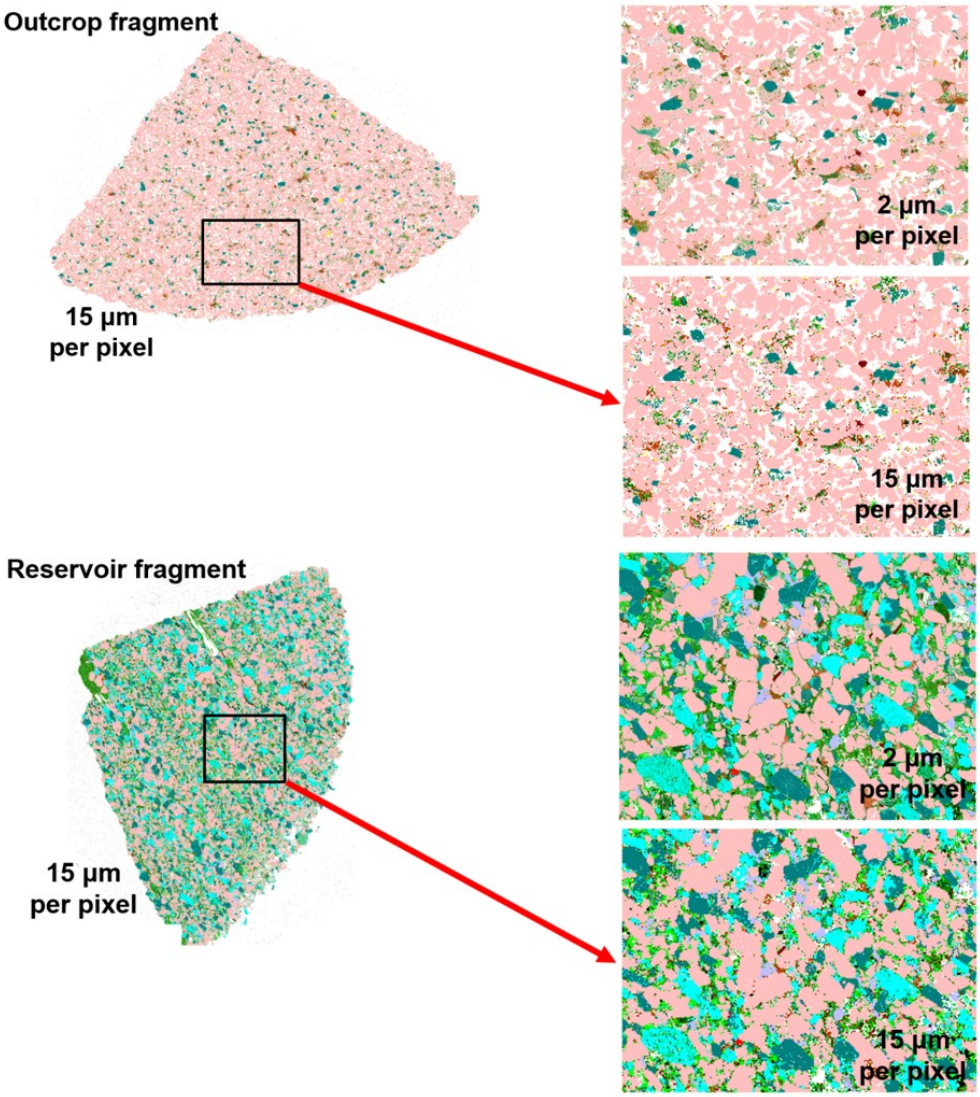

Figure 4.14: QEMSCAN images of extraction of 15 micron resolution section for comparison to 2 micron image.

Figure 4.15 shows the difference between high- and low-resolution fragments of (a) reservoir and (b) outcrop rock. There is a total of 13 and 11 % difference in mineral-pore boundaries in reservoir and outcrop rock respectively as resolution is decreased. Decreasing resolution shows an increase in quartz-pore boundaries. This is expected as a lower resolution scan would not pick up smaller 'fines' such as kaolinite, which is shown to decrease in both. With decreasing resolution, the reservoir rock shows an increase in albite, K-feldspar, chlorite and muscovite; outcrop rock shows an increase in quartz and the mixed feldspars labelled as 'unclassified' which contain a combination of potassium, sodium and/or calcium endmembers in the feldspar.

It can be concluded that the resolution of the image can alter the perceived

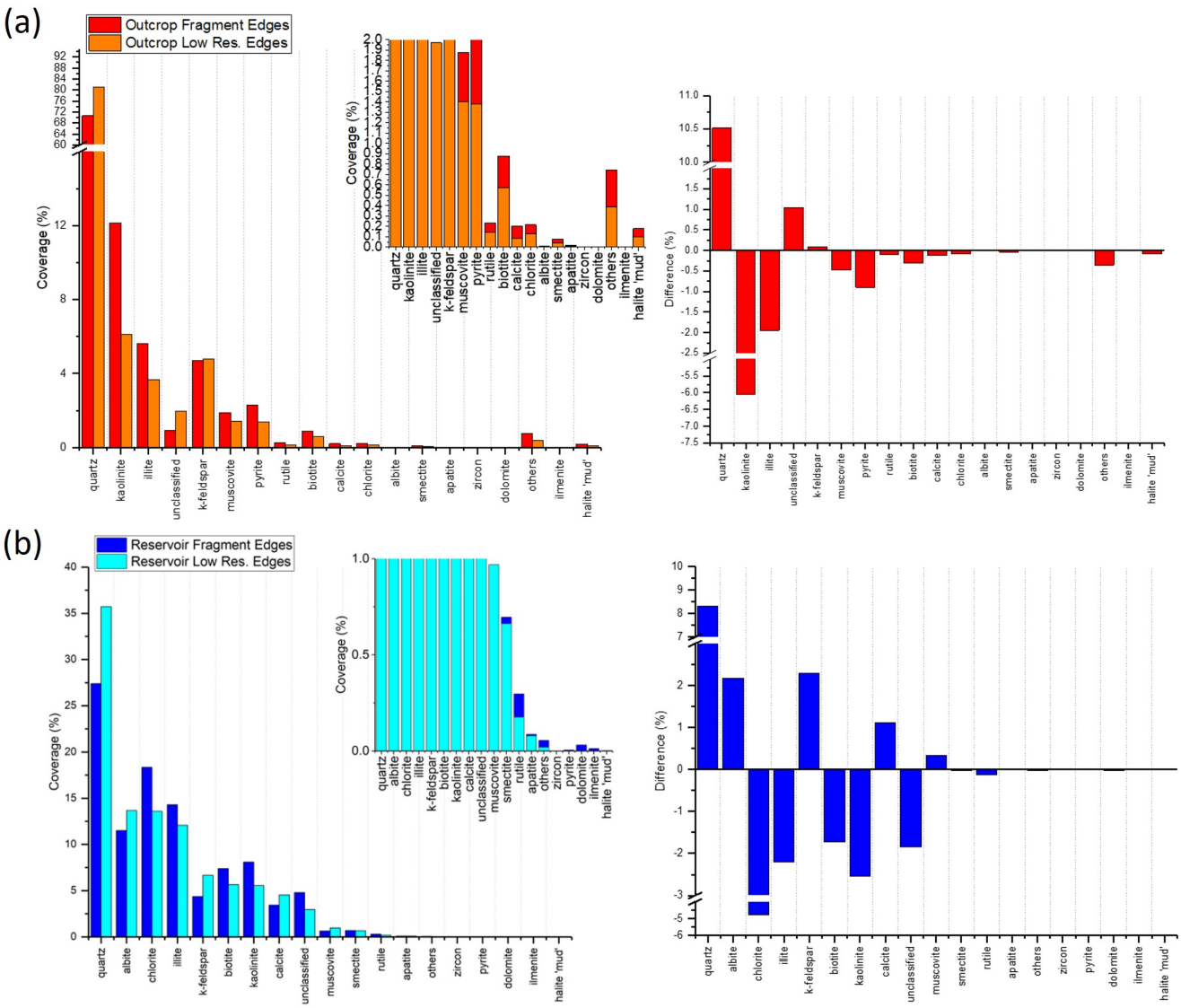

Figure 4.15: Comparison of 2 μm (high-resolution) and 15 μm (low-resolution) for (a) outcrop and (b) reservoir untreated fragment.

composition of the pore walls: mineral pieces smaller than the resolution limit of the image cannot be seen, and in those cases, it will be taken for bulk mineralogy. For example, an image with 15 μm resolution will not resolve particles with a size of 14 μm or less.

The smallest sizes of mineral particle in the rocks that are considered to be influential in recovery are fines, that are 5–50 μm in diameter. This suggests that a 4 μm per pixel image may be sufficient to observe true pore-mineral coverage. However, some pores are smaller than 4 μm; therefore a higher resolution may still be required.

4.3.6 Conclusions

1. The amount of the non-bulk materials determined at the pore linings are a lower estimate of what is there. Increasing the resolution will tend to suggest less quartz than other minerals.
2. The natural sizes of the rock mineral crystallites tend to be 4 microns or bigger (deduced by SEM). Therefore, it is reasonable to suggest there is not a significant population of smaller minerals that have been omitted.

Reservoir and outcrop rock have been analysed as intact fragments, crushed samples and solvent washed samples via QEMSCAN. Analysis of both the bulk mineralogy and minerals lining pore space was conducted to determine the minerals that line pores in outcrop and reservoir rock. QEMSCAN data has shown differences between bulk mineralogy of both reservoir and outcrop rock, showing a statistically significant reduction in quartz between the bulk and pore lining edges in all cases (the fragment, the crushed sample, and the solvent washed sample). The composition of the pore-edges includes a range of clay and silicate-containing minerals, rather than just quartz. However, quartz represents the greatest coverage of pores walls in both cases.

Considering pore lining minerals, the minerals which are of interest here and hence for subsequent ageing to assess organics adsorbing for the reservoir rock are: quartz, albite, feldspar, illite, and pyrite. Minerals of interest for the outcrop rock are quartz, illite, mixed feldspars, kaolinite, and muscovite.

If minerals such as kaolinite and illite, or fines-type minerals are to be investigated, a resolution greater than 4 μm, ideally 2 μm, is required. A lower resolution image is potentially sufficient for mineral-mineral boundary analysis, but the base mineral in the bulk will be over-represented.

For further testing, quartz will be used as the main silica source. Kaolinite and muscovite mica will be used as representative clays covering low and high surface charges. Calcium carbonate will also be included as the dominant mineral in carbonate reservoirs.

4.4 XRF

XRF is used for elemental analysis of major oxides and trace elements. Figures 4.16 and 4.17 show the XRF results for the major oxides (in wt %) and the trace elements (in ppm) of outcrop and reservoir rock as received and following a solvent wash.

Focussing on outcrop and reservoir rocks as received, reservoir rock shows a greater wt % of all major elements apart from SO_2 than the outcrop rock. Volcanic activity and weathering of exposed rock can increase sulphur content. Regarding the remaining major oxides, reservoir rock contains a greater proportion of minerals containing Al, Fe, Mg, Ca, Na, K, (in good agreement with QEMSCAN and literature).[197]

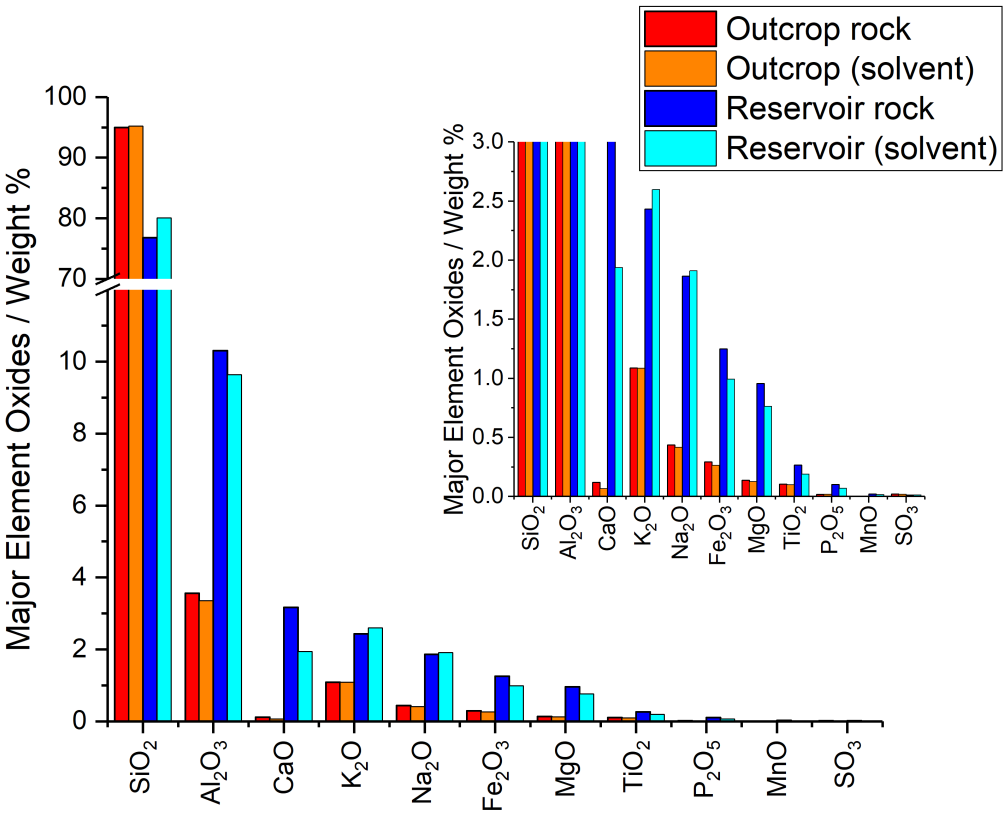

Figure 4.16: XRF of outcrop and reservoir rock major element oxides.

These trace elements such as Co, Cr, Pb, Sn, Cu, Ni, Zr and V may indicate the presence of coordination complexes, such as when a metal ion binds to naturally occurring organic groups such as amino acid ligands, particularly those forming a porphyrin-like structure. The metal ion in a porphyrin usually has a +3 or +2 charge as shown by (Equation 4.1), where M is the metal ion, and L is a

ligand. The porphyrin structure is formed from an amino acid starting material and is transformed via an enzymic reaction. Natural formation of porphyrins, or geoporphyrins, is known to occur in oil locations.[198]

Porphyrin chemistry could be prevalent for (but not limited to) the following trace elements: Co, Cr, Pb, Sn, Cu, Ni, Zr and V.[199–201]

$$\mathrm{H_2[porphyrin] + [ML_n]^{2+} \longrightarrow M(porphrinate)L_{n-4} + 4\,L + 2\,H^+} \tag{4.1}$$

The main geoporphyrins found in oil are Ni and V based. Investigation into presence of Ni and V compounds is assessed in Chapter 5.

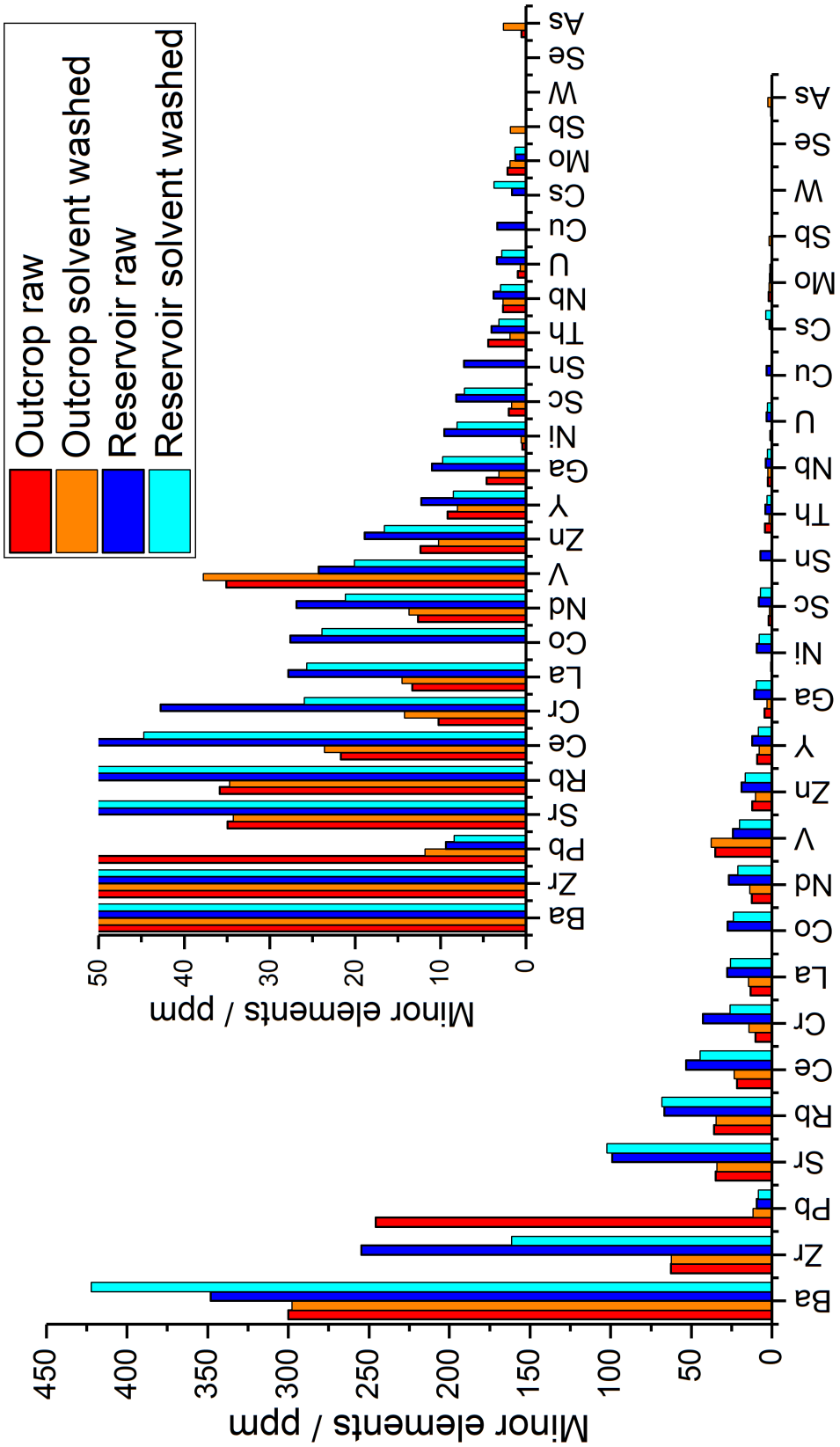

Figure 4.17: XRF of outcrop and reservoir rock minor elements.

4.4.1 Irremovable Compounds

Focussing on the solvent washed outcrop and reservoir rock in Figure 4.16, there is a decrease in major element oxides present in the outcrop, but a small increase in K_2O and Na_2O for the reservoir sample after solvent washing. Outcrop rock shows a decrease in trace element content for the majority of elements, but a significant drop in lead. Reservoir rock also shows a general decrease in trace element content for the majority of elements, but significant drops for tin and copper.

Porphyrins or other organometallic complexes may provide the link between the reductions in major element oxides and trace elements and the expected loss or organic content. Most porphyrins in oil are either nickel or vanadium based. Figure 4.17 shows that in the reservoir rock samples, the vanadium and nickel content has dropped by 0.42 ppm and 1.5 ppm respectively.

4.5 Solution NMR

The core plugs underwent a grinding and a solvent wash process as discussed in section 3.4. The extracted solvent mixture, containing any dissolved organics, was used for analysis via solution ^{1}H and ^{13}C NMR. The extracted mixture is of interest as it may suggest which surface groups are present or the composition of the adsorbed layer, depending on how the extracted groups are bound.

Figures 4.18 and 4.19 show ^{1}H and ^{13}C NMR data for outcrop (red) and reservoir rock (blue) extracts collected after Soxhlet extraction with methanol, THF and chloroform. Both figures indicate several peaks that are difficult to assign individually so have been grouped by environments shown in Table 4.2 and 4.3 for proton and carbon NMR respectively, as discussed in the experimental section.

For ease of interpretation, Table 4.1 shows the functional groups present in the extracts, as detected by NMR.

There is evidence of lots of alkyl carbons that are expected in all samples. However, it is the peaks at higher chemical shift that are of more interest as these represent chemical functionality. Interestingly, outcrop extract shows no peaks to that correspond to aromatic carbons (125–175 ppm) in Table 4.3. Therefore, it is uncertain whether the ^{1}H NMR peak at 8.1 ppm is truly an aromatic proton.[202–204]

The outcrop ^{1}H NMR results show more peaks than the reservoir ^{1}H NMR data results, whereas the ^{13}C NMR show reservoir rock to have more peaks than outcrop rock. The number of peaks is proportional to the number of different moieties present: more peaks suggests a wider variety of organic species. The reservoir rock extract has peaks on the ^{13}C NMR spectra at around 100 ppm, which suggests ether groups. The outcrop rock does not have peaks at 100 ppm.

Overall, a number of chemical environments and groups were successfully assigned from the samples obtained by Soxhlet extractions of outcrop and reservoir rock via solution ^{1}H and ^{13}C NMR. Both outcrop and reservoir rock extracts show alkyl, alcohol, amine (primary, secondary and tertiary), ether, acid, ester, and ketone groups present in the extract. As expected, a greater variety and number of moieties are present in reservoir extract than outcrop. Table 4.1 shows the same functionalities are present in both extracts, but we can visually see the quantities are different from the spectra.

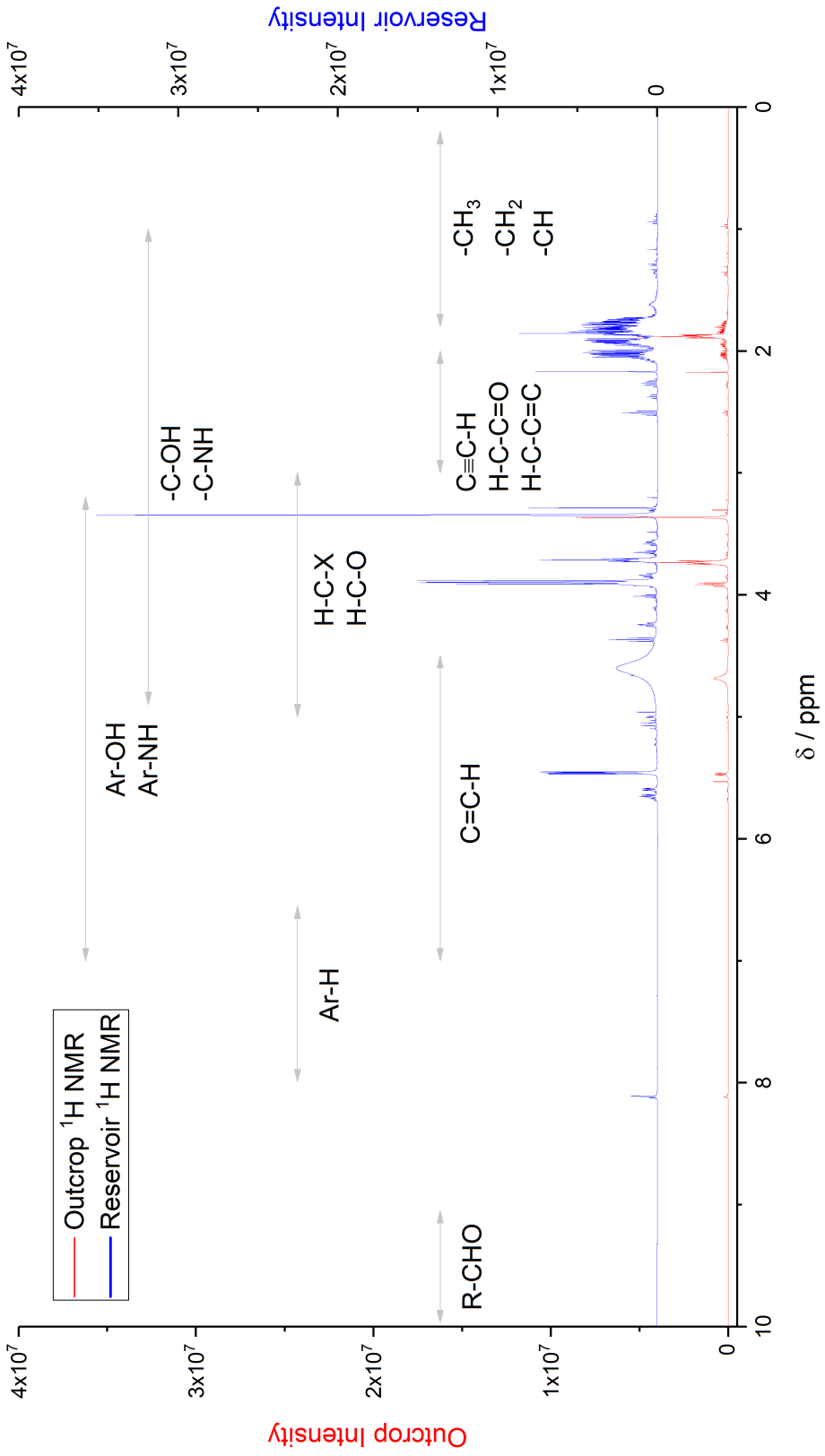

Figure 4.18: Proton NMR for outcrop (red) and reservoir (blue) solvent extracts.

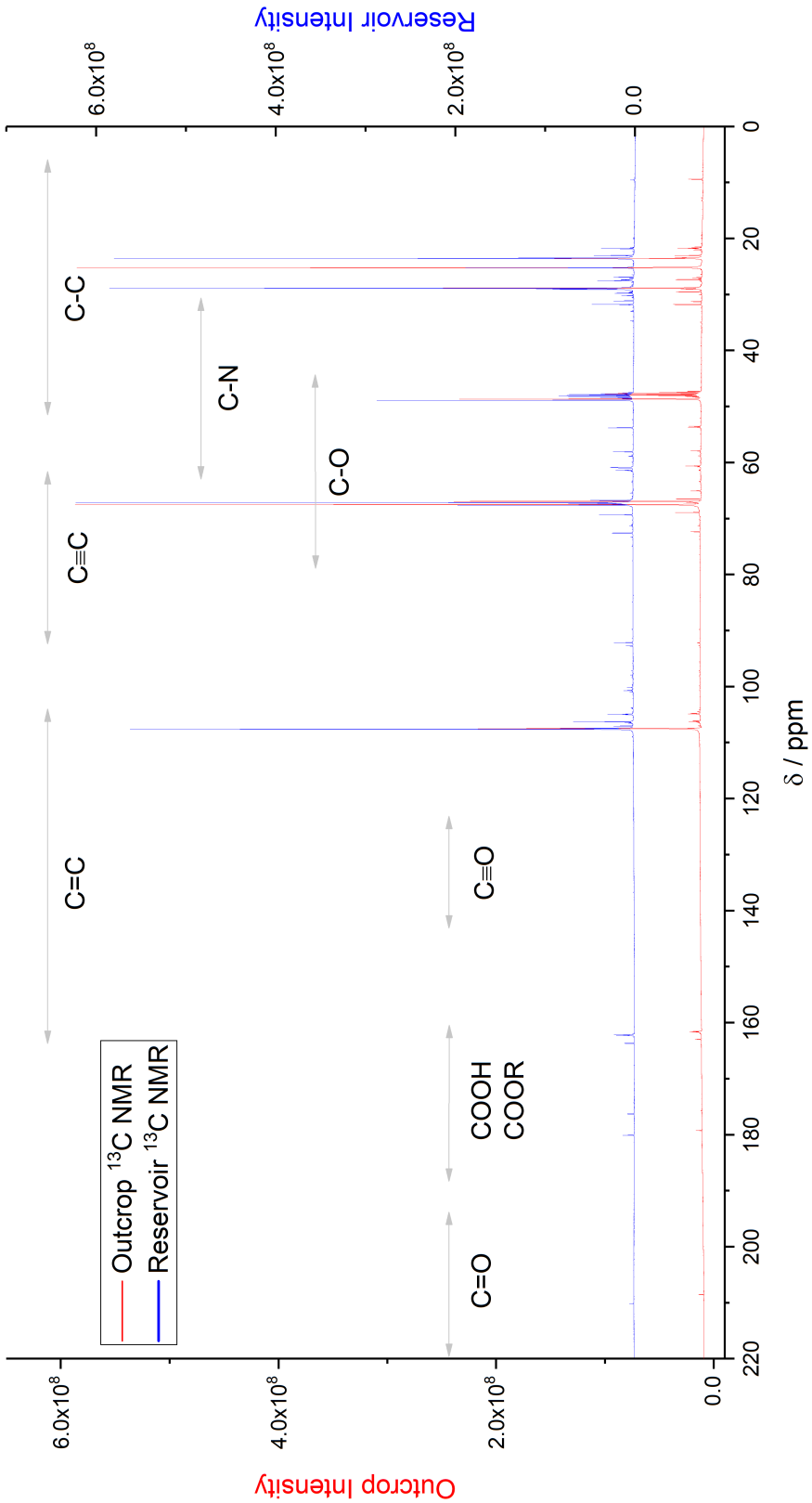

Figure 4.19: Carbon NMR for outcrop (red) and reservoir (blue) solvent extracts.

Functional Group	^{1}H NMR		^{13}C NMR	
	Outcrop	Reservoir	Outcrop	Reservoir
Alkyl	✓	✓	✓	✓
Alcohol	✓	✓		
Ether	✓	✓	✓	✓
Halogen	✓	✓		
Aromatic	✓	✓	✓	✓
Alkene			✓	✓
Ketone			✓	✓
Primary amine	✓	✓	✓	✓
Alkyne			✓	✓
Acid			✓	✓

Table 4.1: Components of outcrop and reservoir rock soxhlet extraction detected by ^{1}H and ^{13}C NMR.

^{1}H NMR		
Outcrop / ppm	**Reservoir / ppm**	**Assignment**
0.9	0.9	R−CH_3
	1.1–1.3	R_2CH_2
	1.6	$R_2C{=}CR(CH_3)$
1.7–2.0	2.1–1.7	C−NH, C−OH
2.1	2.2	CH_3OR, CH_3NR_2
	2.3	$R_2C{=}CR(CH_2R)$
2.4		CH_2COR
3.2	3.2	CH_3OR
3.3	3.3	CH_3OR
	3.4	RCH_2OR
3.6–3.9	3.9–3.5	HCO, HCX
	4.0	HCO, HCX
	4.2	HCO, HCX
4.3	4.3	
4.6	4.6	C=CH, Ar−OH, Ar−NH, C−OH
	5.0	C=CH, Ar−OH, Ar−NH, C−OH
	5.1	C=CH, Ar−OH, Ar−NH, C−OH
5.4	5.5	C=CH, Ar−OH, Ar−NH, C−OH
5.5	5.6	C=CH, Ar−OH, Ar−NH, C−OH
8.1	8.1	ArH, ArOH

Table 4.2: ^{1}H solution NMR results for outcrop and reservoir rock

^{13}C NMR		
Outcrop / ppm	**Reservoir / ppm**	**Assignment**
9.4	9.5	RCH_3
21.7	21.8	R_2CH_2
23.1	23	R_2CH_2
24	23.4	R_2CH_2
25.2	25.2	R_3CH, CH_3CO^-
27	26.9	R_3CH, CH_3CO^-
27.6	27.5	R_3CH, CH_3CO^-
28.9	28.8	R_3CH, CH_3CO^-
29.4	29.1	R_3CH, CH_3CO^-
31.3	31.4	R_3CH, CH_3CO^-, RCH_2NH_2
32.3		R_3CH, CH_3CO^-, RCH_2NH_2
47.7	47.8	CH_3CO^-, RCH_2NH_2
48.8	48.3	CH_3CO^-, RCH_2NH_2
53.5	53.8	RCH_2NH_2, RCH_2O^-
57.8	58.1	RCH_2NH_2, RCH_2O^-
60.6	60.9	RCH_2NH_2, RCH_2O^-
65.2		RCH_2O^-, C≡C
66.5		RCH_2O^-, C≡C
66.9	66.8	RCH_2O^-, C≡C
67.1	67.3	RCH_2O^-, C≡C
68.9	69.3	RCH_2O^-, C≡C
72.4	72.6	RCH_2O^-, C≡C
	92.2	C≡C
	100.7	C=C
104.8	105	C=C
106.2	106.3	C=C
107.5	107.4	C=C
161.7	162.2	C=O (acid and ester)
163		C=O (acid and ester)
179.3	180.1	C=O (acid and ester)
208.5	210.2	C=O (ketone)

Table 4.3: ^{13}C solution NMR results for outcrop and reservoir rock

4.6 TGA-MS

The solution washing analysis above can only probe chemical species that desorb from the minerals upon solvent extraction. However, possibly more important than desorbing molecules are the molecules that remain on the rock after solvent washing. These 'irreversibly bound' materials may be attributed to determining wettability and adsorption/absorption of other oil species. It is important to note that it is more challenging to assess the organics that are not removed by solvent extraction.

TGA-MS and Py-GCMS (Section 4.9) were used in this study to identify which fragments were released from the cores when heating at a constant rate to a high temperature and comparing it with a flash heating. This is a drastic step to remove otherwise irremovable compounds (compounds that are strongly-adhered to the surface) from the silica substrate. The process will be expected to break the bound organics into fragments. The rate of heating is also expected to alter the extent of fragmentation.

Figure 4.20 shows TGA data for raw outcrop, solvent washed outcrop, raw reservoir, and solvent washed reservoir rock at 10 °C per minute up to 900 °C. The results show an initial drop in mass below 100 °C which is attributed to loss of water (i.e. drying of sample). At around 500 °C a further loss of mass begins for all samples. The raw outcrop rock has a mass drop from 500–600 °C which continues to slowly decline until 900 °C, similar to the solvent washed reservoir rock. This is a similarity due to the levels of organic present in both samples. Solvent washed outcrop rock shows a constant decline in mass from 500 to 900 °C. The raw reservoir rock shows the drop before 100 °C, and no change until 500 °C where a first loss in mass occurs, followed by a second large drop in mass at 650 °C before plateauing at 750 °C until 900 °C. The raw reservoir rock shows the biggest mass loss of 2.5 %, whereas both raw and solvent washed outcrop have a loss of 1.5 % and solvent washed reservoir rock loses 1 % of its mass. Therefore, more volatile compounds from the raw reservoir rock are released during TGA than the other rock samples.

Figure 4.21 shows the mass spectrometry results for (a) raw reservoir, (b) solvent washed reservoir, (c) raw outcrop, and (d) solvent washed outcrop rock. The data show there is a greater amount (intensity) of fragments released for the reservoir rock samples compared to outcrop rock. There is a greater number of fragments from the outcrop rock with a higher molecular mass than the reservoir rock. The higher molecular mass fragments from the outcrop could be due to plant-based biomarkers, namely resin-type structures with C_{20} backbones resulting in ∼250 g

mol^{-1} fragments, which are discussed below when coupling TGA-MS data to stable isotope analysis.[205] The lack of high molecular weight fragments in the reservoir rock could be due to fresh oil **not** entering the rock and not refreshing the organics on the rock.[206] One would assume that initially small molecules diffuse and adsorb onto the rock. Over time, it would be thermodynamically favourable for large molecules to adsorb. However, if the large molecules are not present (no fresh crude oil), there is no opportunity for large molecules to bind.

The aim of this experiment was partly to determine if the application of heat will remove adsorbed compounds from reservoir and outcrop rock samples. Overall, the TGA-MS data has shown that the reservoir rock has more material removed (2.5 wt % loss) when heat is applied compared to the solvent washed reservoir rock and outcrop samples. The remaining three samples, solvent washed reservoir rock, as received outcrop rock, and solvent washed outcrop rock all show a loss of 1.5 wt %, suggesting smaller amounts of material are removable by application of heat, as opposed to solvent washing.

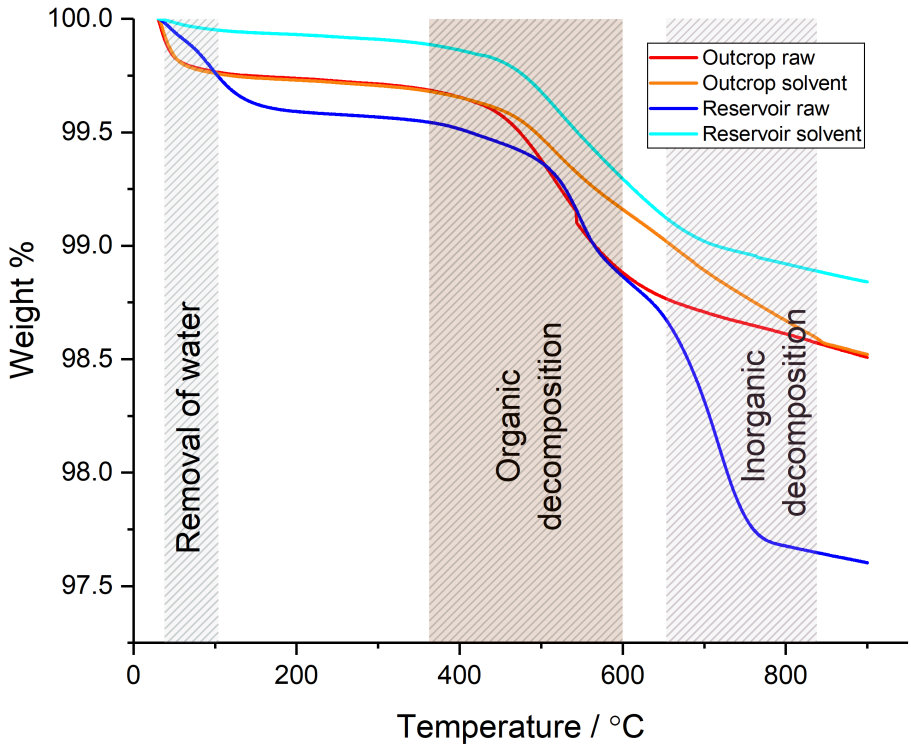

Figure 4.20: TGA data showing TGA results of raw outcrop, solvent washed outcrop, raw reservoir, and solvent washed reservoir rock at 10 °C per minute up to 900 °C.

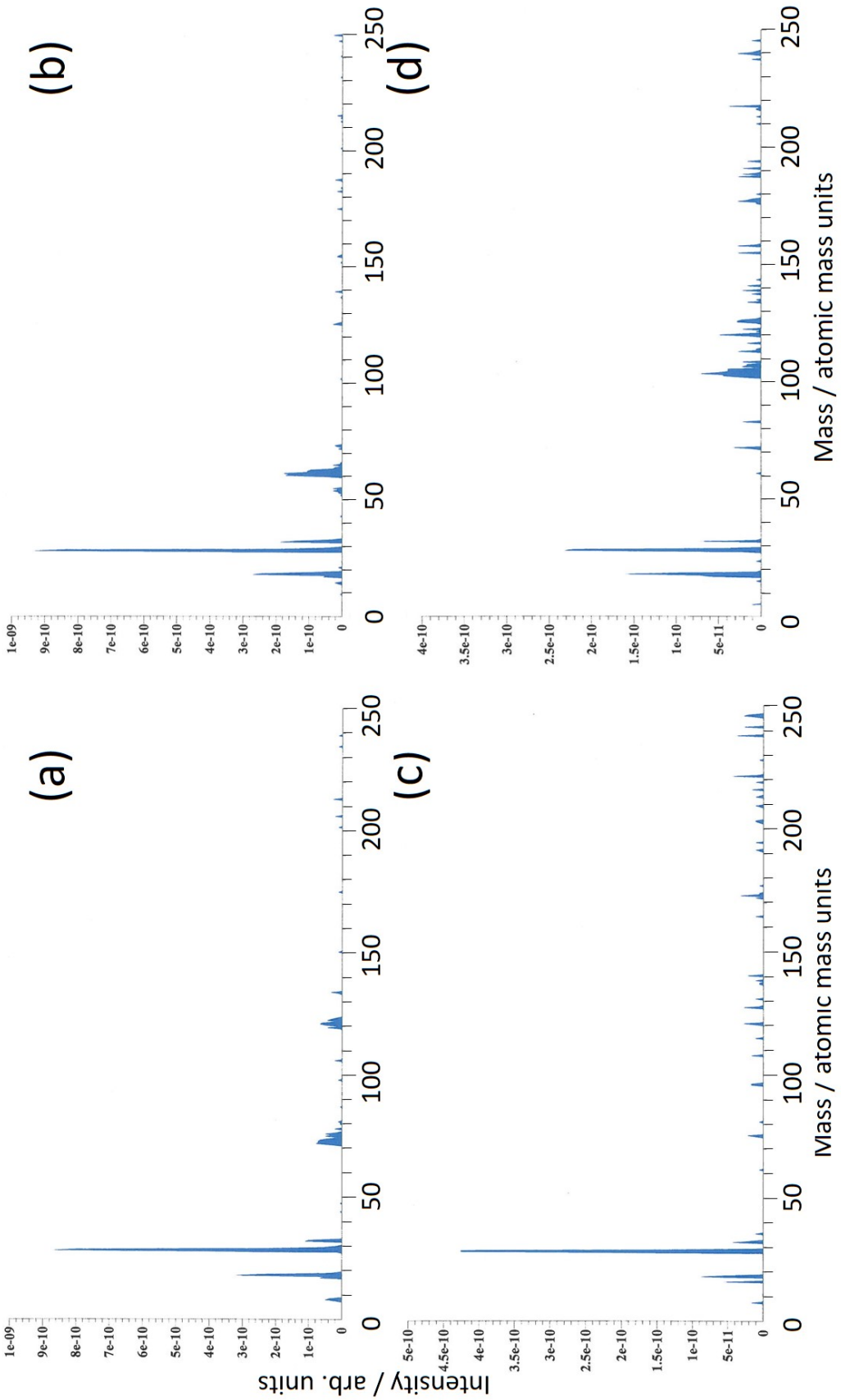

Figure 4.21: Mass spectrometry data from TGA-MS showing results for (a) reservoir, (b) solvent washed reservoir, (c) raw outcrop, and (d) solvent washed outcrop rock. The data show a collation of fragments released throughout heat application as opposed to fragments at one temperature.

4.7 Elemental Analysis

Two types of elemental analysis were conducted on the reservoir and outcrop rocks: CHN analysis and stable isotope analysis. The stable isotope analysis includes a measurement of the total organic carbon (TOC) content. The stable isotope TOC can be compared with total carbon (TC) analysis from CHN after it is normalised to show TOC with QEMSCAN data to remove inorganic carbon (IC) contribution from carbonates.

4.7.1 Carbon Analysis

Figure 4.22 shows the total organic carbon content from stable isotope analysis and TC content from CHN analysis of outcrop and reservoir rock samples.

Focussing firstly on the rock samples as received that has also been crushed: Outcrop rock raw (as received) has 0.015 ± 0.001 wt % and reservoir rock is shown to have 0.791 ± 0.055 wt % TOC from stable isotope TOC. For outcrop rock, there is very little difference between stable isotope TOC and elemental TC as the carbon content is close to the limit of detection of the device. When looking at reservoir rock, the elemental TC results show a lower amount of total carbon (by almost 0.2 %) when compared to the stable isotope TOC values; it might be expected to see a larger amount of TC due to IC arising from mineral carbonates present. Comparing outcrop to reservoir rock, the greater TOC content might be expected from the reservoir rock compared to the outcrop due to the expected oil content in reservoir rock. This is indeed observed.

Irremovable Organics

The solvent washed outcrop shows no difference from the raw outcrop—this is expected as we do not anticipate much organic on the outcrop rock. The reservoir rock shows a loss of organics upon solvent washing: there is no statistically significant drop between TOC levels due to large error ($\Delta_{\text{average TOC}}$ suggests a 0.2 % loss of removable), however the TC show a 0.1 % loss.

Finally IC that are present as carbonates are considered. To remove carbonates from the system, a simple wash in HCl was conducted until effervescence ceased. This yielded a TOC content of 0.135 ± 0.005 %, and TC content of 0.12 ± 0.03 %. To verify this result it can be compared with QEMSCAN data. QEMSCAN showed 3.5 % $CaCO_3$ in reservoir rock, which equates to 0.42 % carbon, therefore a drop is expected from a TC content of 0.63 % to 0.21 %. The H_2O_2 washed

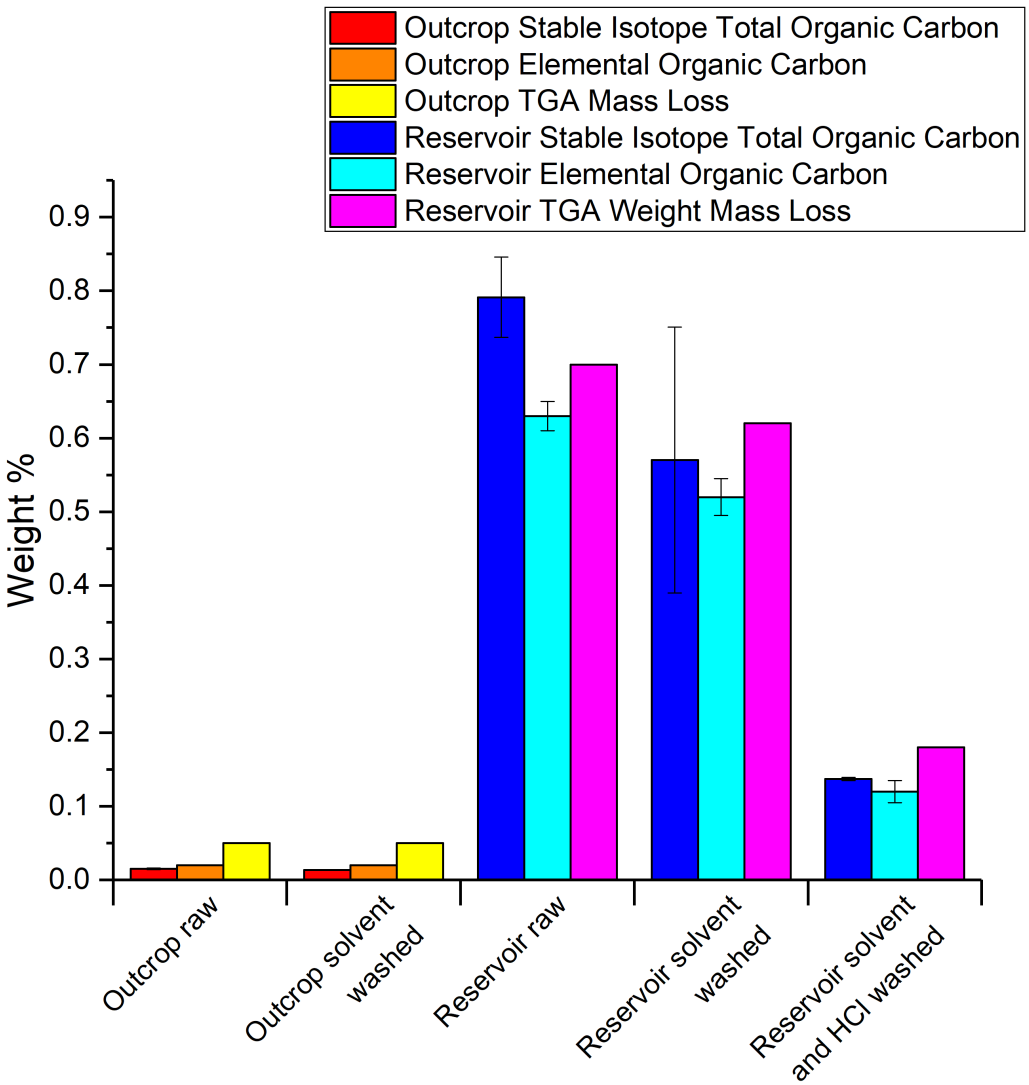

Figure 4.22: Total organic carbon content from stable isotope analysis and total carbon content from CHN analysis of outcrop and reservoir rock samples.

TC data measured a similar reduction although a slightly lower value than 0.21 % was obtained, which may suggest this particular sample was slightly enriched in carbonate. Interestingly, a similar percentage loss is seen for TOC (solvent washed to H_2O_2 washed = $\Delta 0.44$ %). This could suggest carbonates are binding organics strongly.

To support the TOC measurement technique, TGA can be employed using the mass loss between 150 to 550 °C (assuming any mass loss below 100 °C is water, and above 600 °C is decomposition of carbonate minerals). Figure 4.22 shows the TGA samples display similar profiles to the TOC and TC results. This confirms successful removal

of organics via soxhlet extraction and reduction of carbonates via HCl treatment has occurred.

BET Surface Analysis

BET was conducted to deduce the thickness of the organic layer on the reservoir rock. The total amount of adsorbed organic is divided by the surface area. The sample of interest is the 'solvent and H_2O_2 washed' reservoir rock, as the majority of the carbon had been removed; around 90 % of the organics are removed.[207] This sample was selected to avoid potential complications in the BET analysis of absorption of nitrogen into any adsorbed organic layers. Table 4.4 shows an overview of the BET surface area results and the calculations for thickness of the 'organic carbon layer' present. Below is an example of how the calculations were conducted.

Sample	BET / m^2 g^{-1}	Wt % C	Thickness / Å
Reservoir rock as received	2.825 ± 0.053	0.791	11.4
Solvent washed reservoir rock	1.049 ± 0.011	0.570	22.1
Solvent and H_2O_2 washed reservoir rock	3.114 ± 0.040	0.140	1.8

Table 4.4: BET surface area analysis of reservoir rock as received, after a solvent wash, and after a solvent and HCl wash.

The 'solvent and H_2O_2 washed reservoir rock' has a BET surface area of 3.114 m^2 g^{-1}. Considering the 0.14 wt % of carbon from Figure 4.22, the percentage of carbon in 1 g of 'solvent and H_2O_2 washed reservoir rock' is 0.014 g. The density of reservoir rock is 2.46 g cm^{-3} (calculated from the plug as received with a mass of 176.6583 g, length of 6.50 cm, diameter of 3.75 cm). Therefore, a volume of carbon, 5.69 x 10^{-10} m^3, is calculated. Using the BET surface area and the mass used in the BET experiment (rounded to 1 g of rock sample), the thickness of the remaining 'carbon layer' on the mineral is 1.8 Å thick. The length 1.8 Å is comparable to a single molecular layer.[208] It is important to note that this is a very crude estimate and is used to illustrate how much organic is present.

The 'reservoir rock as received' has a layer thickness of 11.4 Å that also corresponds to an adsorbed molecular layer. Similarly, but quite interestingly, the 'solvent washed reservoir rock' shows a layer thickness of 22.1 Å that corresponds to a molecular layer but one that is larger—the solvent washed rock shows a layer that is approximately double the thickness of the organic carbon layer on 'reservoir rock as received'. This interesting result in the calculation assumptions are heavily due to the small BET surface area produced from larger particles in the sample measured. The measurement could not be repeated due to access to the kit. For the solvent

washed sample, a BET surface area of 3 m^2 g^{-1} would yield a carbon thickness of 7 Å, which is more inline with expectations.

In summary, BET surface area has shown that a H_2O_2 wash will dramatically reduce the organic carbon layer present by 84 % and hence can be used to approximately 'clean' the mineral surfaces. The organic layer thickness has been determined to be one molecule thick. This may imply that there is a particular layer of strongly adsorbed molecules that are key to controlling the surface wetting, which is a novel insight.

4.7.2 Stable Isotope Analysis

Figure 4.23 shows stable isotope analysis of outcrop and reservoir rock after solvent washing. The initial stable isotope analysis shows a very high value for raw reservoir rock, suggesting carbonates are present. To remove carbonates from the system, a simple wash in HCl was conducted until effervescence ceased. This yielded a δ^{13}C of -30.7 ± 0 ‰.

The δ^{13}C values of approximately -22 and -31 ‰ for the outcrop and reservoir respectively would suggest a terrestrial source of the bound organics (a value typical of -24 to -28 ‰). It is known that Castlegate outcrop is a non-marine sediment and hence our results are in good agreement with this provenance.

A δ^{13}C value of ∼24–27 corresponds to hydrocarbons and bi- and tri-cyclic compounds that are referred to as diterpenoids and sesquiterpenoids. These are common plant-based biomarkers with a resin-type C_{20} backbone that results in a molecule weight of over 250 g mol^{-1}.[205] It is understandable that the outcrop rock would contain plant-based biomarkers. The δ^{13}C value of outcrop rock is only 2 below this range and linking back to the higher molecular weight values obtained in the TGA-MS (Figure 4.21), it is understandable that the molecular weight of fragments remains high due to the stable cyclic backbone of the biomarkers.

After solvent washing, δ^{13}C remains the same whereas the HCl wash reduces the ratio from -6.76 ± 0.50 ‰to -30.69 ± 0.02 ‰. It is expected that the δ^{13}C remains the same after a solvent wash as the solvent wash should not preferentially remove ^{12}C or ^{13}C.

Some organic carbon was successfully removed by a solvent wash as confirmed by the TOC data (Figure 4.22) and the presence of carbonate was proved, coupled with QEMSCAN data, as a HCl wash reduces the TOC dramatically and changes the δ^{13}C.

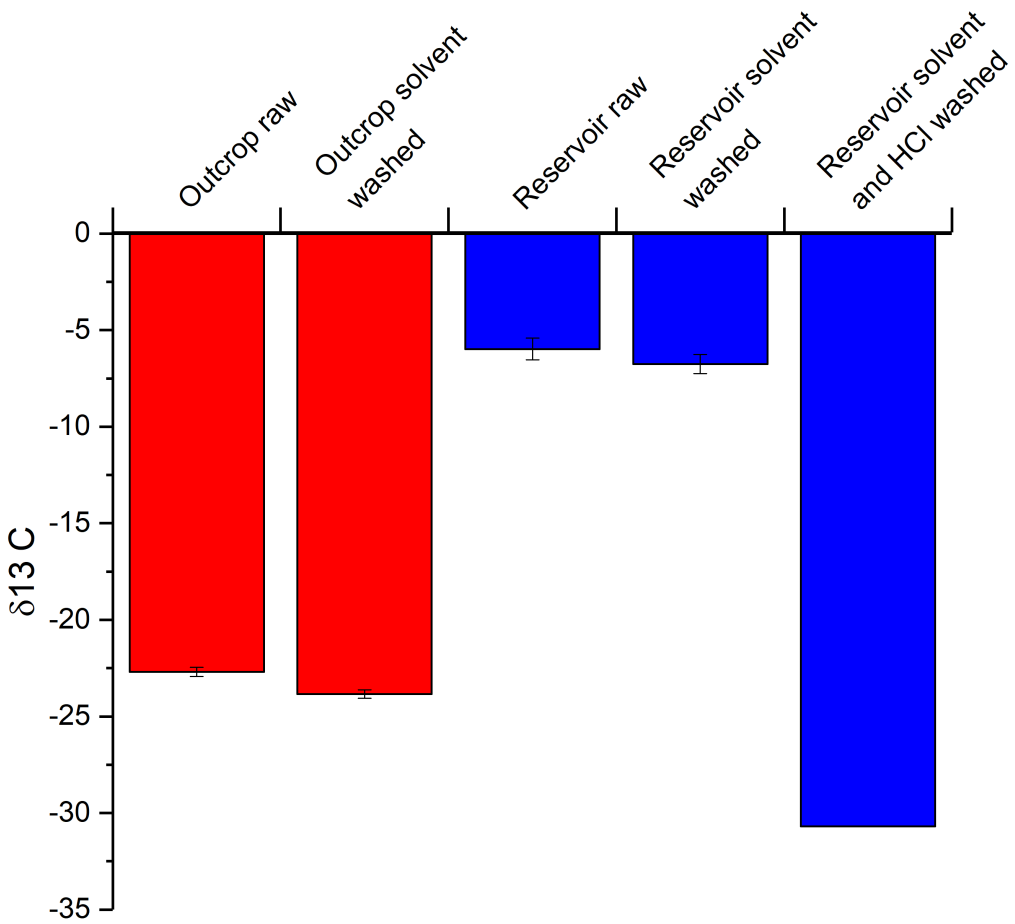

Figure 4.23: Stable isotope analysis of outcrop and reservoir rock after solvent washing.

It can be concluded that the irreversibly bound organic is of terrestrial origin and 0.15 wt % irreversibly bound organic is left on the rock.

4.8 TOF-SIMS

As mentioned above, there are key organic components that are irreversibly bound on the mineral surfaces and few approaches to try and characterise them. The results outlined below were obtained via TOF-SIMS, which can remove important organics and identify them. However, there is likely to be significant fragmentation of the species.

TOF-SIMS was conducted on outcrop and reservoir samples, both raw and solvent washed, to try to identify groups present on the surface, using the approach outlined in the experimental section. A series of MS data were measured (Figure 4.24). However, identification of the organic fragments is difficult and complex.

A procedure was adopted to identify the most likely groups that matched the MS data with possible fragments. The m/z value of each peak can be used to infer possible molecular species. The range of possible fragments for each peak was kept very tight to minimise the possibilities. The presence of other isotopic related species was also investigated as an additional constraint and hence several possible fragments eliminated. In this way, the peaks could be assigned to a limited number of specific functionalities.

Figure 4.25 shows the data for **aliphatic hydrocarbon** matches on raw outcrop, solvent washed outcrop, raw reservoir, and solvent washed reservoir rock. Assignment was conducted using IonTOF software inbuilt library of aliphatic hydrocarbon peaks. The majority of results show a decrease in detected ion intensity when moving from raw to solvent washed sample in both reservoir and outcrop rock – confirming successful removal of organics. Simple hydrocarbons will not be strongly bound to the surface and hence easily removed by solvent. Outcrop rock shows a greater intensity of hydrocarbon ion detected compared to reservoir rock, which is unexpected. The difference in intensity could be due to ease of removal of ions on outcrop rock, if they are not strongly bound. TGA-MS data also shows a higher intensity of high molecular weight molecules.

Figure 4.26 shows the data for **siloxane** matches on raw outcrop, solvent washed outcrop, raw reservoir, and solvent washed reservoir rock. The data shows that at increasing amu the solvent washed samples show a lower intensity than the raw samples for both outcrop and reservoir rock. However, at low amu, there is an increase in siloxane fragments from the solvent washed reservoir rock. The increase may be attributed to removal of organics and subsequent removal of the organic-free and uncovered silica surface due to the highly destructive nature of bombarding the

sample with ions that effectively depth profile the sample. A key issue with the siloxane data is the PDMS impurity discussed in Section 3.14. Like the aliphatic hydrocarbon data, the siloxane fragments have not been matched with their isotopic neighbours.

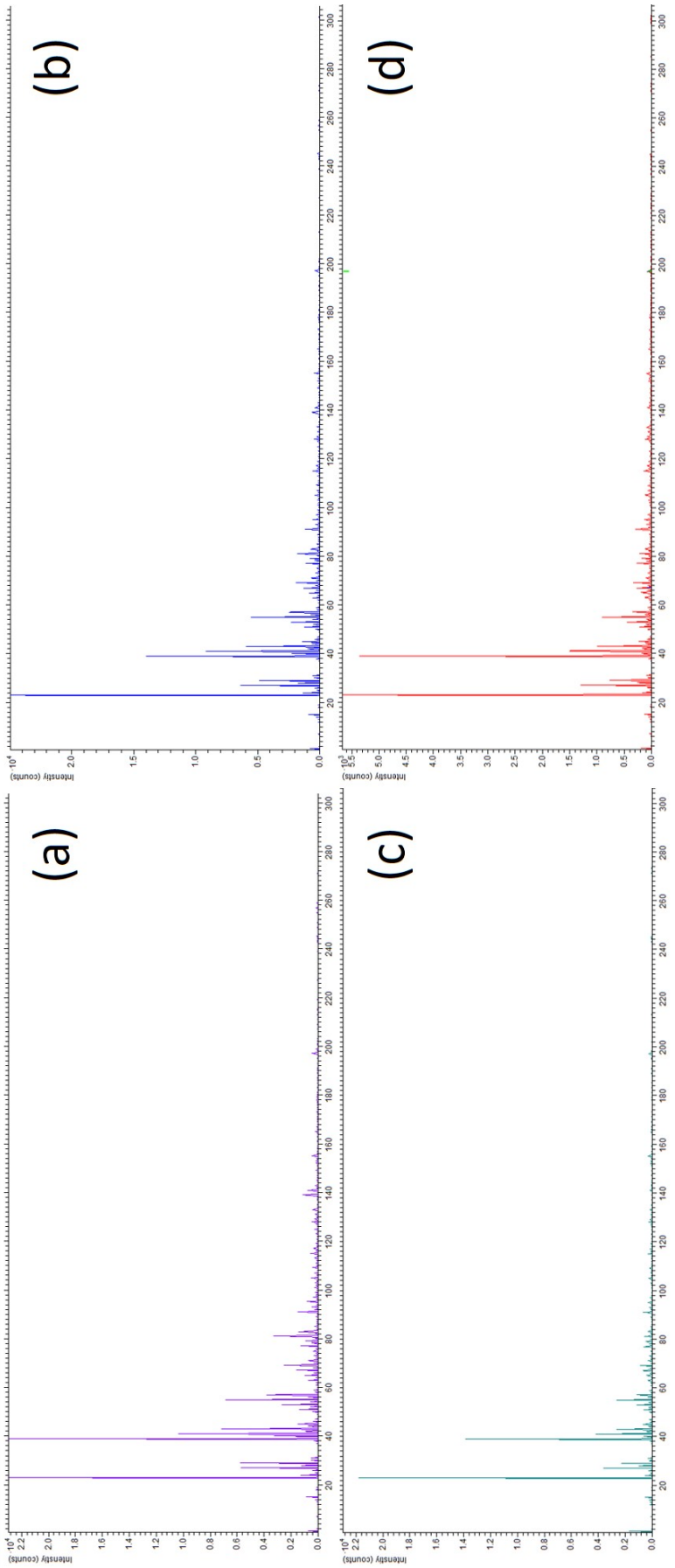

Figure 4.24: TOF-SIMS data for (a) raw outcrop, (b) solvent washed outcrop, (c) raw reservoir and (d) solvent washed reservoir rock.

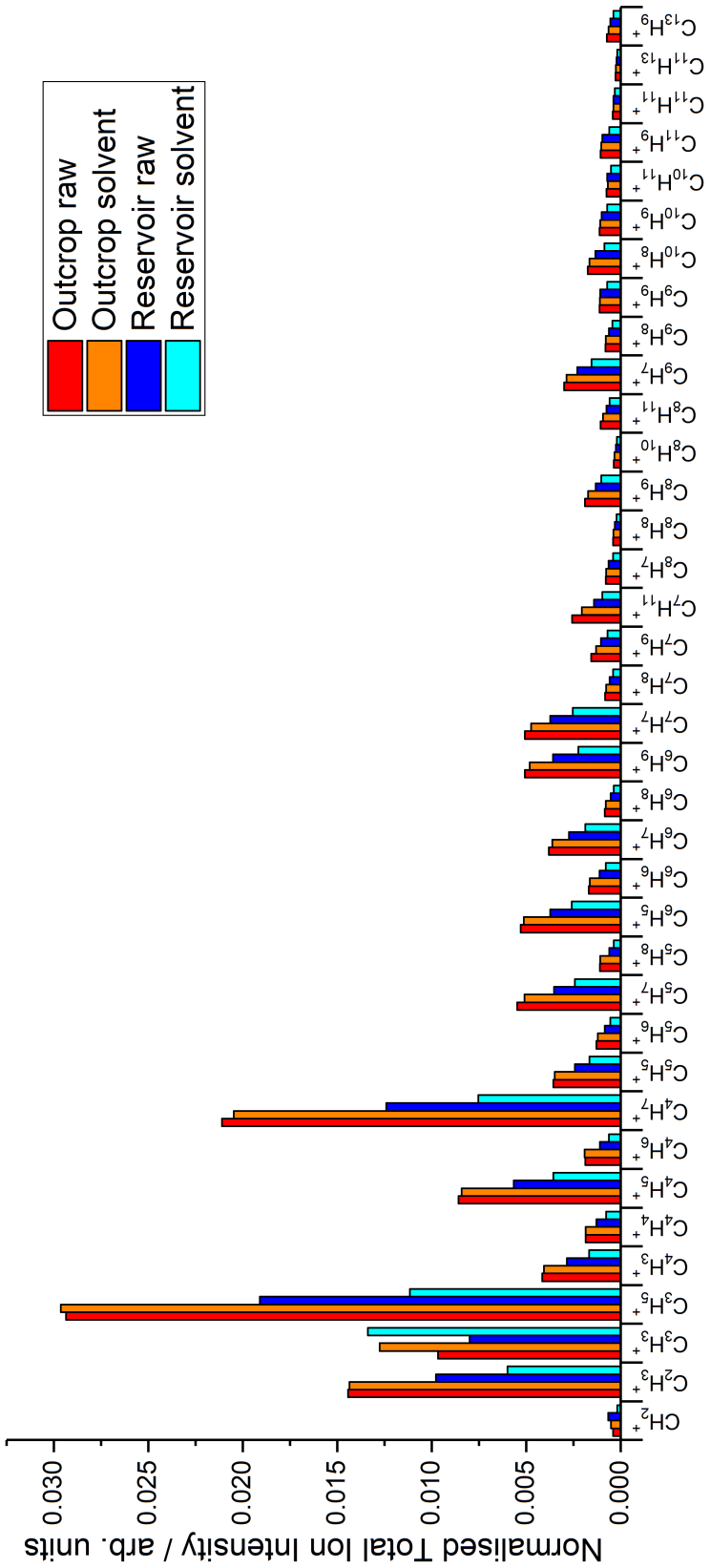

Figure 4.25: TOF-SIMS data of raw outcrop, solvent washed outcrop, raw reservoir and solvent washed reservoir rock showing aliphatic hydrocarbons with increasing m/z ratio. Total ion intensity has been normalised for sample comparison.

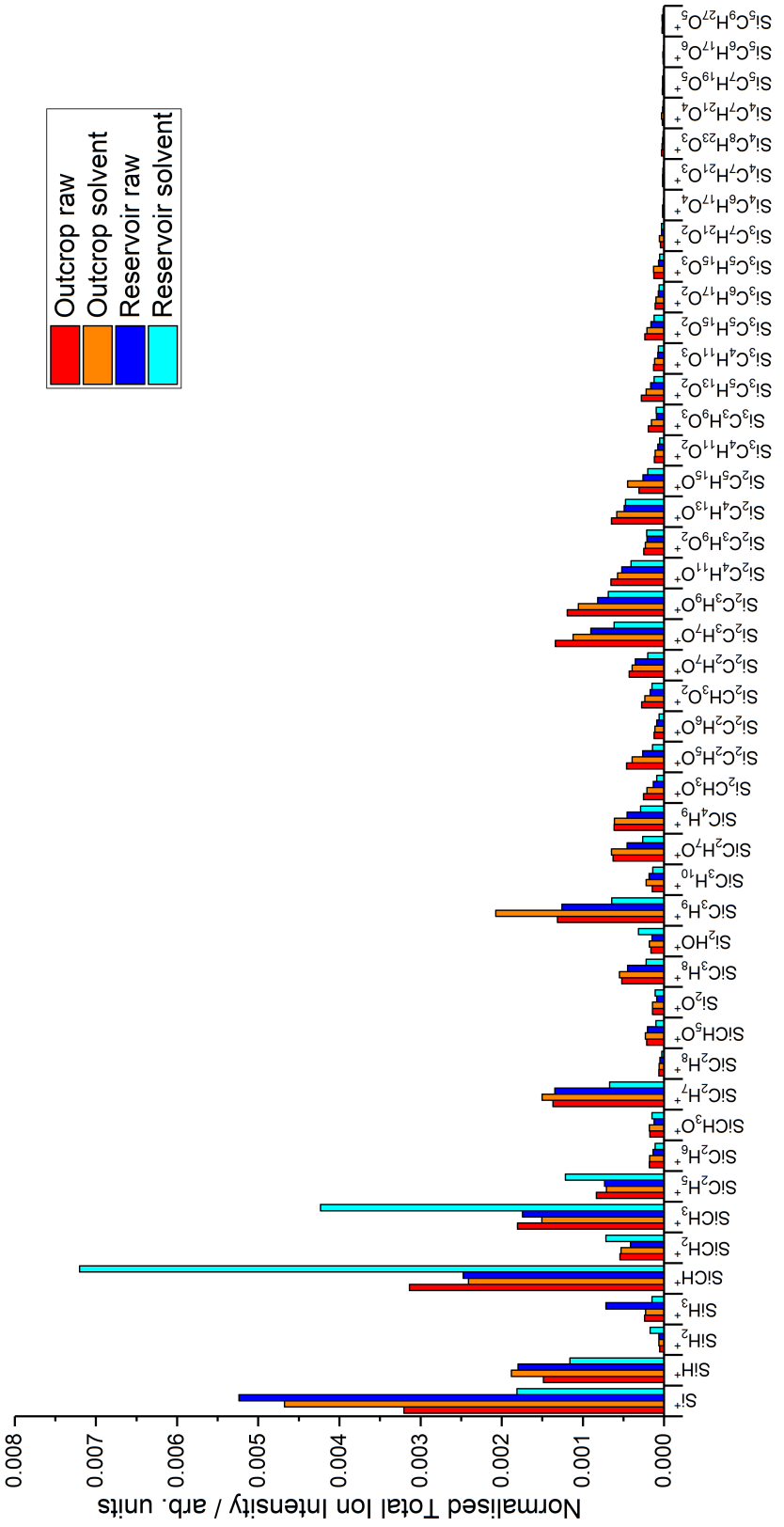

Figure 4.26: TOF-SIMS data of raw outcrop, solvent washed outcrop, raw reservoir and solvent washed reservoir rock showing siloxanes with increasing m/z ratio. Total ion intensity has been normalised for sample comparison.

The data in Figure 4.27 (a) and (b) show the amino acids **serine** and **threonine** fragment matches respectively, on raw outcrop, solvent washed outcrop, raw reservoir, and solvent washed reservoir rock. Both the amino acid peaks are from a database of known compounds. The known raw material is measured via TOF-SIMS and the molecule and its fragments are input into a database. The known fragments for the molecule are compared versus a measured sample spectra and compared to see if the molecule and its associated fragments are present. The measured sample data were successfully matched isotopically on IonTOF software and show a decrease in intensity moving from raw to solvent washed sample in both cases, with outcrop rock scoring a higher intensity than reservoir rock. This is attributed to less organic present in solvent washed samples compared to raw samples. The increase in intensity for outcrop compared to reservoir rock could link to the resin-type molecules present as mentioned in the stable isotope analysis and TGA-MS data.

Figure 4.28 shows data for **poly(2-vinylpyridin)** fragment matches on raw outcrop, solvent washed outcrop, raw reservoir, and solvent washed reservoir rock. Once again, moving from raw to solvent washed samples, the intensity of ion detected decreases for both outcrop and reservoir rock. The outcrop rock generally has a higher intensity than the reservoir rock, with a few deviations from the trend at low amu values. As amu increases, intensity of the ion detected tends to decrease. The highest intensity peaks are from hydrocarbons, whereas nitrogen containing fragments show a lower intensity. This could be attributed to where the nitrogen is bound: the energy required to break a Si−N bond (439 kJ mol^{-1}) is higher than the energy required to break a Si−C bond (435 kJ mol^{-1}). Therefore, it will be more favourable to break the Si−C than Si−N, hence why there may be less intensity for nitrogen containing fragments.

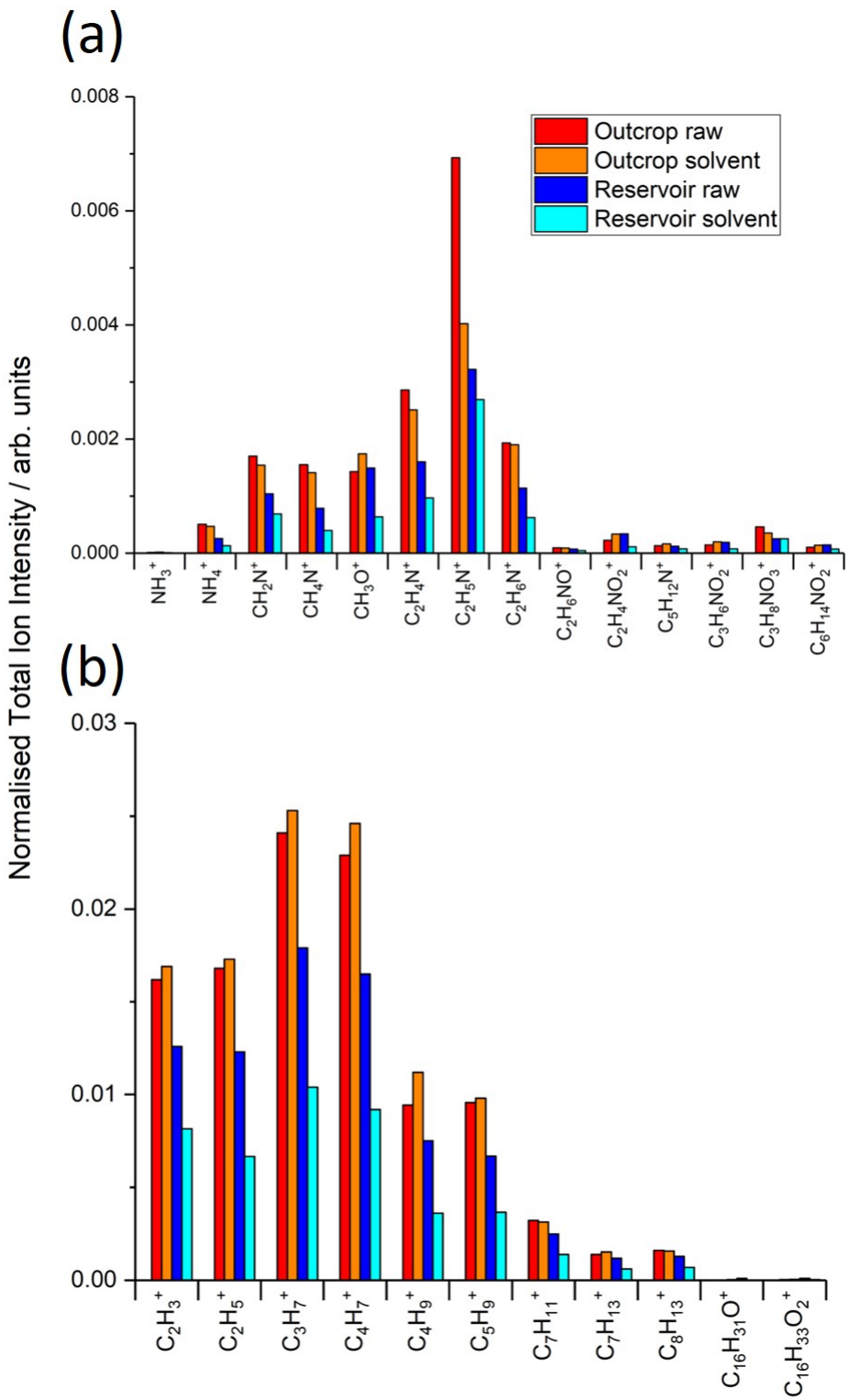

Figure 4.27: TOF-SIMS data of raw outcrop, solvent washed outcrop, raw reservoir and solvent washed reservoir rock showing (a) serine and (b) threonine fragments with increasing m/z ratio. Total ion intensity has been normalised for sample comparison.

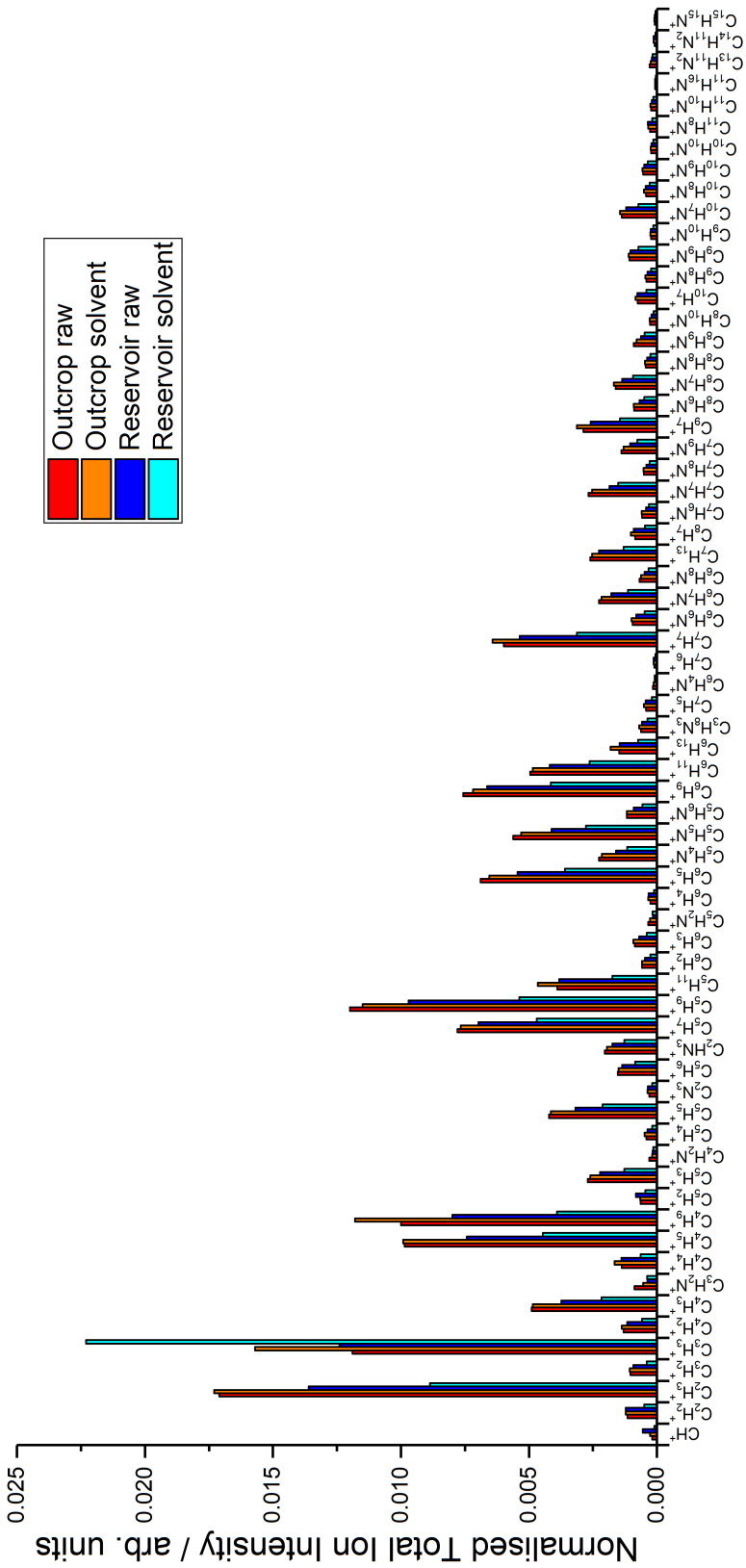

Figure 4.28: TOF-SIMS data of raw outcrop, solvent washed outcrop, raw reservoir and solvent washed reservoir rock showing poly(2-vinylpyridin) fragments with increasing m/z ratio. Total ion intensity has been normalised for sample comparison.

Conclusion

TOF-SIMS was used to conduct surface analysis of raw outcrop, solvent washed outcrop, raw reservoir, and solvent washed reservoir rock. This approach yields evidence for surface bound organics, even after solvent washing, revealing possible irreversibly bound material. The m/z values suggest the types of functionality present.

Evidence for the presence of aliphatic hydrocarbon presence, siloxanes, amino acids and polymeric fragments has been shown. However, this approach requires further investigation to specifically match hydrocarbons, siloxanes, and other groups of interest isotopically to confirm their presence.

4.9 Py-GCMS

Py-GCMS flash heating was conducted on the same four samples (outcrop rock (1) as received and (2) solvent washed; reservoir rock (3) as recieved and (4) solvent washed), as shown by the MS data in Figure 4.29 of the species released from the surface. All samples have a similar intensity background noise due to presence of the helium carrier gas. The data show a smooth line for both outcrop samples, suggesting no molecules are released, whereas the reservoir samples show clear additional peaks after 15–20 minutes.

Interpretation of the m/z values of the fragments collected allows inference that reservoir rock as received contains fragments from: carbamic acid (Figure 4.30 (a)), 5–ethyl, 2–methyl heptane, tridecane, dodecane, and tetradecane with more than 90 % certainty. Solvent washed reservoir rock contained the following fragments at 90 % certainty: carbamic acid, 2,3,7–trimethyl octane, tridecane, 2,6,10–trimethyl dodecane, and tetradecane. The occurrence of hydrocarbon compounds is expected in the reservoir rock as there may be residual oil. Interestingly the carbamic acid group present is the only nitrogen containing group eluted which may suggest this type of structure is the most stable as it has withstood high heat. The presence of carbamic acid could originate from a carbamate H_2NCOO^-, which are known to alter wettability of silica systems.[209] From the peaks in the MS from TGA-MS (Figure 4.21) the Py-GCMS is expected to tag peaks from the outcrop samples but none are tagged.

The fragmentation that is an inherent part of Py-GCMS makes it complex to identify the species on the mineral surfaces. For example, it is uncertain whether the long chain hydrocarbons observed in Py-GCMS data, such as tetradecane are eluted as themselves or as fragments of a larger molecule. In addition, differences may be expected in the extent of fragmentation between physisorbed organics with no formal chemical bond to the substrate and chemisorbed species where at least one chemical bond must be broken to release the species for detection. Hence, more fragmentation for chemisorbed species than physisorbed species may be expected.

To understand the results gained from TGA-MS and Py-GCMS, a further study was conducted, concerning deliberately functionalised silica and molecules adsorbed on silica (section 4.10). In this way, chemisorbed and physisorbed species on minerals are known and can be compared in Py-GCMS. Ideally the Py-GCMS would be re-run at 800 °C, taking into consideration the raw reservoir rock mass loss at 750 °C (Figure 4.20).

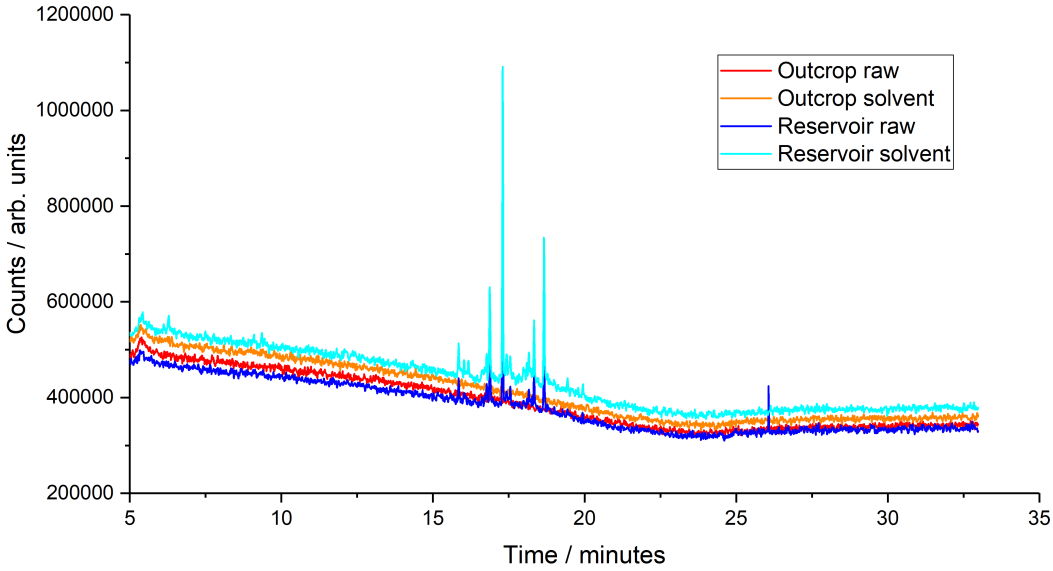

Figure 4.29: Py-GCMS raw data results of raw reservoir, solvent washed reservoir, raw outcrop, and solvent washed outcrop. Samples were flash heated to 550 °C at 10 °C per mS and held for 1 minute at temperature. Results show no peaks detected for outcrop raw and outcrop solvent, whereas peaks were detected (compounds eluted) for reservoir raw and reservoir solvent samples.

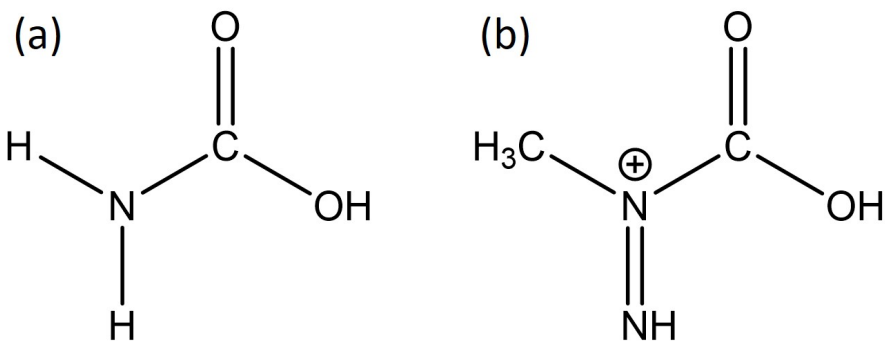

Figure 4.30: (a) Carbamic acid and (b) a carbamic acid style molecule which satisfies the TOF SIMS peak at 90 m/z.

Comparing Py-GCMS and TOF-SIMS data is very complex. Firstly, outcrop data from Py-GCMS showed no peaks eluted, yet TOF-SIMS removed fragments from the sample surface, suggesting there is some removable chemistry present and that TOF-SIMS is better at removing the strongly adsorbed species. Reservoir rock data for Py-GCMS in this work have shown that long chain hydrocarbons eluted, and TOF-SIMS solvent washed reservoir rock data and 'as received' rock supports the data with the presence of long chain hydrocarbons within the spectra that are matched isotopically. The presence of carbamic acid which was eluted in Py-GCMS is a lot harder to confirm with TOF-SIMS as there could be several functional groups

that give rise to a nitrogen signal. When looking at the TOF-SIMS data, carbamic acid is not present as a $^{+}$NCOOH fragment but a similar structure may be present at 90 m/z where a $C_2H_5N_2O_2$ peak is matched isotopically. The peak at 90 m/z suggests a carbamic acid-type molecule with a methyl group and nitrogen (Figure 4.30 (b)).

4.10 TGA and Py-GCMS of Model Adsorbed Systems

Section 4.6 and 4.9 discussed TGA-MS and Py-GCMS results for the as received and solvent washed outcrop and reservoir rock samples. In this section, functionalised silica and silica with adsorbed complex surfactants are analysed via TGA-MS and Py-GCMS. The advantage of this approach is that the adsorbed system is known, allowing a clear distinction between data generated by the chemisorbed and physisorbed silica. Experiments that vary the TGA rate of heating were run in order to measure the enthalpy of adsorption.[210–212]

4.10.1 Results and Discussion

Figure 4.31 shows the TGA data for (a) octadecyl functionalised silica, (b) silica with CTAB, (c) silica with NaAOT, (d) silica with CaAOT at 10, 20, and 30 °C per minute. Pure CTAB, NaAOT, and CaAOT are also included for comparison.

Pure Material TGA Data

The pure CTAB (Figure 4.31 (b)) shows a large mass loss at 250 °C due to the melting point of CTAB (218–247 °C).[213] Figure 4.31 (c) shows pure NaAOT decomposing at 250 °C, which does not correspond with the literature melting point of NaAOT (153–157 °C), suggesting there are some impurities in NaAOT as received. Figure 4.31 (d) shows pure CaAOT decomposing at a similar temperature as NaAOT with a very small amount of water loss.

Adsorbed Material TGA Data

Figure 4.31 (a) shows a loss of mass of 20–21 %. This is attributed to the loss of C18 chains and satisfies the manufacturer's suggestion of 20–22 wt % functionalisation. Figure 4.31 (b) shows a similar mass loss of 12 and 15 % for the rates 10 and 20 °C per minute respectively, compared to the 20 % loss in mass for 30 °C per minute. The decomposition of adsorbed CTAB is at the same temperature of pure CTAB. The large difference in mass loss is due to more CTAB being present—i.e. there is more than would be expected for a monolayer around the silica. There is no consistency with a higher heating rate revealing more adsorbed material, therefore this is deviation in the sample that may have occurred from incomplete washing of the excess.

Figure 4.31 (c) shows silica with NaAOT at heating rates 10, 20, and 30 °C per minute with mass losses of 9, 11, and 8 % respectively. Other than loss of water below 100 °C, the main loss of mass occurs at 250 °C .[214] This could be due to impurities known to be associated with the NaAOT as it was not purified before use. Interestingly, there is a greater amount present on the sample run at 20 °C per minute, possibly due to heterogeneous sampling.

Figure 4.31 (d) shows silica with CaAOT at heating rates of 10, 20, and 30 °C per minute with mass losses of 16, 16, and 14 % respectively. The main mass loss occurs at around 275 °C, which is the decomposition temperature of pure CaAOT used in this study.

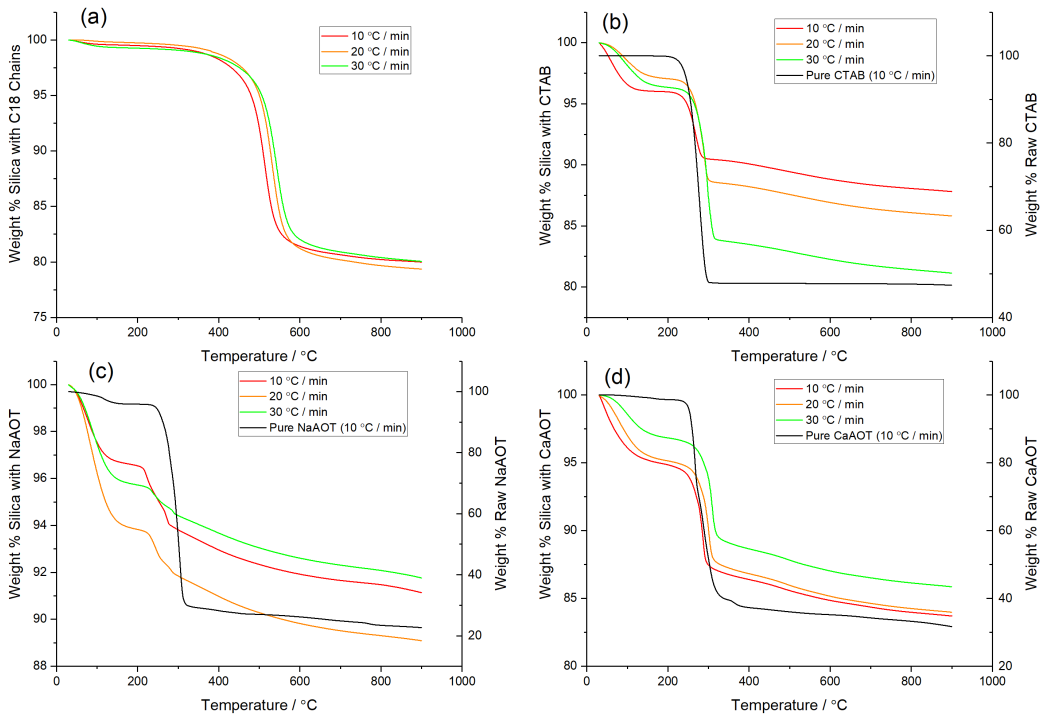

Figure 4.31: TGA data showing results for (a) octadecyl functionalised silica, (b) silica with CTAB, (c) silica with NaAOT, (d) silica with CaAOT at 10, 20 and 30 °C per minute. Pure CTAB, NaAOT and CaAOT are included (black) for comparison.

The main focus of this section is to try and identify what species are desorbed from organics coated on silica substrates and what fragments form.

Figure 4.32 shows TGA-MS data for (a) pure CTAB (black) and silica with CTAB (red), (b) pure NaAOT (black) and silica with NaAOT (red), (c) pure CaAOT (black) and silica with CaAOT (red), and (d) octadecyl functionalised silica. Only MS data from the TGA run at 10 °C per minute up to 900 °C is displayed for simplicity.

A greater number of peaks are observed for the pure Ca/NaAOT compared to silica with the respective additive (Figure 4.32 (b) and (c)). This could be due to inadvertent removal of the additive during the adsorption process—-solvent washing with water or drying at 40 °C may cause the removal of some components.

For all samples, no very large molecular weight fragments (i.e. 250+ amu) are detected (CTAB = 364.45 g mol^{-1}, NaAOT = 444.56 g mol^{-1} and CaAOT =883.14 g mol^{-1}), suggesting the molecules are broken down first rather than the entire molecule staying intact. Most peaks appear below 50 amu.

For (d) the silica with C_{18} chains has a peak at 169 amu which corresponds to $C_{12}H_{25}{}^{+}$. It is interesting to consider where this fragmentation occurs; it could be any one of the C−C bonds along the chain or C−O−Si group holding to alkyl chain to the substrate. The mass of the fragment suggests there are no carbon chains with Si correspond to this peak. C−C and C−O have a lower bond energy (343 and 358 kJ mol^{-1}) than the Si−O bond (535 kJ mol^{-1}), suggesting it's more likely to break mid-chain or at the C−O connecting to the silica surface.[215,216]

Overall, the interpretation suggests the presence of alkyl chain fragments will occur even when more complex functionalities are present. Hence, the alkyl species observed such as tetradecane may well have originated from more complex species with other groups binding to the substrate, but only the alkyl fraction is readily released.

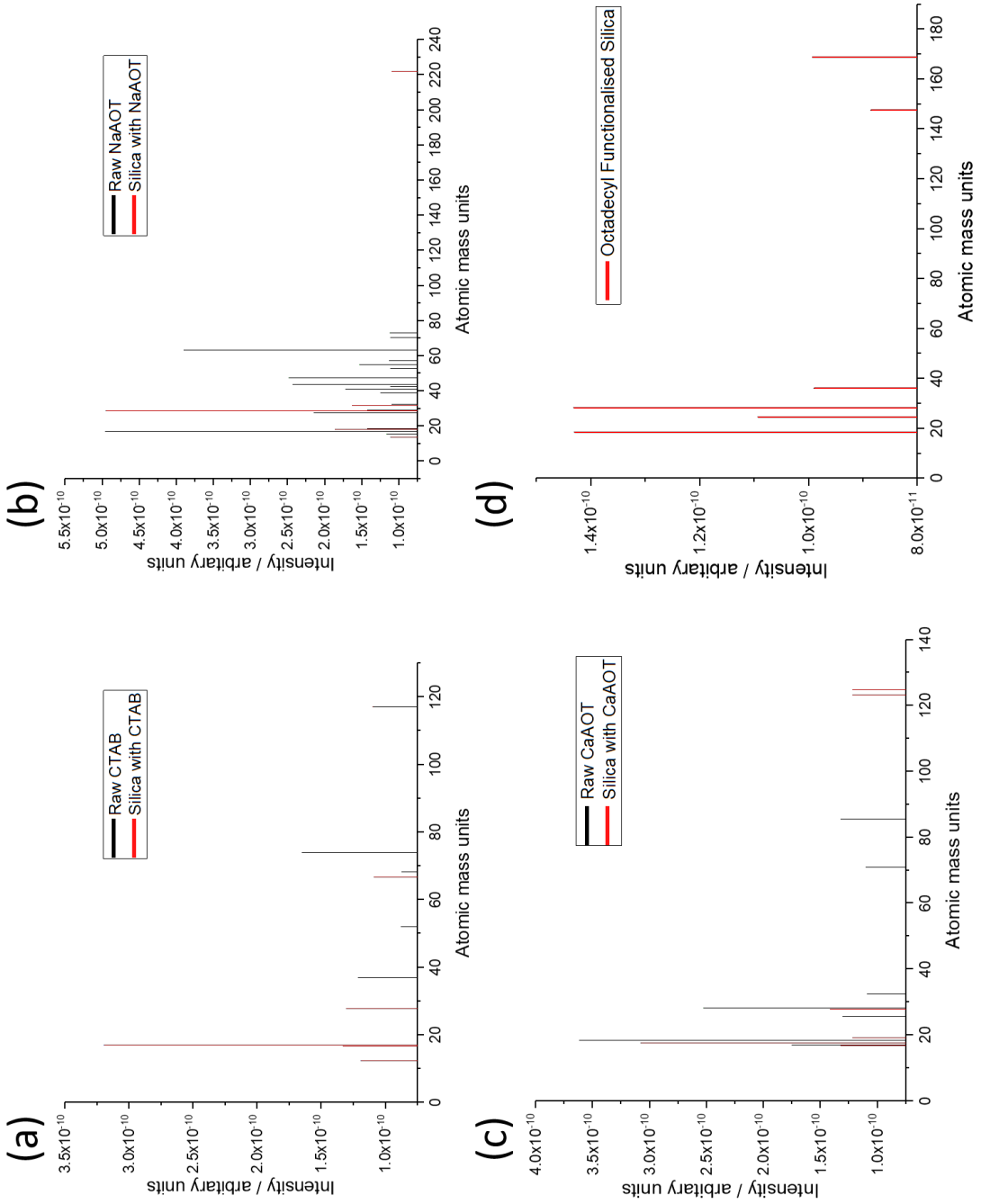

Figure 4.32: MS data for (a) pure CTAB (black) and silica with CTAB (red), (b) pure NaAOT (black) and silica with NaAOT (red), (c) pure CaAOT (black) and silica with CaAOT (red), and (d) octadecyl functionalised silica. MS data is from the TGA run at 10 C per minute up to 900 C. Data show a collation of fragments released throughout heat application.

Figures 4.33, 4.34, 4.35 and 4.36 show Py-GCMS results for octadecyl functionalised silica, silica with CTAB, silica with NaAOT, and silica with CaAOT respectively.

Figure 4.33 shows octadecyl functionalised silica flash heated at 550 °C to assess differences in peaks eluted from GCMS. The data shows peaks are eluted at similar time intervals. Considering if the whole molecule comes off, the largest fragment suggested is nonadecene (C_{19}), which is bigger than the C_{18} side chain on the molecule. However, there are no C_{18} fragments detected. Focussing on other fragments detected, the mass spectrum assigned a homologous series of primary alkenes: 1–octene to 1–nonadecene eluted between 7–21 minutes, with increasing chain length. Interestingly, there are small peaks either side of the central alkene: the left-hand peak is the corresponding alkane and the peak after is dodecadiene. This is concluded to be characteristic of long hydrocarbon chains for Py-GCMS is a small alkane peak, followed by large alkene peak, and a small dodecadiene peak.

Figure 4.34 shows Py-GCMS CTAB data at 550 °C. Similar to Figure 4.33, as retention time increases, chain length eluted increases. The pure compound shows similar peaks. At the start and finish of retention, compounds are detected with different molecular weights. Figure 4.35 shows Py-GCMS data for pure NaAOT and silica with NaAOT at 550 °C. Compounds with similar molecular weights are released by both compounds. The NIST data library matches them as different isomers. Figure 4.36 shows Py-GCMS data for pure CaAOT and silica with CaAOT at 550 °C. At 7 minutes retention time, more compounds are detected for silica with CaAOT compared to the pure CaAOT. Throughout, similar molecular weight compounds are detected in both samples. Overall, this suggests the fragmentation is not specifically related to the molecular adsorption, but an inherent aspect of the Py-GCMS of large, involatile molecules.

Summary TGA-MS and Py-GCMS data from octadecyl functionalised silica, silica with CTAB, silica with NaAOT, silica with CaAOT, pure CTAB, pure NaAOT, and pure CaAOT have been successfully collected. In each case there is no evidence for the release of the intact molecule. Even when not bound to the substrate, very significant fragmentation is observed. It is concluded that it is unlikely to observe the intact chemical species on the outcrop and reservoir rock samples above.

The fragmentation and species that have been released have been important to characterise the fragments that are released. Evidence for trends in the fragments with the pure material (if applicable) is presented, and trends in the nature of the

species arising from the presence of species with long hydrocarbon chains (i.e. alkane peak, alkene peak and diene peaks).

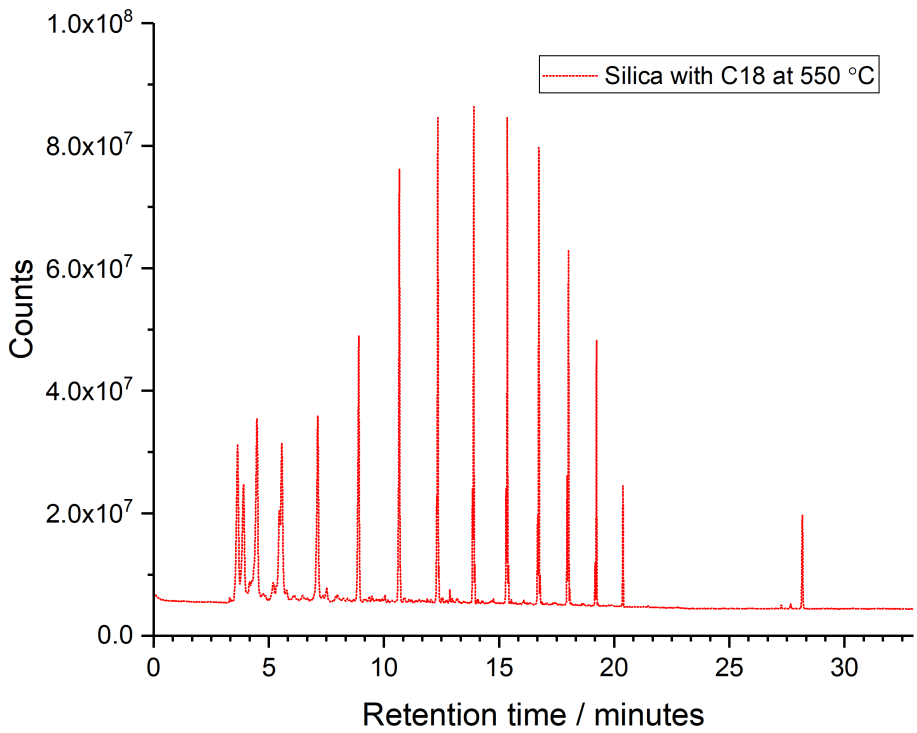

Figure 4.33: Py-GCMS of octadecyl funtionalised silica gel flash heated to 550 °C.

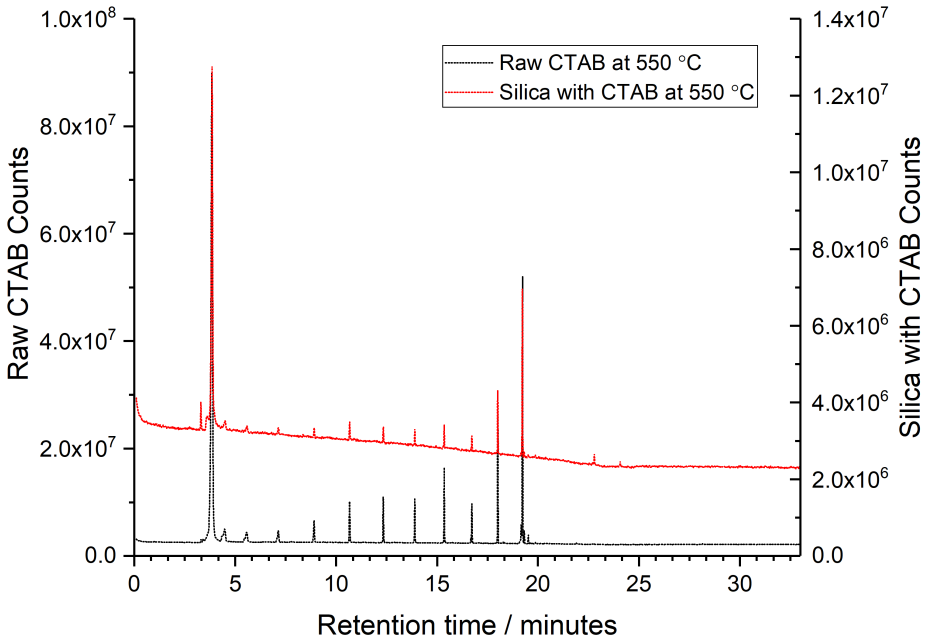

Figure 4.34: Py-GCMS of GCMS of raw CTAB (black) and silica with CTAB (red) flash heated to 550 °C.

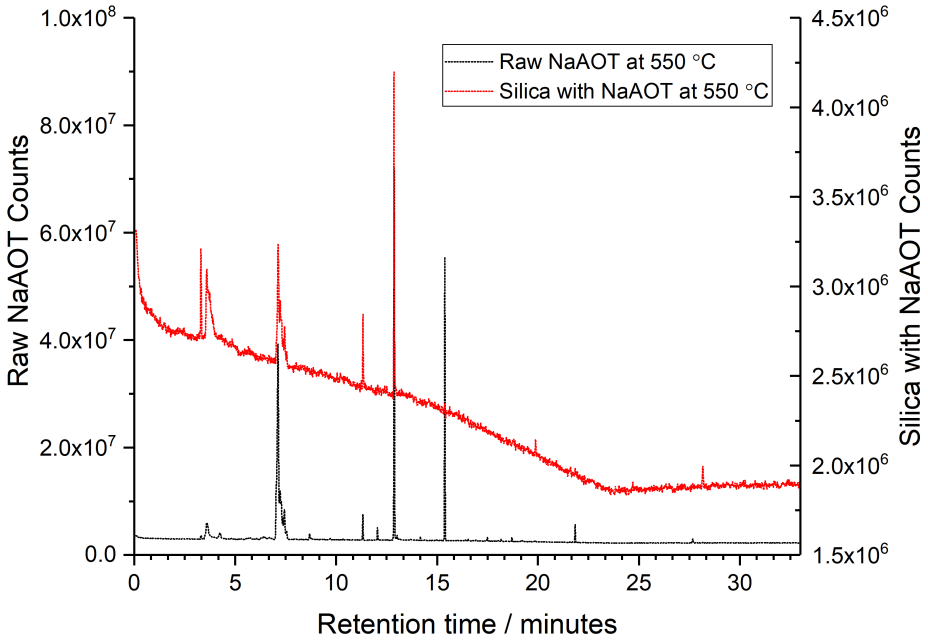

Figure 4.35: Py-GCMS of GCMS of raw NaAOT (black) and silica with NaAOT (red) flash heated to 550 °C.

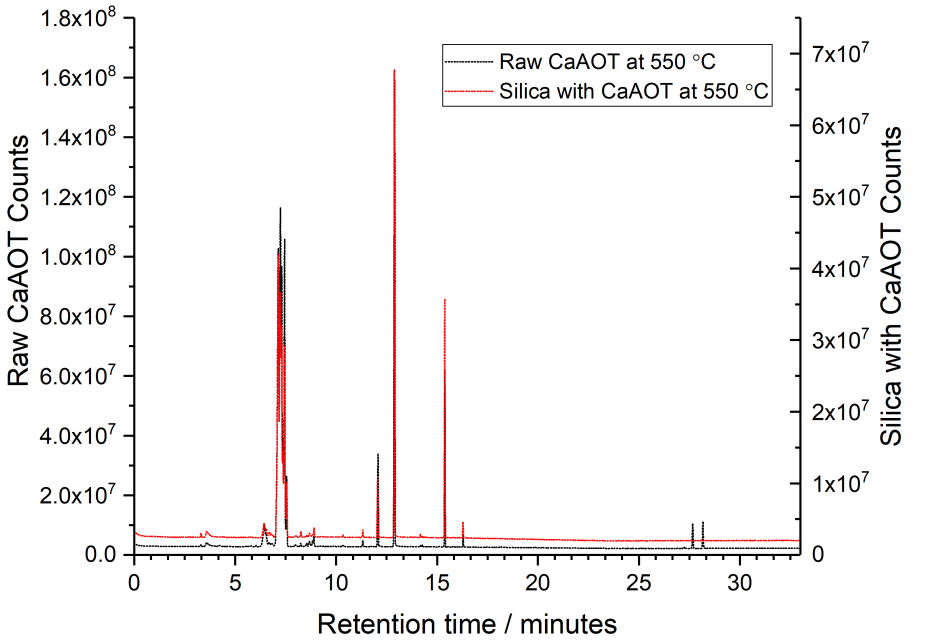

Figure 4.36: Py-GCMS of GCMS of raw CaAOT (black) and silica with CaAOT (red) flash heated to 550 °C.

4.11 Conclusions

Two different sandstone based plugs, outcrop and reservoir rock samples, from BP were intensively studied using an extensive range of modern analytical techniques. In brief, we aimed to (i) characterise the mineralogical and structural nature of the rock samples and (ii) the nature of the organic material irreversibly bound to the rock. Table 4.5 shows a compilation of results from all techniques.

This data will be used to guide analysis of crude oil adsorption on model mineral substrates to capture the key components of reservoir rock.

1) Characterisation of Rock

Micro-CT and mercury porosimetry showed a difference in porosity and distribution of density throughout both samples: the reservoir sample showing a greater density and less porosity compared to the outcrop plug. The micro-CT values are lower than the mercury values, thought to be due to mercury porosimetry destructively creating a porous network. QEMSCAN confirmed the difference in density, which could be attributed to mineralogical differences; a greater proportion of a wider variety of minerals was observed in the reservoir rock. Literature has shown correlations between the mineralogical differences to favour either oil- or water-wet systems. Hence, this alone may partially explain some differences of behaviour.

XRF was conducted and helped us to gain further understanding of the major and trace elemental composition that suggests organometallic complexes or porphyrin-type structures. XRF showed a greater amount of elemental variety in reservoir rock than outcrop rock. Stable isotope analysis was used to determine that the origin of the carbon in both samples was terrestrial,

2) Removable Organics

The samples were extensively solvent washed to remove 'unbound' or ab/adsorbed materials, particularly organic carbon species, confirmed by the drop of TOC present after washing. XRF identified a wider range of elements, which reduced after the solvent wash: losses occurred for most elements, but significant drops for tin and copper were observed, suggesting these elements are bound to organic species, which may help to solubilise them in the non-aqueous solvent used to wash.

3) Irremovable Organics

Characterisation of irreversibly bound organics is a significant experimental challenge. By definition they are not easy to remove and more aggressive methods tend to lead to fragmentation and damage. Novel innovative methods were considered, but the amounts present on the surface seems to be too small to observe above background.

TOF-SIMS was used to analyse elemental fragments released from the surface after ion bombardment. The MS data has been matched with many possible species that may be present, such as aliphatic hydrocarbons, siloxanes, amino acids, and polymeric groups. Finally, TGA-MS and Py-GCMS have been used to assess organic fragment removal on the application of heat. TGA-MS data showed a 1.5 % mass loss for raw outcrop rock, solvent washed outcrop, and solvent washed reservoir rock; a mass loss of 2.5 % was observed for raw reservoir rock, suggesting there is an additional material present in the reservoir rock, as might be expected. Complex MS were produced from this data which similarly showed a greater amount of fragments released from reservoir rock samples compared to outcrop rock.

A separate study to understand chemisorbed and physisorbed organic components adsorbed on silica and how molecular desorption/fragmentation changes the molecular structure observed was conducted using TGA-MS and Py-GCMS to understand behaviour of key functional groups. A series can identified where chemisorbed long chain hydrocarbons produce a series of related species including alkane, alkene and dienes when studied by Py-GCMS. Pure materials show similar molecular weight peaks eluted with their silica-additive counterpart in the Py-GCMS, suggesting this is a feature of the molecules, rather than the binding to the substrate.

TGA-MS was successfully conducted and a range of desorbed fragments were identified. Interestingly, very sever fragmentation occurs and most MS peaks occur below 50 amu, which is much smaller than the intact molecule. However, the technique is not sensitive enough to determine enthalpy of adsorption.

Technique	Results	Use Again For Model?
Mercury porosimetry	Outcrop porosity = 24.21%, reservoir = 10.38% Outcrop and reservoir porosity in agreement with BP and literature	No
Stable isotope / TOC / elemental analysis	Reservoir raw = 0.791 wt % carbon Reservoir solvent = 0.135 wt% carbon Outcrop raw = 0.015 wt % carbon Outcrop solvent = 0.014 wt% carbon	Yes: elemental analysis. No: stable isotope.
BET Surface Area	Reservoir raw = 2.82 m^2 g^{-1} Reservoir solvent washed = 4.11 m^2 g^{-1} Reservoir solvent and H_2O_2 washed = 3.11 m^2 g^{-1} Organic layer thickness = 9.6 Å	No
QEMSCAN	Reservoir rock has larger amount of diff. minerals than outcrop rock.	No
Solution NMR	Reservoir extract: ^{1}H: alkyl groups, alcohol, ether, halogen, aromatic ^{13}C: C-C alkyl, ether, acid, ketone, primary amine, C≡C, aromatic Outcrop extract: ^{1}H: alkyl shifts, alcohol, ether, halogen, aromatic ^{13}C: C-C alkyl, ether, acid, ketone, primary amine, C≡C, aromatic	No. Difficult to deconvolute.
XRF	Reservoir rock = greater proportion of major oxides NOT silica, significantly more Zr. Loss of tin and copper on solvent wash. Outcrop rock = significantly more Pb Loss of some metals on washing	No
TOF-SIMS	Reservoir and Outcrop have complex MS results Reservoir solvent washed has less fragments detected (low counts) showing successful solvent wash. Hydrocarbons, ring structures with decreasing saturation, nitrogen-carbon species present which agree with literature (pyrroles)	No. Spectra too complex.
TGA-MS	Outcrop raw, outcrop solvent, reservoir solvent = loss of 1.5 wt% Reservoir raw showed 2.5 wt% loss: more species to remove MS shows a greater intensity of species from both raw and solvent washed reservoir rock.	Yes. Chemi/ physisorbed, quantity removed.
Py-GCMS	Outcrop rock (raw and solvent extracted) showed no peaks eluted. Reservoir raw: carbamic acid, heptane, tridecane, dodecane, tetradecane Reservoir solvent: carbamic acid, octane, tridecane, dodecane, tetradecane	Yes

Table 4.5: Compilation of results from all techniques used with a key stating whether the technique will be used for analysis of isolated minerals.

4) Comparison with Literature

Table 4.6 shows a comparison between the findings in this thesis and how they compare to literature of the same techniques and similar samples.

Micro-CT appears to underestimate porosity.[217] However, some suggest mercury porosimetry creates pores that were not originally in the rock structure by pushing clay out leading to porosity over estimation.[195] QEMSCAN has been used previously by the oil industry to assess mineralogy distribution and mainly coupled with micro-CT and NMR to calculate pore lining minerals.[27–30,163] QEMSCAN has not been used in the way presented in this thesis previously. Solution NMR is not used to characterise oil, possibly due to the complex nature of crude oil. NMR is mainly used for porosity and permeability inference.[218–221]

XRF has been commonly used to assess the same bulk minerals in this thesis and the data presented matches that of the literature.[197] TOC and stable isotope analysis data also agree with literature.[222,223] Asphaltene extracted from oil was adsorbed onto stainless steel discs in toluene and analysed via TOF-SIMS. Here, carboxylic acids, pyrrolic, pyridinic, thiophenic and sulfite groups were observed.[92,224] This compliments results observed here on the real rock. Similarly, TGA shows a mass loss similar to that observed on dolomite rock aged in crude oil in the literature.[225] Finally, Py-GCMS has been used to investigate kerogen origin on source rock, showing differences based on carbon chain length detected.[226] Carbamic acid that was observed in this thesis was not observed in literature.

Technique	Finding in thesis	Finding in literature	Citation
Micro CT	30 % lower porosity than mercury porosimetry	Micro CT underestimates porosity	[195,217]
QEMSCAN	Use of QEMSCAN on bulk mineralogy	Similar mineralogy distributions	[30,163]
	New and novel way to assess pores	Coupled with micro CT and NMR to calculate clay pore lining rather than purely via QEMSCAN	[27–29]
Solution NMR	Range of functional groups in all soluble extracts	Not used on soluble extract. Mainly used for ideal materials or porosity and structural measurements	[218–221]
XRF	Overall % distribution of minerals	Very similar distributions observed for major minerals	[197,227]
TOC / stable isotope)	Outcrop -23 ‰ δ^{13}C	Agrees with literature	[222]
	0.8 % C on reservoir rock	TOC 1–10 % on 'mudstone'	[223]
TOF-SIMS	Hydrocarbons, ring structures, nitrogen containing compounds	TOF-SIMS not used for reservoir rock. Asphaltene on kaolinite showed as asphaltene deposit increased, contact angle on kaolinite increases	[92,224]
TGA-MS	1.5 % organic mass loss on reservoir rock	2 % organic mass loss on dolomite aged in model oil	[225]
Py-GCMS	Carbamic acid present	Kerogen carbon chain length assessed	[226]

Table 4.6: Table of findings in thesis and respective comparisons in literature.

4.12 Future Work

The aim of this study was to characterise the two cores of interest mineralogically and the organic layer adsorbed on to quartz based reservoir and outcrop rocks, as it is believed to be adhering to bound oil that inhibits recovery. Understanding the interactions between (i) the mineral-organic and (ii) organic-crude is intended to aid enhanced oil recovery in the search for an ideal additive/chemistry to release the oil. Lab based experiments developed on a small scale to inform use in the field. This chapter has presented a characterisation of the rock samples and the organics on them using a wide range of experimental methods, including several never considered previously. It is found that mineralogy can be extracted from the data. However, the chemistry of the irreversibly bound organics remains a significant challenge but there is indication of the chemical nature of the key species.

In the next stage of the work, a number of the methods used in this chapter will be used to understand what happens in the commercial process of ageing that is used to try and produce rock samples that mimic real reservoirs by adsorbing species from crude oil. The simple concept is that the molecules that adsorb underground to the rock will similarly adsorb onto outcrop rock. In this way, representative behaviour for testing is achieved. The process aims to capture the 'real' system by using elevated temperature for ageing. However, the key goal is to establish the correct surface chemistry without having to wait geological periods.

It is not possible to determine the chemical identity of specific molecules present in the irreversibly bound layer using the methodology adopted so far in this work. The best approach was to rip molecules off the surface, reducing them to fragments. This implies they are chemisorbed. Novel methods have been used to assess adsorption in situ, but without success.

Initially a systematic study is proposed in which approaches already used in the oil industry to modify rock and characterise which materials are actually deposited are explored.

1) Ageing of silicon wafers and powders in crude oil

Several selected crude oils with different levels of saturates, aromatics, resins and asphaltenes (SARA) will be used to soak/age relevant mineral substrates, such as silicon wafers/quartz substrates, under conditions and durations used commercially. After a suitable period of ageing and equilibrating, the substrates will be 'rinsed' in a solvent such as toluene, before the organic layer is quantified and characterised.

The use of well-defined, flat, and polished silicon wafers should allow more of the state of the art techniques available to be used.

2) Functionalisation of a quartz sample with small molecules with relevant chemical groups to generate the model rock

One suggested next step that will not be discussed further in this thesis is creating a model functionalised rock, assuming you know the key functionality that drives oil adsorption. One example is adsorption of organic materials to the rock similar to the silanes. These react with the quartz to give very strongly bound organics. However, these are considered to be too hydrophobic to represent a comparable surface to the one of interest.

Hence, a combination of chemical groups on the silanes may present a preferable approach. This could include some alkyl species to produce some hydrophobicity but other more polar species to elevate the polarity of the prepared surfaces. Similar models can be constructed using a blend of thiols on a gold substrate.

Chapter 5

Understanding the Ageing Process: Powders

5.1 Background

To help formulate appropriate enhanced oil recovery methods, it is important to test the formulations on mineral systems that capture the properties of the real reservoir. Cores can be extracted from reservoirs or outcrop structures. However, extracting a core from a reservoir requires drilling thousands of feet below the surface and recovering the core without changing its properties, which is an expensive procedure and therefore commercially undesirable. Outcrop rocks are much more accessible and could provide a convenient substitute. The challenge is that the mineralogy and chemical nature of the cores are generally not the same as the reservoir core, even thought broadly equivalent strata may be accessed. To try and recapture the chemistry of the reservoir rock, one might think of repeating the processes that lead to the surface chemistry of the real reservoir rock (such as cooking the material at elevated temperature).

However, to capture the real process would take geological timescales. Hence, outcrop cores are aged within vessels with crude oil at the temperature and pressure of the reservoir. The ageing process and what the process actually does to the minerals and their surface chemistry is complex. The complexity is partly due to the crude oil composition but also the wide variety of minerals that might be involved.

In this study, the aim is to replicate the ageing process by looking at isolated mineral samples, rather than in a complex multi-mineral rock. Analysis of organics

depleted from the ageing crude oil solution and organics adsorbed onto individual minerals will help understanding of how each mineral interacts with crude oil and potentially drives wettability changes within the oil well. Recombining the minerals in appropriate amounts should indicate the expected behaviour of the aged outcrop. In this work, the key idea is that ageing leads to deposition of chemical species on minerals that determines their recovery behaviour.

As discussed in the QEMSCAN results (Section 3.8.1), the global mineralogy of the rock is not actually the material representative of the mineral surface. The surface mineralogy is where the changes in behaviour due to organic ageing is expected to occur. Deconstructing the ageing process of the minerals aims to consider minerals representative of those exposed on surfaces.

This work will focus on substrates of quartz, calcite, kaolinite and mica to capture most of the mineralogy lining the pores of real rock. The involvement of pretreating the minerals with low or high salinity water is also investigated to understand how water impacts organic adsorption from crude oil.

5.2 Crude Oil Characterisation

As discussed in Section 2.1.3, crude oils are very complex mixtures of a range of chemical components. A full molecule by molecule breakdown would be an immense amount of work, if even possible. A molecular breakdown would not necessarily help understanding of the broader behaviour as the next crude oil considered would have similar complexities. Therefore, general rules are potentially more powerful. However, it is common to characterise the crude oil composition into classes of components, particularly by SARA analysis. SARA analysis captures the key variations of interest without the complexity of a full molecular composition.

In this study, three crude oils are used: **high asphaltene** content oil from a silicate well (HA oil), **low asphaltene** content oil from a silicate well (LA oil) and low asphaltene content oil from a **carbonate well** (LA-carb oil). These cover the main parameters of interest at this stage. This section discusses characterisation of the three crude oils.

5.2.1 SARA Analysis

SARA analysis of HA oil and LA oil was conducted by BP upon initial acquisition of the oil. SARA of LA-carb oil was not conducted by BP prior to sending the crude oil

sample to Cambridge. SARA was re-run for HA and LA oil using the samples sent to assess any changes between batches and LA-carb was tested at the same time. The same company and method was used in both cases to reduce any error in the SARA analysis—as discussed in Section 2.1.3 there are varieties of SARA analysis. The results for SARA of all three oils is shown in Figure 5.1. Firstly, there is a similar amount of aromatics are present in all oils (∼26 %). Focussing on HA oil, it has a lower number of saturates are more resins than LA oil with a similar amount of resins to LA-carb oil and a significantly greater amount of asphaltenes than the other oils. This similar amount of aromatics is based on data from BP data and supported by the re-runs. For LA oil, it has more saturates than both other oils. Interestingly, the LA oil has low resins in the results from BP, but similar levels of resins seen when the sample was re-run. There was also a significantly low amount of asphaltenes. The LA-carb oil shows a middle range of saturates—between the levels of HA and LA oils—resins of the level of HA oil and significantly lower asphaltene content.

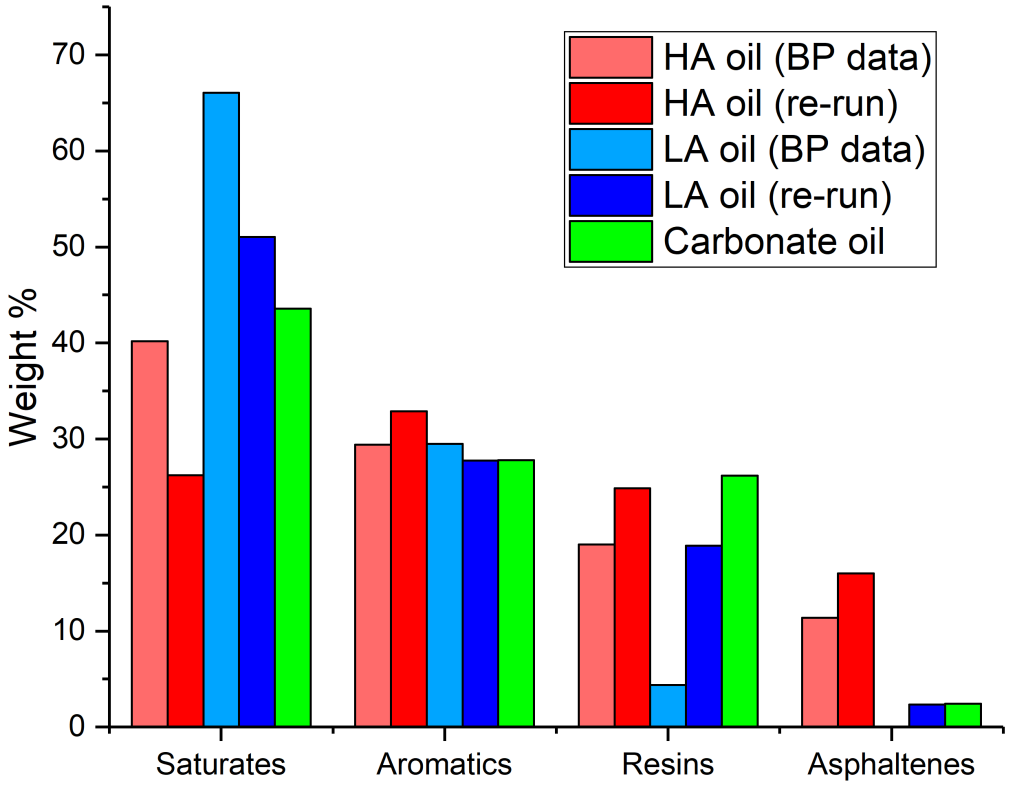

Figure 5.1: SARA analysis of HA, LA and LA-carb crude oils.

Figure 5.2 shows a difference map comparing the values of the received data for HA and LA oil versus re-run samples from the sample batch received. For both

oils, the data show the samples supplied to Cambridge have less saturates, an increase in resins and an increase in asphaltenes compared to the BP analysis of the same oils. HA oil shows an increase and LA shows a small (<2 %) loss of aromatics. The difference between data from BP and re-run samples could be for several reasons:

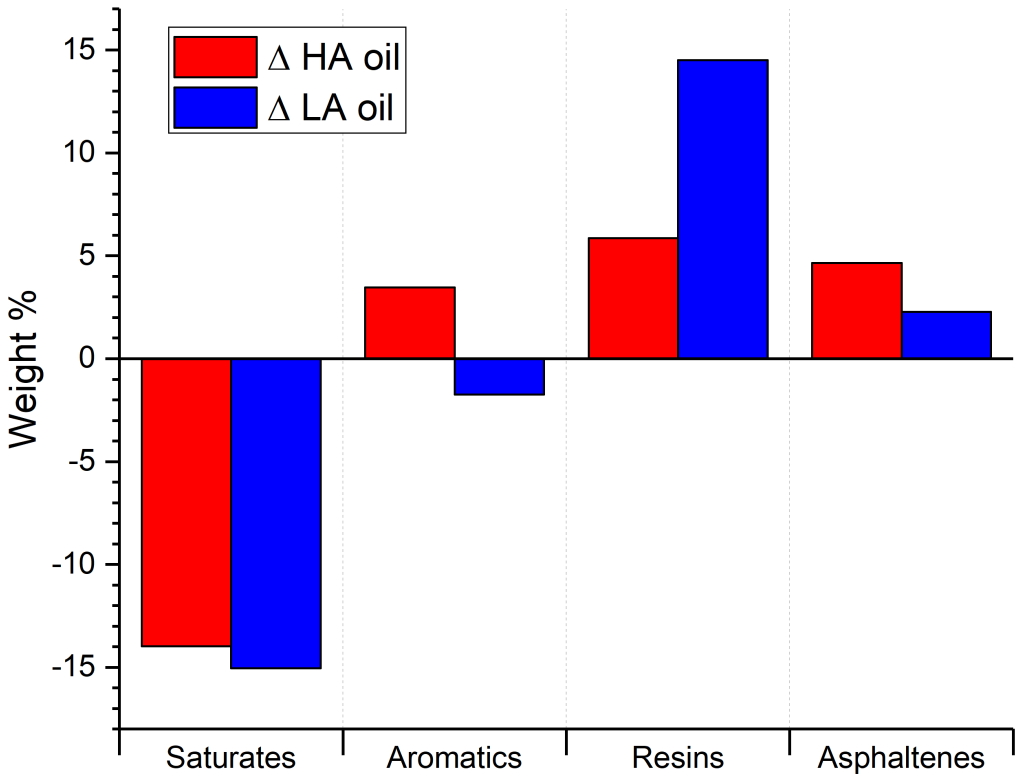

Figure 5.2: Difference map of SARA analysis for HA and LA crude oils, data received from BP and re-run analysis.

1) Batch-to-Batch Discrepancy

SARA analysis is conducted on the oil that is sent to BP Sunbury from the oil well. SARA analysis is not conducted in-house; it is outsourced to an external company. The tests are costly and time consuming due to the steps mentioned in Section 2.1.3. The SARA data are used for the oil in-house experiments and the same data are passed on to other researchers who are investigating oil properties. Re-testing of SARA is rarely conducted. The bottom of a barrel of oil may contain more dense molecules such as resins and asphaltenes. Ensuring the container is mixed before decanting is important to retain the same amounts of components, although seldom performed. Even if a crude oil comes from the same well, there may be variations in properties as different regions of the well are depleted. In addition, a typical facility usually pulls fluids from several wells that are mixed below ground. The flow from different channels can also change over time.

2) Degradation

Crude oil will degrade if exposed to air and light over time. It is unknown if the sample received was kept under nitrogen during its time at BP Sunbury (therefore possibly generating different results to the SARA analysis directly from the oil well). Degradation in the form of oxidation increases the acid content. This is observed with an increase in total acid number (TAN). The acid content increase may come as a result of resin/asphaltene cores oxidising and possibly releasing their long hydrocarbon side chains, resulting in a larger saturates weight %. However, a larger saturates weight % is not observed. Therefore, a batch-to-batch difference seems more likely for these samples in this case.

Crude oil samples received in Cambridge from BP Sunbury were all stored under nitrogen to limit degradation.[194] Whether the difference in SARA analysis comes from minor degradation from exposure during decanting of crude oil from the main bottle when pouring or if there is batch-to-batch discrepancy, the above graphs suggest that SARA analysis must be conducted for the batch of crude oil being used, irrespective of if SARA has been conducted on oil from the oil well previously. Any use of SARA analysis in this study will use the values obtained from the rerun analysis as opposed to data supplied by BP.

5.2.2 Vanadium and Nickel Content

Vanadium and nickel are two elements of interest in crude oil as they link to kerogen structures and thus source rock type and deposition environment.[88] Both elements are reported to appear in porphyrin structures where the nickel or vanadium is a central atom surrounded by the organic porphyrin backbone. Detection of either metal ion could suggest porphyrins present. Porphyrin and kerogen-type molecules are most likely to be present in the high molecular weight resin and asphaltene fractions.[228] V and Ni are usually reported as a V:Ni ratio.[88,229,230]

Figure 5.3 shows the Ni and V content for all three crude oils run via organic solvent inductively coupled plasma (ICP) externally by the company SGS Ltd. For HA, LA and LA-carb oil, the V:Ni ratio is 3.98, 0.48 and 3.29 respectively. The data suggest it is more likely for HA oil to contain complex kerogen-like molecules as well as porphyrins compared to the LA and LA-carb oils. This is reinforced by the SARA analysis above (Figure 5.1) showing lower numbers of resins in LA oil and lower asphaltenes in LA and LA-carb oil compared to HA oil.

Vanadium and nickel content was also assessed by aqueous solvent (both via different solutions of 2 % nitric and 2 % piranha solution) ICP-OES (optical emission spectroscopy) at Cambridge. However, neither element was present in the analysis, suggesting vanadium and nickel are only dissolved into organic solvents as used in the above method and hence complexed to organic species.

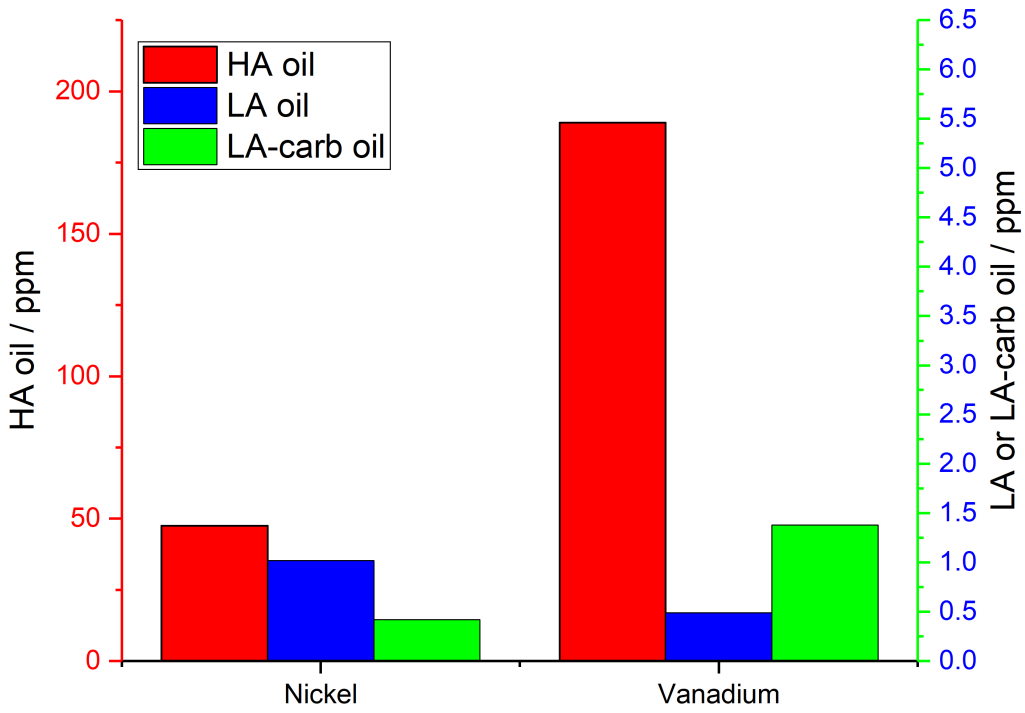

Figure 5.3: Nickel and vanadium content of crude oils.

5.2.3 Elemental Analysis

CHN elemental analysis was conducted on the crude oils and is shown in Figure 5.4. Carbon levels for HA and LA oil are similar (∼85 %) whereas the carbon for LA-carb oil is significantly lower (67 %). Hydrogen and nitrogen levels are shown on the right-hand y-axis: for hydrogen, LA oil has 1 % more hydrogen than HA oil, and HA oil has 1 % more than LA-carb oil. The nitrogen levels for HA and LA oil are the same, whereas LA-carb oil has almost 6 times the nitrogen content. The nitrogen content is of interest as asphaltenes are thought to drive wettability on oil and asphaltenes contain heteroatoms such as nitrogen. Nitrogen is also present in porphyrins. Porphyrins can have a nickel or vanadium central atom, and may bind to surfaces via the metal ion or possibly via van der Waals interactions with the nitrogen. More nitrogen suggests more porphyrins; however, considering Figure 5.3 and Figure 5.4 although HA oil has a high amount of nickel and vanadium, it does not have a high nitrogen content, suggesting the metals may not be present solely as porphyrins. Nitrogen can also be present in a range of forms, such as pyridines, pyrroles and carbazoles.[66,92,231,232]

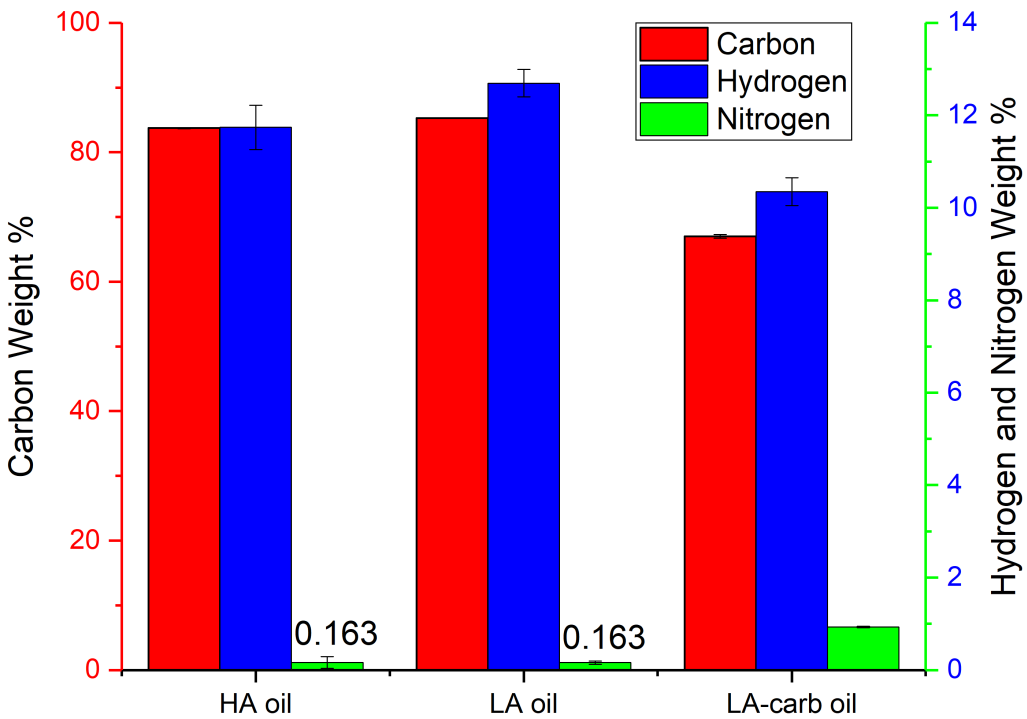

Figure 5.4: C, H and N content of crude oils.

Interestingly, CHN analysis only accounts for 95.97, 98.27 and 77.65 % of the weight % content of HA, LA and LA-carb oil respectively. For HA and LA oil one would

assume the remaining percentage might consist of heteroatoms (O and S), halides (F, Cl, Br and I) and metal atoms. Accounting for LA-carbs missing 22.35 % of chemistry is more difficult. However, given the high resin content (25 %), a substantial amount of the weight % could be found in the resin structure through heteroatoms and metals.

To determine the number of rings and π-bonds of an organic species with a known molecular formula, a calculation that analyses the degree of unsaturation, also known as the double bond equivalent (DBE), is used (Equation 5.1).[233] DBE for HA, LA and LA-carb are shown in Table 5.1.

$$\begin{aligned} DBE &= (a+1) - \frac{b-c+f}{2} \\ &= C - \frac{H}{2} - \frac{X}{2} + \frac{N}{2} + 1 \end{aligned} \tag{5.1}$$

where

a = number of carbon atoms in the compound

b = number of hydrogen atoms in the compound

c = number of nitrogen atoms in the compound

f = number of halogen atoms in the compound

Oxygen and other divalent atoms do not contribute to the degree of unsaturation, as 2 - 2 = 0.

If the exact molecular formula is unknown, a second way to compare organics that was devised for this study is via the degree of saturation (DoS)—how many protons surround a carbon or nitrogen atom. This is different from a DBE where C=C bonds are considered. Equation 5.2 shows how the DoS is calculated. This equation takes into considering the quantity of hydrogen as a function of carbon and nitrogen content. Methane would have a DoS of 4 (maximum) and a porphyrin or benzene ring has a saturation level of 1. Table 5.2 shows common molecular components of the crude oil in this study and their DoS and unsaturation (DBE) levels. Importantly, although the model asphaltene displayed in Table 5.2 shows a very high DBE due to the polyaromatic backbone, the DoS is higher than that of benzene due to the hydrocarbon side chains. DoS for HA, LA and LA-carb are shown in Table 5.1. This result suggests all oils contain significantly more polyaromatic

Oil	DBE	DoS
HA	1.67	0.59
LA	1.78	0.55
LA-carb	1.85	0.53

Table 5.1: DBE and DoS values for crude oil, assuming CHN results produce one fragment.

molecules than long chain hydrocarbons. Obviously this result does not consider other hydrogen binding elements such as oxygen, sulfur or halogens as the focus is on C, H and N content, which is a contributing factor to the low DBE value in Table 5.1.

$$\begin{aligned} Degree\,of\,Saturation &= \frac{\left(\frac{wt\%H_{sample}-wt\%H_{initial}}{H_{RMM}}\right)}{\left(\frac{wt\%C_{sample}-wt\%C_{initial}}{C_{RMM}}\right)+\left(\frac{wt\%N_{sample}-wt\%N_{initial}}{N_{RMM}}\right)} \\ &= \frac{\Delta wt\%H}{\Delta wt\%C+\Delta wt\%N} \end{aligned} \tag{5.2}$$

Overall, elemental CHN analysis reveals some significant differences in carbon and nitrogen content that could lead to understanding what is binding on the surface. The levels of degree of saturation suggest similar polyaromatic molecules dominate all the oils considered here.

Ratio	Molecule	Formula	RMM / g mol^{-1}	Degree of Saturation	Double Bond Equivalent
C_nH_{2n+2}		C_5H_{12}	72	2.40	0
C_nH_{2n}		C_5H_{10}	70	2.00	1
C_nH_{2n-2}		C_6H_{10}	82.1	1.67	2
	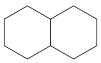	$C_{10}H_{18}$	138.2	1.80	
		C_4H_6	54.1	1.50	
C_nH_n		C_6H_6	78	1.00	4
Polyaromatic	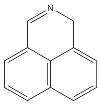	$C_{12}H_9N_1$	167	0.75	9
Porphyrin	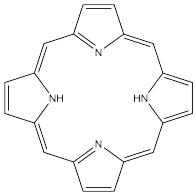	$C_{20}H_{14}N_4$	310.12	0.70	16
Asphaltene	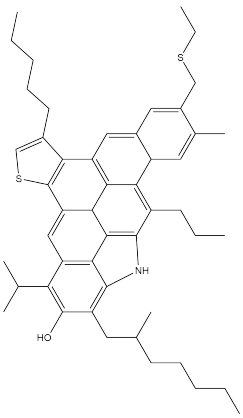	$C_{49}H_{61}NOS_2$	744.15	1.24	20

Table 5.2: Structures and values of common molecules with their DoS and DBE.

5.2.4 High Resolution Mass spectrometry

High resolution mass spectrometry (HRMS) is a recent technology that has been utilised by BP to assess the content of the crude oil. Here, crude oil is dissolved into xylene or toluene and run through the MS. The main use for HRMS is investigating extractions of solvent washes of aged samples (solvent washes are discussed in Section 5.3). The principle benefit is that the very high resolution of m/z means that organic species can be readily and unambiguously identified.

HRMS is able to establish the identity of essentially all the species that can be visualised in different ways such as by carbon number, DBE and ratios of NOS.[55,56,94,234] It has been used in this study to investigate molecules removed by solvent washing of substrates after ageing. Due to access limitations, only organics exposed to mica were investigated.

5.3 The Ageing Process

Figure 5.5 shows the schematic for the ageing process. Crude oil was stored at room temperature under nitrogen prior to use. The substrate (15 g powder or 15 flat substrates)—pretreated with (1) ultrapure 18 MΩ.cm or (2) brine (Table 5.3) or (3) no pretreatment—was loaded into a 100 mL glass bottle fitted with a PTFE cap. Within a nitrogen purged glove bag, room temperature crude oil (∼20 mL) was added and the bottle purged with a stream of nitrogen using a seal and needle for 60 seconds to produce a positive pressure within the bottle. The bottle was sealed and placed in an oven at 70 °C for the allotted time.

The standard operating procedure for crude oil ageing of minerals in industry requires removal of old crude oil and fresh crude oil to be added to the system every week—this is suggested to promote adsorption of any components that have not already adsorbed. One idea is that a component adsorbs initially, for example asphaltenes, and this is depleted in the initial crude oil. Subsequent crude oil replenishments would contain more asphaltene and would adsorb more until a plateau is reached.[20,100,235]

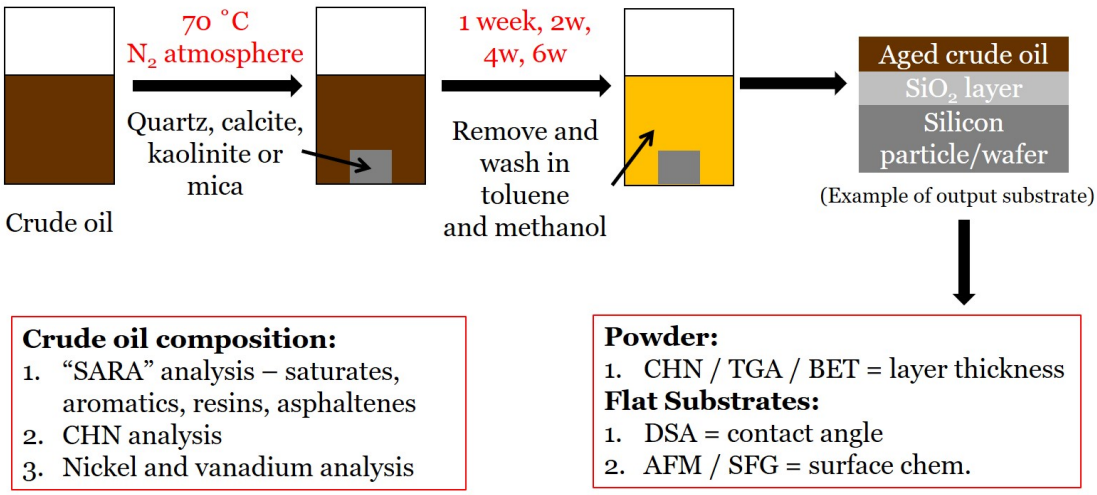

Figure 5.5: Schematic of ageing process.

Salt	g / L
$CaCl_2 \cdot 2\,H_2O$	13.2051
$MgCl_2 \cdot 6\,H_2O$	2.0075
KCl	0.7436
NaCl	57.8840

Table 5.3: Composition of brine.

To replenish the crude oil, the sample bottle was opened in a glove bag and excess

crude oil supernatant was removed and stored in a vial under nitrogen. If required, a sample of substrate (2 g powder or 3 flat substrates) was removed too. Fresh crude oil was added—enough to cover the substrate (∼5 mL)—and the bottle resealed under the stream of nitrogen as described above.

Extracted aged substrates were washed in toluene to remove any bulk oil remaining. When the toluene ran clear, the substrate was washed in fresh methanol until the washings ran clear. The washings of fresh toluene followed by fresh methanol were continued until each solvent had been run through the sample nine times. Samples were air dried before being stored. Any extracted samples (liquid, powder substrates or flat substrates) were stored under nitrogen until analysis was conducted.

5.4 Ageing Particles

A number of analytical methods were used to characterise the adsorption. In some cases, quantification of amount of material bound to a surface is assessed. To facilitate that measurement and have a significant absolute amount to measure, it is usually convenient to use high surface area powders. In contrast, other characterisation techniques (SFG, AFM and DSA) to be considered, require a large, single flat substrate surface. This section is focussed on the results from particles that were aged in crude oil. Section 6.1 discusses results from flat substrates.

5.4.1 Bare Particle Characterisation

Prior to characterisation of the materials after various stages of ageing, it is important to characterise the bare starting materials, which is described below.

CHN

Figure 5.6 shows the CHN results for quartz, calcite, kaolinite and mica particles used for ageing.

Calcite has a significant amount of carbon present, However, a large amount of carbon is expected from the inorganic carbon (12.0 %) within the crystal structure from the carbonate ion. Given that this amount of carbon is observed, it can be implied that there are no other significant carbon contaminants. There was no significant nitrogen or hydrogen in the calcite sample.

Kaolinite also indicates hydrogen present. This is in good agreement with expectations, although 0.4 % less hydrogen is observed than expected from the archetypical structure $Al_2Si_2O_5(OH)_4$ (1.5 %). This is attributed to small variations typical of a naturally occurring mineral. There is no evidence of other significant contaminants.

Mica CHN data indicate hydrogen again in very similar amounts to that expected from the structure $KAl_2(AlSi_3O_{10})(OH)_2$ (0.5 %), although again slightly less by 0.2 %, attributed to natural variations of a mineral. There is no evidence for other contaminants.

Quartz CHN data is found to contain hydrogen, attributed to surface silanol groups and small carbon contamination (0.2 %) with no formal origin, attributed to atmospheric impurities. No nitrogen content is evident within the precision of the measurement.

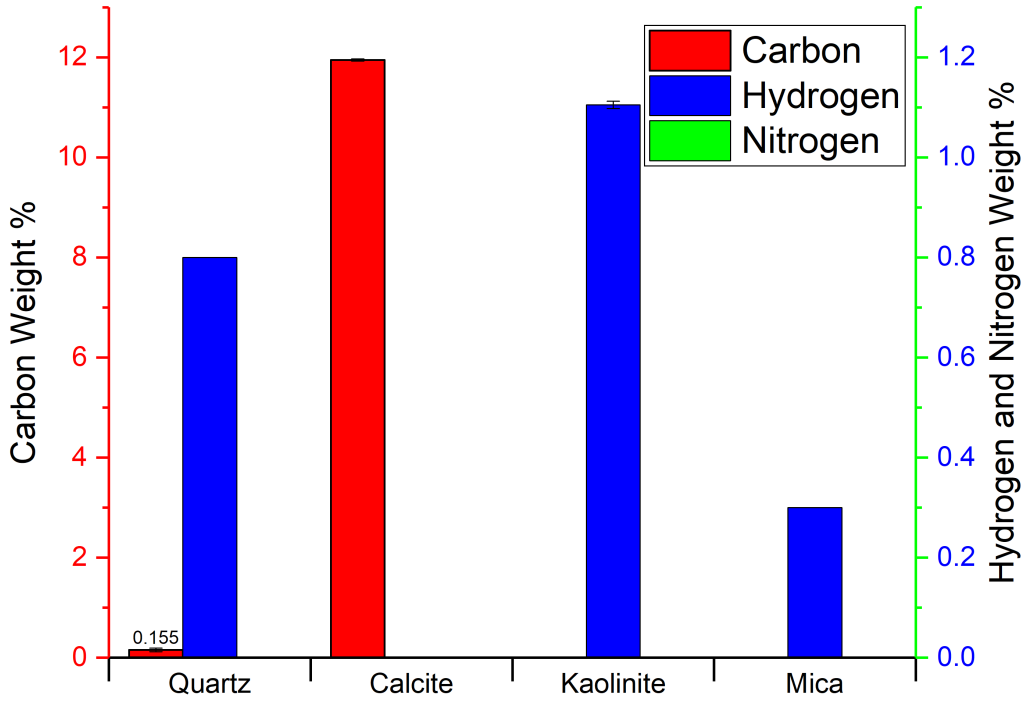

Figure 5.6: CHN of quartz, calcite, kaolinite and mica used for crude oil ageing.

BET

Table 5.4 shows the specific surface area of these powdered substrates determined by BET analysis and adsorption of nitrogen for quartz, calcite, kaolinite and mica particles used for ageing. Given the manufacturer data for quartz of diameter 1.0 μm and knowing the density of quartz is 2.65 g cm^{-3}, a specific surface area of 2.26 m^2 g^{-1} is expected.[236] The measured value is 2.4 m^2 g^{-1}, showing the data is in good agreement with manufacturer data.

It is important to note that the quartz used in this study is monodisperse, spherical and non-porous—removing porosity removes the opportunity for molecules to adsorb within the pores and become trapped via capillary forces rather than chemical adsorption. Molecules trapped by in pores, rather than chemically adsorbed, would give false results when combusting samples to determine the amount of organic species irreversibly bound.

Substrate	BET Surface Area / m^2 g^{-1}
Quartz	5.04
Calcite	18.20
Kaolinite	7.99
Mica	1.87

Table 5.4: BET surface area of quartz, calcite, kaolinite and mica.

5.4.2 Ageing Quartz

This section summaries the elemental analysis results from the exposure of quartz to the three crude oils of interest, with and without aqueous pretreatment and over an extended ageing period of up to 6 weeks. As outlined in Section 5.3 above, these experiments exposed a powdered substrate to these fluids/pretreatments at 70 °C under nitrogen. The resulting aged solids were separated by filtration and washing with toluene and methanol and characterised by CHN elemental analyses. The data presented here are the elemental analyses of the aged powdered quartz and any adsorbed layer it has gained as part of the ageing process.

CHN Analysis of Quartz

1) HA Oil

Figure 5.7 shows the elemental carbon results for quartz aged in HA oil with and without the pretreatments (see Section 5.3 for the details of these treatments).

1.1) Untreated Substrate

Figure 5.7 shows that for the untreated quartz overall there is a significant rise in carbon content over the ageing process.

There is a very small amount of carbon (0.2 %) in the original quartz (attributed to impurities of the sample and/or adsorption of adventitious carbon from the atmosphere). There is a 0.5 % increase in carbon from the starting material to the 1 week aged quartz and further increase until the data may indicate a plateau at 4–6 weeks. The plateau corresponds to 1.4–1.6 % carbon. This value and the specific surface area of the powdered quartz can be used to estimate the organic layer thickness. The specific surface area of quartz used is 5 m^2 g^{-1}, therefore a 1.4 % carbon content of a 100 g sample corresponds to 1.4 g of carbon (0.117 moles) on 500 m^2. Hence, there are 0.00023 moles m^{-2} or 1 $Å^2$ per carbon. The van der Waals radius of a carbon atom is 1.7 Å (or a footprint area of 9 $Å^2$ $atom^{-1}$). Hence, there is approximately a 10-atom thick layer. This is a very crude estimate of the layer thickness and assumes the carbon is spread uniformly across the whole exposed quartz surface. Hence, it can be concluded that the adsorbed materials is comparable to molecular dimensions, approximately a molecular monolayer, or slightly more.

This crude oil, HA, has been confirmed to have a reasonably high asphaltene content. These molecules have often been associated with adsorption and surface activity, which is in good agreement with the results presented here.[82,85,237]

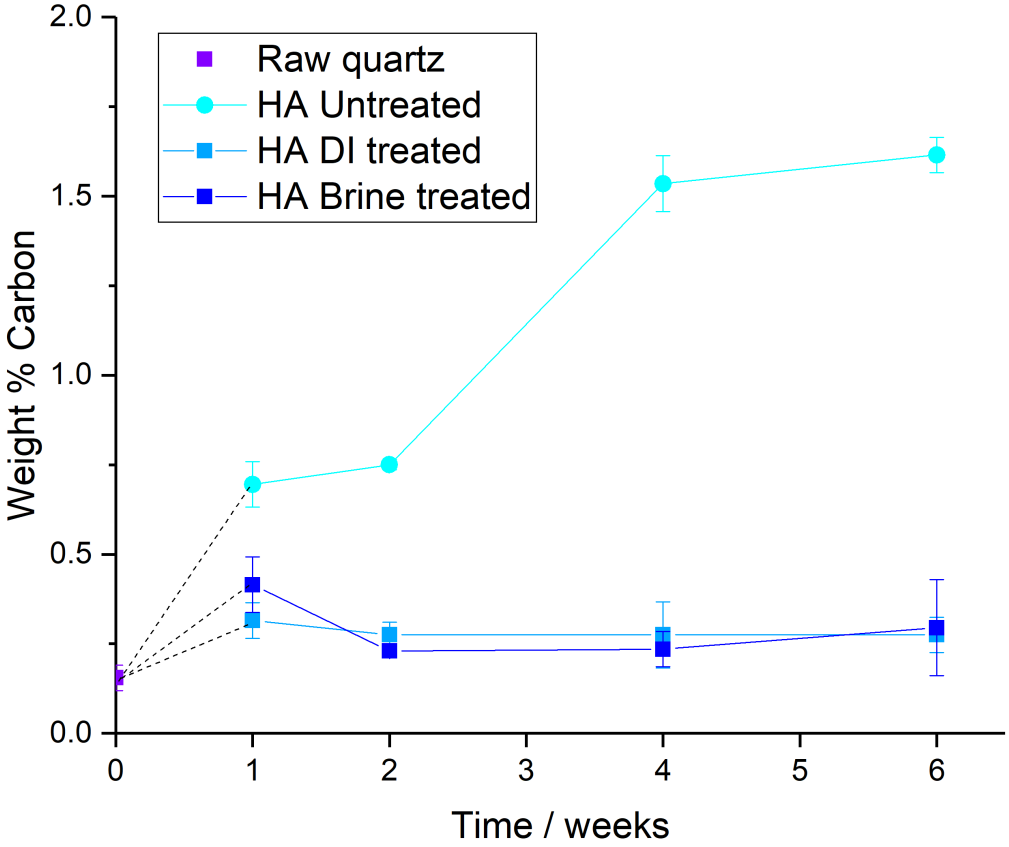

Figure 5.7: Carbon analysis of quartz, aged in HA oil, with pretreatments (no pretreatment, DI water or brine). Error shows standard deviation of 2–3 repeats. Dotted lines are added to guide the eye between starting substrate and aged substrate.

Interestingly, this result agrees with the CHN result from the estimated thickness on the as received reservoir rock that also suggest the presence of an adsorbed layer of approximately molecular dimensions (Section 4.7.1). In this sense, this approach appears to be successful for recreating aspects of a real core.

1.2) Treated Substrate

The data in Figure 5.7 show that after quartz is treated with DI or brine, the amount of carbon present does not change significantly (given the size of the error bars). There is a slight rise after the first week of ageing, but this is only slightly above the estimated error and hence it is assumed this is not statistically significant.

This is an interesting, possibly unexpected and significant result. One might have expected these crude oils to be very ‘sticky‘ and would adhere to any solid surface they are exposed to, particularly if for a significant period. Hence, it must be concluded that the water, with or without added salts prevents the adhesion of the

crude oil.

The surface nature and charge of quartz is discussed in Section 2.3.2. Given the strongly hydroxylated nature of the surface, one might expect that quartz would rather be in contact with water than oil. Generally, quartz-based sandstones are begin as water-wet. This confirmed later in the chapter (Section 5.5) with Castlegate and Berea sandstone outcrop spontaneously imbibing water whilst untreated. It is therefore not surprising that the pretreatments of DI and brine have caused no oil to bind to the quartz surface: water binds first, repelling the hydrophobic oil, and causing no further binding even after a 6 week ageing period (Figure 5.8).

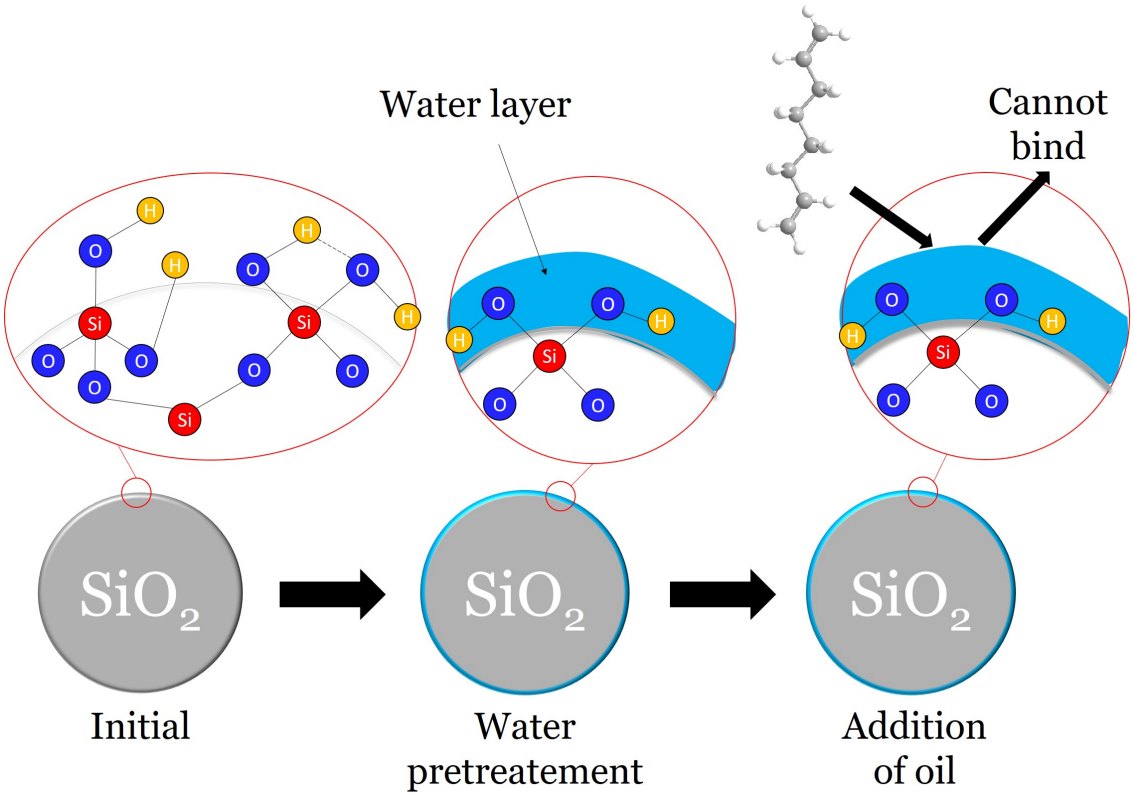

Figure 5.8: Schematic of water binding onto quartz and preventing crude oil binding.

However, this simple picture may not capture the complexity of the crude oil, which is expected to contain a good number of hydrophilic groups (fatty acids, alcohols etc.) that might have been expected to bind to the quartz substrate. The results presented here suggest these functionalities cannot outcompete the presence of water. This may also be a concentration effect: adsorption tends to increase when more of a species is present and there will be a lot of water.

Without exposure to water, the quartz surface would rather be covered by any condensed phase than nothing. Considering only van der Waals forces, the number

of interactions is much higher for the quartz in contact with the crude oil than with air/gas. Hence, adsorption of the crude oil is observed on the untreated quartz.

An important note of caution is that the CHN analysis is not able to detect very small amounts of adsorbed layers compared to the bare initial substrate if the amount is smaller/comparable to the inherent error of the method. The data above demonstrate detection of a molecular layer of a few atoms thick. However, the presence of smaller amounts of organic (estimated to be a third of a monolayer) cannot be excluded.

2) LA Oil

Figure 5.9 shows the CHN carbon results for quartz aged in LA oil with and without pretreatments. HA oil data are included for comparison. LA oil is an oil from a silicate well and, importantly, has relatively low asphaltene content compared to HA oil.

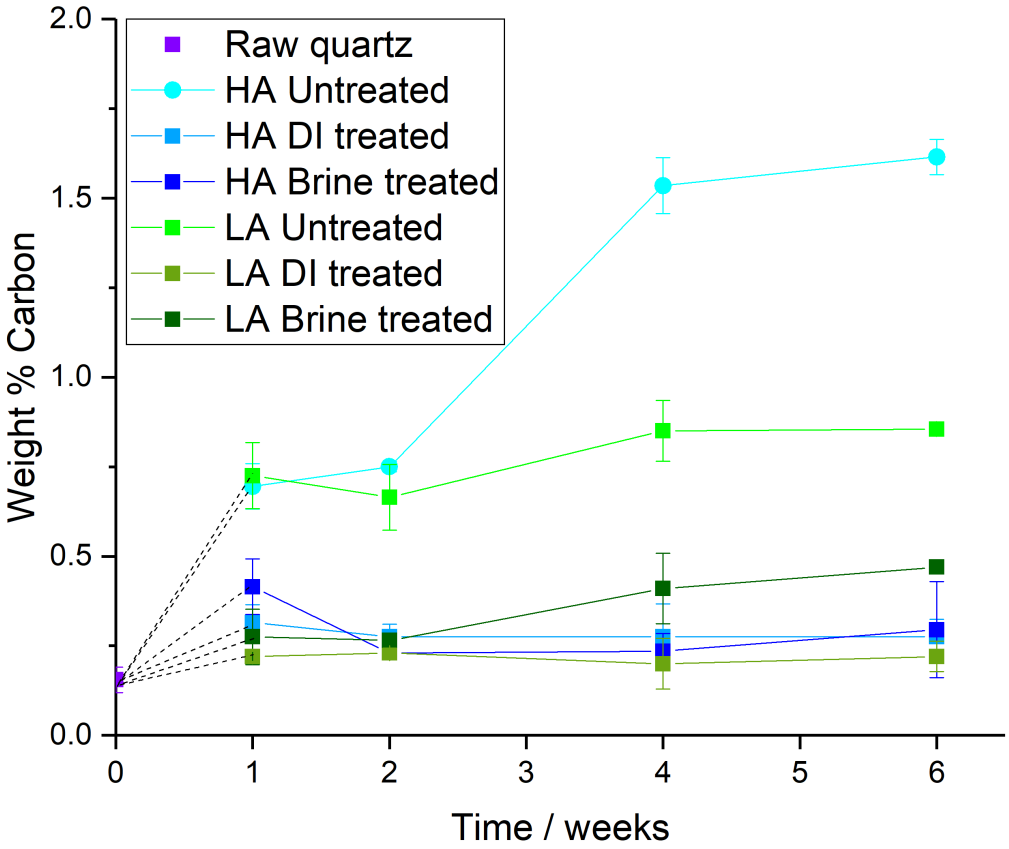

Figure 5.9: Carbon analysis of quartz aged in HA or LA oil, with pretreatments (no pretreatment, DI water or brine). Error shows standard deviation of 2–3 repeats. Dotted lines are added to guide the eye between starting substrate and aged substrate.

The untreated quartz shows a significant percentage of carbon adsorbing to the quartz even after one week. Interestingly, there is not a statistically significant rise with further ageing time. This contrasts with the more asphaltenic HA oil crude, which kept adsorbing until 4–6 weeks. This suggests that the asphaltenic components are important in long term, high levels of adsorption.

It is interesting to consider why the HA oil takes so long increase the adsorbed amount and then reach a plateau. It is easier for a small molecule to diffuse through a liquid and adsorb to a surface compared to a large molecule (asphaltene). A combination of the results from HA and LA oil might suggest a mechanism where lighter molecules (long chain hydrocarbons, saturates, the smaller of the SARA group) can more easily diffuse through the oil and bind to the surface first. This is followed by asphaltenes, which are bigger and slower and adsorb preferentially over time, where present in the oil. Figure 5.10 shows a crude mechanism. As outlined in the introduction, larger molecules tend to adsorb preferentially due to the entropic gain from release of several solvent molecules. This method could be proved with model crude oil that contains smaller long chain fatty acids or alkanes and model asphaltenes from literature.[64]

The data in Figure 5.9 also show that the amount of carbon adsorbed for the DI and brine pretreated quartz is essentially unchanged from the original quartz. This is similar behaviour to that observed with HA oil. Hence, it again can be hypothesised that the hydrophilic nature of the quartz surface preferentially adsorbs the water over the crude oil components, even though they may have some polar groups. This is again subject to the sensitivity caveat that very small, sub-monolayer amounts may not be detectable relative to the experimental error.

3) LA-carb Oil

Figure 5.11 shows the CHN carbon results for quartz aged in LA-carb oil. The data for HA and LA are included for ease of comparison. Similarly to the untreated aged quartz previously discussed, the untreated quartz aged in LA-carb oil (pink) shows an adsorbed amount that is consistently above zero, from week 1 onwards. The data show a trend matching the low asphaltene content LA oil, although with a slightly lower adsorbed amount than LA oil. This may not be considered surprising, hypothesising that asphaltenes are key to adsorption, as SARA results for LA-carb oil also showed a low asphaltene content, similar to LA oil. There are some fluctuations in the carbon content, e.g. at week 6, however this is comparable to the error, and this is not considered a significant feature here.

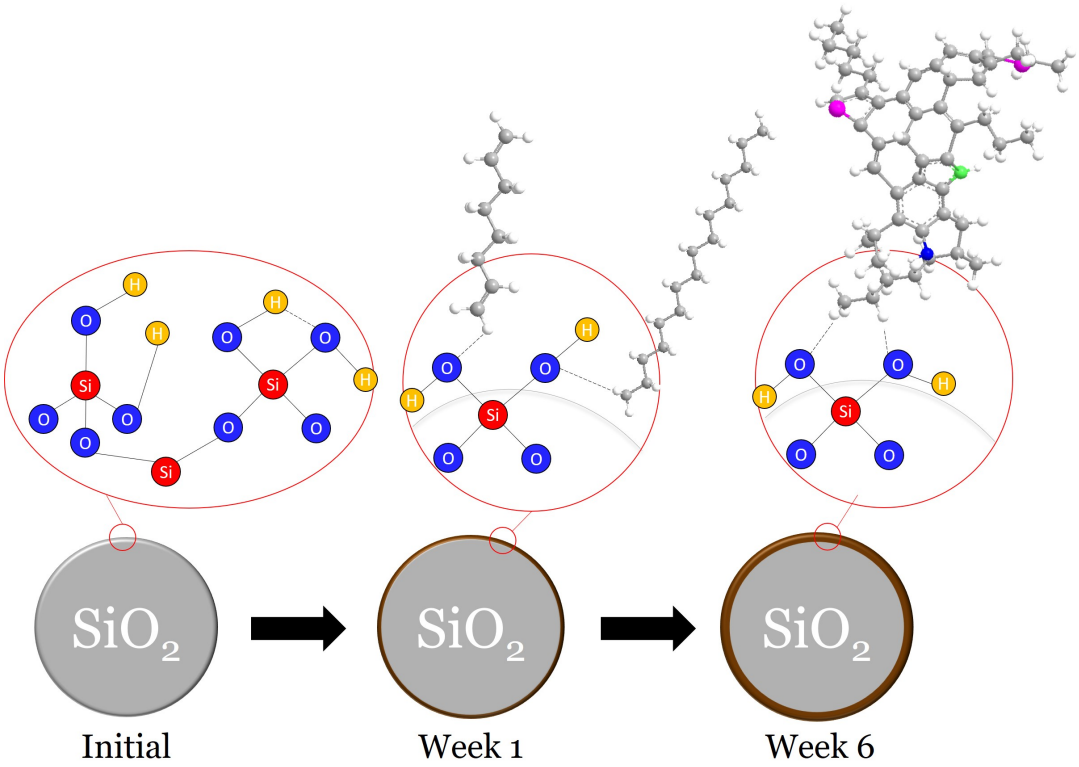

Figure 5.10: Example of molecules binding on to quartz surface. Initially, smaller molecules diffuse through crude and adsorb. Overtime, more entropically favoured larger molecules adsorb to the surface.

For the DI and brine pretreated quartz in LA-carb oil (light red and dark red): these samples show a small fluctuation of carbon content around 'zero'. Values for DI pretreated (light red) show no significant change in carbon content compared to the starting material. This is in very good general agreement with pretreated samples for HA and LA oil discussed above. The brine pretreated (dark red) data show a fluctuation/increase at week 2 followed by a return to the starting material value at week 4. Hence, the week 2 data is attributed as a statistical anomaly and this is not contributing to any significant adsorption changes.

Considering all 6 samples pretreated with water or brine to represent a constant level corresponding to zero additional carbon, this suggests that the fluctuation in the data is around 0.2 %.

This 0.2 % level is the level at which any small amount adsorbed would be taken as equal to zero. In fact, there may be a small amount of organic adsorbed, but it is not considered statistically significant with regards to elemental analysis data.

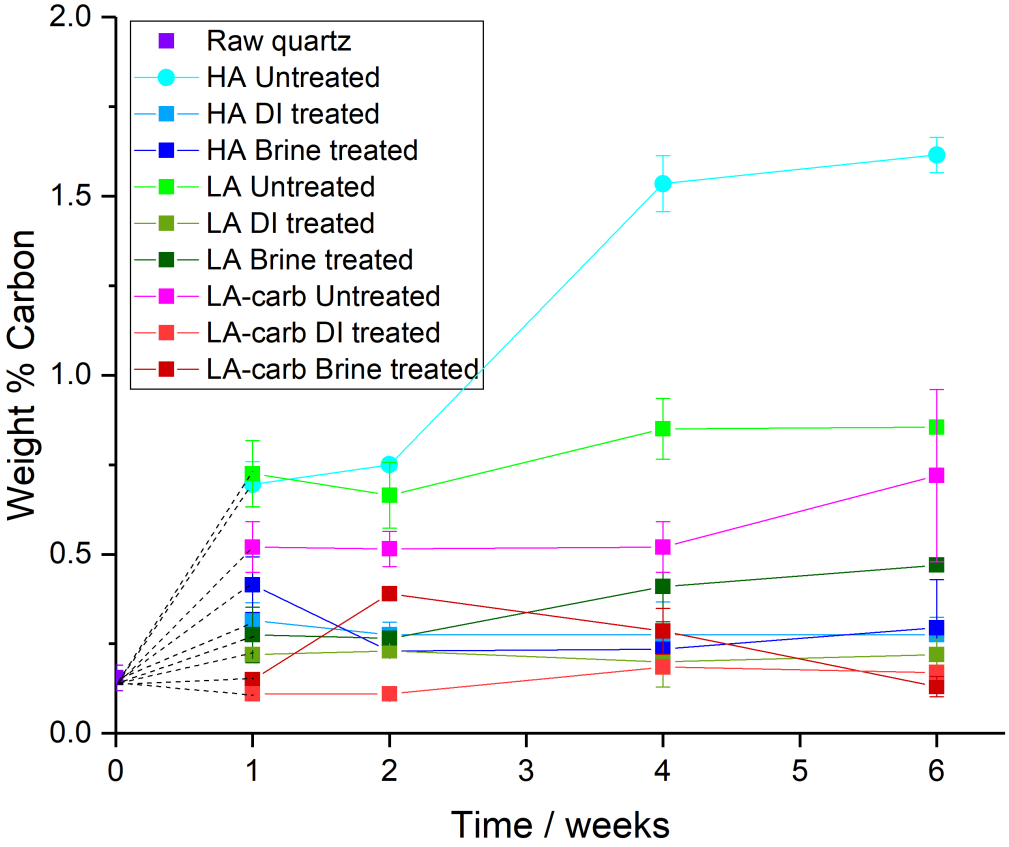

Figure 5.11: Carbon analysis of quartz aged in HA, LA or LA-carb oil, with pretreatments (no pretreatment, DI water or brine). Error shows standard deviation of 2–3 repeats. Dotted lines are added to guide the eye between starting substrate and aged substrate.

4) Degree of Saturation

This section considers the C:H ratio determined by elemental analysis of the aged rock/organic samples as an indication of the nature of molecules that adsorb, particularly the degree of saturation. As outlined in section 5.2.3 a C:H ratio can vary from approximately 2.4, which indicates a saturated hydrocarbon, whereas 0.6 is typical of fused polyaromatic systems/asphaltenes. The difficulty with the data presented here is that the changes to be measured are relatively small, and this can lead to large, unphysical, apparent variations in the C:H ratio. Hence, the data and interpretation in this section should be treated with some caution.

Figure 5.12 shows the degree of saturation of the organics adsorbed on untreated quartz from ageing in HA, LA and LA-carb oil. Importantly, it is noted that DI and brine pretreated samples are not included in this data. This is due to results discussed above where it is concluded that water preferentially binds to the surface

preventing a significant amount of the organics from sticking. Hence, it is not possible to discuss the C:H ratio of organics that are not present. Similarly, there is also the possibility that any amount of water present on the surface (H containing) will also confuse any estimate of the C:H ratio that is otherwise attributed to any organics present.

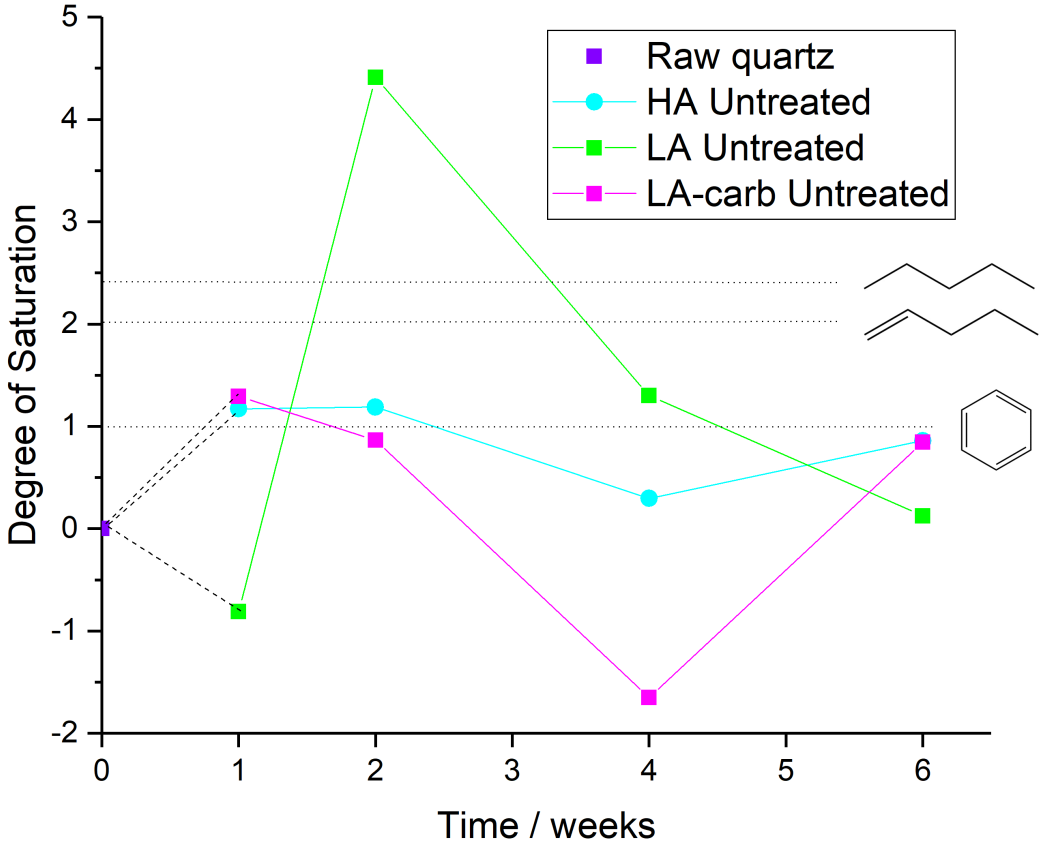

Figure 5.12: Degree of saturation for untreated quartz in HA oil (blue), LA oil (green) or LA-carb oil (pink).

Note that TGA data may be used to identify bound water considering the mass loss below 100 °C may be assumed to be water. This value would need to be subtracted from the CHN hydrogen, to produce organic hydrogen. A similar concept regarding organic carbon is discussed for calcite in Section 5.4.3 to separate inorganic and organic carbon. However, as noted here, in the presence of water pretreatment, the water prevents any significant binding of the organics.

Figure 5.12 indicates that the data for HA (blue line) is in the range 0–1 saturation level essentially independent of ageing time. This saturation value is typical of benzene ring species. This is slightly different from what might have been expected

	Outcrop Rock	Outcrop Solvent	Reservoir Rock	Reservoir Solvent
DoS	23	11	2	7
DBE	0.98	0.99	1.00	1.00

Table 5.5: Degree of saturation and double bond equivalent for outcrop and reservoir rock in Chapter 4 normalised to take into account hydrogen-containing minerals.

from adsorption of an asphaltene poly aromatic ring (more C to H). However, a real asphaltene is usually a combination of aromatic cores and alkyl side groups. Hence, this saturation level may not be unreasonable and could be consistent with the deductions made above.

Considering solvent washed outcrop and reservoir rock characterised in Chapter 4, the expected DoS is 11 and 7 respectively (Table 5.5). This value is significantly higher than the expected value for highly polyaromatic molecules such as asphaltenes. However, the as untreated reservoir rock shows a DoS of 2 that relates to alkene-type molecules. This shows the model aged quartz may be able to replicate some of the functionality present on real reservoir rock.

Figure 5.12 indicates that data for LA-carb oil (pink) are also in the range of 0–1 saturation level typical of that associated with a benzene rings. The point at 4 weeks is very low and unphysical and can only be attributed to experimental error. Similarly, to the HA data, this is consistent with asphaltene adsorption suggested by elemental analysis above.

The LA oil data (Figure 5.12, green) show values that are much more dispersed than expected with very high and a negative value. Due to the way degree of saturation is calculated, a negative value suggests there is less hydrogen on the substrate than at the start. For quartz this might be explained by formation of Si−O−Si bonds, from SiOH formed via the release of H_2O.

The peak at 2 weeks ageing time is above a degree of saturation of 4. This suggests more hydrogen is present on the substrate than would be if a fully saturated hydrocarbon were on the surface (notionally the upper extreme of the range of possible values). This may be attributed to additional water content, although none was specifically added.

In summary, although the majority of the data generally support the hypothesis that asphaltenic species may dominate the adsorption, there is very significant uncertainty in this conclusion. Although it can be rationalised for both the very high and negative values, it is considered unlikely that a single system would oscillate

so dramatically in this way with steady aging. Hence, at this stage definitive conclusions about the unsaturation of the adsorbed species cannot be drawn from this data.

5) Double Bond Equivalent

The method for calculating DBE is shown in Section 5.2.3. Figure 5.13 shows the DBE for untreated quartz aged in HA, LA or LA-carb oil. All values are at ~0.6, which is between a saturated hydrocarbon and a single double bond containing alkene. This result is somewhat unexpected as the previous CHN data suggest more organic adsorbing over time for untreated quartz in HA oil (possibly via diffusion of smaller molecules before larger molecules adsorb). However, the DBE data does not show an increase in molecule complexity over time. DBE shows molecules remain the same complexity and level of hydrogen deficiency throughout the 6 week ageing duration.

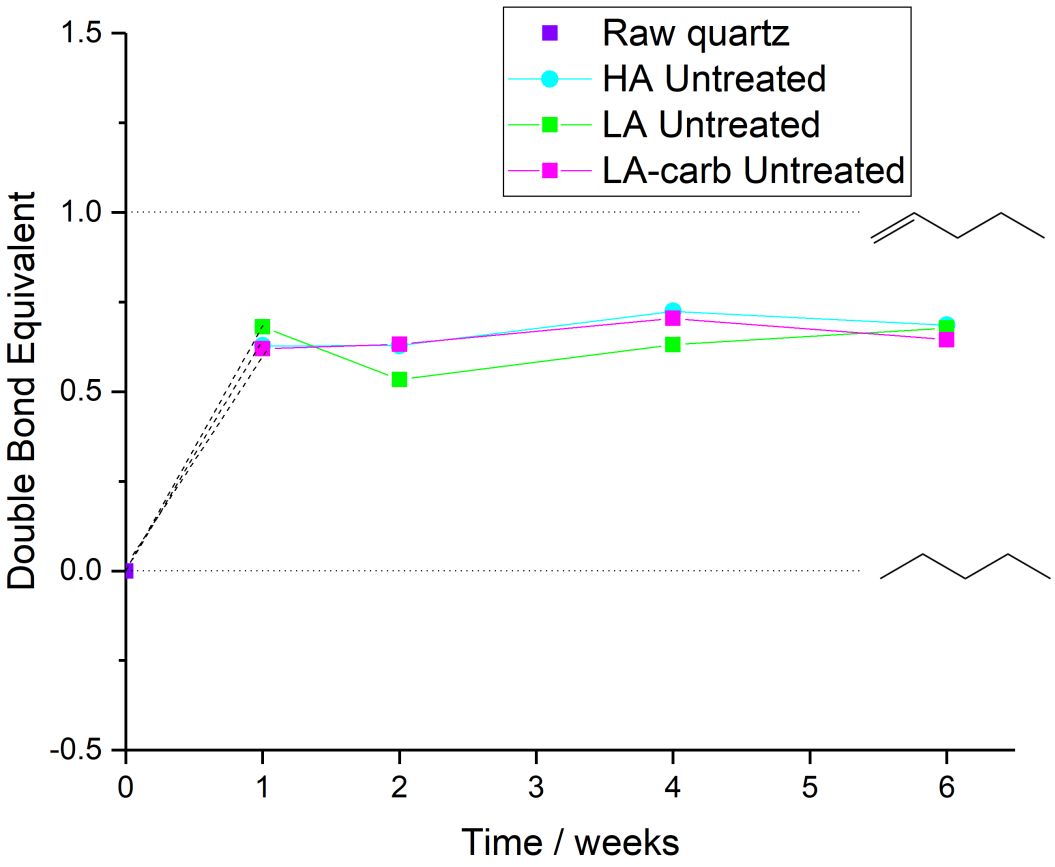

Figure 5.13: Double bond equivalent for untreated quartz in HA oil (blue), LA oil (green) or LA-carb oil (pink).

Comparing the DBE of model quartz aged in crude oil to the values of outcrop and reservoir rock in Chapter 4, Table 5.5 shows the DBE of both as received and solvent washed samples is at 1, which is that of alkenes. This is slightly higher than the model values. However, it is in very close agreement with suggested molecule-types present.

6) Nitrogen

Figure 5.14 shows the amount of nitrogen adsorbed onto quartz aged in HA, LA, or LA-carb oil. Note that the values are rather small but do appear to be larger than the experimental uncertainty. The DI or brine pretreated samples have again been omitted as there is very little organic adsorbed. For HA oil (blue) there is a pronounced elevation in the amount of nitrogen relative to the starting bare substrate. Once this amount is adsorbed, there is no statistically significant change over time.

The data in Figure 5.14 for LA oil (green) indicates a clear increase in the adsorption of nitrogen over the bare substrate. Interestingly, there is rather little adsorption after one week and only after 2 weeks is there some suggestions of adsorption and a plateau. It is interesting to speculate why there is a delay in nitrogen adsorption when the carbon content rises immediately. This suggests an exchange is occurring at the surface with initial adsorption of species with rather little nitrogen adsorbing first, followed by exchange for species with more nitrogen. This may suggest initial adsorption of one species followed by another with time.

Figure 5.14 indicates that the LA-carb oil (pink) shows an initial adsorption evident after one week. There is some suggestion of a further rise after 6 weeks. However, caution should be taken when basing a significant conclusion on a single data point, although error is of standard deviation of three repeats. The increase at 6 weeks may indicate further adsorption or exchange of non-nitrogen containing species for nitrogen containing species with time. It is not obvious why this is expected to occur after 6 weeks and not as a gradual exchange over time.

To rationalise the behaviour above, surface chemistry can be considered. The quartz surface has a negative charge at the pH of crude oil (pH 9–11). However, technically water should be present to impact the surface deprotonation of the SiOH groups. There are several forms for nitrogen in the crude oils. Most significant here is that several forms are cationic. Hence, it is anticipated that nitrogen adsorbed onto the quartz surface will be in the form of a quaternary amine or other cationic functionality such as pyridinium ion. These groups may be found in both alkyl and

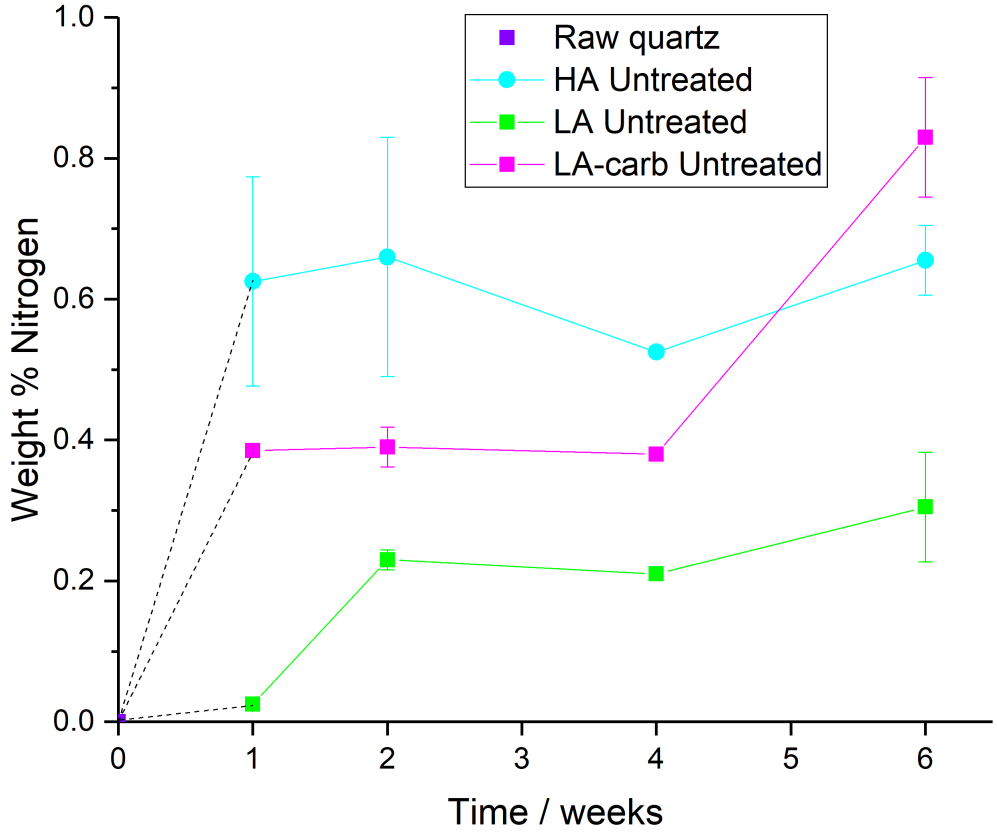

Figure 5.14: Nitrogen analysis of quartz aged in HA, LA or LA-carb oil, with pretreatments (no pretreatment, DI water or brine). Error shows standard deviation of 2–3 repeats. Dotted lines are added to guide the eye between starting substrate and aged substrate.

aromatic crude oil species.

The asphaltene and aromatic content of HA is greatest of all the oils in this study and show the most carbon, hydrogen and nitrogen adsorbed. LA and LA-carb oil have similar asphaltene contents and if asphaltene content was the dominant influence they would be expected to be similar. However, the LA-carb oil has more resin by 7.3 % (as a reminder, resins are similar to asphaltenes as they are similarly doped with heteroatoms) and fewer saturates by 7.5 %. This could explain the increase in nitrogen at the end of the process, considering the suggested mechanism: smaller saturates are diffusing and adsorbing first, followed by larger molecules that in this case are resins.

Table 5.6 shows a comparison of the nitrogen content of adsorbed organics after 6 weeks to the nitrogen content in the crude oil. The weight % for nitrogen adsorbed onto quartz aged in HA oil is 3.7 times greater than the weight % of nitrogen in

Oil	Nitrogen in oil / weight %	Nitrogen on substrate / weight %	Increase
HA	0.16	0.61	x3.7
LA	0.16	0.27	x1.7
LA-carb	1.00	0.85	x-0.2

Table 5.6: Comparison of nitrogen in crude oil and adsorbed onto quartz after 6 weeks.

HA oil. This suggests molecules containing nitrogen preferentially bind onto quartz. An increase in amount of nitrogen adsorbed compared to LA oil is seen, where 1.7 times the content is adsorbed. Interestingly, the LA-carb shows slightly less nitrogen adsorbed than what is present in the starting LA-carb oil, contradicting the possible mechanism of nitrogen containing molecules preferentially binding.

Overall, the nitrogen data enable a conclusion that nitrogen containing molecules do adsorb. However, they do not appear to drive initial adsorption of the organics: carbon containing molecules adsorb before nitrogen molecules adsorb. An increase in nitrogen does not translate as an increase in carbon content. If nitrogen drove adsorption, the carbon and nitrogen data would show a similar rate of increase.

7) Conclusions

For ageing quartz in crude oil the following conclusions can be drawn:

- Carbon species adsorb when water is not present.
- Water (DI or brine) out competes the organics for the quartz surface.
- Nitrogen containing species adsorb but do not direct initial carbon species adsorption.
- Degree of saturation suggests aliphatic amines adsorb.

5.4.3 Ageing Calcite

This section summaries the elemental analysis results from the exposure of calcite to the three crude oils of interest, with and without aqueous pretreatment and over an extended ageing period of up to 6 weeks. As outlined in Section 5.3 above these experiments exposed a powdered substrate to these fluids/pretreatments at 70 °C under nitrogen. The resulting aged solids were separated by filtration and washing with toluene and methanol. The data presented here there are elemental analyses of the aged powdered calcite and any adsorbed layer it has gained as part of the ageing process.

CHN Analysis of Calcite

1) HA Oil

Figure 5.15 shows the elemental carbon results for carbon aged in HA oil with and without the pretreatments.

Disentangling carbon content from carbonate and adsorbed organics:

From initial analysis of HA oil ageing, around 13 % carbon is present in the untreated (no water exposure) samples, whereas DI and brine treated contain 12 %. However, the elemental carbon results for calcite will include both the organic and inorganic carbon: organic carbon from any adsorbed organics and inorganic carbon from the carbonate ions of the bulk crystal. The two can be deconvoluted using TGA. The schematic Figure 5.16 presents representative TGA data from an aged calcite sample. The decomposition of calcium carbonate into carbon dioxide and calcium oxide (Equation 5.3) occurs at a known temperature (700–800 °C). The data in Figure 5.16 show a series of significant falls in sample mass. Each of these are attributed to loss of some component from the sample on heating. Here it is assumed that the decreases in mass over the temperature range 50–100 °C are attributed to weakly bound water, from 100–550 °C are adsorbed organics desorbing/decomposing and from 700–800 °C is the decomposition of calcium carbonate.

To estimate the amount of carbon in the sample the stoichiometry of the decomposition reaction is used, in Equation 5.3 below. Hence, the fall in mass over the calcite thermal decomposition range is stoichiometrically related to the amount of CaO that remains and hence the original amount of $CaCO_3$.

Employing the weight % change from the decomposition of calcium carbonate, the total inorganic carbon can be calculated (Equation 5.4). Subtracting this

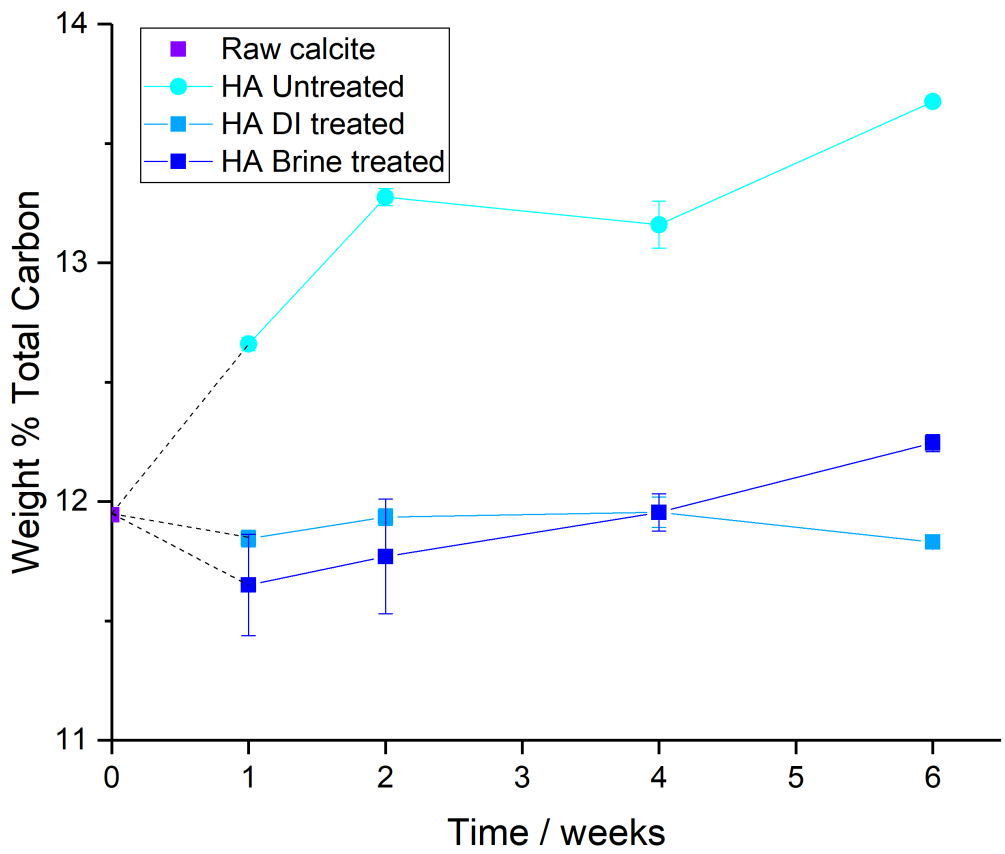

Figure 5.15: Total carbon of calcite, aged in HA oil, with pretreatments (no pretreatment, DI water or brine). Error shows standard deviation of 2–3 repeats. Dotted lines are added to guide the eye between starting substrate and aged substrate.

experimentally determined value of the inorganic carbon in the sample from total carbon measured in the elemental analysis, the organic carbon content can be determined.

$$CaCO_3 \longrightarrow CaO + CO_2 \tag{5.3}$$

$$Total\,carbon = (inorganic\,carbon) + (organic\,carbon) \tag{5.4}$$

The amounts of organic carbon in our samples and the variation with treatments and ageing can be determined via this approach. Note that the amount of inorganic carbon will always be very large as this is a very big fraction of the substrate mass. However, the data and analysis do seem to indicate some interesting observations. Figure 5.17 shows the organic carbon data for calcite aged in HA oil with and

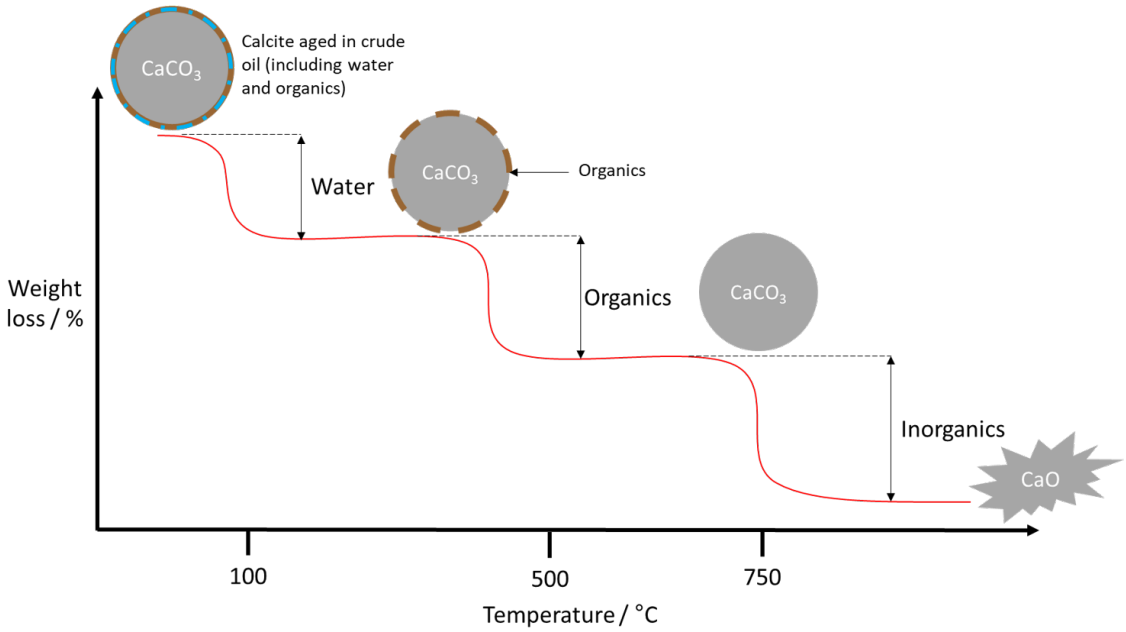

Figure 5.16: Schematic of TGA data showing decomposition of calcium carbonate with bound organics and water. TGA is used to deconvolute elemental analysis data and determine organic carbon and organic hydrogen values.

without pre-treatments (calculated using the TGA data as discussed above).

1.1) Untreated Substrate

The data in Figure 5.17 show that after untreated calcite is aged in HA oil there is a significant rise in organic carbon content over the ageing process.

There is a very small amount of organic carbon in the original calcite (0.2 %), which is similar to the levels seen in the quartz starting material used, attributed to a small error in the calculation of the organic carbon content, impurities of the sample and/or adsorption of adventitious carbon from the atmosphere. There is a 1.0 % increase in carbon from the starting material to the 1 week aged calcite and further increase to a potential plateau at weeks 2 and 4. There may be a small further increase at week 6, although this may be comparable to the plateau value at weeks 2 and 4, possibly indicative of one long plateau (Figure 5.17, red dashed line). The final organic carbon value (6 weeks) is 2.3 %. The specific surface area of the calcite used is 18 m^2 g^{-1}. Therefore, 2.3 % organic carbon content of a 100 g sample corresponds to 2.3 g of carbon (0.192 moles) on 1800 m^2. Hence, there are 0.00011 moles m^{-2} or ~0.5 $Å^2$ per carbon. The van der Waals radii of a carbon atom is 1.7 Å (or a footprint area of 9 $Å^2$ per atom). Hence, there is approximately a 5-atom thick layer. This result is approximately half the estimated thickness

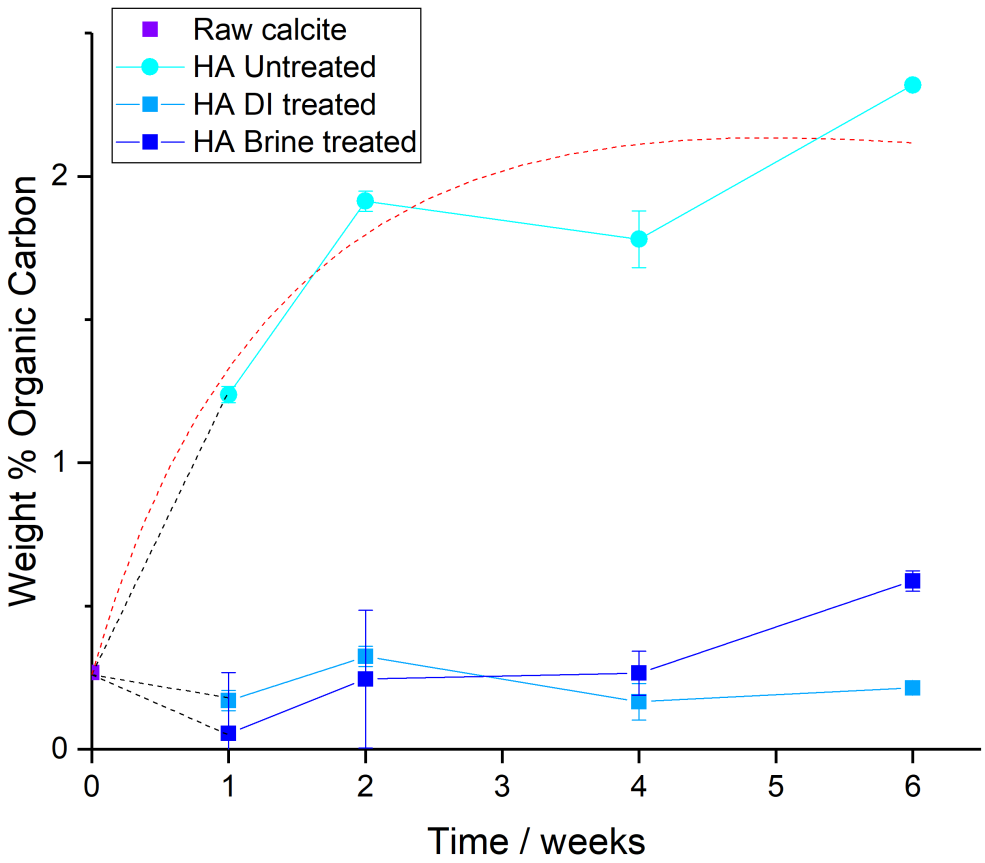

Figure 5.17: Organic carbon of calcite, aged in HA oil, with pretreatments (no pretreatment, DI water or brine). Error shows standard deviation of 2–3 repeats. Black dotted lines are added to guide the eye between starting substrate and aged substrate. Red dotted lines are to guide the eye to a suggested plateau.

of the layer on quartz (Section 2.3.2). It must be stressed that these are indicative calculations only. A lower amount adsorbed compared to the quartz discussed above could be due to the lower surface energy of calcite compared to quartz, resulting in weaker molecular interactions and more easily removable molecules during solvent washing.[238,239]

1.2) Pretreated Substrate

Figure 5.17 also presents the organic content for the calcite with pretreated with DI water or brine. DI and brine pretreated calcite aged in HA oil shows no significant organic carbon adsorbing. However, it could be suggested that after 6 weeks the brine pretreated sample begins to adsorb a small amount of organic carbon. This result may not be statistically significant as previous data from quartz has shown a

potential for 0.2 % error in the measured amount of carbon. Hence, there would be no increase in carbon compared to the starting material. Overall, less organic carbon adsorbs onto DI or brine pretreated calcite compared to untreated calcite.

The surface nature and charge of calcite is discussed in Section 2.3.3. Given that the calcite surface will be populated with calcium hydroxide, it would be expected to interact preferentially with water compared to oil. [240]

Similarly to quartz, it is not surprising that the water (DI and brine) pretreatments have prevented oil binding to the calcite surface. This supports the mechanism outlined above, where water binds first and repels the hydrophobic oil (Figure 5.18).

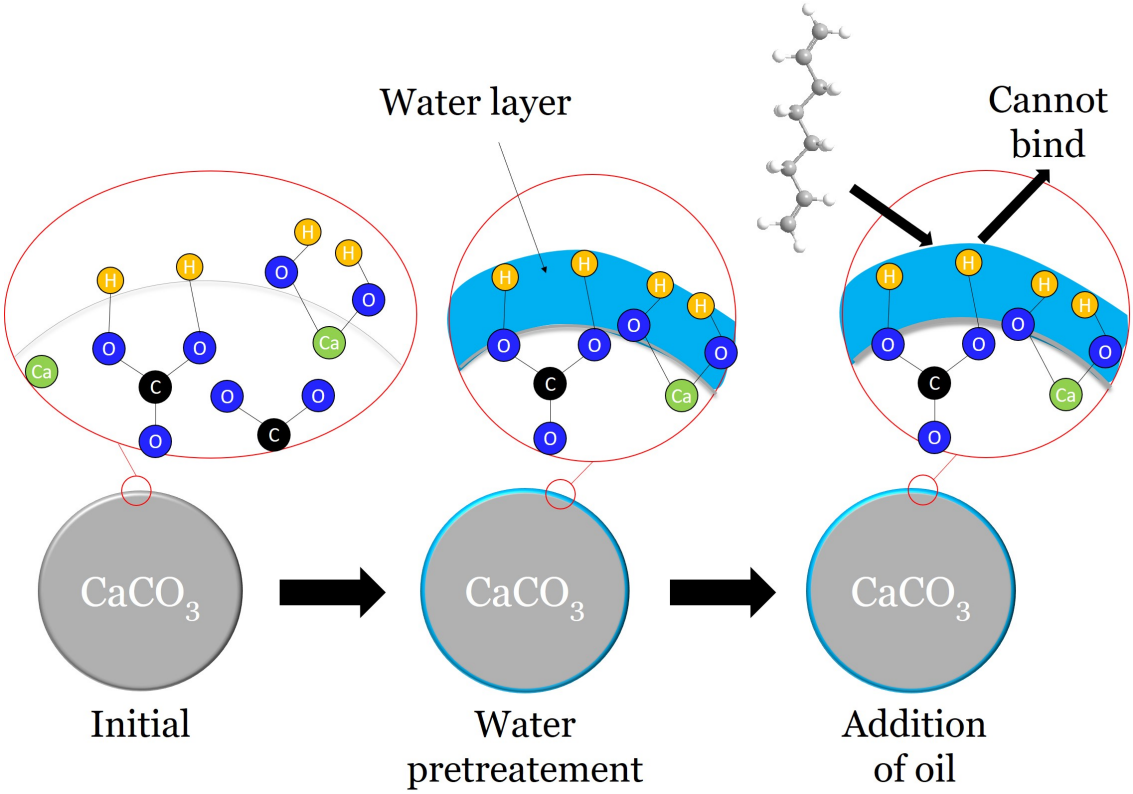

Figure 5.18: Schematic of water binding onto calcite and preventing crude oil binding.

2) LA Oil

Figure 5.19 (a) shows the total carbon from elemental analysis. The untreated calcite stays at the same carbon content level until week 6 where it increases by 0.2 %. DI pretreated calcite shows a sharp increase at week 2 (+0.3 %) and tends to a plateau for following weeks. The brine pretreated calcite starts off with significantly less carbon content after week 1 and 2 by -0.3 %, before increasing to +0.2 and a

further +0.25 % in week 4 and 6 respectively.

Figure 5.19 (b) shows the organic carbon content of calcite aged in LA oil, normalised by TGA data. There is a similar trend and profile to those observed in the non-normalised data: untreated calcite has a very small increase in carbon content after 6 weeks, DI pretreatment tends to a plateau after week 2 and brine pretreatment suggests loss of carbon initially before an increase and flattening out to form a plateau.

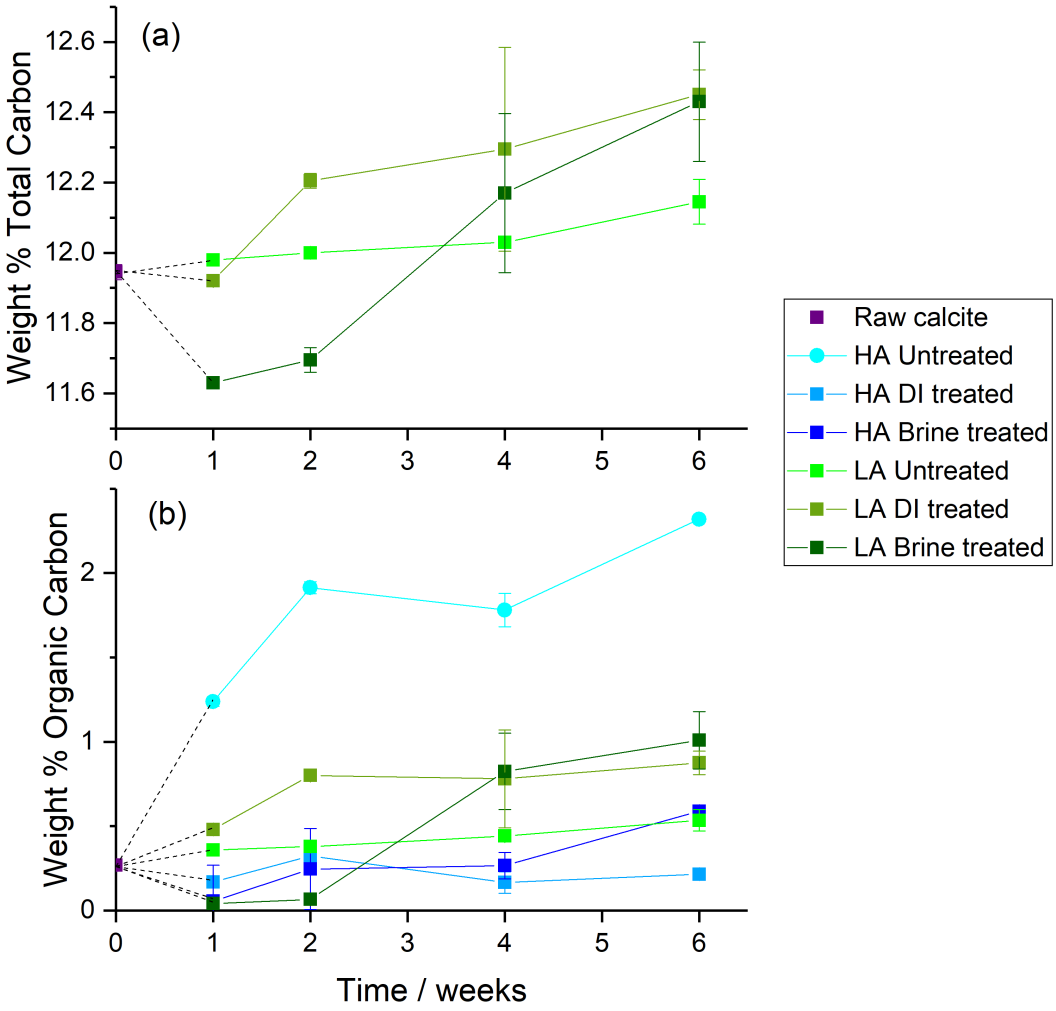

Figure 5.19: (a) total carbon and (b) organic carbon on calcite aged in LA oil, with pretreatments (no pretreatment, DI water or brine). HA oil is included for reference. Error shows standard deviation of 2–3 repeats. Black dotted lines are added to guide the eye between starting substrate and aged substrate.

There may be adsorption for all calcite samples aged in LA oil, but the amount adsorbed is less than untreated calcite in HA oil that contains asphaltenes (Figure 5.19 (b)). Asphaltene content in HA oil is over six times greater than in LA oil. The amount adsorbed by untreated calcite in HA oil compared with all three calcite samples aged in LA oil is four to five times higher. This suggests the amount of asphaltene in the crude oil is almost proportional to the amount of adsorbed organics.

The increased carbon content for DI and brine pre-treated calcite suggests water may play a role in aiding adsorption of organics on calcite. This could occur via the equilibrium between bicarbonate surface groups and protons in water that will lead to an emission of CO_2, which may explain the initial drop of carbon content with DI pretreatment. The initial sharp increase from brine pre-treatment suggests ions accelerate the organic adsorption process, possibly via ion bridging that outcompetes the complex aqueous solution equilibria of calcite.[94,241,242] This effect could be argued to be seen in the brine treated sample aged in HA oil.

3) LA-carb Oil

Figure 5.20 (a) shows the total carbon from elemental analysis and Figure 5.20 (b) shows the organic carbon deduced with parallel TGA data. Both sets of LA-carb carbon data show similar trends when compared to each other. Interestingly, all values are below the starting content of the calcite substrate. The untreated calcite begins with a loss of carbon on week 1 and this tends to a plateau, totalling a loss of 0.5 % carbon. DI and brine pre-treated carbon also begins with a loss, but it is far greater at almost 1.5 %; This loss is sustained throughout the ageing process. A loss in carbon content must be due to a loss of carbonate anions in the calcite (the only source of carbon in the original material). The ions could be replaced in the crystal structure with another anion such as sulfate.[36] If there is bulk exchange then a significant change will occur. However, ions exchanging at the surface will be a very small contribution. One way to investigate whether the crystal structure has changed is via PXRD.

Figure 5.21 shows the PXRD for calcite (red) and calcite aged in LA-carb oil pre-treated in DI water (green) or brine (blue). There is no significant shift in the peak positions expected if there was isomorphic substitution of one ion for another in the crystal structure. Therefore, it is concluded that the carbonate ions have not been replaced in the bulk. However, a drop of 1.5 % carbon observed in Figure 5.20 corresponds to a very small amount, more typical of a surface layer

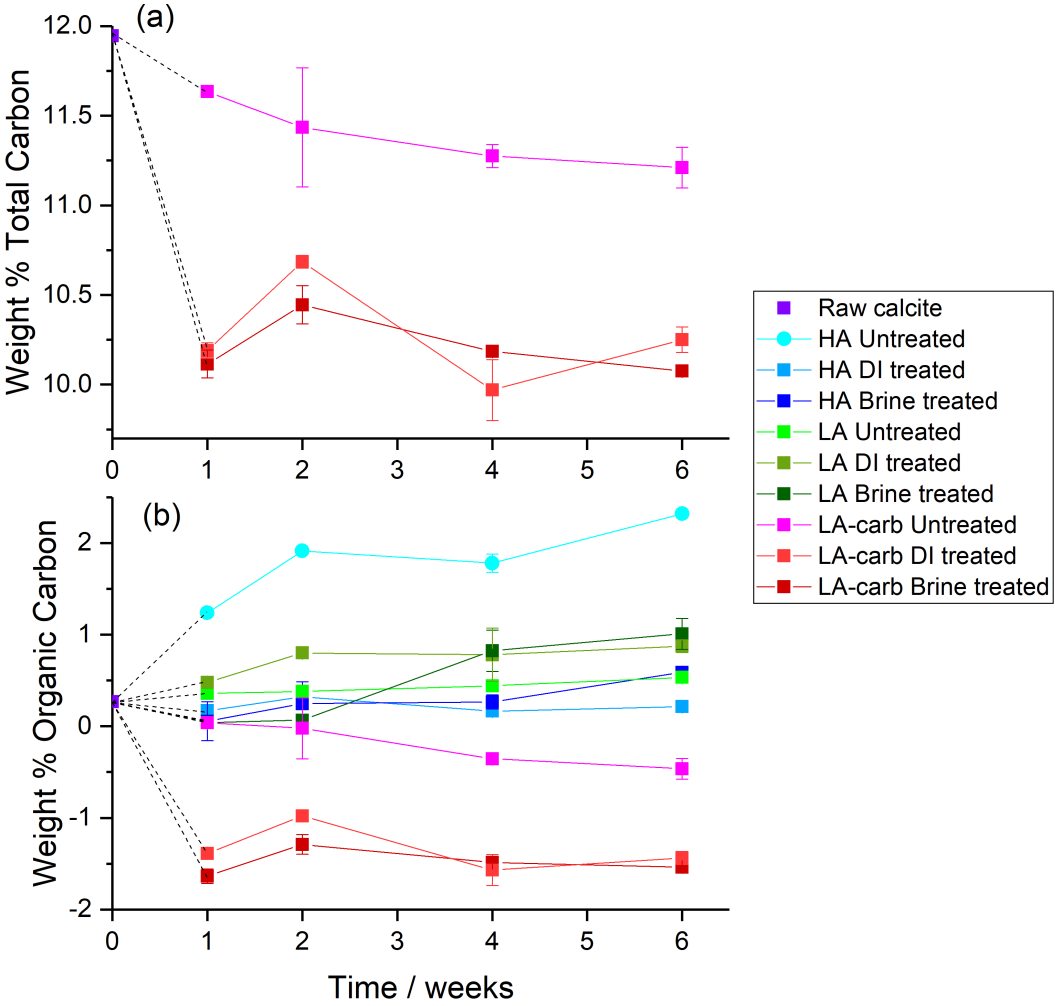

Figure 5.20: (a) total carbon and (b) organic carbon on calcite aged in LA-carb oil, with pretreatments (no pretreatment, DI water or brine). HA and LA oil is included for reference. Error shows standard deviation of 2–3 repeats. Black dotted lines are added to guide the eye between starting substrate and aged substrate.

removal/exchange of carbonate ions. Tentatively the conclusion is that only the surface carbonate ions have been exchanged.

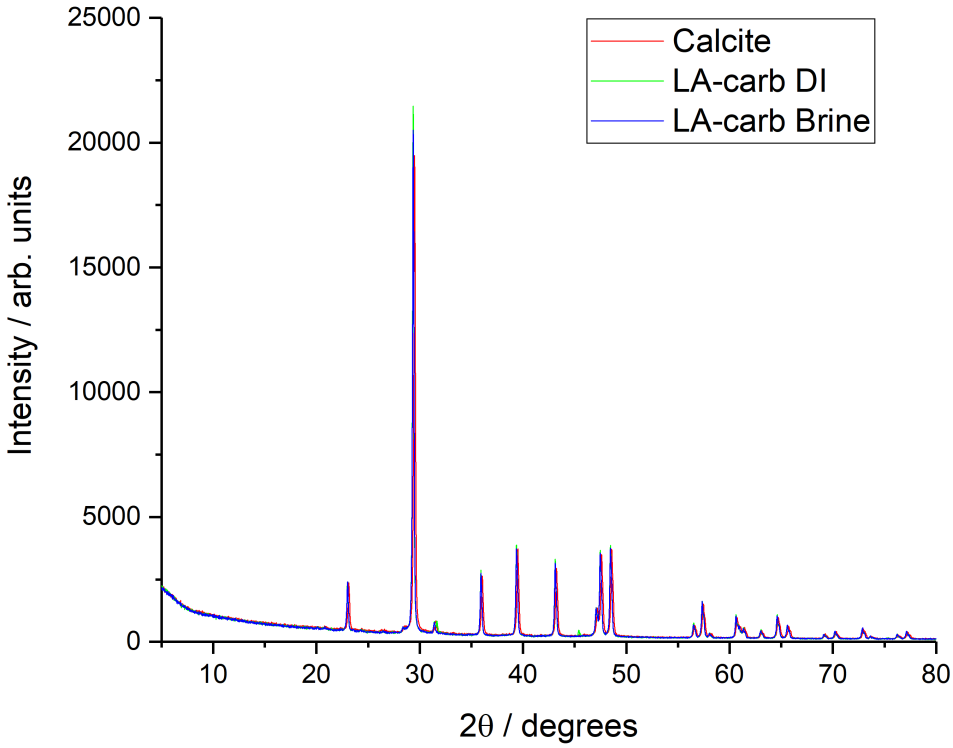

Figure 5.21: PXRD of calcite (red), aged in LA-carb oil and pretreated in DI water (green) or brine (blue).

4) Degree of Saturation

In this section C:H ratio determined by elemental analysis is considered and normalised into organic carbon and organic hydrogen, in combination with TGA data.

Figure 5.22 shows the degree of saturation of untreated calcite in HA, LA and LA-carb oil. DI and brine treated samples were not included as they are considered noise.

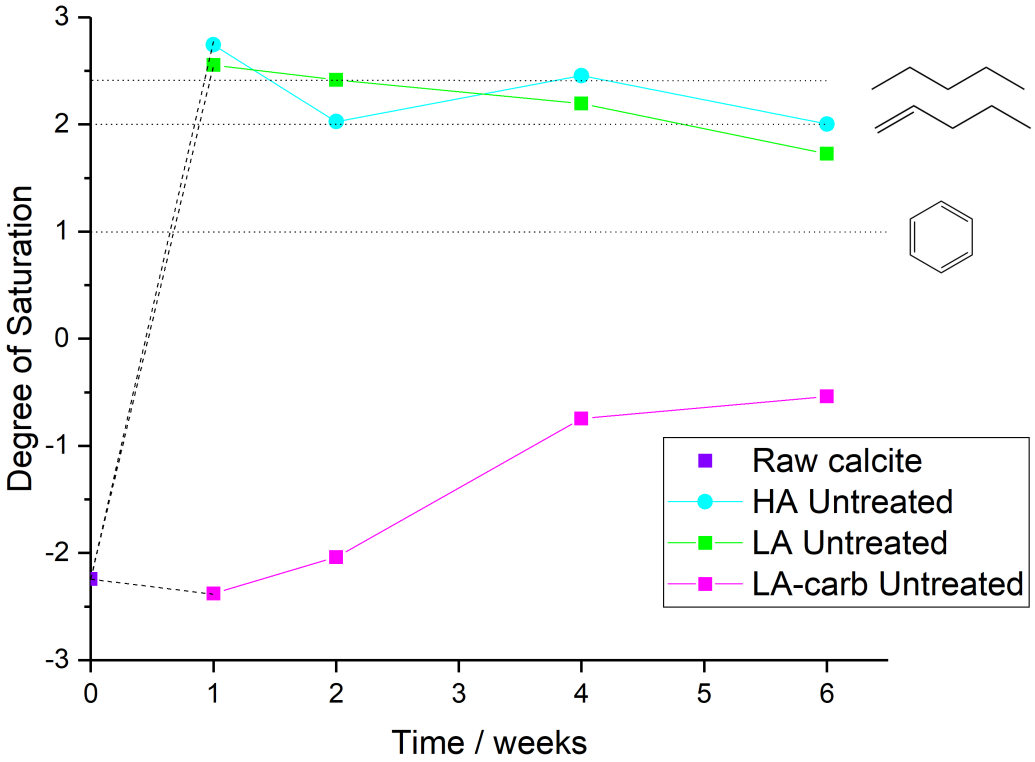

Figure 5.22: Degree of saturation for untreated calcite in HA oil (blue), LA oil (green) or LA-carb oil (pink).

The data for untreated calcite aged in HA (blue) and LA oil (green) are in the range 2.5–1.9 that is typically associated with hydrocarbon aliphatic chains, moving slightly towards more saturated aromatic molecules over the 6 weeks. However, this range is also associated with asphaltenes as they have a polyaromatic core with several long hydrocarbon chains (Table 5.2). The time dependent adsorption data suggest small molecules may be adsorbing first and more complicated larger molecules adsorb over time, similarly to the results of quartz, confirming the mechanism of adsorption suggested in Section 5.4.2.

The DI and brine pre-treated calcite data begin with a high unsaturation level before arriving at a similar end saturation level to the untreated calcite. This suggests small molecules are adsorbing first and asphaltenes are adsorbing last.

5) Double Bond Equivalent

Figure 5.23 uses the organic carbon, organic hydrogen and nitrogen values for untreated calcite aged in HA, LA and LA-carb oil. The data for untreated calcite in HA oil (blue) show an immediate increase to over 2 DBE (a decalin-type molecule) and slowly increasing above 3 DBE (a benzene-type molecule). This result may be expected as it reinforces the diffusion and adsorption of more complex molecules overtime. LA oil (green) stays at a level of 1.5 throughout, reaffirming the suggestion that the small number of asphaltenes in LA oil bind initially and form a layer and no more is adsorbed.

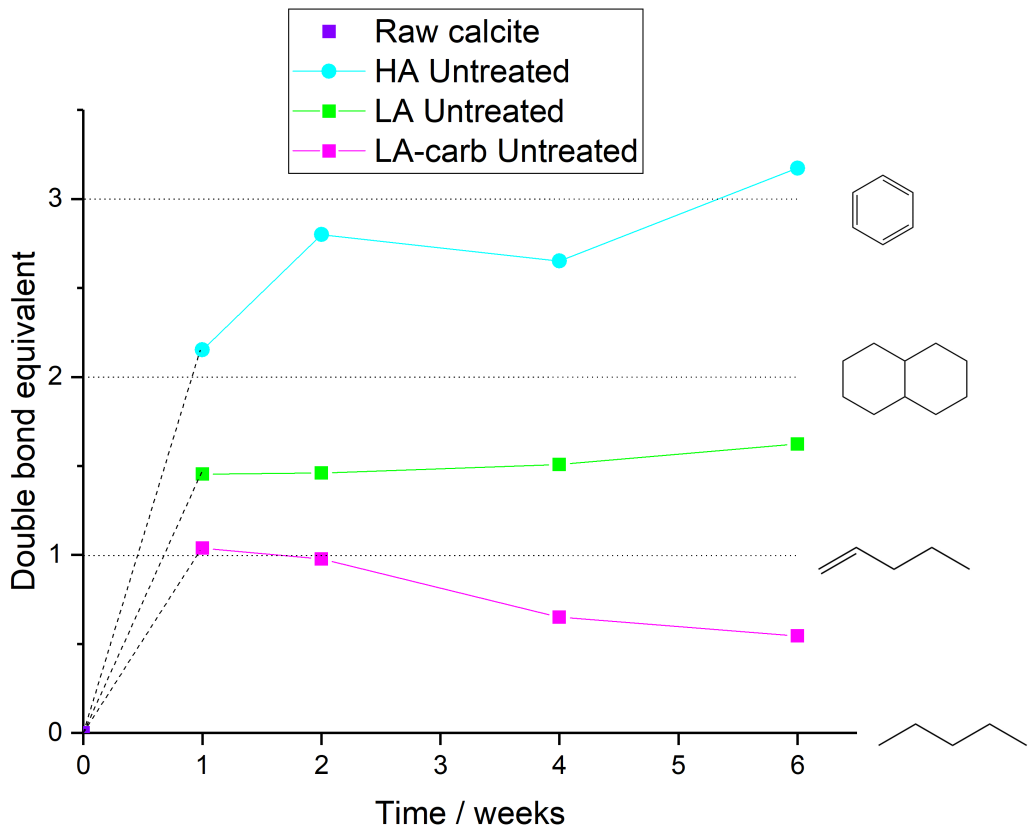

Figure 5.23: Double bond equivalent for untreated quartz in HA oil (blue), LA oil (green) or LA-carb oil (pink).

Interestingly, LA-carb oil DBE begins at 1 and decreases to 0.5 over 6 weeks. This reduction directly relates to the loss of carbonate anions observed in the CHN

data.

5) Nitrogen

Figure 5.24 shows the amount of nitrogen adsorbed onto calcite aged in HA, LA or LA-carb oil. The DI or brine pre-treated samples have been omitted. As described above, no significant amounts of organics are adsorbed.

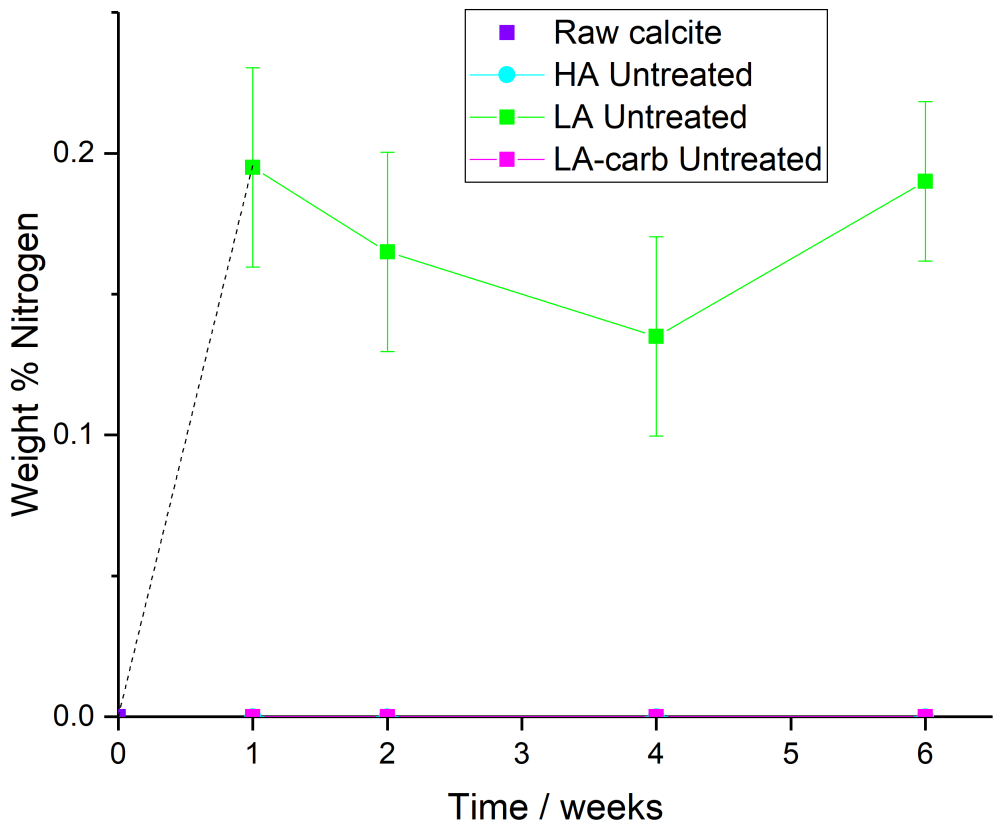

Figure 5.24: Elemental analysis results for nitrogen on calcite in either HA, LA or LA-carb oil. Error shows standard deviation of 2–3 measurements.

Figure 5.24 indicates that no additional nitrogen is detected in the adsorbed material from HA or LA-carb on aged calcite. However, importantly calcite aged in LA oil does show a significant amount of nitrogen adsorbed well above the as received blank calcite value. This level of nitrogen is maintained throughout the ageing (0.15 %). It is interesting that this value is similar to the nitrogen value of 0.2 % seen in quartz also aged in LA oil.

The weight % level of nitrogen in LA oil is 0.16 %, which is the same weight % as detected in the organics adsorbed. Hence it can be concluded that a component of

LA oil may drive nitrogen species to preferentially bind onto calcite.

6) Conclusions

For ageing calcite in the three crude oils of interest the following conclusions can be drawn:

- Carbon species adsorb when water is not present.
- Asphaltene content of oil is proportional to organic carbon adsorbed onto calcite.
- LA oil causes the highest proportion of nitrogen containing species to adsorb.

5.4.4 Ageing Kaolinite

This section summarises the elemental analysis results from the exposure of kaolinite to the three crude oils of interest, with and without aqueous pretreatment and over an extended ageing period of up to 6 weeks. As outlined in Section 5.3 above, these experiments exposed a powdered substrate to these fluids/pretreatments at 70 °C under nitrogen. The resulting aged solids were separated by filtration and washing with toluene and methanol. The data presented here are the elemental analyses of the aged powdered mica and any adsorbed layer it has gained as part of the ageing process.

CHN Analysis of Kaolinite

1) HA oil

Figure 5.25 shows the CHN elemental analysis for powdered kaolinite aged in all three crude oils, with and without pretreatments. Figure 5.25 (a) shows untreated kaolinite aged in HA oil having a significant (1.3 %) carbon adsorption. Considering the BET surface area of kaolinite (7.99 m^2 g^{-1}), a 100 g sample of kaolinite has 1.3 g of carbon (0.108 moles) is adsorbed on 799 m^2. Therefore, 0.000136 moles m^{-2} or 0.5 $Å^2$ that corresponds to a 5-atom thick layer, concluding the amounts of organic adsorbed are of molecular dimensions.

DI and brine treated samples peak at 0.2 % carbon after 1 and 4 weeks respectively. These values could be significant, but they are also within the region of equipment noise (0.2 %). All three untreated and treated HA oil aged kaolinite values have plateaus that are similar with the results from ageing on quartz (Figure 5.7). This is expected as the surface of kaolinite is similar to that of quartz with a surface hydroxyl group.

Figure 5.25 (b) shows the hydrogen values for aged kaolinite. Kaolinite, chemical formula $Al_2Si_2O_5(OH)_4$, should have 1.5 % hydrogen. However, 35 % less than expected is observed in the raw kaolinite with only 1.1 % detected. As the error margin for these results is 0.2 %, these results are not statistically different from the values detected for the starting materials. Considering this, hydrogen content of DI and brine pretreated kaolinite aged in HA oil aged samples may be considered not to deviate from the raw material hydrogen content. The untreated kaolinite has similar content adsorbed (1.3 %) before spiking to 1.8 % at 6 weeks. The spike after 6 weeks could be due to more saturated molecules adsorbing onto kaolinite: this hypothesis goes against the previous suggestion of simple long chain hydrocarbons

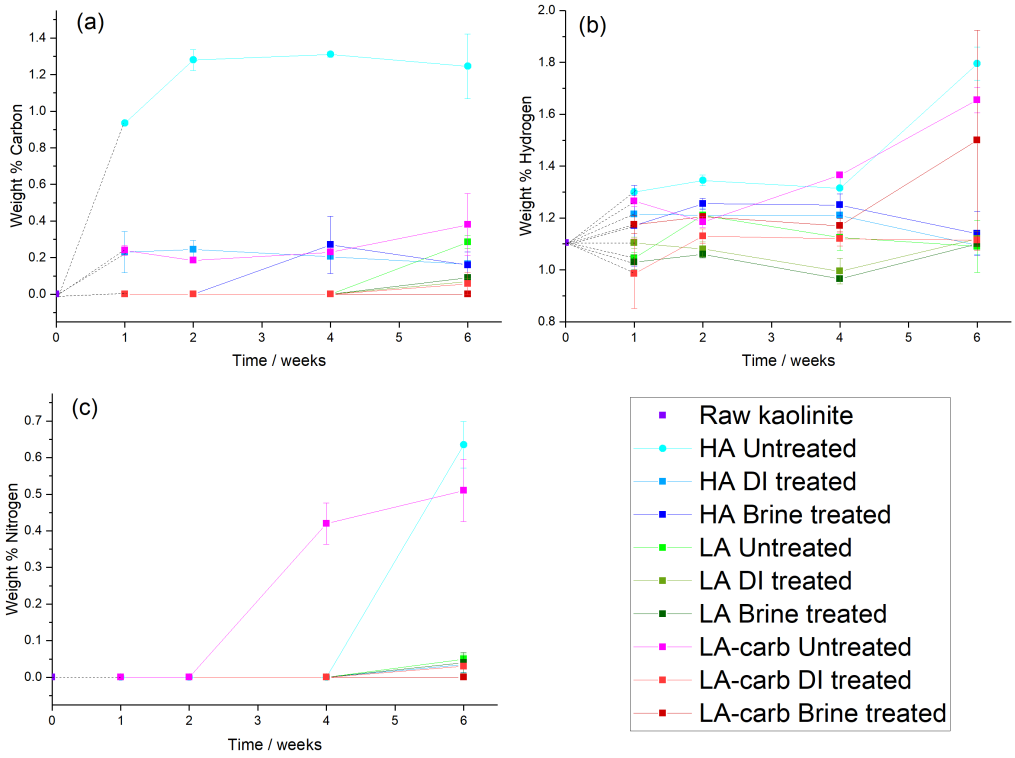

Figure 5.25: Elemental analysis results for (a) carbon, (b) nitrogen and (c) hydrogen on kaolinite in either HA, LA or LA-carb oil. Error shows standard deviation of 2–3 measurements.

adsorbing first before larger polyaromatic moieties adsorb.

The spike in hydrogen could relate to the nitrogen-containing molecules adsorbing at the same time. Figure 5.25 (c) shows a spike at 6 weeks for untreated kaolinite in HA oil. The spike in hydrogen and nitrogen suggests that as the nitrogen containing species have adsorbed, they have brought hydrogen possibly in the form of a porphyrin or a long chain hydrocarbon with an amine terminating group.[243] However, literature that considers ageing of substrates in crude oil suggests aliphatic amines are unstable during the ageing process and turn into more stable pyrdines, indoles and carbazoles.[66] The possible detection of aliphatic amines in the system in this thesis could be due to the differences between the model system presented and a real reservoir condition.

2) LA oil

Considering kaolinite aged in LA oil when untreated and pretreated in DI and brine, Figure 5.25 (a), (b) and (c) shows there is no statistically significant change

in carbon, hydrogen or nitrogen adsorption respectively. It could be argued that after 6 weeks the untreated carbon content does increase, but this is within machine error (0.2 %).

Upon first glance, the lack of adsorption could be attributed to a lower asphaltene content oil: kaolinite could prefer asphaltenes to bind first and remain bound. However, the results for the LA-carb oil suggest differently.

3) LA-carb oil

Untreated LA-carb oil shows carbon adsorption occurs immediately and stays at a plateau between 0.2–0.3 %, which is comparable to the adsorption of DI and brine treated HA oil aged kaolinite. Hydrogen levels for the untreated and brine treated sample begin to rise at the 4 week mark and this is reflected in the nitrogen levels of the untreated sample too; untreated LA-carb oil reaches similar levels of hydrogen and nitrogen as untreated HA oil.

There is possibly a nitrogen containing species in LA-carb oil and HA oil that is binding after 4 weeks. It does not appear to be asphaltene or carbon driven. If the nitrogen species was a porphyrin, it would most likely be a vanadium porphyrin: the initial levels of vanadium in HA oil is ∼180 ppm and LA-carb oil is 1.5 ppm, whereas it is only 0.5 ppm in LA oil. The 1.5 ppm could be enough to promote diffusion of the larger porphyrin through the system and aid adsorption after 4 weeks. One way to assess vanadium adsorption would be measure levels of vanadium in the supernatant of oil. This is not possible due to the amount of sample needed and safety issues with scaling the experiment. However, it could possibly be investigated using a ICP-OES set up for organic solvent analysis.

4) Degree of Saturation and DBE

Figure 5.26 shows (a) the degree of saturation and (b) double bond equivalent of aged kaolinite samples. The degree of saturation graph suggests organics adsorb from HA oil starts off aliphatic and tends to more polyaromatic systems. The opposite is shown for HA oil in the DBE graph where a tendency towards saturated hydrocarbons occurs at 6 weeks. This could be rationalised by the presence of hydrogen-binding atoms, such as metals and sulfur, in HA oil that are not considered in the DoS equation. These atoms will increase the DoS and produce saturated hydrocarbons that match the DBE data.

LA oil remains the same throughout both graphs. LA-carb oil shows a very high

degree of saturation (over 5 for all weeks). Levels higher than 2.4 suggest there is more hydrogen present than can be contained on carbon and nitrogen atoms. One possibility for this is a breakage of siloxane (Si−O−Si) linkages in favour of terminating silanol groups. LA-carb DBE shows a steady decrease after 2 weeks, suggesting molecules are becoming more saturated. This result suggests unsaturated molecules adsorb first before saturated molecules adsorb in increasing amounts. However, this could be from the nitrogen containing species starting to adsorb, assuming the nitrogen containing species are long chain hydrocarbons.

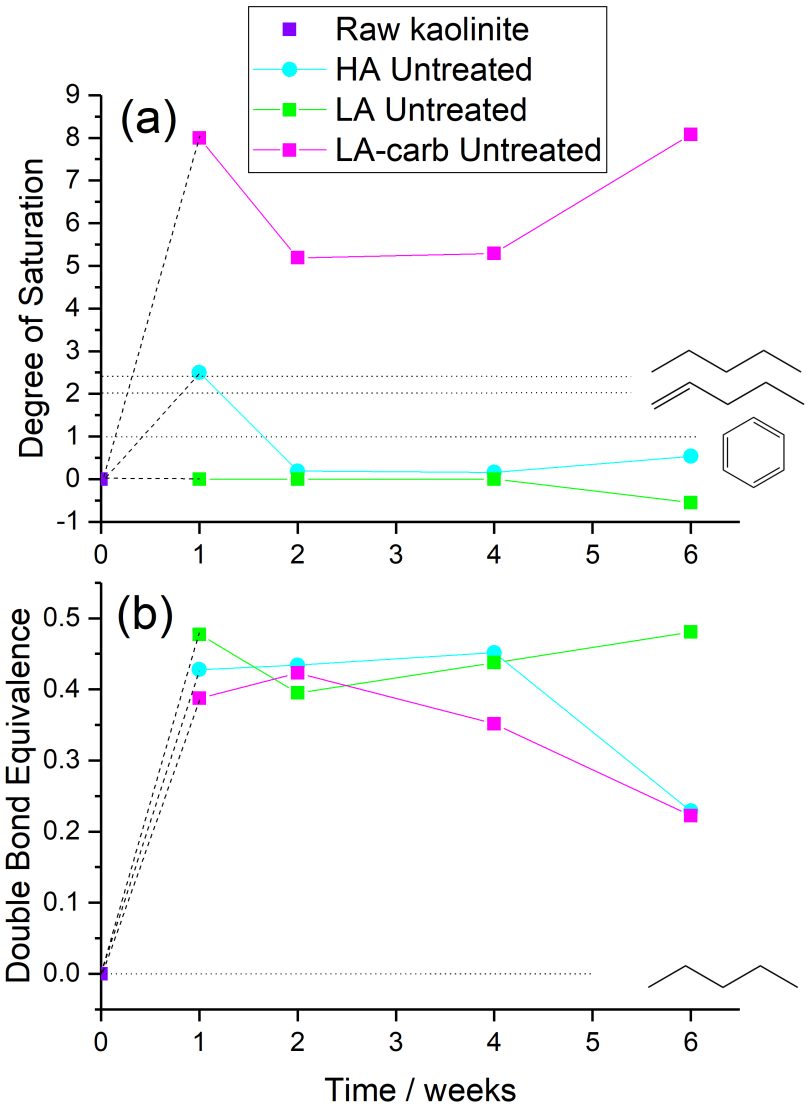

Figure 5.26: (a) Degree of saturation and (b) double bond equivalent of aged kaolinite.

5) Conclusions

For ageing kaolinite in crude oil the following conclusions can be drawn:

- Carbon species adsorb from high asphaltene oil when water is not present.
- Hydrogen levels remain unchanged from the raw kaolinite for all samples apart from at 6 weeks with untreated HA and LA-carb oil and the brine treated LA-carb oil.
- Nitrogen levels spike and 6 and 4 weeks for untreated HA and LA-carb oil respectively.
- Nitrogen levels could be indicative of the adsorption of long chain hydrocarbons to adsorb. Vanadium porphyrins could possibly be adsorbing too.

5.4.5 Ageing Mica

This section summaries the elemental analysis results from the exposure of muscovite mica to the three crude oils of interest, with and without aqueous pretreatment and over an extended ageing period of up to 6 weeks. As outlined in Section 5.3 above, these experiments exposed a powdered substrate to these fluids/pretreatments at 70 °C under nitrogen. The resulting aged solids were separated by filtration and washing with toluene and methanol. The data presented here are the elemental analyses of the aged powdered mica and any adsorbed layer it has gained as part of the ageing process.

1) CHN Analysis of Mica

Very significantly for mica aged in all three oils, with or without pretreatment, no significant amount of carbon or nitrogen are adsorbed (Figure 5.27 (a) and (b)). However, the data show the same amount of hydrogen present in aged mica as present in the starting material (Figure 5.27 (c)). The chemical formula of muscovite mica is $KAl_2(Si_3Al)O_{10}(OH_F)_2$, and therefore should contain 0.5 weight % hydrogen present. However, the elemental analysis shows a value of 0.3 weight %—a drop of 0.2 % hydrogen. The level of ∼0.3 % is maintained for all mica aged in every crude oil, suggesting there is no change to the surface of the mica. This is reinforced by the lack of carbon present which suggests no organic adsorbed.

No degree of saturation values can be calculated as no organic is shown to have adsorbed. All DBE calculations were ∼0.83. However, these are an inaccurate representation because they use a carbon value of 0 and only consider the hydrogen values measured that are from the surface silanol groups.

2) Discussion

Previous work considering organics adsorbing to the mica surface has been via cation bridging of surfactants such as DDAB and CTAB.[49,244] Here the siloxane surface (referred to as the basal plane) is exposed on the outside of a mica sheet where a hydroxyl group protrudes from the octahedral sheet.

The siloxane surface does not bind well to water, so in the absence of charge substitutions, the surface may be considered hydrophobic. However, due to the isomorphic substitutions within the mica structure, the negative charges make it possible to strongly adsorb cations at the surface and polar water molecules. One suggestion for a binding mechanism of crude oil on mica is a layer of brine film

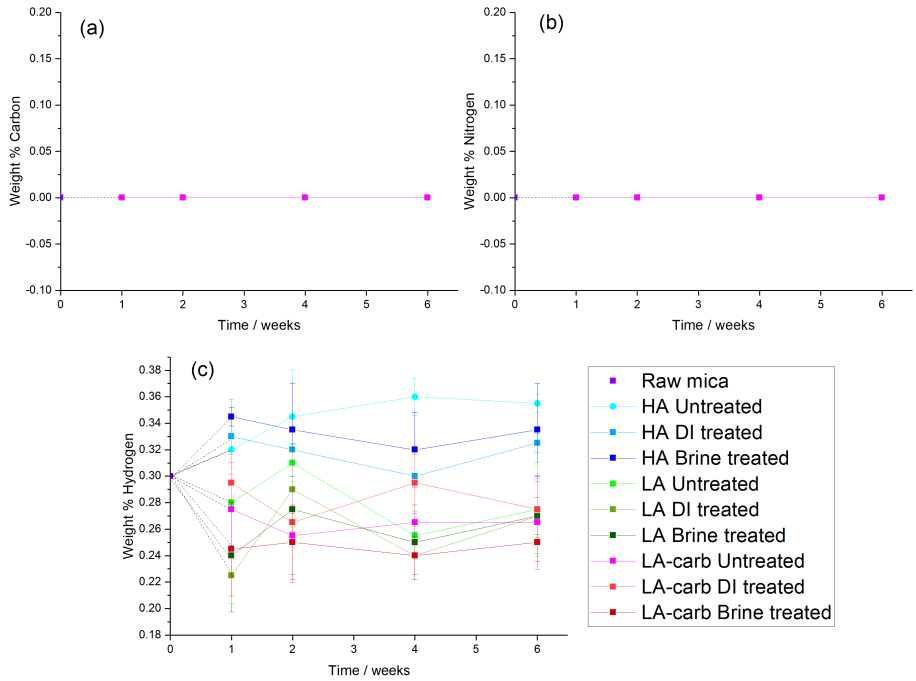

Figure 5.27: Elemental analysis results for (a) carbon, (b) nitrogen and (c) hydrogen on mica in either HA, LA or LA-carb oil. Error shows standard deviation of 2–3 measurements.

forming on top of mica, followed by a layer of organic. This mechanism is similar to a cation-bridging mechanism, except water acts as a bridging species.

It may be possible that a hydrated layer of salt binds to the mica surface preferentially first, before addition of crude oil. This could explain the lack of adsorption of brine treated mica, where there is 0.6 ± 0.1 wt% of water content according to TGA data of mica aged in HA oil. However, there is only 0.1 wt% water content on the untreated mica. This could be enough to cover the basal plane where organics will adsorb.

A further investigation into ageing flat mica discs in crude oil is conducted in Section 6.3.

3) Conclusions

For ageing mica in crude oil the following conclusions can be drawn:

- Interestingly and unexpectedly, no carbon species adsorb after a toluene and methanol wash of the aged substrate, irrespective of no pretreatment or water

pretreatment. Although initially this does not match literature, in the next chapter (Section 6.3.2) this is discussed further and the differences between the toluene and methanol wash on mica are investigated.

- Hydrogen levels remain the same as the raw material, reinforcing the conclusion that no organic adsorbs.
- No nitrogen adsorbs onto mica.

5.4.6 Py-GCMS

HA oil and quartz, calcite, kaolinite and mica aged in HA oil were analysed with Py-GCMS and compared to the reservoir rock Py-GCMS spectra that picked up hydrocarbons, polyaromatics and carbamic acid molecules. The results are shown in Table 5.7. The data show HA oil contains hydrocarbons and polyaromatics, as does calcite. However, no organic fragments were eluted for quartz, kaolinite and mica. This result is expected for mica as there was no carbon detected in the CHN analyses. However, quartz and kaolinite should have peaks corresponded to organics eluted from the sample. One possible reason for lack of organics eluted could be that the fragments adsorbed too strongly to the GC column and were retained. However, upon cleaning the column by heating the system and running a long elution over 3 hours, there were still no peaks evident from eluted compounds, which suggests no fragments from previous runs remained in the column.

Reservoir rock	**HA oil**	**Quartz**	**Calcite**	**Kaolinite**	**Mica**
		All treatements	**All treatements**	**All treatements**	**All treatements**
Hydrocarbons	✓	x	✓	x	x
Polyaromatics	✓	x	✓	x	x
Carbamic acid	x	x	x	x	x

Table 5.7: Py-GCMS of minerals aged in HA oil after 6 weeks with or without pretreatments.

Overall the difficulty in obtaining relevant data suggest Py-GCMS is not the best technique to assess organic adsorption from crude oil onto these mineral surfaces. Given that TGA and elemental analysis data clearly indicates adsorption, it is concluded to be a sensitivity issue.

5.4.7 Removing Bulk Calcite

The previous section considered ageing minerals (quartz, calcite, kaolinite and mica) in three different types of crude oil, with and without water pretreatment with the aim of understanding the differences in organic adsorbed as a function of mineral and condition. One problem with the previous method is the organic layer is swamped by the bulk material; at maximum, the organic layer remaining adsorbed after solvent washing is only around 1.5 wt% of the total material. It would be advantageous to remove the bulk and focus in on the organic layer to characterise the layer in more detail.

It is possible to dissolve away a quartz or calcite substrate: quartz would require a HF treatment and calcite requires a HCl treatment. Due to safety considerations, HF usage was not possible in this study. Therefore, this section considers ageing calcite in crude oil and then dissolving the bulk calcite with the aim of recovering and investigating the organic layer without bulk interference.

Untreated calcite was aged in HA oil for 1 week as this had a 1.2 % carbon result in the CHN analyses earlier.

Experimental Procedure

The ageing procedure is almost the same as above in Section 5.3. The main difference is that the sample is aged for one week and there are further acidification and separation steps as shown in Figure 5.28. This approach follows a method where, after ageing and washing, the sample is sonicated in fresh toluene for 30 minutes before being stirred for 24 hours. [67] The supernatant is extracted and this is referred to as the 'adsorbed asphaltenes'. A combination of THF, choloform and 4M HCl is used in a ratio of 1:1:2 to dissolve calcium carbonate, producing CO_2 and separating aqueous and organic phases. The aqueous phase is separated and the THF and choloform is evaporated, before the remaining solid is redissolved in toluene and the 'irreversibly bound organics' are extracted.

A sample of the 1 week aged calcite was washed using the toluene and methanol washing method in the previous chapter. These samples, which are the CHN compositions of the organic on the rock after the solvent washing, were used for comparison in the results section below.

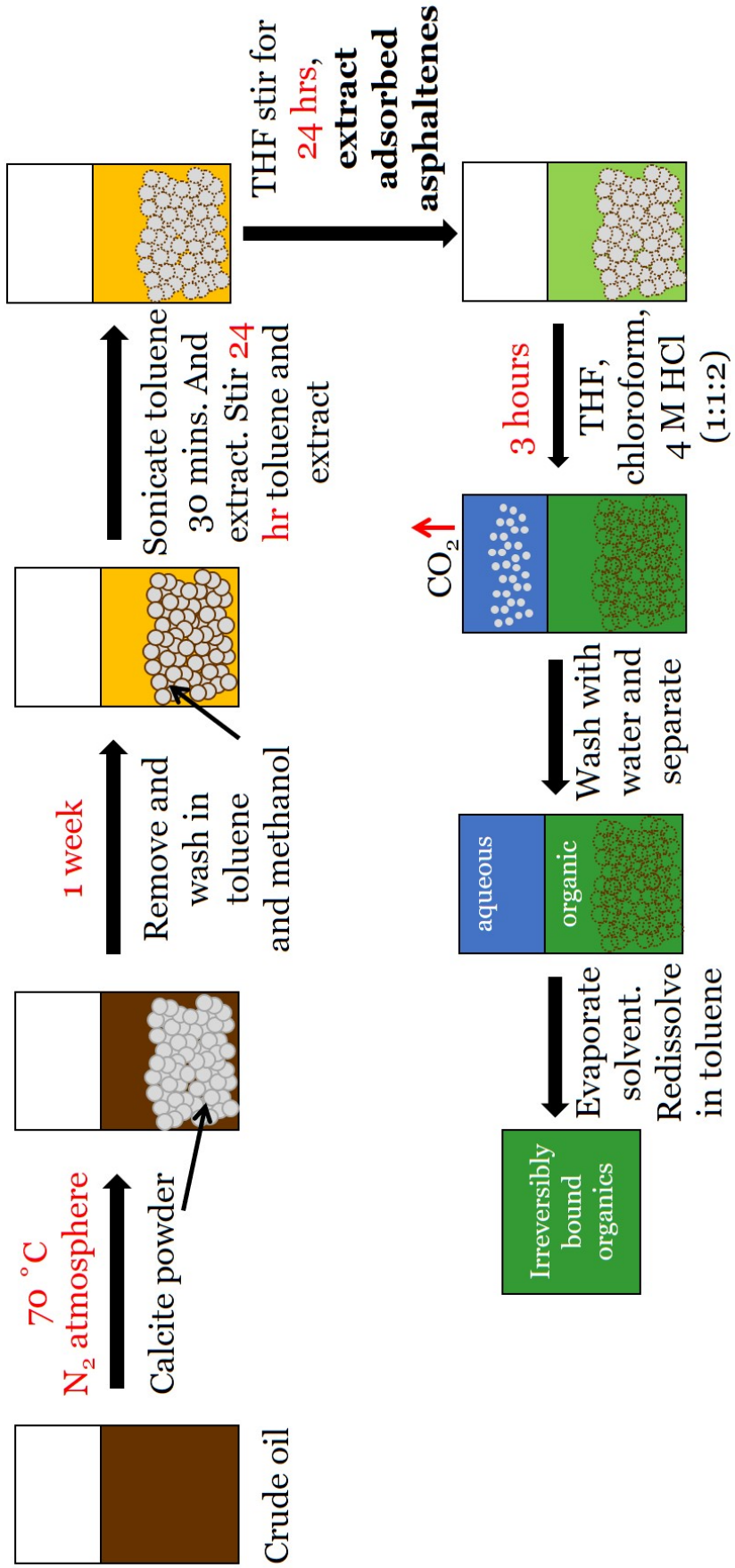

Figure 5.28: Schematic of ageing process with removal of calcite.

Results

1) CHN

Figure 5.29 shows the normalised CHN results for four samples: HA oil, calcite aged for 1 week in HA oil and washed in toluene, calcite aged for 1 week in HA oil and washed in rotation in toluene and methanol and finally the irreversibly bound organics isolated using the method in Figure 5.28. To normalise the data, the percentage of an element (whether C, H or N) was divided by the total sum of the percentage of C, H and N. Aged calcite and irreversibly bound organics have been converted into 'organic carbon' and 'organic hydrogen' values using TGA data as mentioned in Section 5.4.3. The irreversibly bound organics should be compared with the toluene and methanol-washed sample as the irreversibly bound organics have been through a toluene and methanol wash.

The organic carbon and hydrogen content of all samples are similar, with around 85 % carbon and 12 % hydrogen. Regarding nitrogen values, after ageing for 1 week and washing in just toluene, the nitrogen content increases 7 times. Upon a methanol wash nitrogen species are removed, suggesting the nitrogen species are present in a polar molecule form. The most likely reason for not observing any nitrogen in the toluene and methanol washed aged calcite is that the amount present is under the limit of detection for the machine. Interestingly, the irreversibly bound organics show double the relative amount of nitrogen present as in the crude oil starting material. This result is unexpected as nitrogen was not detected in Section 5.4.3 and the calcite surface is thought to be positively charged and would repel any molecules where a nitrogen cation is the point of binding. Therefore, a nitrogen anion would be more expected. These could be in the form of nitrides or, more likely, pyridine-type molecules.[93] The negatively charged nitrogen-containing molecules would preferentially bind to the positive calcite surface and thus be present in the bound layer in a high relative amount than that of the crude oil starting material.

For the irreversibly bound organics raw, none normalised data, just under 38.0 % of the irreversibly bound organics are carbon. Only 41.9 % of the content is accounted for with CHN analysis meaning there is another 58.1 % unaccounted for in the form of other species such as heteroatoms, heavy metal ions and halides.

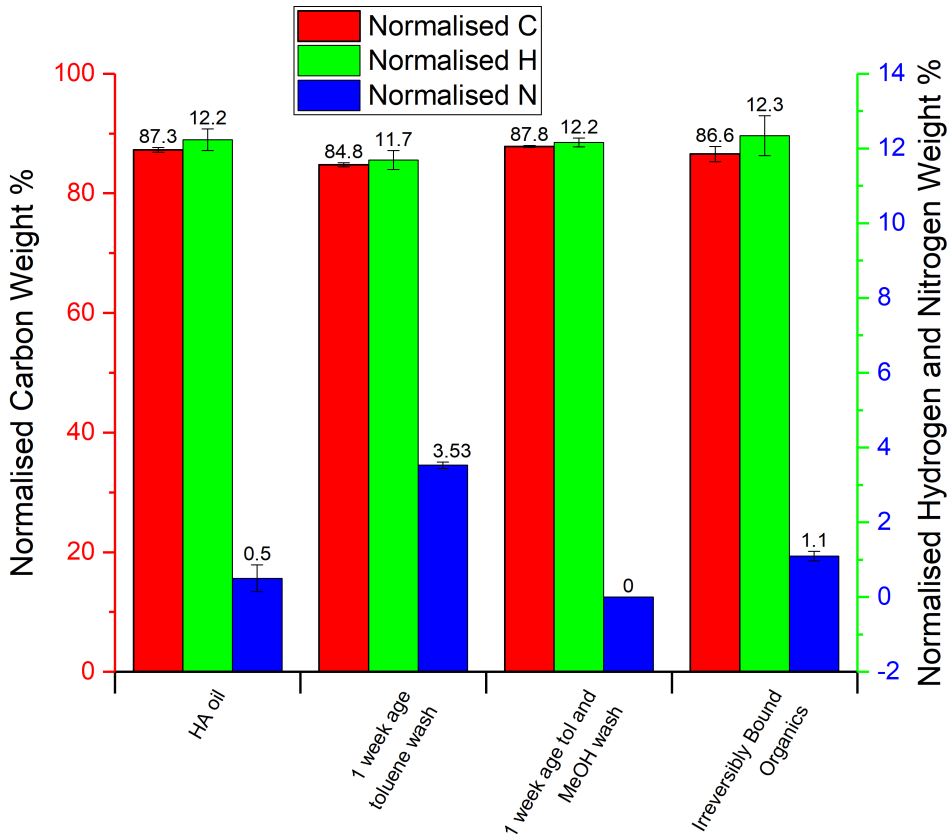

Figure 5.29: CHN results for irreversibly bound organics on calcite. Values for HA oil and particles aged and washed in toluene and methanol are included for comparison.

2) Degree of Saturation and DBE

Figure 5.30 shows the data for degree of saturation and DBE for HA oil, calcite aged for 1 week in HA oil and washed in toluene, calcite aged for 1 week in HA oil and washed in rotation in toluene and methanol and finally the irreversibly bound organics.

Focussing on the oil content, the HA oil begins with a mid-range degree of saturation in the range of cyclohexene and an unsurprisingly high DBE of over 80 due to the complex nature of crude oil containing large amounts of polyaromatics (asphaltenes/resins). After ageing calcite in HA oil for only one week and washing in toluene then methanol the degree of saturation increases (more hydrogen present) suggesting simple, hydrogen saturated, molecules are binding onto the surface. This is reflected in a DBE of 2–3 (cyclohexadienes and benzene rings) that is also expected as simple, small, molecules diffuse through the crude and adsorb initially.

Looking at the composition of the irreversibly bound organics, there is a large drop

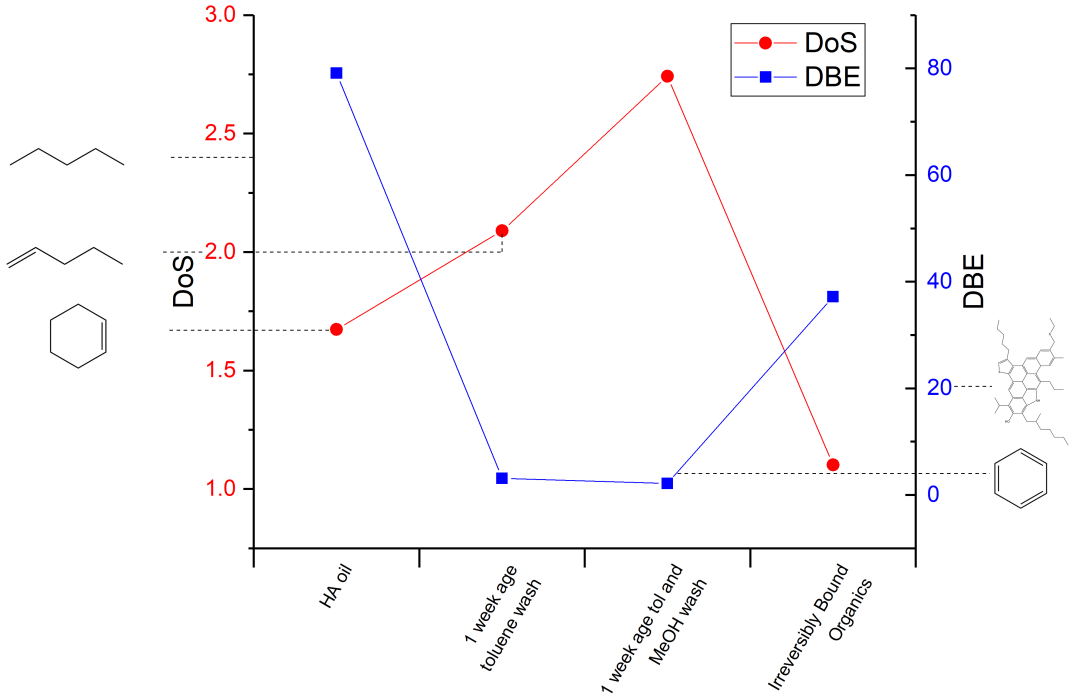

Figure 5.30: Degree of saturation and DBE results for irreversibly bound organics on calcite. Values for HA oil and particles aged and washed in toluene and methanol are included for comparison.

in degree of saturation to ∼1 (corresponding to benzene) that suggests the beginning of more aromatic and large molecules adsorbing. The observation is reinforced by the DBE value increasing to just under 40. This is half the DBE value of the crude oil. However, it suggests there are complex molecules adsorbing. To truly assess which components of the oil have been adsorbed, SARA was conducted on the toluene and methanol washings (after toluene and methanol was evaporated) to confirm species adsorption.

3) SARA analysis

Figure 5.31 shows the data for the SARA content of the toluene and methanol supernatant. The data show asphaltene and aromatics are removed in the toluene and methanol wash when compared to the HA oil. Therefore, asphaltene and aromatics have been adsorbed onto the calcite surface and will be in the irreversibly bound organic layer. The DBE data confirms this finding.

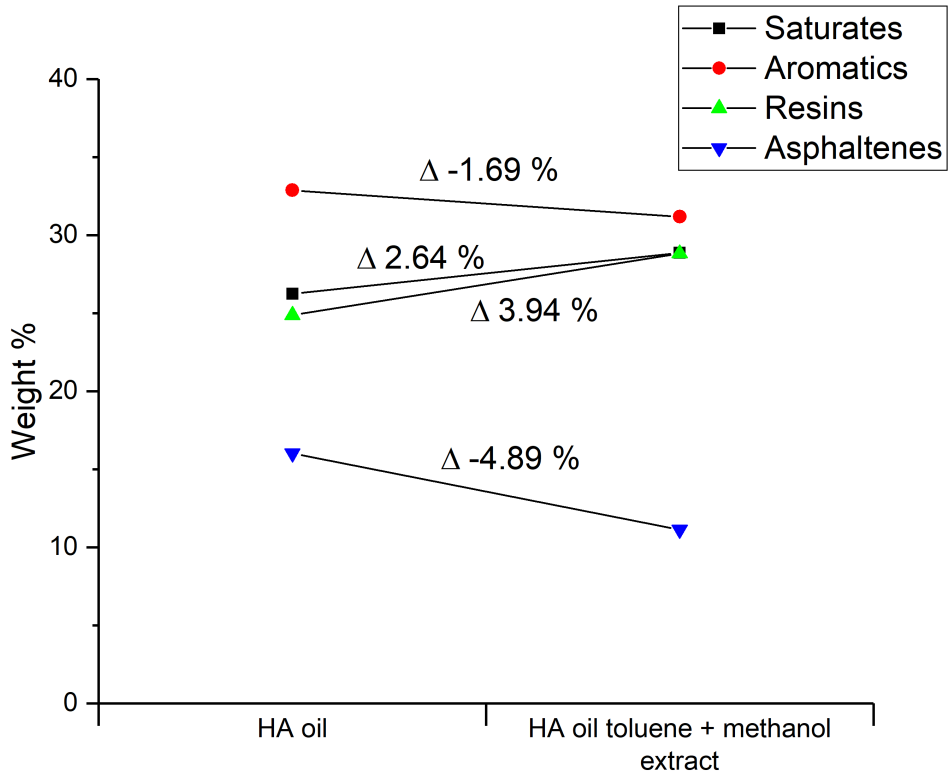

Figure 5.31: SARA results for irreversibly bound organics on calcite compared to HA oil.

Summary

Calcite powder has been aged in HA oil and the irreversibly bound organic layer has been successfully separated from the bulk calcite by dissolution of the mineral. The irreversibly bound layer was found to contain nitrogen of an equal percentage to that of HA oil. Coupling CHN elemental analysis to produce DBE data has shown a large number of double bonds present in the bound organic. This finding is reinforced by SARA analysis suggesting asphaltenes and aromatic species are adsorbing to the calcite surface and are therefore present in the organic layer that was removed.

5.4.8 What if the Oil is not Refreshed?

In-house ageing experiments by BP have suggested weekly removal of aged crude oil and replenishing the system with fresh crude oil during ageing of reservoir and outcrop rock showed results with core flooding responses that correspond to that of the oil well they are trying to replicate.[194] The experiments conducted in Section 5.4 have so far considered ageing particles and refreshing the oil every week. This section discusses CHN results for untreated quartz, calcite, kaolinite and mica powder aged in HA oil after 6 weeks without weekly refreshes of the oil. Data for refreshing the oil and 1 week is included as this is the same quantity of oil the same is exposed to but at a shorter duration. Samples aged in HA oil for 6 weeks is including a refresh of oil is also included for comparison.

Quartz

Figure 5.32 shows the data for untreated quartz aged in HA oil for 6 weeks without refreshing the oil. Data for refreshing the oil is shown for comparison.

Focussing firstly on the CHN data, comparing 6 week with a refresh to 6 week aged without a refresh, there is less adsorbed. For carbon, a loss of 33 %; hydrogen has a loss of 40 % and nitrogen a loss of just 48 %. These results show that species in the oil adsorb and are used up on adsorption. The favourable species continue to adsorb once more are supplied by replenishing the oil with a fresh batch.

When comparing the 6 week aged quartz without an oil refresh to the 1 week aged quarts with an oil refresh, without a refill there is a 50 % increase in carbon, a similar hydrogen loss as above of 38 % and the same 48 % loss of nitrogen as the 6 week aged sample. This suggests that over time, without a refresh of oil, nitrogen containing species are not remaining adsorbed. The loss of hydrogen suggests larger polyaromatic molecules have had time to diffuse through the crude and adsorb. This can be assessed via DoS and DBE below.

Values for DBE stay the same (just under the mono-double bonded alkene range). However, when DoS is taken into consideration, there is a dramatic change as not refreshing the system causes a loss of over a third of hydrogen atoms, moving from a benzene type molecule to a system that contains more hydrogen atoms than carbon atoms, such as fused ring systems. The change in DoS could be due to other species adsorbing that contain hydrogen, such as sulfates and halogen, as opposed to the complex molecules with a polycyclic carbon backbone mentioned previously.

Overall, not refreshing the crude oil when ageing quartz causes a drop in carbon,

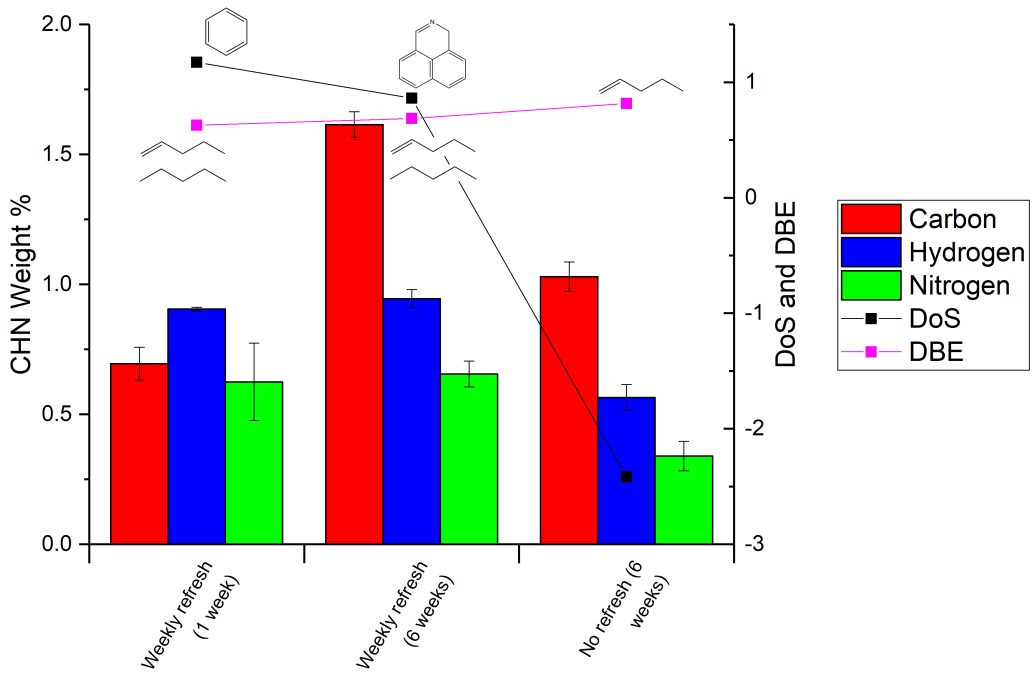

Figure 5.32: CHN, DoS and DBE for aged quartz without an oil refresh. Error shows standard deviation.

hydrogen and nitrogen. DBE remains almost constant.

Calcite

Figure 5.33 shows the data for untreated calcite aged in HA oil for 6 weeks without refreshing the oil. Data for refreshing the oil is shown for comparison.

Focussing firstly on CHN data, a similar trend is seen between the carbon and hydrogen contents as seen in the quartz sample above; when the sample is not refreshed with crude oil weekly, there is a 40 % drop in carbon. There is a total loss of hydrogen, where none is detected. No nitrogen is measured in any of the samples. For calcite, not refreshing the oil yields results closer to only ageing the calcite for 1 week. Similarly to the quartz sample, the lack of carbon adsorbed could be due to a species in the crude oil preferentially adsorbing in the first week and being used up. Replenishing the oil will replenish the favourable carbon species and increase quantity of carbon adsorbed.

For DoS the trend over the weeks of samples with oil refreshed suggests an decrease in saturation, moving from saturated hydrocarbons towards alkenes. A DoS value cannot be calculated for the sample with no oil refresh because there is no measurable hydrogen content. However, we can calculate a DBE: the DBE value for the calcite

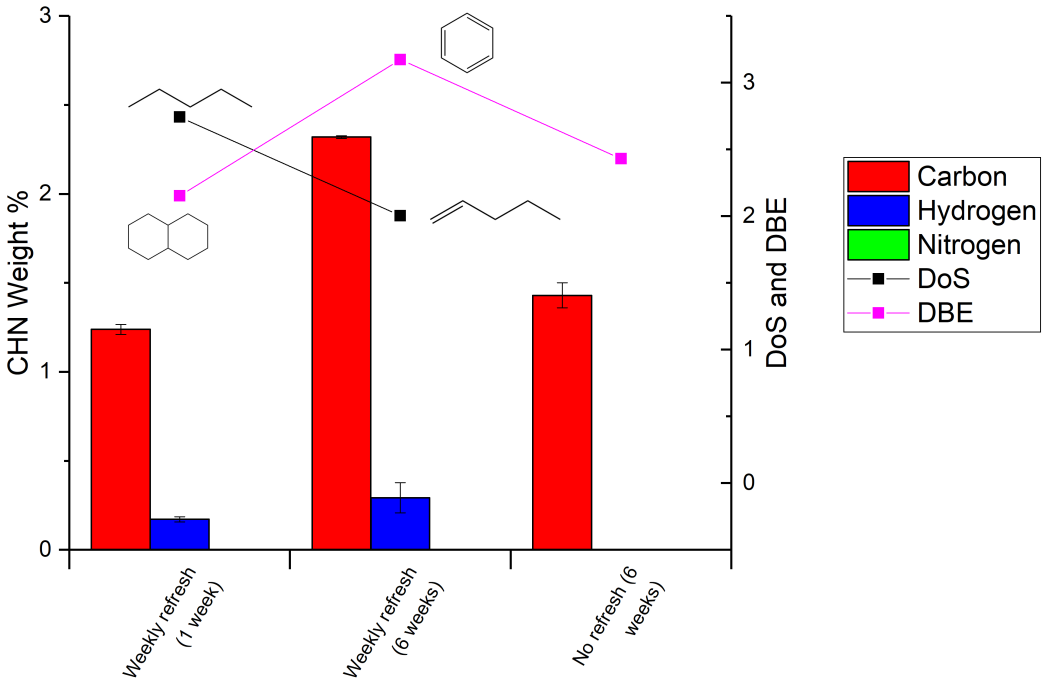

Figure 5.33: CHN, DoS and DBE for aged calcite without an oil refresh. Error shows standard deviation.

without an oil refresh (DBE = 2.5) falls between the values for 1 and 6 week aged samples (DBE = 2 to 3). This is expected as the carbon value falls between week 1 and 6 with a refresh.

Overall, not refreshing the crude oil when ageing calcite causes less carbon to adsorb and hydrogen is no longer in a detectable quantity. There are no changes to values of nitrogen can be concluded from this data.

Kaolinite

Figure 5.34 shows the data for untreated kaolinite aged in HA oil for 6 weeks without refreshing the oil. Data for refreshing the oil is shown for comparison.

CHN data for the non-refreshed sample closely resembles the sample only aged for 1 week. Comparing the 1 week aged kaolinite to the 6 week aged kaolinite without oil refreshing, after 6 weeks there is slightly (0.07 wt %) more carbon and no statistically significant difference in hydrogen values. No nitrogen adsorbs in either.

Continuing to compare the 1 week aged sample to 6 week aged without a refresh, the DBE remains the same, showing a combination of saturated hydrocarbons and alkenes. DoS values for the sample without a refresh is between the 1 to

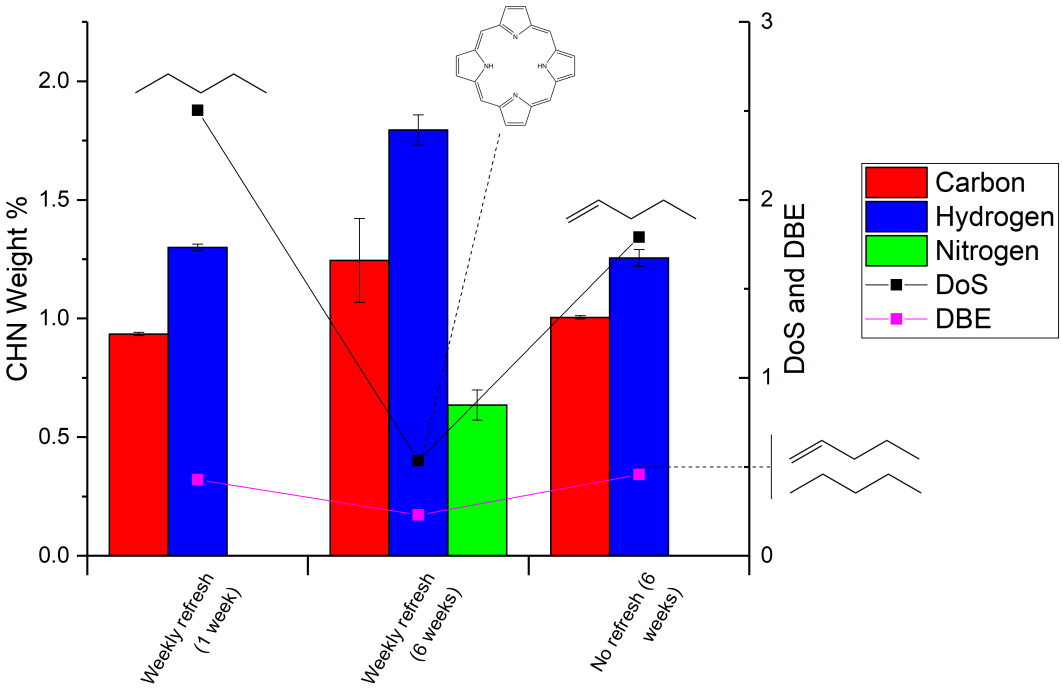

Figure 5.34: CHN, DoS and DBE for aged kaolinite without an oil refresh. Error shows standard deviation.

6 week sample, showing alkenes adsorbing, confirming observations from DBE calculations.

Overall, the data suggest nitrogen species adsorb after refreshes of oil, possibly because they are out-competed by other species. A higher concentration of nitrogen-species present in solution may be required before they adsorb.

Mica

Figure 5.35 shows the data for untreated mica aged in HA oil for 6 weeks without refreshing the oil. Data for refreshing the oil is shown for comparison.

CHN data confirms that carbon and nitrogen are not significantly adsorbed through the ageing process. Hydrogen remains at the same values as the mica starting material, relating to the surface silanol groups.

No degree of saturation values can be calculated as no organic is shown to have adsorbed. DBE cannot be determined as there is no organic hydrogen.

Overall, not refreshing crude oil has no impact on the lack of adsorption observed when ageing mica powder in crude oil.

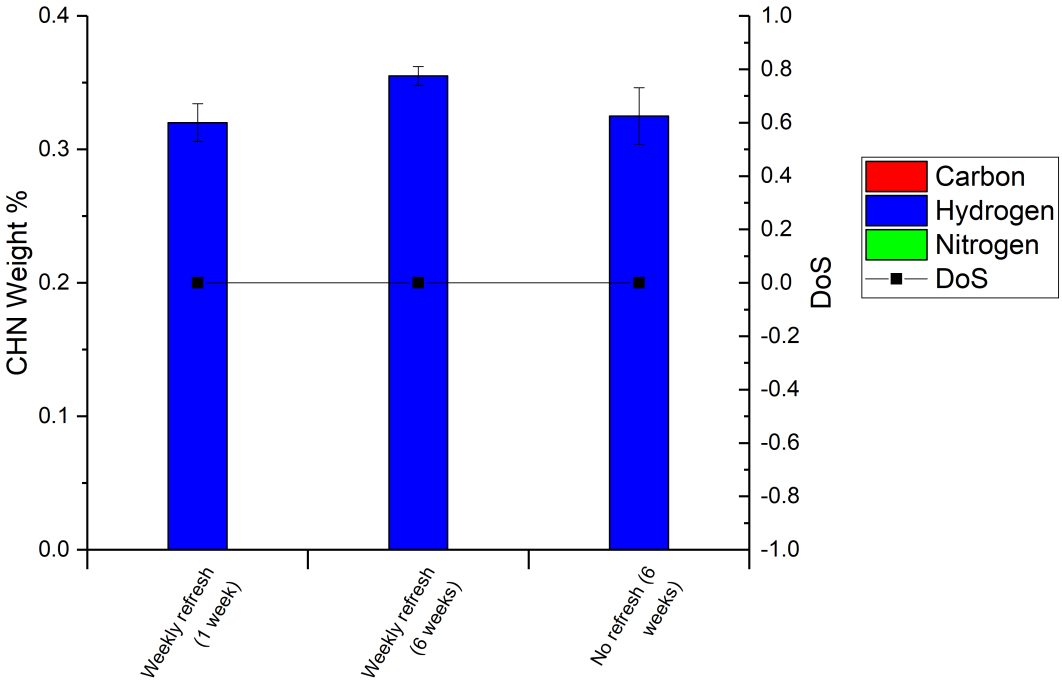

Figure 5.35: CHN and DoS for aged mica without an oil refresh. Error shows standard deviation.

Summary: Ageing Without Refreshing Crude Oil

In general, all substrates show significantly less adsorption of material if the crude oil is not refreshed. This suggests that the crude contains particular species that adsorb and these become sufficiently depleted and that without exchange there is 'none' left. With the exchange of fluids, more of these key components are provided, which can adsorb more.

The trends in unsaturation broadly suggest that where these are clear changes, the DoS is seen to fall without exchange. This suggests that the component that is adsorbing has a high DoS.

5.4.9 Summary: Powder Substrates

The section above has considered four minerals (quartz, calcite, kaolinite and mica) aged in three different types of crude oil, with and without particle pretreatment. The adsorbed materials have been characterised with an extensive series of experimental analysis. Table 5.8 below shows the summary of results from this body of data:

Substrate	Finding
Quartz	• Carbon species adsorb when water is not present • Nitrogen containing species adsorb initially but do not direct adsorption • Degree of saturation suggests aliphatic amines adsorb • More organics adsorb when oil is refreshed with higher DoS • Water (DI or brine) prevent significant amounts of adsorption
Calcite	• Carbon species adsorb when water is not present • Water (DI or brine) prevent significant amounts of adsorption • Asphaltene content of oil is broadly proportional to the amount of organic carbon adsorbed • LA oil leads to maximum adsorption of nitrogen species from oil • DoS suggests small molecules adsorb first; more complex molecules adsorb by 6 weeks • LA-carb oil possibly removes carbonate anion from the calcite surface • More organic species adsorb when oil is replenished, with higher DoS
Kaolinite	• Carbon species adsorb when water is not present, mainly from HA oil • Hydrogen levels remain the same for all kaolinite samples apart from untreated HA and LA-carb and brine treated LA-carb • Nitrogen levels spike at 6 and 4 weeks for untreated HA and LA-carb respectively • Nitrogen levels could be due to adsorption of long chain hydrocarbons • Vanadium porphyrins possibly adsorbing too • Nitrogen species only adsorb when oil is refreshed
Mica	• No carbon or nitrogen adsorbs • Hydrogen levels remain the same as the raw mica, suggesting no surface changes

Table 5.8: Summary of results from aged minerals in crude oils.

5.5 Washburn Method

The work presented in this Section 5.5 was completed as a part of an iCASE placement with BP at their laboratories in Sunbury. Here, the background of low salinity water flooding to enhance oil recovery is discussed before investigating the impact of brine concentration and composition, as well as aged outcrop Berea and Castlegate sandstones with regards to contact angle generated by the Washburn Method.

5.5.1 Washing Aged Outcrop and Reservoir

After a core is aged and oil is extracted, the core is cleaned. The traditional cleaning method used by BP in-house varies depending on whether a reservoir or outcrop is used. For reservoir rocks, a single xylene and methanol wash is used. However, outcrop rocks undergo a rotation of xylene followed by methanol for a total of nine repeats for each solvent. Effluent is collected and analysed if the study requires knowledge of organic loss at each washing stage.

5.5.2 Experimental

Materials

Castlegate outcrop and Berea outcrop rock was obtained from BP. The samples were ground and sieved so that both had a particle diameter of < 300 μm, confirmed by measurements using a Malvern Mastersizer 3000, which showed an average particle size of 296 μm for both samples.

Brines were made up with sodium chloride or calcium chloride dihydrate of varying concentrations (Table 5.9). The same brine used in the study in the above section was produced with sodium chloride, calcium chloride dihydrate, magnesium chloride hexahydrate and potassium chloride in the amount shown in Table 5.3 above. This is used as a standard brine in BP's multitude of reservoir tests

n-Heptane was used as the completely wetting liquid before testing with deionised water (Millipore 15 MΩ.cm) or base oil (Clairsol 370).

Ageing of Castlegate and Berea rock was conducted in a low salinity responsive crude oil and was performed at room temperature and atmospheric pressure. Toluene and methanol were used for washing.

Brine	Density / g cm^{-1}
NaCl 0.01 M	1.0082
NaCl 0.1 M	1.0046
NaCl 1 M	1.0396
$CaCl_2$ 0.01 M	1.0006
$CaCl_2$ 0.1 M	1.0091
$CaCl_2$ 1 M	1.0857
Brine	1.0472

Table 5.9: Brines used in this study and their measured densities.

Method of Ageing

Due to safety requirements associated with xylenes, the washing study below uses toluene instead. The ageing study below concerns the ageing of outcrop rock at room temperature and atmospheric pressure for 1 day or 3 weeks, followed by assessment of contact angle via the Washburn method. Figure 5.36 shows a schematic of the ageing and washing processes. Two different washes were used: a toluene wash (where toluene was run through the sample until it ran clear), or an extended wash (mentioned above, toluene wash followed by methanol wash, repeated nine times).

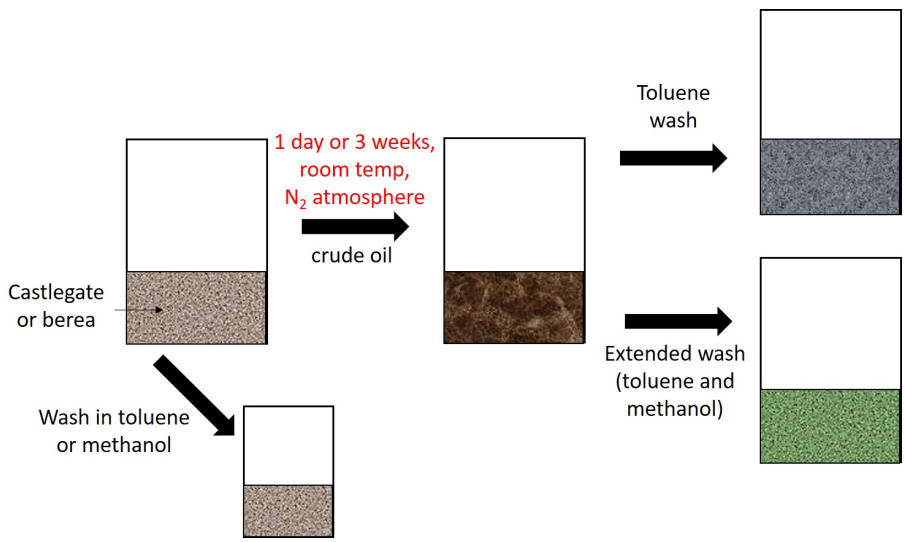

Figure 5.36: Schematic of ageing and washing procedure of Castlegate and Berea.

5.5.3 Reference Compounds

Krüss suggest using Low Iron Sand from Fisher Scientific, which should give a contact angle of 70°as a reference sample with a well known behaviour. Extensive research using aluminium oxide (alumina) powder as a reference compound for Washburn methods has been conducted in previous literature, and shown the contact angle with DI water to range between 64 to 72°.[245–247] For this reason, alumina was also used as a standard.

Figure 5.37 shows the literature and experimental values of the contact angle for low iron sand and alumina powders. Considering low iron sand, there is a 15° (20 %) difference with the experimental value showing the powder to be more wetting. A similar story is seen for alumina: a difference of 20° between literature and experiment values, where experimentally determined value is more wetting. Although the literature utilises the Washburn equation, the method of sample preparation is different to the experimental method conducted in this study due to the nature of different equipment. Literature shows a machine compressed cylinder of powder put in contact with liquid, where as the method in this section uses a hand packed cylinder where the powder is retained in a glass tube before measurement.

Due to the large difference in contact angle of reference compounds between literature and experimental, the precise contact angle values measured cannot be taken to be absolute. The aim of the Washburn method below will be to rank the wettability of samples.

5.5.4 Results

Effect of Brines on Wettability of Castlegate and Berea

Brines of increasing concentration of NaCl or $CaCl_2$ were chosen to assess any changes with mono- or di-valent cations. Figure 5.38 shows the contact angle for Castlegate and Berea as a function of brine concentration. The black bars represent the outcrop rock wettability with DI water. There is a significant difference of 20° between Castlegate and Berea with DI water, where Berea rock is the more hydrophobic surface. Considering Berea, upon addition of salinity, there is limited change in contact angle.

However, Castlegate shows a wider variation and sensitivity to brines than Berea. 1 M NaCl provides a change in contact angle of 8° from DI water, showing the Castlegate is less brine/water wet. Lower concentrations of NaCl do not provide a

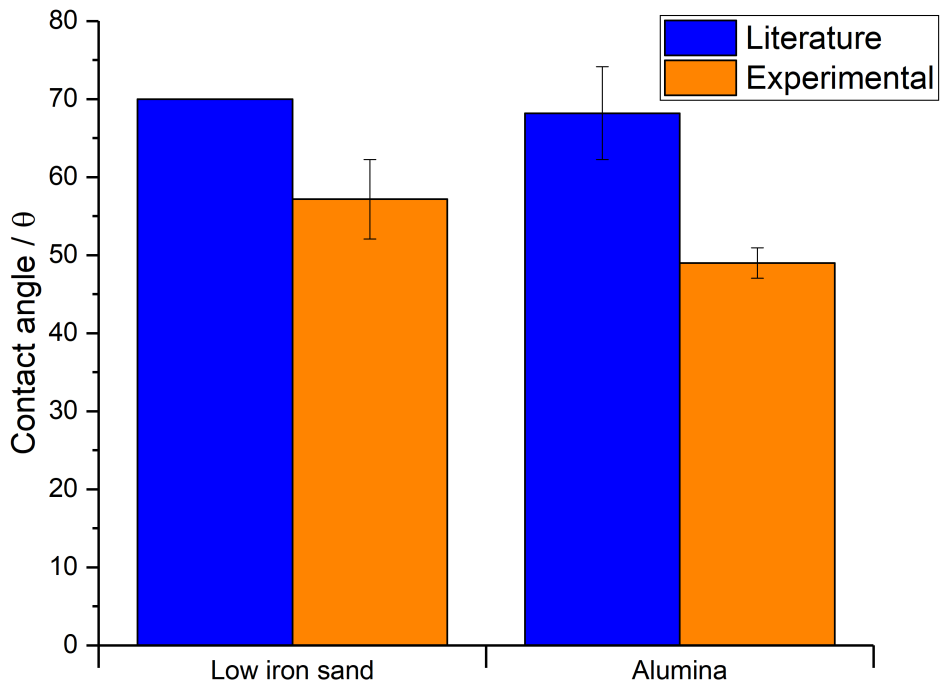

Figure 5.37: Literature and experimental values of contact angle for 'low iron sand' and alumina powder on DI water. No literature error was given for Low Iron Sand. Experimental error bars are standard deviation of five measurements.

significant change. For $CaCl_2$ the data suggest that as $CaCl_2$ concentration increases, the brine wettability decreases. The change in contact angle between DI water and 1 M $CaCl_2$ on Castlegate is 12°.

The brine shows an increase in contact angle that is equivalent to the 1 M concentration of both the monovalent and divalent cation brines. The data suggest there is no difference between mono- or divalent brines on unaged outcrop rock. Considering the trend with concentrations of salt, hydrophobicity increases with increasing concentration of divalent pretreatment. Monovalent pretreatment is less clear but it could be argued there is a general increase in hydrophobicity between 0.01 and 1 M.

BP have reported during core flooding experiments that Castlegate and Berea do behave differently: Castlegate behaves more like reservoir rock, compared to Berea. This can be related to the Washburn experiments where a Castlegate shows a clear sensitivity to brines whereas Berea shows no response. Although both outcrops

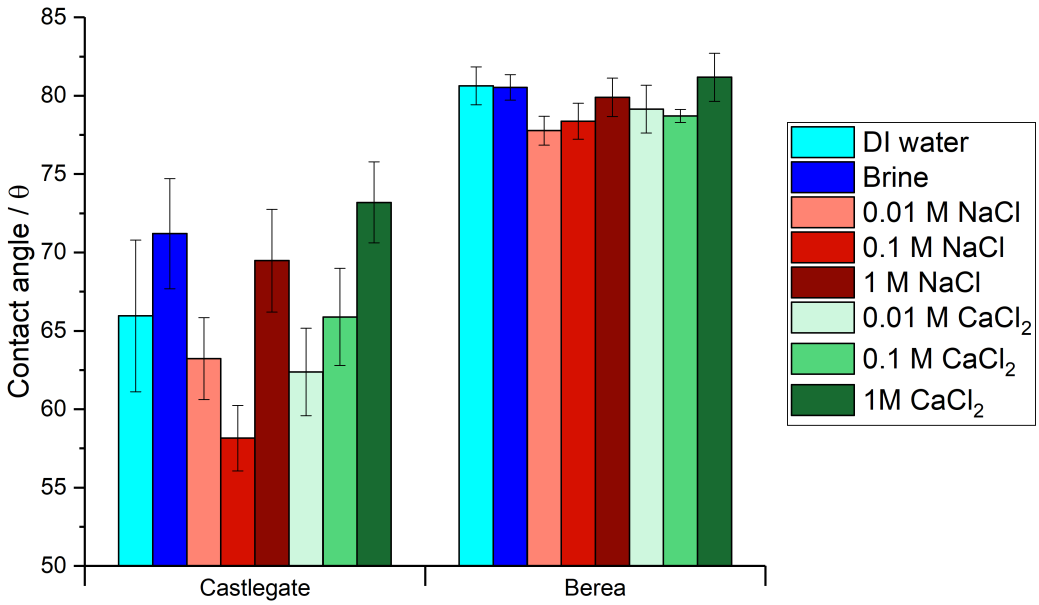

Figure 5.38: Effect of brine concentration on contact angle for Castlegate and Berea. Error is standard deviation of five measurements.

are silica based, the key understanding of what chemical/mineral surface of the substrate is truly in contact with the brines will be the cause of the change in contact angle.

Effect of Washing Procedure on Aged Castlegate and Berea

Figure 5.39 shows the results for ageing of Castlegate and Berea for one day or three weeks, and either having just a toluene wash or an extended wash. The first key feature is the water wettability of both Castlegate and Berea that have been aged for one day and three weeks, but only washed in toluene: the samples became very hydrophobic, and therefore no contact angle was measurable with the Washburn method. This suggests toluene does not completely wash away all organics. The fact that toluene is not a sole factor, and it is the organics from the crude oil causing a change in wettability, is confirmed by the 'CG tol' and 'B tol' which are the outcrops washed in toluene, but not aged. These samples both show that toluene alone does not change the water wettability.

The error in Castlegate is greater than that of Berea contact angles. This could be due to separation of minerals and clays during the methanol wash: it was observed that flakes of clay-like substrate floated to the top of the methanol during washing. This would subsequently cause a sampling issue if the washed samples

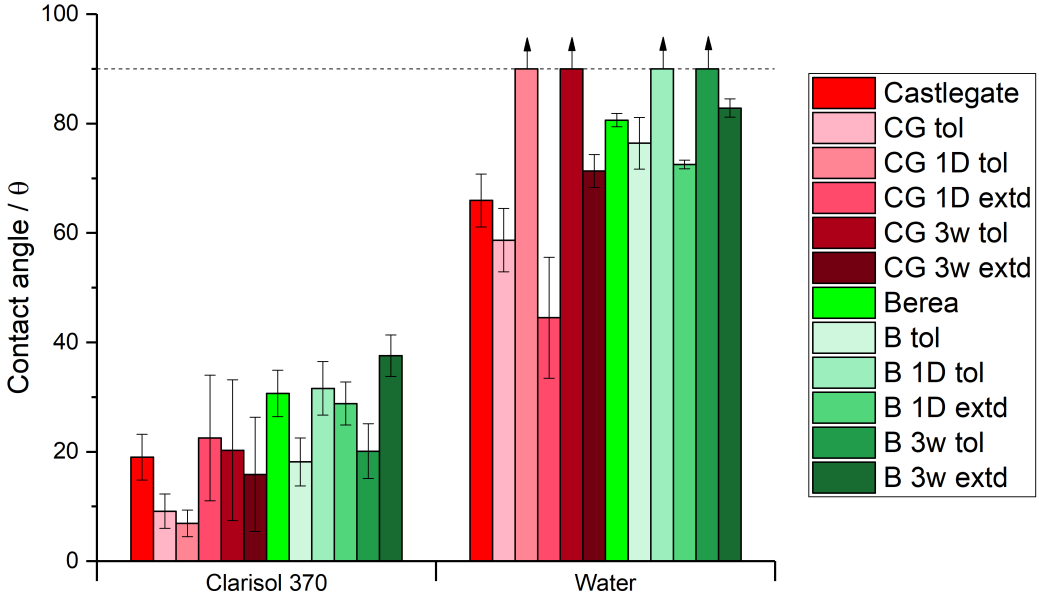

Figure 5.39: Effect of ageing and washing method for Castlegate and Berea on water and oil wettability. Samples aged for one day (1D) or three weeks (3w), and washed with either just toluene (tol) or extended wash (extd). Wettability tested in Clairsol 370 (base oil) or DI water. Errors are standard deviations of five measurements.

were not homogeneous when testing: the packed bed inside the Washburn tube may consist of sections of clay and sections of mineral, resulting in varied rates of liquid uptake.

Focussing on water wettability for extended washes, Berea water wettability increases after a day of ageing and extended wash ($\Delta 10°$), whereas there is no change after ageing Berea for three weeks and an extended wash. For Castlegate extended washes, water wettability shows a similar trend: increasing after one day but decreasing after three weeks. Considering oil wettability, both samples are more oil wet than water wet in all ageing and washing scenarios. Castlegate samples are indistinguishable from each other. Berea samples 'B tol' and 'B 3w tol' samples show an increase in oil wettability, whereas all other Berea samples show no change for oil wettability.

5.5.5 Summary

The Washburn Method has been used to evaluate wettability of Castlegate and Berea pretreated in a range of brines. Overall, Castlegate shows a more hydrophobic surface than Berea when treated with the same brines. For Castlegate, a significant change in contact angle is only observed when the 0.01 and 0.1 M NaCl, 1 M $CaCl_2$

or brine is used. There is no significant change between DI treated Berea and any range of brine pretreatments.

Upon ageing Castlegate and Berea and washing in only toluene, the surface becomes very hydrophobic—implying not all organics are washed off. After a methanol wash, the samples return the starting wettability.

5.6 Conclusions

Four powdered substrates (quartz, calcite, kaolinite and mica) have been investigated after no pretreatment or pretreated in DI or brine, followed by a 6 week ageing process in three different crudes, HA, LA or LA-carb crude oil.

1) Quartz Powder

CHN analysis shows that carbon containing species adsorb onto quartz when water is not initially present. It is possible that some organic species adsorbs, but in quantities too small to measure by CHN analysis. Estimates suggest that this must be less than a third of a molecular layer, or the presence of the adsorbed material would have been evident via carbon analysis.

2) Calcite Powder

The results for calcite powder show that carbon adsorbs when water is not present and adsorbs when the oil is replenished. These data have demonstrated that there is some evidence that asphaltene content of oil is proportional to the organic carbon adsorbed, although this is acknowledged to be a crude approximation. After removing contributions from the carbon content of the bulk calcite with HCl (Section 5.4.7) and assessing the supernatant via SARA, asphaltenes are inferred to be deposited on the calcite surface from the crude oil. The weight % of nitrogen adsorbed from LA oil is approximately the same weight % as in the oil itself. Hence, it cannot be concluded that nitrogen containing species are directly involved in the surface binding, although that is perhaps not surprising given that nitrogen species tend to be cationic and the calcite substrate also tends to be positive at a neutral pH. However, as discussed above, CHN analysis would not be able to detect a layer less than a quarter of a monolayer.

3) Kaolinite Powder

Carbon species are found to adsorb by CHN analyses when water is not present. This is attributed to competitive adsorption of the water for the clay surface. There is some evidence of adsorbed nitrogen species that only adsorb when oil is replenished every week. Nitrogen levels spike at 6 and 4 weeks for HA and LA-carb oils, possibly due to porphyrin molecules adsorbing.

4) Mica Powder

No adsorption of carbon, hydrogen or nitrogen species is observed on mica powder. The lack of observed adsorption could be due to such a small amount adsorbed resulting in below the detection sensitivity of the methods.

5) Wettability of Real Powdered Rock

Powdered Berea and Castlegate rock was crushed and characterised with the Washburn method to measure the contact angle. Overall, Castlegate shows a more hydrophobic surface than Berea when treated with the same brines.

Upon ageing Castlegate and Berea in crude oil and washing in only toluene, the contact angle goes above 90°, rendering a very hydrophobic surface, suggesting not all organic matter is washed off/removed. After a methanol wash, the samples return to the starting wettability, suggesting that all the adsorbed organics have been removed. These data support observations seen in the studies of the individual minerals where a methanol wash also returns most crude oil aged silicon wafers and mica discs to the contact angle of the starting material, discussed in Chapter 6.

5.7 Future Work

In Chapter 5, the ageing process of model minerals with and without pretreatments was investigated. The aim of the chapter was identify where the crude oils deposit organics on the minerals and to characterise the adsorbed organics on these mineral surfaces with regards to chemistry present in the crude oils and expressed in terms of contact angle/wettability, which is used commercially to infer the extent of oil recovery. In particular, the ageing process is used to try and convert readily accessible outcrop rock/minerals and convert the surface chemistry to be more characteristic of a reservoir rock, that is usually prohibitively expensive to obtain. In this way, representative rock samples are available to test various enhanced oil recovery additives and water chemistries, particularly the roll of ions and brines.

1) Wettability of Two or More Minerals

As discussed and investigated in Chapter 4, specifically Section 4.3, natural rocks are a complex combinations of minerals. As only individual model minerals were considered in Chapter 5, it would be advantageous to begin to mix known quantities of ideal minerals and age them in crude oil, analysing the amount adsorbed by CHN, to see if the binary mixtures can be considered as a liner sum of the two components. Regarding the wettability assessment of a mixture of minerals, two approaches could be taken to generate substrates for assessment:

- Washburn method of a mixture of aged minerals.
- Spin-coat the mixture of minerals onto a glass slide or press minerals into a disc, age in crude oil, and measure the two-phase contact angle.

2) Re-ageing of Reservoir Rock

Reservoir and outcrop rocks that have been previously used for studies are reused for ageing. It is believed toluene and methanol washing procedures completely clean the substrates, meaning all organics on the surface are removed. However, this study has proved this to be untrue: a significant amount of organic species remains adsorbed in some cases. It would be interesting to age the reservoir rock in crude oil for a duration, wash in toluene and methanol, and measure chemistries and wettability present, then re-age again and repeat to see how much fluctuation in the surface layer occurs with regards to amount of organic adsorbed and wettability. This would allow an expected lifetime of a rock for ageing to be determined.

Chapter 6

Understanding the Ageing Process: Flat Substrates

6.1 Background

This section summarises contact angle results from the exposure of silicon wafers or mica discs to the three crude oils, with and without aqueous pretreatment and over an extended ageing period of up to 6 weeks. As outlined in Section 5.3 above, these experiments were performed at 70 °C under nitrogen. The resulting aged flat substrates were separated from the crude oil and washed with toluene and methanol prior to the contact angle investigation.

Flat substrates are used because they allow analysis via sessile drop contact angle and more modern techniques such as SFG, where powdered materials are inherently more difficult to analyse.

6.2 Silicon wafers

This section considers silicon wafers aged in HA, LA or LA-carb oil with or without DI or brine pretreatment that are assessed via DSA to measure contact angle wettability.

6.2.1 DSA

The data presented here are the two-phase contact angle of water (18.2 MΩ.cm) on the aged flat silicon and any adsorbed layer it has gained as part of the ageing process.

As usual, the silicon surface will have a small layer of native silicon dioxide and it is this silicon dioxide layer that any organics will adsorb onto.

1) Bare Silicon Wafer

The contact angle was measured of pure water on the bare silicon wafer. The silicon wafer underwent cleaning prior to ageing. The wafers were cut into squares (1.5 cm by 1.5 cm) with a diamond pen and soaked in nitric acid (70 %, 2 hours) after which they are rinsed in ultrapure (18.2 MΩ.cm) water and dried by nitrogen. Finally, the silicon wafers are exposed to UV-ozone for 15 minutes. The wafers are loaded into the bottles for ageing immediately after cleaning.

For the bare substrate, the impact of cleaning regimes on the contact angle was measured in three scenarios:

1. Silicon wafer after acid wash
   (a) Bare substrate immediately after acid wash
   (b) Bare substrate after acid and toluene wash
   (c) Bare substrate after acid, toluene and methanol wash
2. Silicon wafer after UV-ozone
   (a) Bare substrate immediately after UV-ozone
   (b) Bare substrate after UV-ozone and toluene wash
   (c) Bare substrate after UV-ozone, toluene and methanol wash
3. Silicon wafer after UV-ozone and acid wash
   (a) Bare substrate immediately after UV-ozone and acid wash
   (b) Bare substrate after UV-ozone, acid and toluene wash
   (c) Bare substrate after UV-ozone, acid, toluene and methanol wash

Measuring the contact angle under each three scenarios above allows analysis of how the cleaning procedures affect the bare substrate and subsequent washing procedures affect the contact angle. Figure 6.1 shows the contact angle data for the three scenarios and cleaning regimes. The data for acid wash only (red) show a contact angle of ∼50° and, interestingly, no statistically significant deviation between contact angle after acid wash and subsequent toluene and methanol washes. This might

be unexpected: the acid might have been expected to give a low contact angle (approximately zero), but is higher. This is discussed further below.

After only a UV-ozone treatment on the bare silicon wafer (Figure 6.1 (white)), the contact angle is dramatically reduced, resulting in a hydrophilic surface that was unmeasurable via DSA. This is complete wetting such that water spreads across the surface. Again, no statistical deviation is observed between this UV only treated sample and those after toluene and methanol washes.

Combining the acid wash and a UV-ozone treatment (Figure 6.1 (purple)) increases the contact angle very slightly to just over 4°. This could be due to the presence of residual surface siloxane bonds mentioned in the paragraph below. Again, no statistical deviation between toluene and methanol washes is observed.

The contact angle displayed by the acid wash only data (red) is the most hydrophobic out of all three scenarios considered. Wettability of a solid surface depends on surface free energy—which influences attractive forces between a liquid and solid—and surface morphology. Assuming a surface layer of silicon dioxide with hydroxyl groups present on the surface, these surface hydroxyl groups cause the surface to be hydrophilic. Nitric acid is an oxidising agent and would possibly cause siloxane bonds to form via the release of surface hydrogen in the form of water. The presence of siloxane bonds makes the surface hydrophobic.[121,248]

For the subsequent measurements, silicon wafers were initially pre-cleaned by a wash in nitric acid followed by a rinse with copious DI water and a 15 minute UV-ozone treatment. Therefore the starting contact angle is 4.2°(Figure 6.1 purple) and is displayed as a pink starting point in the contact angle graphs below. The clean silicon wafers underwent a pretreatment and age in crude oil.

2) HA oil

Figure 6.2 (a) shows the contact angle data for silicon wafers aged in HA oil with no pretreatment (left), DI pretreatment (middle) and brine pretreatment (right). The oil was removed and replenished after each week. The error shows the standard deviation of three runs. The bare silicon wafer (acid and UV-ozone) contact angle is included in each graph (pink) for comparison.

2.1) Untreated Substrate

The left-hand graph in Figure 6.2 (a) shows the untreated substrate contact angle. After just a toluene wash, the contact angle stays around 90° for the duration of the ageing. After a methanol wash, the contact angle for the first week of ageing is not

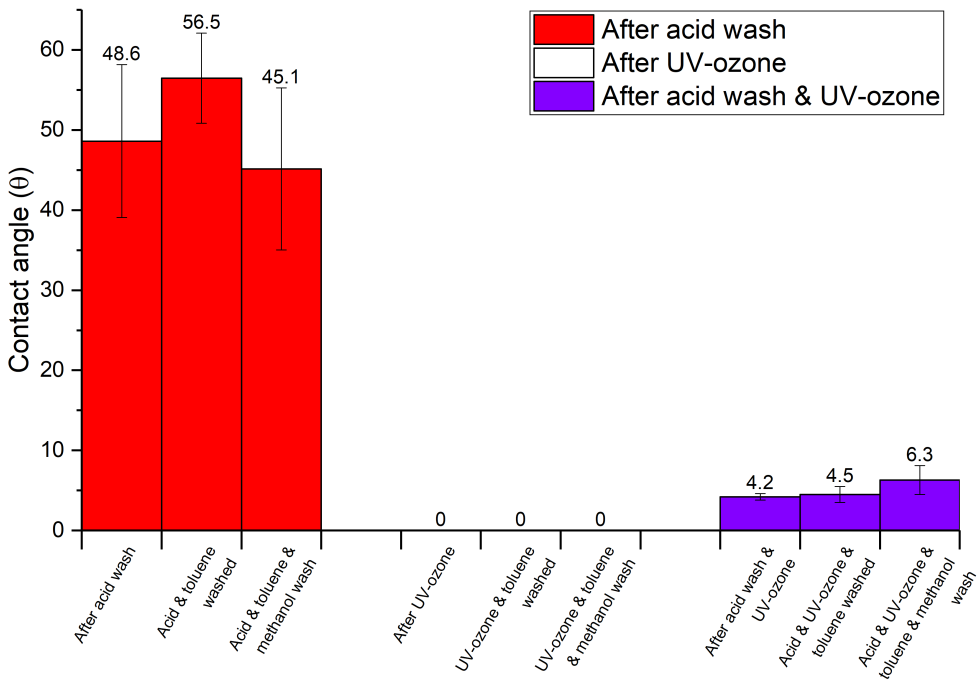

Figure 6.1: Contact angle measurements of bare silicon wafer after cleaning regimes: acid wash (red), UV-ozone (white) and acid wash with UV-ozone (purple). Error shows standard deviation of three measurements.

statistically different from the toluene wash. However, after a methanol wash, weeks 2, 4 and 6 show a loss of 18, 15 and 11° respectively. The data show a methanol wash increases hydrophilicity, suggesting the molecules lost in the methanol wash are hydrophobic, or some methanol is incorporated in the surface layer and the OH groups impart some hydrophilicity.

The contact angle data imply organic had adsorbed and is not washed off, resulting in a contact angle greater than the bare surface. A similar conclusion is drawn with CHN elemental analyses data as it shows 1.5 % carbon adsorbing onto the quartz surface.

2.2) DI treated Substrate

The middle graph in Figure 6.2 (a) shows the DI treated substrate contact angle. After just a toluene wash, the contact angle stays around 95° for the duration of the ageing, which is comparable to but slightly more hydrophobic than the untreated substrate. Upon a methanol wash, the contact angle is again lower (more hydrophilic) by 10 and 15° for 1 and 2 weeks respectively. However, there is no statistically significant difference between weeks 4 and 6 toluene wash and the methanol wash.

The data suggest some molecules bind to silicon dioxide and alter the wettability. Interestingly, these are not inhibited by DI water—the wettability altering molecules adsorb immediately and remain adsorbed. If DI water inhibited the binding of the wettability-altering molecules, the graph would show a contact angle remaining the same as the bare silicon wafer. However, this is not the case.

The contact angle data implies organic has adsorbed and is not washed off. However, CHN analysis suggests all organic is removed (Figure 5.7). This suggests that a small layer, which is less than a third of a uniform monolayer is adsorbed and undetectable via CHN analysis, which alters wettability.

2.3) Brine treated Substrate

The right-hand graph in Figure 6.2 (a) shows the brine treated substrate contact angle. After a toluene wash, a similar trend is seen as observed in the previous HA aged samples: a contact angle of ∼90° is maintained for the duration of ageing. After a methanol wash, the contact angle is once again reduced, but this time more significantly lower: from 60° after one week and to 70° at week 4 where the contact angle plateaus at 70°.

The data suggest that brine does not inhibit adsorption of wettability altering molecules and that methanol removes some molecules that make silicon wafers more

hydrophobic or adsorbs to reduce the contact angle.

Comparing to CHN data, a similar story is seen as observed in the DI treated sample: CHN data does not detect any organic adsorbing, yet contact angle data suggest organic species are adsorbing. This suggests a sub-monolayer may be present to alter wettability.

Overall, HA oil with or without pretreatment increases the hydrophobicity of silicon wafers after one week. Interestingly, DI and brine pretreatments do not inhibit adsorption of wettability altering chemistry. The methanol wash reduces hydrophobicity. However, chemistry is still present as the contact angle remains significantly higher than the starting material.

The DSA results are interesting when compared to the elemental analysis above. The DSA data indicates species adsorbing, resulting in a large change in contact angle. However, in contrast, the CHN analyses did not show evidence of organics adsorbing. The differences are attributed to the sensitivities of the methods. As noted above, in many cases, there was evidence of very significant amounts of adsorbed organic readily detectable by the CHN. However, several samples did show some evidence of small levels of adsorption. These were comparable to the experimental uncertainty. Estimates based on the quantitative amounts adsorbed mean that a third of a monolayer worth of organics can be identified using CHN. There is less confidence with identifying a smaller amount. Hence, the amount of organic that leads to the changes in contact angle cannot be thicker than a molecular layer and is most likely less than a third of a monolayer (0.5 wt % carbon). If it were greater than a third of a monolayer, it would be observed in the carbon analysis data.

This is a very interesting observation and implies that even fractional coverage of a mineral surface can have a profound impact on the wettability as determined by contact angle measurements.

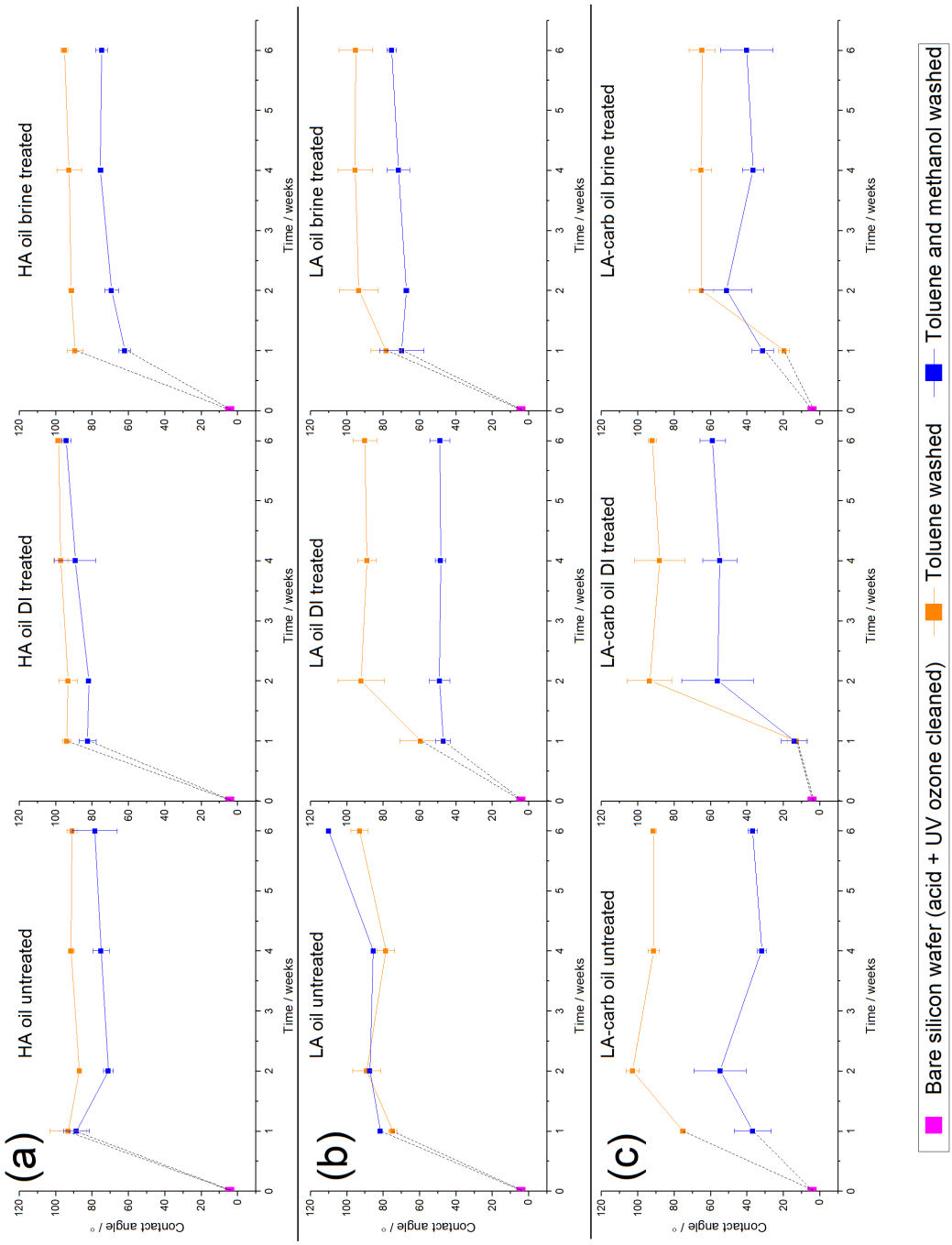

Figure 6.2: Contact angle of aged silicon wafers in (a) HA (b) LA or (c) LA-carb oil with or without pretreatment. Error shows standard deviation of three repeats. Dotted lines are to guide the eye from the starting substrate.

3) LA oil

Figure 6.2 (b) shows the contact angles of silicon wafers aged in LA oil with no pre-treatment, DI water, or brine each week over a 6 week ageing period. The oil was removed and replenished after each week. The error shows the standard deviation of three runs. The contact angle of water on the bare silicon wafer is included in each graph for comparison.

3.1) Untreated Substrate

The left-hand graph in Figure 6.2 (b) shows the untreated substrate contact angle. After a toluene wash, the contact angle fluctuates between 75–90° over the 6 week ageing period. This is a similar contact angle to that measured for the silicon wafer aged in HA oil. Interestingly, after a methanol wash, the contact angle remains the same as the toluene washed sample. There is some evidence of a significant increase to ∼110° at 6 weeks. However, this is only a single data point and interpretation of its significance should be approached with caution. The data suggest wettability altering molecules adsorb initially and are not washed off with toluene or methanol.

3.2. DI treated substrate Data for the DI treated substrate (Figure 6.2 (b) middle) show the contact angle is initially approximately 90° with the toluene wash, comparable to the untreated system. Interestingly, it takes two weeks to reach this value. All other samples discussed so far attained the long term value within one week. Interestingly, after a methanol wash, the contact angle halves, suggesting a very significant reduction in adsorbed organic species. This behaviour can be compared to the elemental analysis data, where it must be recalled that the data was collected after washing with both toluene and methanol. Hence, based on the contact angle data, a significant amount of organic would be expected on the surface if only a toluene wash was used. The contact angle after both toluene and methanol would suggest less organic adsorbed. This would be reflected in only small amounts evident in the CHN elemental analysis. This is in reasonable agreement with the CHN data where there was a lack of carbon or only small amounts adsorbed on quartz particles pretreated in DI water. Hence, concluding again that the amount of carbon adsorbed is too small to measure by CHN analyses, but is enough to cause contact angle changes.

3.3. Brine treated substrate Data for the brine treated substrate (Figure 6.2 (b) right) show the contact angle to be in the range 70–80° throughout the 6 week ageing and the difference between toluene washed or toluene and methanol washed is similar to the error of the measurements. The fact that a level of hydrophobicity—above

the starting material level—is retained is supported by the CHN data: we see a very small (0.2 %) increase in carbon content. Some organics remain adsorbed after solvent washing. The data show that brine does not inhibit adsorption of a small level of organics.

Overall, LA oil increases hydrophobicity of silicon wafers after one week. DI and brine pretreatments do not inhibit adsorption of wettability altering chemicals. The methanol wash can reduce hydrophobicity, presumably by removing some species, not soluble in toluene. However, it can be concluded that some organics are still present as the contact angle remains significantly higher than the starting material. It could be argued that LA oil may have less organic material adsorbed compared to HA oil due to a lower contact angle in LA oil after the methanol wash, although the amount and the chemical nature of the species may also account for these changes.

4) LA-carb oil

Figure 6.2 (c) shows the contact angles of silicon wafers aged in LA-carb oil 7 with no pre-treatment, DI water, or brine each week over a 6 week ageing period. The oil was removed and replenished after each week. The error shows the standard deviation of three runs. The contact angle of water on the bare silicon wafer is included in each graph for comparison.

4.1) Untreated Substrate

The data for untreated substrate aged in LA-carb oil (Figure 6.2 (c) left) after a toluene wash show a contact angle of $\sim 70°$ for most of the duration of ageing (although, noting again the adsorption does not appear to be complete within one week). After a methanol wash the substrate becomes significantly more hydrophilic with a contact angle 40° lower than untreated HA and LA oil samples. The data for untreated quartz powder aged in LA-carb oil showed carbon and nitrogen content remains after the toluene and methanol wash. Linking this to the contact angle data, the type of molecules that adsorb from LA-carb oil on untreated quartz can be assumed to promote hydrophobicity and possibly contain nitrogen cations (to adsorb to the negative silica surface).

4.2. DI treated substrate

The DI treated substrate data (Figure 6.2 (c) middle) show interesting results: the contact angle after 1 week is increased to $\sim 12°$ for both toluene and methanol washed samples and only after two weeks does a long term, stable contact angle appear. The delay in increase could be linked to the change in adsorbed content in the previous

chapter (Section 5.4.2, Figure 5.11) as there is a rise at week 2 for carbon content that could be the hydrophobic molecules adsorbing.

The increase in the contact angle suggests hydrophobic species are initially adsorbing. Interestingly, a significant drop in contact angle (40°) occurs after the methanol wash. The CHN data for DI pretreated quartz aged in LA-carb oil (washed in toluene and methanol) suggest no/very little organic species have bound. This is broadly in agreement here, where more organic adsorbed, some of which was washed off by toluene, but more by methanol, such that the small amount remaining was not enough to detect by CHN analyses.

4.3. Brine treated substrate

The brine treated substrate (Figure 6.2 (c) right) show contact angles smaller than all the previous results, except the bare substrate. The toluene washed contact angle is plateauing at ∼60° and the methanol washed sample at 30°. Both remain the same contact angle after 4 weeks of the ageing process and take two weeks to reach a stable value.The CHN data show no detectable level of carbon adsorbing, which is reconciled by suggesting small patches of organic that are not detected by CHN analysis that adsorb, but these patches are present on silicon wafers and change the contact angle.

5) Conclusions

- Ageing the silicon substrates in these crude oils results in very significant increases in contact angle, suggesting the adsorption of hydrophobic species. For most cases this occurs within the shortest time period investigated (1 week). However, some samples take two weeks. This is interesting as one might expect small molecules to adsorb quickly and easily complete in one week. Hence, this suggests some more complex behaviour such as slow adsorption of larger molecules, possibly asphaltenes, or displacement of one species for another.
- Washing crude oil aged silicon wafers in toluene and methanol makes the surface relatively less hydrophobic compared to washing the aged substrate in only toluene. This is attributed to removal of hydrophobic components and retention of more hydrophilic methanol at the surface, or competitive exchange of methanol for the initially adsorbed species. The removal of hydrophobic species by the very hydrophilic methanol may be unexpected. However, it is reasonably well known that alcohols and water can effectively outcompete some additives for mineral surfaces

- HA oil makes silicon wafers hydrophobic. A DI or brine pretreatment does not reduce or inhibit wettability altering molecules from adsorbing. This contradicts Section 5.4.2 on aged quartz powder where DI and brine is shown to inhibit adsorption of carbon species.
- The untreated silicon wafer aged in LA or LA-carb oil shows $\sim 10°$ lower wettability compared to untreated HA oil aged silicon wafers. This result correlates with Section 5.4.2, where a lower amount of organic adsorbs onto quartz powder from LA or LA-carb oil compared to HA oil. This could suggest amount adsorbed is proportional to contact angle.
- DI and brine treated silicon wafers aged in LA-carb oil result in a more hydrophilic system than the counterpart silicon wafers aged in HA or LA oil.
- DSA confirms surface chemistry is altered for the silicon/silica surface to a greater or lesser extent for all crude oils. However, the amount of species adsorbed are too small to be confidently measured by CHN analyses. Although, some modest variations in the CHN data were evident above, but these could not be confidently assigned.

6.3 Mica Discs

This section considers adsorption onto the large flat surfaces of mica discs aged in HA, LA or LA-carb oil with or without DI or brine pretreatment. As a powder cannot be used to measure contact angle, a flat substrate must be used. Similar signals of noise and no clear signals were observed with SFG of flat mica as mentioned above with silicon wafers. The data is not presented here.

6.3.1 DSA

The data presented here is the two-phase contact angle of water on the aged flat mica discs and any adsorbed layer it has gained as part of the ageing process.

1) Bare Mica Disc

Bare mica discs were used as received. Ideally, freshly cleaved mica would be used in the experiment. However, the cleaving method uses sellotape that may introduce contamination on one side of the mica disc and thus adds another variable at the interface that may affect the binding of organic species. Therefore, cleaved mica was not used in the ageing process. Comparison of the contact angle between mica as received and the cleaved mica followed by a wash in toluene and then a methanol wash is conducted to assess the bare mica starting material. The following is analysed in the section below:

1. Mica disc as received
   (a) Bare substrate as received
   (b) Bare substrate after toluene wash
   (c) Bare substrate after toluene and methanol wash
2. Mica disc after cleaving
   (a) Bare substrate after cleaving
   (b) Bare substrate after cleaving and toluene wash
   (c) Bare substrate after cleaving, toluene and methanol wash

Figure 6.3 shows the contact angle measurements for water drops on mica as received and on cleaved mica. Data for the bare mica as received (red) show a contact angle of approximately 15°. There is no significant change for the water contact angle compared with after a toluene and after a methanol wash. Interestingly, the contact

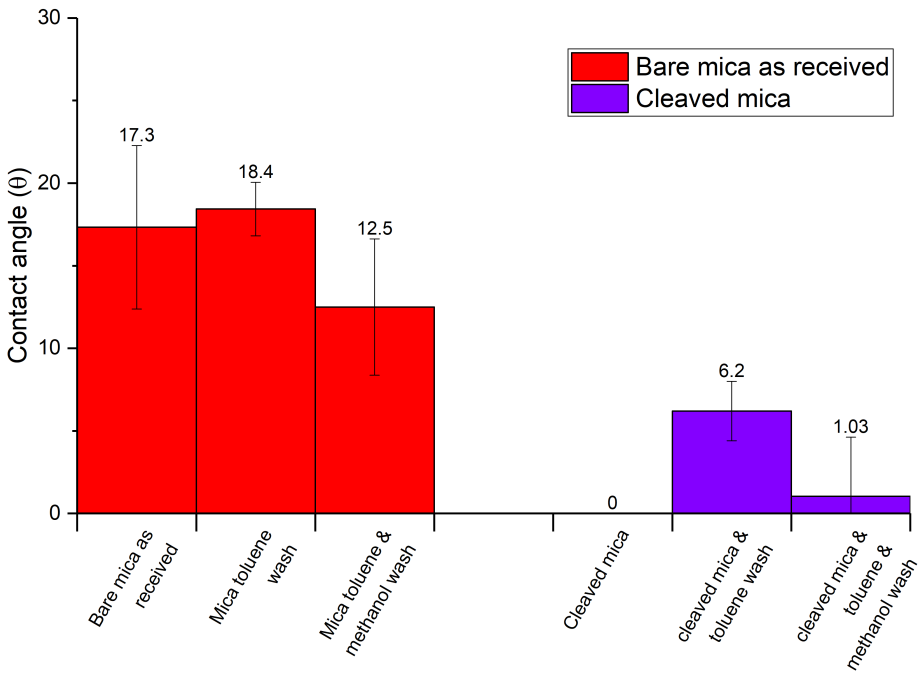

Figure 6.3: Contact angle measurements of bare mica discs as received (red) and after cleaving (purple) with toluene and methanol washes. Error shows standard deviation of three measurements.

angle is non-zero, suggesting some degree of hydrophobicity, but rather modest. This may be due to minor contamination from deposition from the air.

The data for cleaved mica (purple) show a lower contact angle and in some case the drop spreads, indicating a hydrophilic surface (complete wetting) where contact angle is zero and cannot formally be measured using DSA. Interestingly, there is an increase in contact angle upon toluene and methanol washes, suggesting these solvents actually impart some hydrophobic nature to the surface. However, there is no difference between the contact angle after the two washes. It is possible, for example, that the OH of the methanol is bound to the OH on the mica surface or to the surface bound K^+ ions. Once bound in this way the hydrophobic end of the methanol $-CH_3$ may be exposed to the air and the surface will appear to be more hydrophobic.

2) HA Oil

Figure 6.4 (a) shows the contact angles of mica discs aged in HA oil with pretreatments (no pretreatment, DI water, or brine) over a 6 week ageing period.

The oil was removed and replenished after each week. The error shows the standard deviation of three runs. A bare mica disc as received is included in each graph for comparison.

2.1) Untreated Substrate

The data for the untreated substrate (Figure 6.4 (a) left) show that after a toluene wash the contact angle is much higher than the initial bare mica. The contact angle remains approximately the same (80°) throughout the 6 week ageing process, suggesting hydrophobic molecules bind to mica and do so promptly. After a methanol wash, the data suggest a very significant fraction/all of the adsorbed molecules are removed as the surface returns to essentially the same contact angle as bare mica (20°). The contact angle data are comparable to the CHN data as after a methanol wash the CHN data also shows no organic adsorbed, which correlates with a reversion back to the contact angle of bare mica. As mentioned above in the CHN discussion, this was a surprising result, so it is interesting to see it supported by both CHN and contact angle data.

2.2) DI treated Substrate

The DI treated substrate data (Figure 6.4 (a) middle) show that a toluene wash provides a similar contact angle as the untreated substrate with a significant increase in contact angle compared to the bare mica. Interestingly, for the first week after a toluene and methanol wash (brown) the contact angle reverts back to that of the starting material. However, in subsequent weeks the methanol wash contact angle is the same as for the toluene wash: methanol no longer removes the contact angle altering molecules from the mica surface. This is an interesting finding and suggests species that were initially reversibly bound become irreversibly bound over time. Building on this, the oil is refreshed each week so it cannot be a chemical modification of the fluid crude, it must be some change of the surface and adsorbed species.

CHN elemental analysis showed no organic adsorbing (for toluene and methanol washed samples). However, contact angle data does show organic adsorbing after two weeks. The fact that the organics can be removed in methanol, which is polar protic, and not in the non-polar toluene suggests that the molecules in the layer directly adsorbed to mica surface are polar and anions. Therefore, when the DI treated mica aged in HA oil retains contact angle altering organics after the methanol wash suggests the molecules that remain are cationic and may be removed by a polar aprotic solvent such as acetone. This result is reinforced in Section 6.3.3 where HRMS is used to investigate the methanol washings and cationic molecules are not

in high enough abundance leading to only anionic molecule investigation.

2.3) Brine treated Substrate

The brine treated substrate data (Figure 6.4 (a) right) show similar results compared to the untreated mica aged in HA oil: a significant elevation of the contact angle of 80° with one interesting difference that the week 1 sample does not show any change in contact angle when compared to the bare mica surface. This suggests some slow process in the wettability alteration.

Again, similarly to the untreated substrate, after a methanol wash the contact angle returns to the contact angle of the bare mica. It can be concluded that brine does not inhibit molecules adsorbing onto mica after 2 weeks of ageing. However, the molecules that do adsorb are easily removed with methanol. As outlined above, this may be a solvency issue or one of competitive adsorption.

The contact angle data is in agreement with the CHN data as after a methanol wash the CHN data also show no organic adsorbed. As mentioned above, this was a surprising result and it is good to have both CHN and contact angle data to support this conclusion.

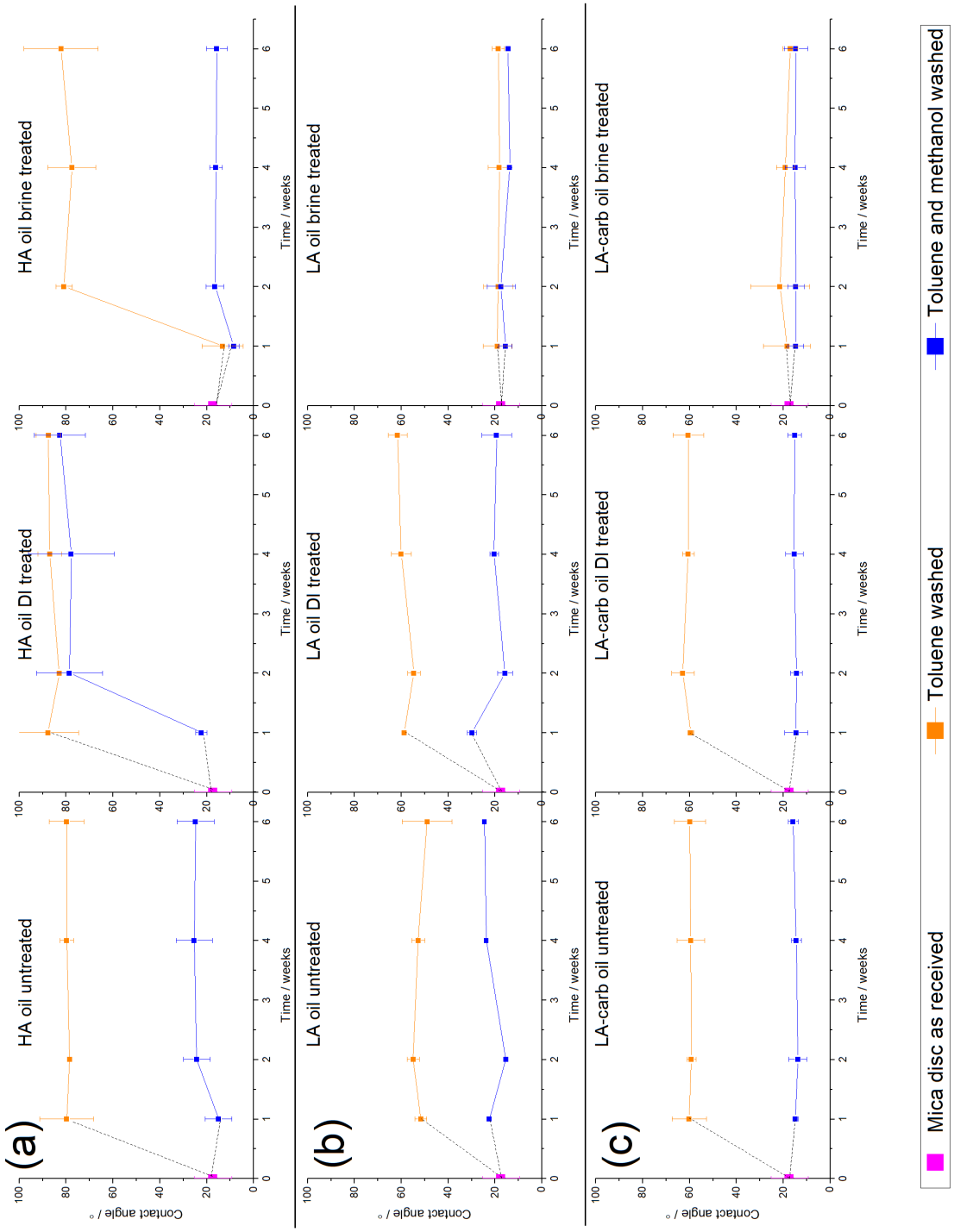

Figure 6.4: Contact angle of aged mica discs in (a) HA (b) LA or (c) LA-carb oil with or without pretreatment. Pink point at t=0 is water contact angle on mica as received. Error shows standard deviation of three repeats. Dotted lines are to guide the eye from the starting substrate.

3) LA Oil

Figure 6.4 (b) shows the contact angle of mica discs aged in LA oil with no pretreatment, DI water, or brine over a 6 week ageing period. The oil was removed and replenished after each week. The error shows the standard deviation of three runs. The contact angle for a bare mica disc as received is included in each graph for comparison.

3.1) Untreated Substrate

The data for the untreated mica aged in LA oil (Figure 6.4 (b) left) show a similar story to the untreated mica aged in HA oil: a dramatic rise on contact angle, which then remains essentially the same throughout the ageing process (50°). However, the contact angle for mica aged in LA oil is less hydrophobic than mica aged in HA oil by around 30°. The main difference between HA oil and LA oil is the asphaltene content. Coupling the contact angle data to SARA data leads to the suggestion that asphaltenes bind and make mica more hydrophobic with HA oil. After a methanol wash, the contact angle returns to the value of bare mica. The contact angle data is again in good agreement with the CHN data as after a methanol wash the CHN data also show no organic adsorbed.

3.2) DI treated Substrate

The data for DI treated mica aged in LA oil (Figure 6.4 (b) middle) after a toluene wash show that a contact angle of 60°, which is retained throughout the ageing process. This contact angle is ∼20° lower than the angle measured when aged in HA oil, suggesting again that the asphaltene content of HA oil is altering wettability, as mentioned in the above paragraph. Upon methanol washing the contact angle goes to ∼20°, which is that of bare mica. It can be concluded that methanol removes the contact angle altering species from the mica substrate.

3.3) Brine treated Substrate

The data for brine treated mica aged in LA oil (Figure 6.4 (b) right) after both toluene and methanol washes are unexpectedly very similar. The contact angle for the duration of ageing is between 15–17° and there is no statistically significant difference between the two and interestingly, all the data are at the same contact angle of the bare mica surface.

It could be argued that there is residual methanol on the substrate. However, the substrates were left to air dry for an hour before measuring. Therefore, it is assumed that all solvent has evaporated. A toluene washed mica substrate has the same contact angle as a bare mica substrate (∼20°). After a methanol wash on the

same substrate, the contact angle almost halves to just above 10°. If methanol had remained on the surface in the above experiments, the contact angle would have been 10° and not 20°. It seems more likely that a hydrated layer has formed on the mica surface via the cations in brine, which removed any possibility for bound organics.

Overall, the removal of organics left in place by toluene but removed by methanol could have several origins, as outlined above:

- Solvency of the methanol removing all the adsorbed crude components
- Absorption of methanol onto the surface to make a region more hydrophilic
- Competition by the methanol for the surface sites over the organics

Most interesting is the return of the contact angle to essentially the same value as the starting mica. If there was absorption of methanol, it might be lower than the starting material contact angle, but there is no reason to think it should be so close to the bare mica value, other than by change. Similarly, if there was competitive adsorption of the methanol for the mica surface, the contact angle would be 10 and not 20°. Hence, it is concluded that mica substrate is cleaned. This is a significant conclusion: solvent can completely remove all adsorbed organics arising from the ageing process. This has important implications for EOR.

4) LA-carb Oil

Figure 6.4 (c) shows the contact angles of mica discs aged in LA-carb oil with no pretreatment, DI water, or brine over a 6 week ageing period. The oil was removed and replenished after each week. The error shows the standard deviation of three runs. A bare mica disc as received is included in each graph for comparison.

4.1) Untreated Substrate

The data for the untreated substrate (Figure 6.4 (c) left) show that a contact angle of 60° is retained throughout the ageing process. This is a similar contact angle to that observed in LA oil, which has a similar level of asphaltenes. After a methanol wash of mica aged in LA-carb oil, there is a large reduction in contact angle to that of bare mica. This result suggests that methanol again removes adsorbed organics that make a hydrophobic surface.

4.2) DI treated Substrate

The data for the DI treated substrate (Figure 6.4 (c) middle) show the same trend and essentially the same values as the untreated substrate: after toluene wash a

contact angle of 60° was observed, and after a methanol wash the contact angle returned to the value of bare mica. Hence, it is concluded that DI water does not stop hydrophobic molecules from adsorbing onto mica. However, the methanol wash removes these molecules.

4.3) Brine treated Substrate

The contact angle of brine treated mica aged in LA-carb oil (Figure 6.4 (c) right) show after a toluene wash, that the contact angle returns to that of the bare mica. After a methanol wash, the values are not significantly different from the toluene wash/bare mica. The data suggest brine inhibits organics from binding to the mica surface as no changes in contact angle are observed.

The role of brine could be explored more to investigate why it inhibits binding: one would expect cation bridging between the negatively charged mica surface, salt cations and nitrogen anion containing molecules (such as pyridines). An excess of crude oil could be tumbled with brine for 24 hours, before extracting the brine and investigating any molecules adsorbed by HRMS. Knowing what types of molecules are soluble in the brine from the crude oil will aid understanding in why these chemical functionalities are not binding onto the mica surface.

5) Conclusions

- In most cases, the ageing process adsorbed hydrophobic species to the mica surface. The exceptions to this are LA and LA-carb oil with a brine pretreatment and toluene wash, where the adsorption is completely inhibited. This is an interesting and significant finding. The brine is able to prevent any adsorption to the mica. We attribute this to the low asphaltene content of both, as HA oil showed adsorption. Asphaltene content appears to be a key driver in adsorption.

- Toluene and methanol washed samples, have contact angles essentially that of the starting material. This strongly suggests that any adsorbed material remaining after a toluene wash is completely removed by methanol. This finding is in good agreement with CHN data where no organics are seen on the mica powder after ageing. The only substrate to deviate from the trend is DI treated mica disc aged in HA oil, where the contact angle remains hydrophobic (80°) after a toluene and methanol wash. This is attributed to the higher asphaltene content and the presence of a small amount of adsorbed organics, too small to be detected by CHN, but large enough to modify the contact angle.

6.3.2 Heated Brine Pretreatment

A recent paper from Mugele's research group, Twente, suggesting mica substrates do undergo organic adsorption during ageing, as evidenced via the contact angle.[45] The study discussed in this thesis (Section 6.3) concludes that organic species adsorb, but are removed with a methanol wash. The main differences between Mugele's study and the study above are:

1. In the study in this thesis, brine is added at room temperature and oil added immediately after washing substrates in brine. Mugele treats substrates with brine at a temperature of 60°for 24 hours before adding oil.
2. In this thesis, the substrates are washed in toluene after ageing, and then in methanol. Mugele only washes in toluene.
3. Mugele measures a three phase contact angle of a crude oil droplet (water droplet in oil). In this thesis, a two phase water contact angle on a solid substrate is measured.

Considering **point 1** above, if heating the brine is key to functionalision of mica by crude oil, it suggests heating the brine and submerging mica in brine for 24 hours could be key to isomorphic substitution by cations in the brine within the mica structure to promote a negative surface charge, thus allowing cation-bridging to bind asphaltenes. However, the study by Mugele suggests the surface charge is too small to measure in situ and when measured ex situ the flat sections have strong negative charges whereas protrusions are neutral.

Addressing **point 2** above, the data in Figure 6.4 on the right hand side show that all brine treated substrates have adsorbed organic matter removed after a toluene and methanol wash. The only outlier is HA oil, where a toluene wash shows organic matter remains adsorbed after 2 weeks of ageing. Interestingly, the same HA oil supplied to Cambridge is one of the oils used in Mugele's study. Both Mugele and this thesis use the same brine too, which allows for direct comparison between methods.

To compare the study in this thesis with Mugele, additional measurements were made with mica discs pretreated with brine at 70 °C for 24 hours prior to ageing. Substrates were aged for 6 weeks and compared. After a toluene wash, Mugele's three-phase contact angle of a drop of HA oil on aged mica pretreated in brine is 120–150° through the oil drop (Mugele supplementary Figure 2, B, crude B). This means a contact angle between 30–60° is expected from a two-phase water contact

angle.

Figure 6.5 shows the data for mica aged in HA oil with brine treatment at room or heated brine treatment. The data show a heated brine pretreatment followed by HA oil ageing (red) immediately makes mica hydrophobic after a toluene wash. When mica has a room temperature brine pretreatment (orange), it takes until week 2 for hydrophobicity to occur. The two studies align well, as the contact angle is at the higher end of the 30–60° range, with no difference to the plateau value between toluene washed samples.

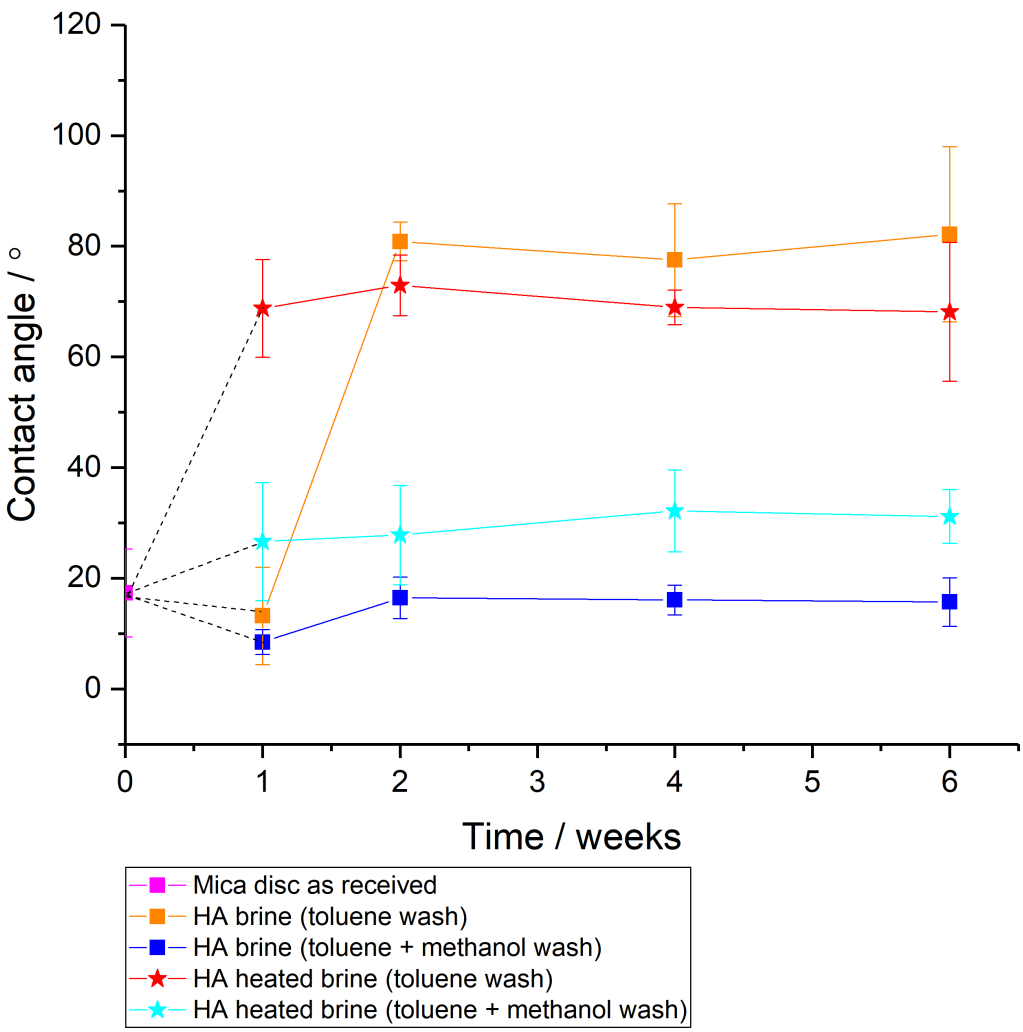

Figure 6.5: Contact angle measurements of mica pretreated with brine. Square-points show mica aged in brine at room temperature for seconds before ageing in HA oil. Star-points show mica pretreated in brine added at 70 °C for 24 hours before ageing. Error shows standard deviation of three measurements.

After a methanol wash, Figure 6.5 (light and dark blue) show the contact angle

returning to that of bare mica. This confirms observations seen in the CHN data where no organics adsorb. This also shows the key difference in the two studies (this thesis compared to Mugele) is the toluene vs methanol wash: washing with just toluene leaves significant organic binding onto the mica surface. A methanol wash removes adsorbed organic.

Overall, the work in this section of the thesis agrees with the work seen by Mugele when compared to similar systems prepared in the same way. In addition, the section above has addressed a much wider range of samples/substrates and conditions that the Mugele paper as well as the elemental composition data. Therefore, data from both groups are unified and complete a picture of mica wettability alteration.

6.3.3 HRMS

Background

High resolution mass spectrometry is an upcoming method utilised by BP to investigate liquid extracts from solvent washings when removing adsorbed crude oil components from aged rock core. Recent investigations have shown that following a traditional core cleaning of toluene and methanol wash with tetrahydrofuran (THF) and tetramethylammonium hydroxide (TMAH) will recover organics from the core.[55–57] There are clear differences between functional groups present in the crude oil and the solvent extracts from the core washings. Differences can also be observed between the molecules yielded from different solvents used to wash.

The important advance is that the very high resolution now available with the HRMS allows all components of the complex mix in a crude oil type sample to be resolved and identified. This provides a very extensive data set that can then be characterised in different ways and compared to related fluids after various processes.

Considering how HRMS will link to this thesis, after ageing untreated mica discs in HA oil and washing in toluene to remove bulk toluene, the mica discs show an increase in the contact angle (of a water droplet). The surface is significantly more hydrophobic than that of the starting material; this is typical of a wettability altering material and is what the Twente group reported above. Upon a single methanol wash, the contact angle returns to that of the starting material. This suggests the methanol wash removes the contact angle determining species. It is these species that HRMS may identify.

Experimental

The aim of this study is to use HRMS to investigate the species in the methanol wash and suggest functional groups that possibly drive the change in the contact angle. Similar to other MS approaches, fragmentation is expected. Therefore, the higher mass end of the spectrum will be important for identification of molecules. Importantly, washing in methanol does not require extreme conditions to release molecules, which is in contrast to methods above where fragmentation occurs simply by releasing the molecule from the surface (e.g. TOF-SIMS). Due to time and access limitations, only untreated mica aged in HA oil after 6 weeks was investigated.

To prepare the crude oil, the solution was diluted with toluene to reach 1 mg/ml. For methanol extracts, 1.5 mL of sample was left to evaporate in a fume hood

to concentrate the sample before injection. It is important to note the action of letting methanol evaporate from the sample is a gentle process and not expected to significantly damage the sample. However, evaporation could result in oxidation of the sample. The samples were characterized using Electrospray Ionisation (ESI) in negative mode. Possible compounds linked to their classes are in Table 6.1.

Typical Class	Compound
N_1 ($C_xH_yN_1$)	Carbazole-type species
O_1 ($C_xH_yO_1$)	Benzylphenols
O_2 ($C_xH_yO_2$)	Carboxylic acids

Table 6.1: Key classes for the negative electrospray ionisation are acidic and compound suggestions are above.

A positive ESI was run for the toluene and methanol extracts but the signal was too weak to provide a useable spectrum. It is interesting that the positive ESI did not provide fragments in high enough abundance because it may be expected that cationic molecules will bind to the negative mica basal plane. The lack of abundance of positive fragments suggests the mechanism of crude oil components binding to the mica surface is not one of surface charge or cation bridging. A mechanism that produces negative fragments predominantly suggests a van der Waals type interaction with the surface: the molecules are removed with a solvent and most likely not chemically bound. Therefore, a weak interaction is suggested.

1) Classes

The first step to deconvoluting the HRMS data is categorising species/fragments into classes. Fragments are classed depending on the number and combination of heteroatoms (N, O or S) and a high abundance of ^{13}C fragments. The hypothesis is that the methanol extract will contain a higher abundance of some fragments that are found in crude oil, suggesting preferential adsorption. It will be these fragments that drive a change in the contact angle on the mica surface.

Figure 6.6 shows the percentage relative abundance of HA oil, toluene extract and methanol extract as a function of class distribution. Focussing firstly on the difference between HA oil and the methanol extract, there are a greater abundance of $O_{2\text{-}5}$ and $O_{3\text{-}5}S_{1\text{-}2}$ classes for the methanol extracted species than in HA oil. Origin of the O_x classes could be from oxidation of the extract during evaporation in air. However, there is no clear origin for an increase in sulfur content. Therefore, the sulfur fragments must have originated from the crude oil. It is concluded that

the sulfur containing species are preferentially adsorbed from the wettability alter material.

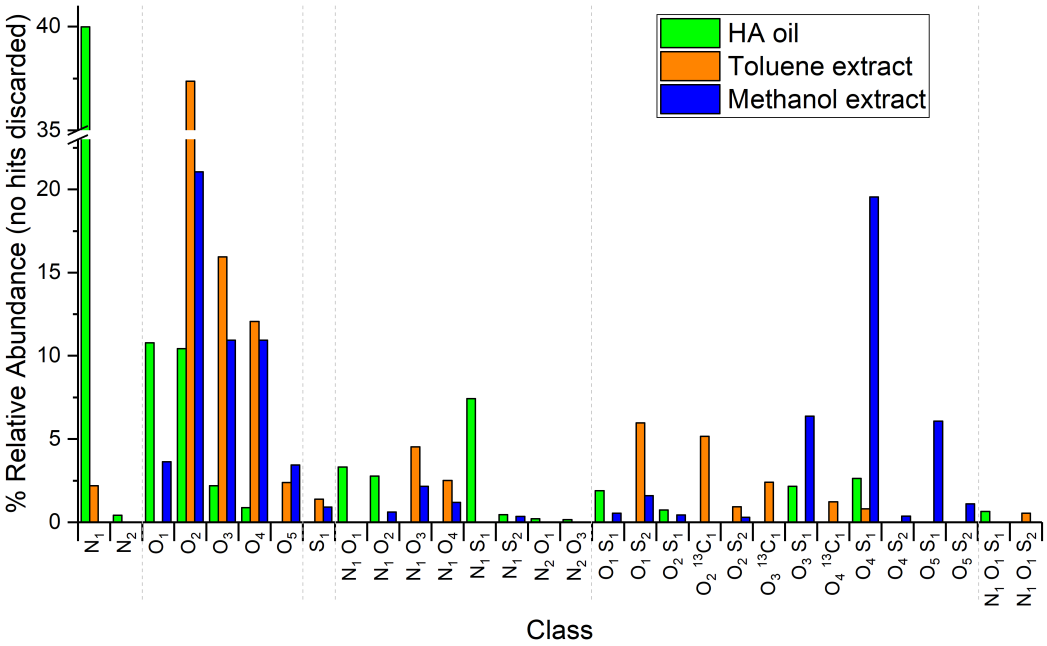

Figure 6.6: Percentage relative abundance of class distribution in HA oil (green), toluene extract (orange) and methanol extract (blue). Grey vertical lines are to roughly guide the eye between broad classes.

The HA oil (green) shows fragments that contain nitrogen-only (N_1) or oxygen-only (O_1) as the heteroatoms. However, sulfur-only (S_1) is not present whereas that class of fragments are observed in toluene and methanol extracts. In HA oil, there are consistently fragments with fewer heteroatom combinations (N_1O_1, N_1S_1, O_1S_1, N_1O_1, S_1). However, when number of heteroatoms increase and complexity of combinations increase ($N_1O_{3–4}$ and $O_{1–2}S_2$) the relative abundance is reduced for species in HA oil or not present.

The toluene extract (orange) shows a greater abundance of oxygen-containing fragments than the HA oil. Although there are nitrogen-containing classes (N_1, $N_1O_{3–4}$, $N_1O_1S_2$), there are fewer present in the toluene extract than the HA oil.

To understand the O_x, $O_{3–5}S_1$ and $O_{4–5}S_2$ classes further, the carbon number via the relative molecular mass and DBE can be used to infer a structure of the most abundant fragments of each class. The molecules found in the methanol extract that differ from the toluene and HA oil are from the following classes: O_5, $O_{3–5}S_1$ and

$O_{4–5}S_2$. The O_2 class will also be investigated as this has the highest abundance in the methanol extract.

In summary, species with a certain combination of heteroatoms are found (referred to as 'classes'). These are plotted by carbon number versus DBE. The most abundant fragments are selected and chemical structures of the most abundant molecules are suggested. These are discussed below.

2) Determining Structures

2.1) O_2 and O_5 Class

Fragments containing two oxygen atoms are the most abundant in the methanol extract. Figure 6.7 shows the double bond equivalence of the HA oil (a) and methanol extract (b) plotted as a function of carbon number for the molecules that contain two oxygen atoms. Figure 6.7 (c) shows the O_5 class for the methanol extract, which is included because there is a higher abundance than both the HA oil and toluene extract.

For the O_2 class, the data show a significant enrichment of low DBE ($\sim$1) molecules with low carbon number in the methanol wash compared to the HA oil, suggesting long chain saturated fatty acids are present in the methanol wash and were wettability altering on the mica surface. A similar result of low DBE and carbon number is observed for the O_5 class methanol extract, suggesting low aromaticity and short side chains. A possible origin for this class is sample oxidation as the sample had to be left open to the air to evaporate and concentrate. The following suggested structures from fragments with high abundance can be identified and are shown in Table 6.2.

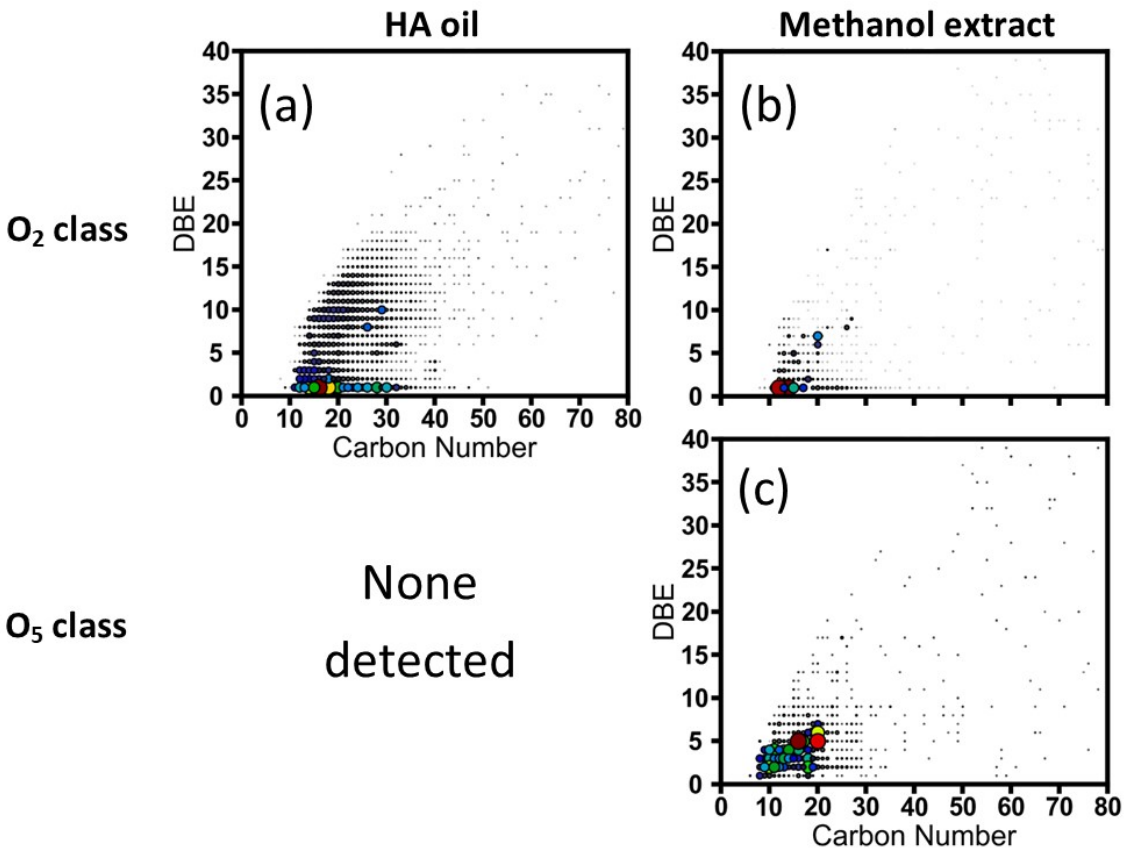

Figure 6.7: Double bond equivalence as a function of carbon number for (a) HA oil and (b) methanol extracts of the O_2 class and (c) methanol extract for the O_5 class.

Class	m/z	DBE	Formula	Suggested Structure
O_2 class	227.2012	1	$C_{14}H_{28}O_2$	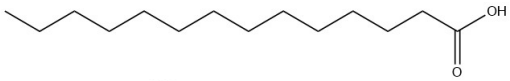
	299.2016	7	$C_{20}H_{28}O_2$	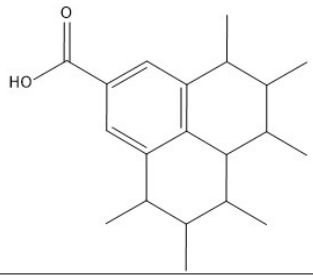
O_5 class	295.1551	5	$C_{16}H_{24}O_5$	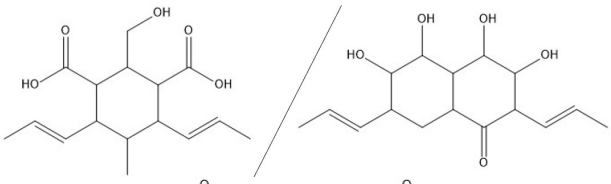
	349.2021	6	$C_{20}H_{30}O_2$	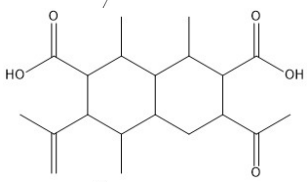
	349.2021	2	$C_{10}H_{18}O_2$	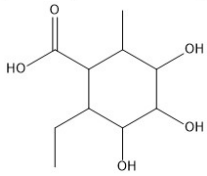

Table 6.2: Suggested molecules for the O_2 and O_5 class in the methanol extract.

2.2) O_3S_1 Class

Figure 6.8 shows the double bond equivalence of the HA oil and methanol extract plotted as a function of carbon number for the molecules that contain three oxygen atoms and a sulfur atom. The data are show a low DBE, which suggest low aromaticity. Carbon number for the most abundant molecules is between 8–18, suggesting short side chains. Suggested molecules are in Table 6.3.

The toluene extract analysed was the toluene extracted after the washings ran clear (Figure 6.9, T4 and T5). Therefore, only the strongly adsorbed molecules that are dissolvable in toluene are included and investigated here. It is assumed that toluene will remove any asphaltenic molecules if they are bound and the energy of solvation is greater than the energy of binding. Although asphaltenes are defined to dissolve in toluene, they may provide significant competing adsorption influence It is expected that the asphaltenic molecules will have a high DBE and high carbon number, possibly in the realm of the coordinate (20, 10) on the oil graph (Figure 6.8). Interestingly, the toluene extract does not detect any fragments of the O_3S_1 class. This suggests that the strongly bound molecules that are also soluble in toluene are not asphaltenic. It is possible that O_3S_1 class asphaltenic groups are present in the toluene washings to remove 'bulk' oil but their lack of presence here suggests the solvation energy is greater than the binding energy of O_3S_1 class asphaltenes.

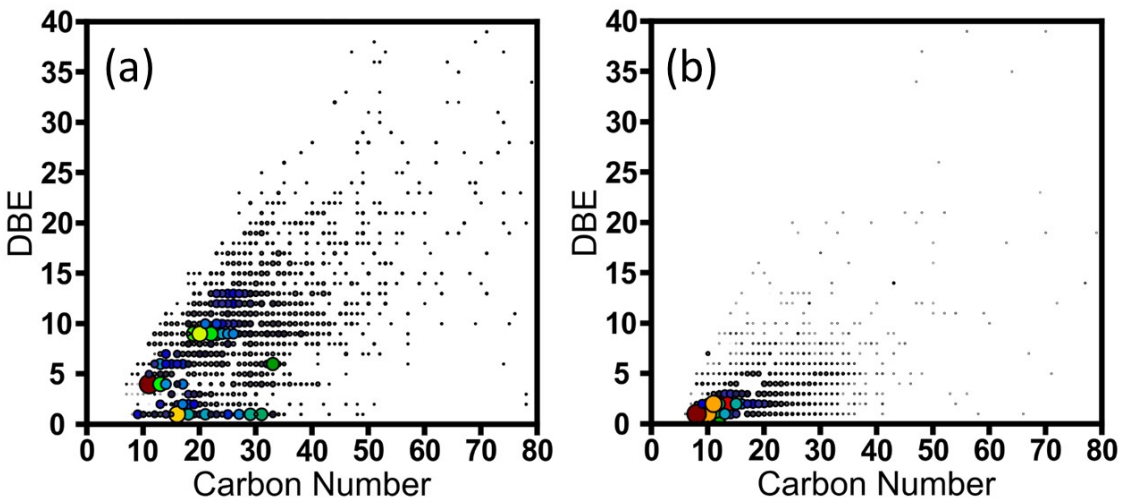

Figure 6.8: Double bond equivalence as a function of carbon number for (a) HA oil and (b) methanol extracts of the O_2 class.

m/z	DBE	Formula	Suggested Structure
191.0739	1	$C_8H_{16}O_3S$	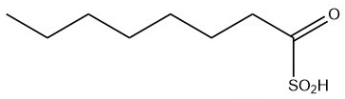
259.1373	2	$C_{13}H_{24}O_3S$	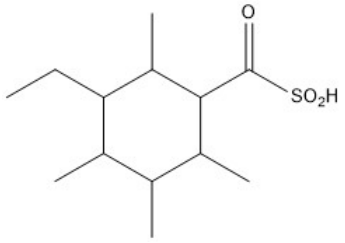

Table 6.3: Suggested molecules for the O_3S_1 class in the methanol extract.

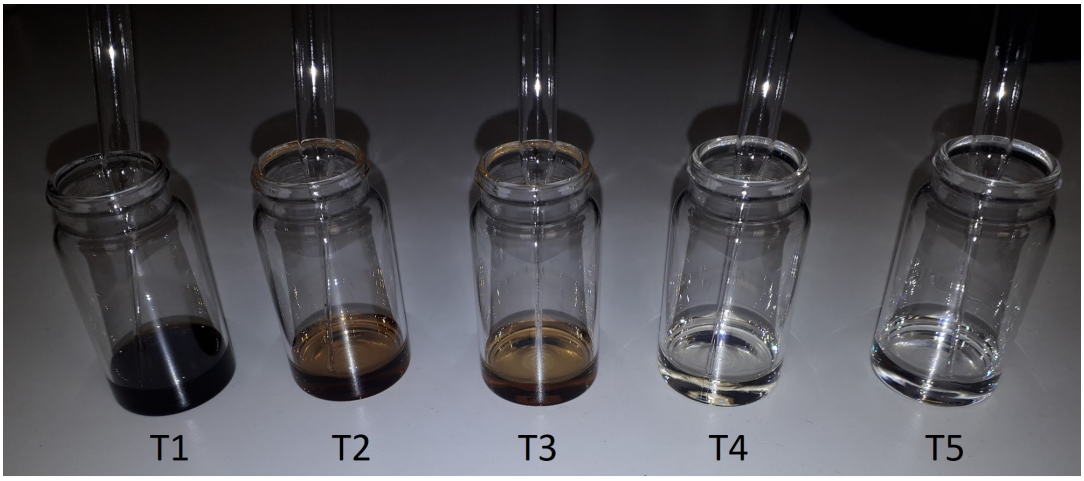

Figure 6.9: Toluene washings from untreated mica disc aged in HA oil moving from first wash after removal from crude oil (T1) to final toluene wash (T5).

2.3) O_4S_1 Class

The second most abundant class are fragments that contain four oxygen atoms and one sulfur atom. Figure 6.10 shows the DBE and carbon number of HA oil and methanol extract for the O_4S_1 class. The data show similar levels of DBE and a greater spread of carbon number in the methanol extract compared to the HA oil. This suggests fragments with longer side chains are present in the methanol extract. Possible structures are suggested in Table 6.4.

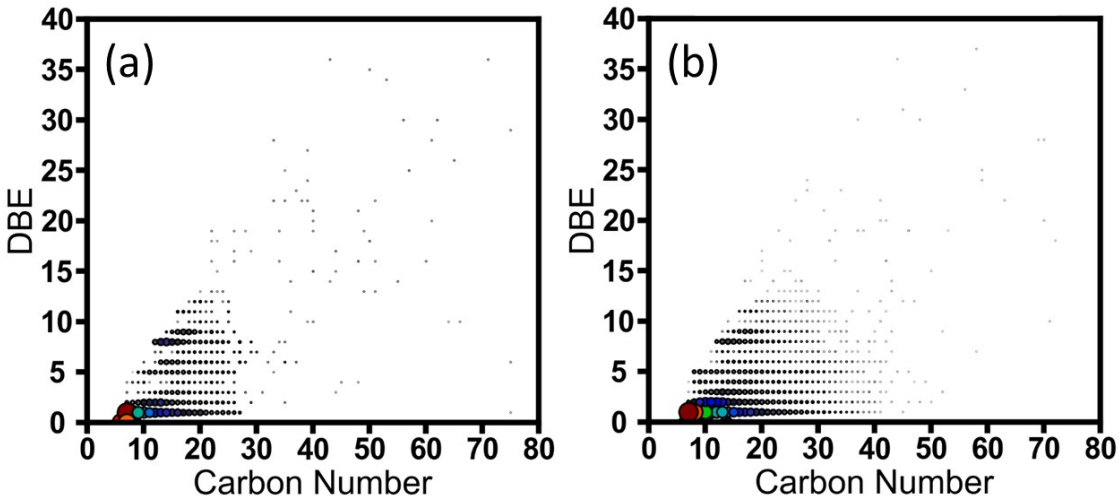

Figure 6.10: Double bond equivalence as a function of carbon number for (a) HA oil and (b) methanol extracts of the O_4S_1 class.

m/z	DBE	Formula	Suggested Structure
191.0739	1	$C_7H_{14}O_4S$	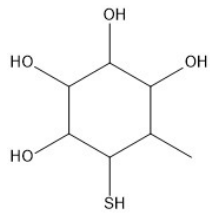
305.1793	1	$C_{20}H_{30}O_2$	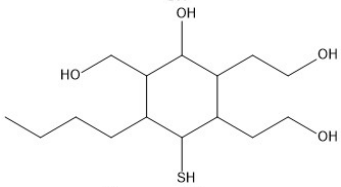
233.0850	2	$C_{10}H_{18}O_2$	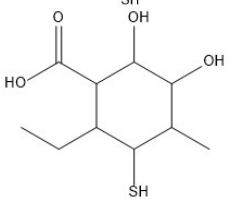

Table 6.4: Suggested molecules for the O_4S_1 class in the methanol extract.

2.4) O_5S_{1-2} Class

The data in Figure 6.11 show the DBE and carbon number of the (a) O_5S_1 and (b) O_5S_2 class from the methanol extract. These classes were not observed in the HA oil. Therefore, they are possibly oxidation products of the O_4S_1 class mentioned above. A low DBE and carbon number is observed for both classes, suggesting low aromaticity and small side chains. Suggested molecules are displayed in Table 6.5.

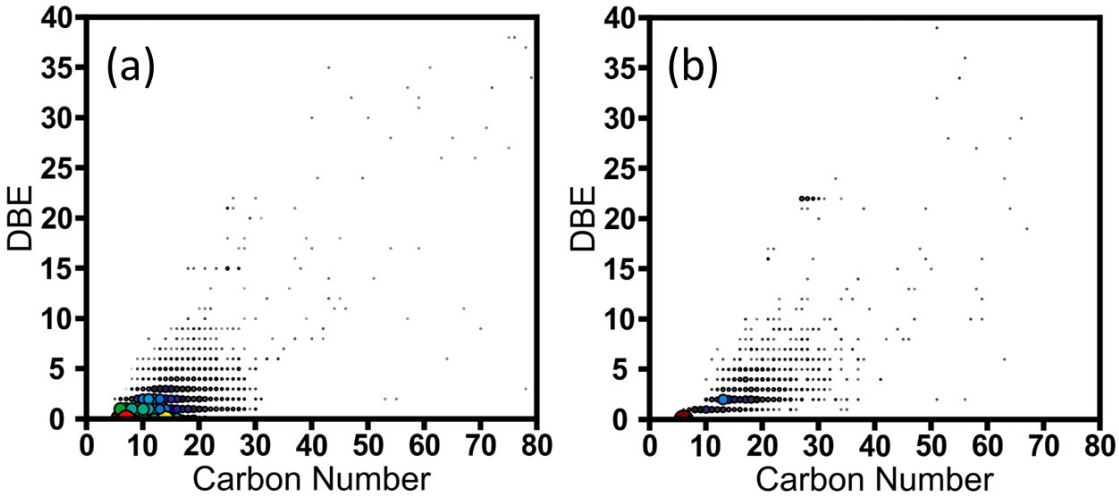

Figure 6.11: Double bond equivalence as a function of carbon number for (a) O_5S_1 class and (b) O_5S_2 class in the methanol extract.

m/z	DBE	Formula	Suggested Structure
197.0482	0	$C_6H_{14}O_5S$	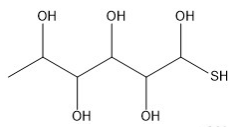
229.0201	0	$C_6H_{14}O_5S_2$	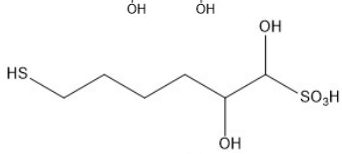
323.0993	2	$C_{13}H_{24}O_5S_2$	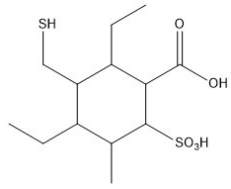

Table 6.5: Suggested molecules for the O_5S_x class in the methanol extract.

3) Discussion and Conclusions

As mentioned in the Method Section, (−)ESI provided a high enough signal to allow evaluation of the data, where as (+)ESI did not. Assuming no bound crude oil remains on the surface after a methanol wash, which is clearly suggested by the contact angle data returning to that of the starting material after a methanol wash, this suggests the molecules that bind are anionic. This is an unexpected result as it is expected that cationic species would bind more strongly on the negative mica surface. This may be due to cation bridging or van der Waals forces between polarising fragments (e.g. sulfur and hydrogen on Al−OH groups from mica).

The main class of molecules found in the methanol extract that differ from the crude oil are from the following classes: O_x, $O_{3–5}S_1$ and $O_{4–5}S_2$. The methanol extract has consistently contained molecules with a lower DBE than the HA oil, suggesting methanol removes molecules that have a lower degree of aromaticity from the mica surface. It could be suggested that less aromatics are not on the surface as these are removed by toluene. However, this is proven not to be true as the data suggests no highly aromatic molecule are adsorbing at all. One example is the O_3S_1 class (Figure 6.8) where there is a significant, large, fragment detection of DBE around 10 and much smaller amount with DBE around 10 in the methanol extract. The toluene extract shows no presence of O_3S_1 detected (Figure 6.6). This suggests the molecules in the methanol wash are not polyaromatic with high DBE and are smaller, more saturated molecules (such as fatty acids). This low degree of unsaturation is interesting as it is commonly anticipated that asphaltenes are the dominant species controlling wettability and literature shows asphaltenes can be applied onto mica.[46,249] Evidence in this section has suggested otherwise.

In crude oil, sulfur has been detected as a terminating thiol group (R−SH), sulfide (R−S−R) or disulfide (R−S−S−R).[250] However, the data presented here show that even if a functional group is present in crude oil, it does not correlate directly to functional groups on the surface of substrates. As (−)ESI detects acids, the structures suggested are sulfonic acid ($R-SO_3H$) groups, which are a stronger acid than sulfinic acid ($R-SO_2H$).

Overall, after mica is aged in HA oil and washed in toluene then methanol, it can be concluded that sulfur and oxygen containing molecules are enriched in the methanol extract compared to the HA oil. The methanol wash causes the mica surface to lose hydrophobicity. The HRMS data suggest functional groups containing sulfur and oxygen drive a change in the contact angle on the mica surface. **It can be concluded that these are species that drive the hydrophobic nature of**

the surface.

An ideal system could be created to assess the functional group/combination of functional groups that drive the contact angle changes on the mica surface. The contact angle of a water droplet on functionalised mica with thiol, sulfonic or carboxylic acid terminating groups should be compared with a crude oil aged mica sample to determine the ideal model system.

6.4 Conclusions

Section 6.2 and 6.3 focused on measuring the contact angle of water droplets on silicon wafers and mica discs pretreated in DI or brine or untreated, in HA, LA or LA-carb oil via DSA water contact angle. It is worth reiterating that the contact angle is not only the solid-liquid surface: if any components dissolve into the water and change the air/water surface tension, contact angle changes will also occur. For that reason, contact angle measurements should be used as a complimentary measurement for surface characterisation.

The study on **silicon wafers** has shown that differences between cleaning methods can lead to different contact angles: acid treatment possibly oxidises the silicon wafer, to form a SiO_2 surface with siloxane bonds, resulting in a more hydrophobic surface, with a non-zero contact angle. Application of a 15 minute UV-ozone clean is hypothesised to form hydroxyl groups to yield a hydrophilic surface, although it was not possible to observe these groups directly.

When the **silicon wafers** are aged and washed in toluene to remove excess crude oil, all crude oils used in this study were found to make silicon wafers more hydrophobic. After a toluene and methanol wash the substrate either:

- retains the same hydrophobicity
- or the contact angle is reduced and the substrate becomes less hydrophobic, but more hydrophobic than the starting material

DSA has suggested that the surface chemistry is altered in all cases. However, the amounts of the various species adsorbed in some cases are found to be too small to be measured by CHN analysis. Hence, they must be present at sub-monolayer quantities.

When crude oil ageing of **mica discs** was followed by a toluene wash, all untreated and DI treated samples show an increase in hydrophobicity of the mica substrate. Interestingly, LA and LA-carb oil with a brine pretreatment do not show any evidence of a change in contact angle to the bare mica, suggesting no organic adsorbs, whereas the brine pretreated HA oil aged mica shows an increase in contact angle. This suggests asphaltenes alter contact angle of mica substrates. Upon a subsequent methanol wash, all samples (apart from DI treated and aged in HA oil) have a reduction in contact angle, back to the contact angle of the bare mica surface. This is an interesting and unexpected result. It has long been considered that crude oil components stick very strongly to mica and other clay minerals, particularly

asphaltene species. The data presented demonstrates by CHN and contact angle measurements that although some organics do bind to the mica surface, they are readily removed by methanol even after 6 weeks ageing. In addition, for low asphaltene crudes and in the presence of a brine pretreatment, nothing adsorbs even after a mild toluene wash.

Employing a new HRMS approach, investigation of the methanol extract from an untreated mica disc aged in HA oil after 6 weeks has shown an enrichment of oxygen and sulfur-containing fragments. The fragments are consistently low aromaticity and low carbon number compared to the contents of the crude oil. Therefore, the wettability altering species on the mica are the oxygen and sulfur-containing compounds, they are not asphaltenic and may cause a change in contact angle on the mica basal plane through cation bridging or van der Waals interactions.

If the contact angle and CHN data suggest there is material present after a toluene wash, they may not be asphaltenes. This may be a significant finding as it is common in the commercial field to attribute wettability changes to adsorbed asphaltenes. The work in this chapter has demonstrates that this cannot be the case every time. However, consideration must be taken that if the binding energy is higher than the solvation energy, the materials that remain stuck could be ashpaltenes. The toluene wash removes free asphaltenes but some chemically bound ones may be irreversibly adsorbed.[82,251]

No matter the adsorbed species, although not removed by toluene, many are removed by methanol. Hence, attention must be redirected to other classes of species, specifically sulfur compounds, for the surface bound organics that may determine the subsequent binding of other species.

Chapter 7

Effect of Stearic Acid on the Calcite Surface

This chapter is an isolated section of work that illustrates the level of detail that is accessible with modern experimental methods. Presented below is a detailed adsorption study fo a simple organic (stearic acid) from a non-aqueous solvent (toluene) to the surface of a common reservoir mineral (calcite). Work in this chapter was completed in collaboration with several academics under guidance from myself and Prof. Clarke:

- Isotherms by Rose Ng (Part III Student, Department of Chemistry) and Lana Farren (Junior PhD student, Clarke Group)
- Karl Fischer titration by Hunter Group, Deptartment of Chemistry
- NR beamtime assistance from David Madden (postdoc, Clarke Group) and Lana Farren, with data interpretation help from Prof. Clarke
- SFG with the help from Mike Casford (senior postdoc, Clarke Group)
- XRR interpretation help from Mary Wood (postdoc, EPFL)

7.1 Background

Calcium carbonate is one of the world's most common minerals and is utilised in several industries, from a paper filler to an overbasing agent. Calcium carbonate is often used in combination with adsorbed organic compounds for several reasons, such as facilitating its dispersion in non-aqueous solvents. Previously, research into calcium carbonate and organics has predominantly focussed on adsorption from

aqueous systems. However, the overall adsorption in these systems is generally low.[252] For example, Lahann *et al.* reports that palmitic acid has a plateau adsorption of 30 x 10^{-8} mol m^{-2} (555 $Å^2$ $molecule^{-1}$), equating to a surface coverage of only 3.6 % when compared to the close-packed area of an alkyl chain of approximately 20 $Å^2$ $molecule^{-1}$.[253]

When adsorbing species to calcium carbonate from water, one also needs to consider issues with surface (and bulk) speciation, particularly as these can change with pH. For example, there is reported to be an increase in adsorption of anionic species with falling pH, which may be attributed to the more positive surface charge, as discussed in Section 2.3.3.[254] However, even in these cases, the area per molecule is still much lower than one might expect for a close-packed adsorbed layer.

Stearic acid (Figure 7.1) is a widely used additive in many industries: food production, detergency, cosmetics, and lubricants and is made up of a hydrophobic tail and a hydrophilic head. Although stearic acid can adsorb to a calcium carbonate surface, competitive adsorption of water and/or hydration of the calcium carbonate surface may be expected to impact the distribution of the stearic acid. Equally, it may be that not all surface sites can be used to bind these adsorbing species, but possibly only edges or kinks, possibly explaining low coverage. It may be for these reasons that a densely packed monolayer of stearic acid is difficult to achieve in an aqueous system.

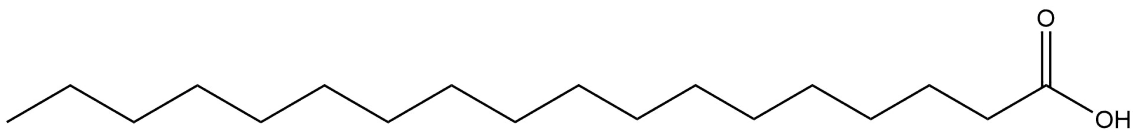

Figure 7.1: Structure of stearic acid.

It has been suggested that stearic acid chemisorbs to calcite.[255] Other studies suggest two regimes of adsorption, a chemisorbed monolayer directly on precipitated calcium carbonate (PCC) and further physisorbed layers of calcium stearate.[256] In good agreement with the results discussed previously for palmitic acid, Suess *et al.* reported the formation of a stearic acid monolayer consisting of 30.8 x 10^{-8} mol m^{-2} (540 $Å^2$ $molecule^{-1}$) from distilled water at 60 °C.[257] The authors suggest that stearic acid molecules in dilute aqueous solution interact mainly with Ca^{2+} sites on calcite, the surface concentration of which is 8.25 x 10^{-8} mol Ca m^{-2}.[257]

Adsorption onto calcite from non-aqueous systems has been much less frequently reported. However, it is significant that adsorption from oil-based systems appears to be much more pronounced, with the formation of closely packed layers. This

difference may lead to the conclusion that there is effective competition between water and the adsorbing organic additives for the calcite surface in aqueous systems because less organic is adsorbed, which is not observed in oil-based systems. Stearic acid adsorbed from chloroform at 50 °C on calcite powder is reported to form a monolayer with a coverage of 1 x 10^{-5} mol m^{-2} (16.6 $Å^2$ $molecule^{-1}$), suggesting well-packed upright molecules.[258]

Osman et al. reported that a chemisorbed stearic acid monolayer forms on calcite powder from toluene at room temperature, with a coverage between 7.8 x 10^{-6} and 9.7 x 10^{-6} mol m^{-2} (21.3–17.1 $Å^2$ $molecule^{-1}$).[259]

In this study stearic acid adsorbed on calcite from toluene at room temperature is investigated with more structural detail than previously considered and different experimental methods (such as NR and SFG). In addition to investigating adsorption from dry toluene, the possibility of competitive adsorption between stearic acid and water by observing what happens as water is 'added back' in controlled amounts.

7.2 Materials

PCC (Multifex-MM ®) for batch adsorption isotherms was obtained from Specialty Minerals Inc. The crystal habit was calcite with a rhombohedral particle shape, an average particle size of 70 nm and a specific surface area of 18.3 m^2 g^{-1} (determined using nitrogen BET isotherm). The specific surface area was on the smaller scale of that reported by the manufacturer (17–32 m^2 g^{-1}).

Calcite single crystals for NR were purchased from P&S Calcite Export Ltd. and cut and polished by Crystran Ltd. to a size of 40 × 45 × 15 mm^3 minimum, exposing the stable $\{10\bar{1}4\}$ face. Prior to NR experiments, the roughness of the crystals was checked via XRR at ISIS Materials Laboratory to ensure samples were sufficiently flat; the roughness was determined to be 8 and 15 Å for the two crystals used in this study. Crystals were cleaned by UV/ozone treatment for 20 minutes using a ProCleaner™ Plus (Bioforce Nanoscience). The calcite blocks were clamped against a PTFE trough that can be filled with the solutions of interest and hence form a solid/liquid interface (Section 3.17.9).

H-Stearic acid, illustrated in 7.1, (Sigma, ⩾ 98.5 % purity, lot #BCBW8354) and H-toluene (Sigma, 99.8 % purity, lot #STBH7660) dried with molecular sieves (VWR Molecular sieve 3A, lot 16K144127) were used for isotherms. For NR experiments, the same H-stearic acid or D-stearic-D35 acid (Sigma, 98 atom % D, lot

#MBBC6293), used as received, was made up to an equilibrium concentration of 30 mM in H-toluene or toluene-d8 (Fisher Scientific, 99.5 % D, lot #A0402314).

7.3 Depletion Isotherms

7.3.1 Results

A plot of surface excess against equilibrium concentration for stearic acid on calcite powder is shown in Figure 7.2, along with a fitted Langmuir, Freundlich and BET isotherm model show that the data are characteristic of BET behaviour. This form of isotherm is consistent with a monolayer of stearic acid adsorbing strongly to the calcite surface, and additional layers of molecules subsequently adsorbing more weakly, as the concentration of stearic acid in the toluene solvent approaches the saturation limit.

The adsorption rises sharply with equilibrium concentration until approximately 1.7 mM, above which it rises at a much slower rate, before sharply increasing in rate as it approaches the solubility limit. Lower concentrations were not achievable due to sensitivity of the equipment. The solubility limit of stearic acid in toluene at this temperature is reported to be 60 mM, consistent with our observations of the solutions.[260]

An estimate of the plateau can be used to estimate the adsorbed species molecular area. In this case, the plateau is not flat but is rising, making the estimation of area per molecules less clear. Taking the value at the knee of the isotherm where the first layer is expected to be completed obtains an area per molecule of approximately 16.37 ± 0.14 Å^2 per molecule. Taking values towards the end of the plateau yields 9 Å^2. These have been calculated using the specific area of calcite of 18.3 m^2 g^{-1}.

The cross-sectional area of an alkyl chain is approximately 20 Å^2 and would be the value expected if determined by a close packed layer of upright, all-trans alkyl chains. A value lower than this may suggest a bi- or multilayer adsorption. A bilayer seems unlikely as either side of the calcite surface would have a hydrophobic tail or the oil would have a hydrophilic head group, neither of which is favourable. Although the isotherm is fitted to a BET fit, this does not mean a multilayer is present and is unlikely due to the amount of stearic acid adsorbed. Hence, at the initial completion of a packed monolayer implying an essentially upright almost all-trans alkyl chain.

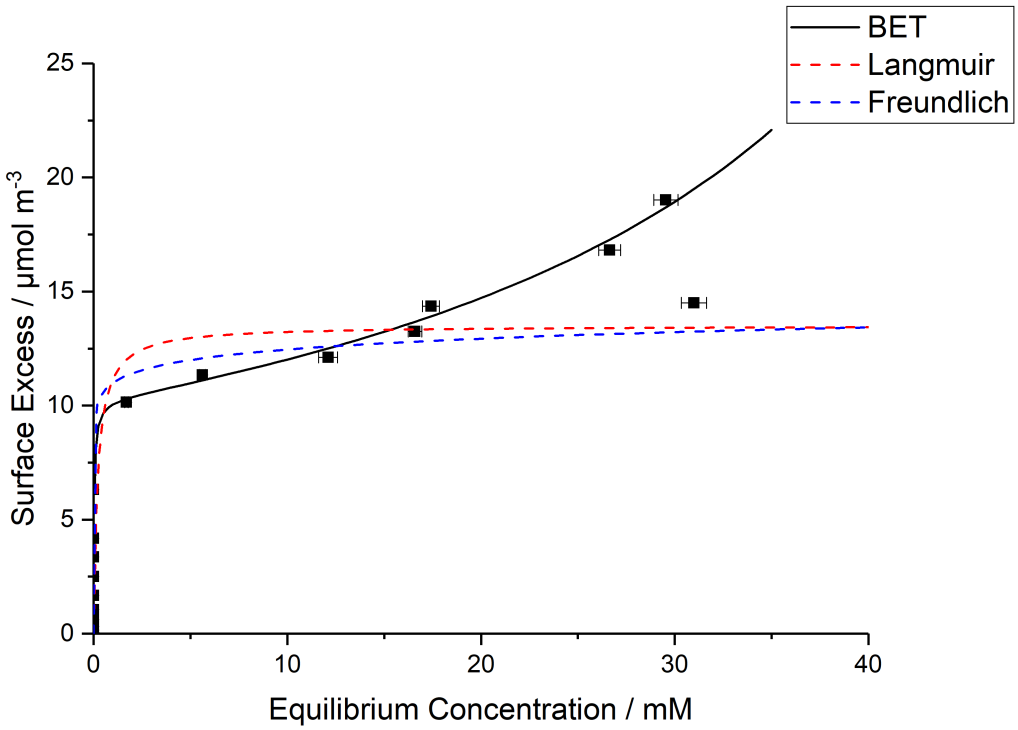

Figure 7.2: Adsorption isotherm of stearic acid on calcite from toluene, fitted to a BET isotherm (black). Langmuir (red) and Freundlich (blue) fits shown for comparison. Note: y-errors are in the order of 10^{-3} and thus not visible on the graph.

Adsorption in the presence of water

To see whether there was any effect of water competing with the stearic acid, an isotherm was also obtained with toluene that was pre-saturated with water. To pre-saturate the toluene with water, an equal volume of toluene is tumbled with an equal volume of water for 24 hours. The amount of water dissolved in the toluene under these conditions was measured by Karl-Fischer titration and the values are shown in Figure 7.3. It reveals that 'dry' toluene has a small level of dissolved water. To prevent the calcite crystal dissolving, the water had been pre-saturated with calcium carbonate, before equilibration with the toluene. This approach prevents the presence of water at a concentration above the saturated limit.

Interestingly, and unexpectedly, data below in Figure 7.4 show no significant difference in the adsorption of the stearic acid compared with toluene containing water, suggesting that competition with this amount of water has little/no effect on the adsorption of stearic acid from toluene on calcite. The water is usually expected to outcompete the acid for the calcite surface (evident by lower amounts of acid adsorbed from bulk water). This suggests the chemical potential of the water is not

enough to outcompete the acid.

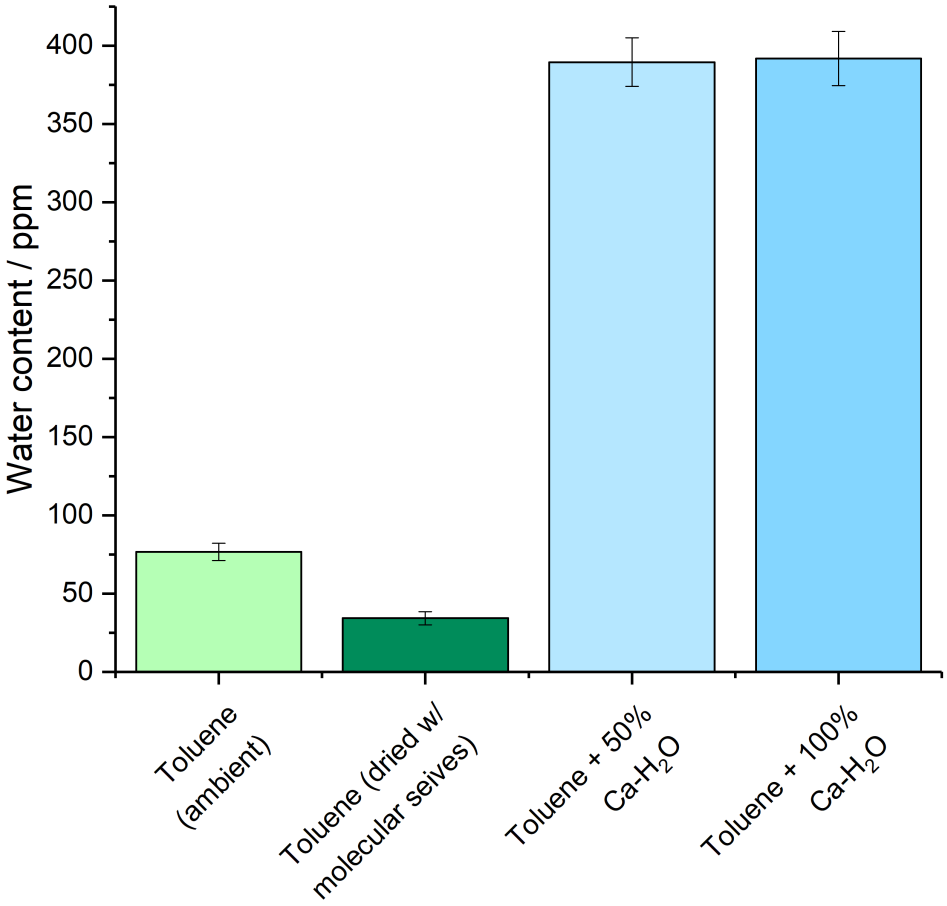

Figure 7.3: Water content of solvents used analysed via Karl Fischer titration. Error is standard deviation.

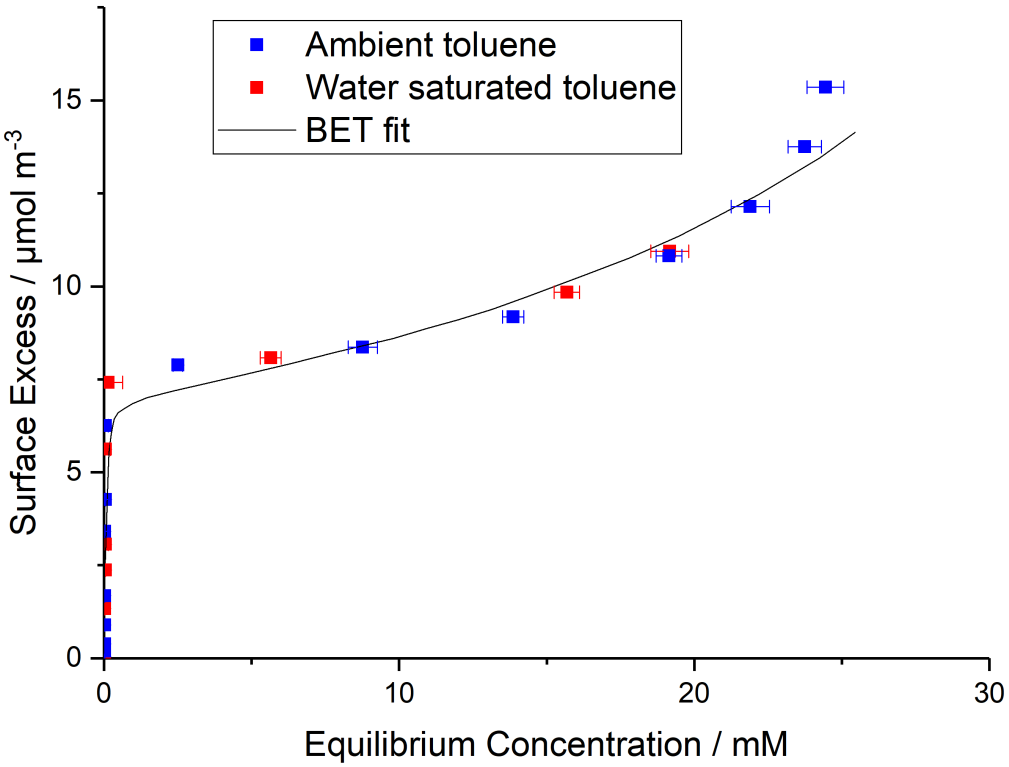

Figure 7.4: Adsorption isotherm of stearic acid on calcite from toluene saturated in water, fitted to a BET isotherm (black).

7.4 Neutron Reflectometry

For NR, initially, the bare calcite substrates were characterised with pure toluene, then 30 mM stearic acid in toluene was used to characterise the adsorption of the acid. Finally, a combination of stearic acid in toluene and water was used to investigate the possibility of competitive adsorption between the acid and water and any surface dissolution. Two crystals were used in the study: the location of adsorbed stearic acid was the focus of the investigation with Crystal 1, and Crystal 2 was used to focus on the location of any adsorbed water. In each case, appropriate selective deuteration/protonation was used to highlight the component of interest. Table 7.1 shows the material SLDs used in this study.

Material	**Formula**	**SLD / x 10^{-6} Å^{-2}**
Calcite	$CaCO_3$	4.69
CaO	CaO	3.77
$Ca(OH)_2$	$Ca(OH)_2$	1.59
H-stearic acid	$CH_3(CH_2)16CO_2H$	-0.07
D-stearic acid	$CD_3(CD_2)16CO_2H$	7.40
H-toluene	C_7H_8	0.95
D-toluene	C_7D_8	5.67
H-water	H_2O	-0.50
D-water	D_2O	6.34

Table 7.1: SLDs of materials used in this study.

7.4.1 Adsorption of a stearic acid monolayer

NR data obtained from Crystal 1 with pure H-toluene, pure D-toluene, and a solution of H-stearic acid in dry D-toluene are shown in Figure 7.5 (left) along with model fits. The H-acid in D-solvent contrast used with Crystal 1 is most sensitive to the presence of an adsorbed acid layer on the calcite surface and structural features of the layer. The pronounced change in reflectivity evident in Figure 7.5 on the addition of stearic acid to the D-toluene is clear evidence of the formation of a monolayer of stearic acid, which is in good agreement with depletion data above.

The reflectivity profiles from Crystal 1 with pure D-toluene and with a solution of H-stearic acid in D-toluene were fitted simultaneously. In order to minimise the number of fitted parameters, it was assumed that the surface layers are conformal (i.e. they have the same roughness as the calcite substrate): the roughnesses of the interfaces were not fixed in the fitting process, but they were constrained to take the same value. The background scattering levels could usually be read directly from the data, rather than requiring fitting.

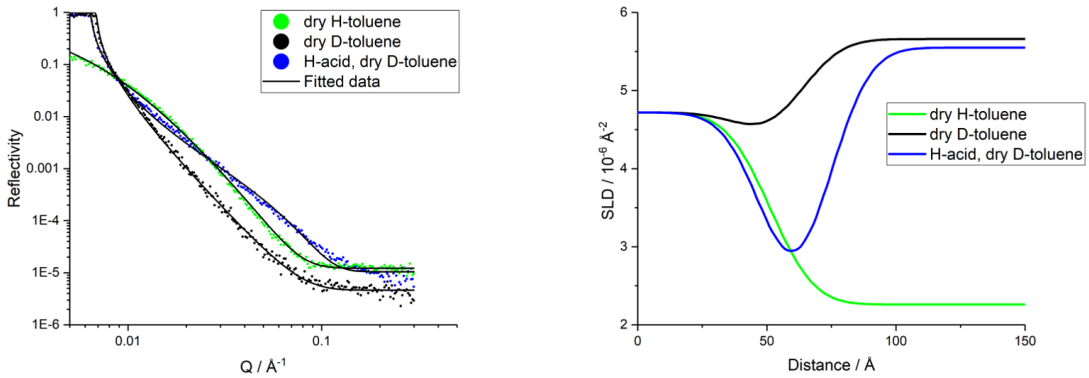

Figure 7.5: (left) NR data from Crystal 1 exposed to pure D-toluene, pure H-toluene, and a solution of H-stearic acid in D-toluene; (right) SLD profile fitted to the data

Figure 7.5 (left) indicates that there is a very small shift in the critical edge from the data obtained with D-toluene to that obtained with H-stearic acid in D-toluene, attributed to incomplete solvent exchange. When initially filled with pure D-toluene, the fitting gives an SLD that is in very good agreement with the expected value (5.67 x 10^{-6} Å^{-2}), but the sample run after exchanging from H-toluene indicates a very slightly lower SLD (5.55 x 10^{-6} Å^{-2}), implying that a small amount of H-toluene remains. Therefore, SLDs of the continuous phases were determined from the position of the critical edge, where present, further constraining the fitting process.

Calcite surface

Each calcite crystal will have a surface roughness and surface composition that is specific to that crystal. The surface layer is a result of atmospheric moisture, producing calcium hydroxide. Once the surface layer is characterised, the same parameters are used for all other contrasts with the same crystal.

For Crystal 1, the roughness was determined to be 13.5 (± 0.5) Å. There is some evidence of a region of low SLD on the bare surface, which could have several origins, including calcium oxides or hydroxides formed by reaction with water in the air or adventitious organic deposits. Our previous work has demonstrated that UV-ozone is the best way to remove any organics, and this method was employed here.[251]

The thickness and SLD of the low SLD calcite surface layer are found to be coupled when fitting the data, with a lower SLD and a thicker layer fitting the data as well as a higher SLD and a thinner layer. Importantly, the parameters of the fitted stearic

acid layer do not depend significantly on which model is adopted for the low SLD region. Hence, the structural characterisation of the stearic acid, that is of most interest here, is not affected by the surface layer model used. The surface layer on Crystal 1 was therefore taken to be calcium hydroxide, and the SLD was fixed (at 1.59 x 10^{-6} Å^{-2}) with a layer thickness from the fitting process of 4.6 (± 0.3) Å.

Stearic acid layer

The H-stearic acid adsorbed from D-toluene was modelled as a single layer, with its thickness and SLD allowed to vary in the fitting minimisation. Any D-toluene included in the layer would increase the SLD; as such, the value was constrained between the SLDs of pure H-stearic acid (-0.07 x 10^{-6} Å^{-2}) and pure D-toluene (5.67 x 10^{-6} Å^{-2}). The SLD obtained (-0.06 (± 0.1) x 10^{-6} Å^{-2}) is very close to the lower bound of the range, indicating an essentially pure H-stearic acid layer. The thickness of the acid layer was found to be 12.2 (± 0.2) Å. This is somewhat smaller than expected for the fully extended alkyl chain and may imply that the molecules are inclined on the surface.

7.4.2 Reversible adsorption of a stearic acid monolayer

Additional NR experiments on Crystal 1 in Figure 7.6 below indicate that exchanging the solution of stearic acid in toluene for pure toluene (or vice versa) led to desorption (and re-adsorption) of the stearic acid layer. This reversibility of the adsorption indicates that the strength of interaction between the stearic acid and the calcite surface is relatively weak, suggesting that physisorption is more likely than chemisorption.

7.4.3 Influence of addition of water

The reflectivity profile obtained from Crystal 1 was not significantly changed when the H-stearic acid in dry toluene was replaced with H-stearic acid in 'D_2O-wet' toluene, containing either half of the saturation concentration of water ($C_{sat}/2$) or, as in the data shown in Figure 7.7, the saturation concentration of water (C_{sat}). In both cases, the D_2O was itself pre-saturated with calcium carbonate, as discussed above. As the contrast is most sensitive to the presence of the H-stearic acid, the lack of change indicates that this amount of water does not out-compete the acid that remains adsorbed on the calcite surface. It can be concluded that **dissolved water does not out compete the acid for the calcite surface**.

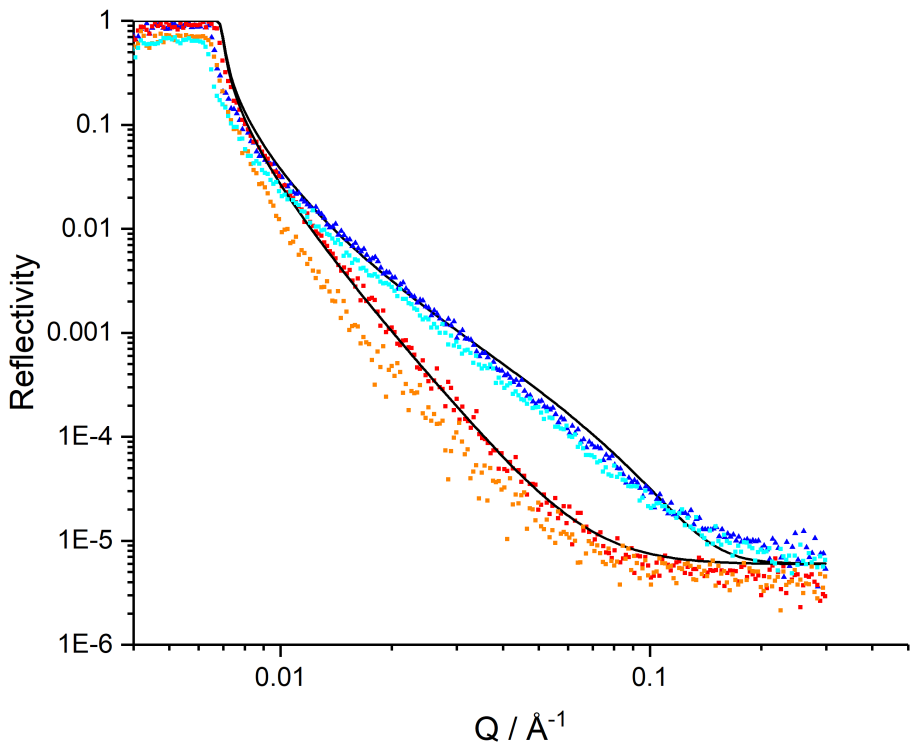

Figure 7.6: The removal and reapplication of stearic acid on calcite in toluene. Initial calcite crystal in toluene (red), addition of stearic acid in toluene (dark blue), addition of pure toluene and removal of stearic acid (orange), reapplication of stearic acid in toluene (light blue)

On addition of a droplet of D_2O, there is a very pronounced change on the reflectivity, particularly the loss of the critical edge (Figure 7.7, green), possibly attributed to a very rough interface. This may have a number of causes, such as dissolution of the calcite surface or deposition/precipitation of significant amounts of solid on the surface.

NR data for Crystal 2 exposed to D-stearic acid solutions in dry and H_2O-saturated D-toluene, and with an extra drop of water added to the H_2O-saturated D-toluene are shown in Figure 7.8. The D-acid in D-toluene contrast used with Crystal 2 is most sensitive to the presence and role of water, H_2O (and changes to the calcite substrate): as the acid and solvent are both deuterated, the reflectivity is not sensitive to the presence of adsorbed acid, and any H_2O present is distinct. As with the D_2O described above, all of the H_2O used was pre-saturated with calcium carbonate, to try to prevent dissolution of the calcite substrate.

As expected, the NR data shown in Figure 7.8 corresponding to D-stearic acid in

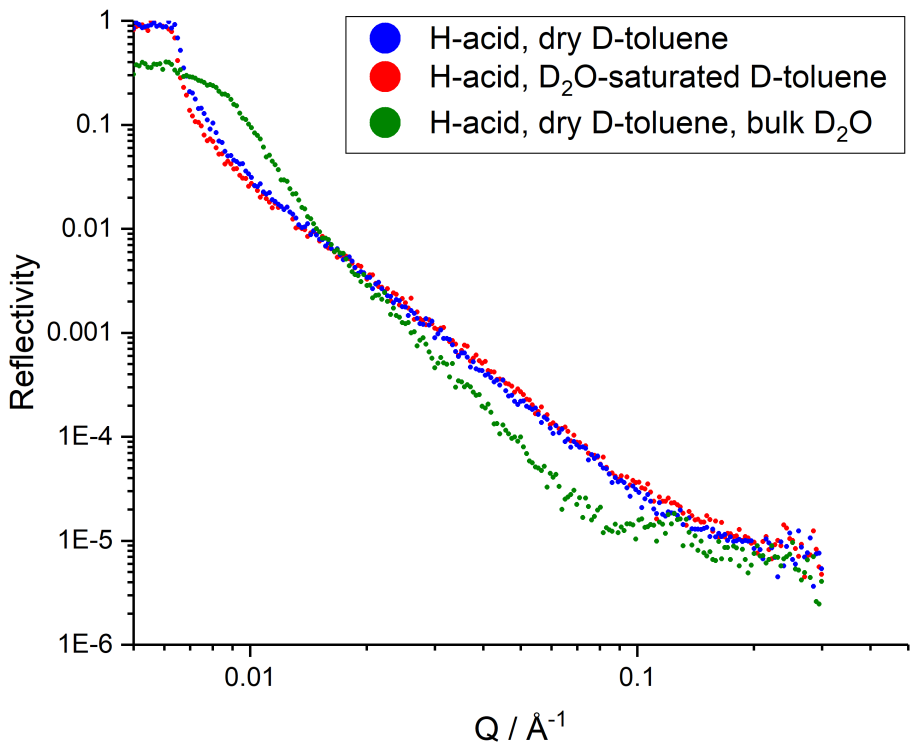

Figure 7.7: NR data from Crystal 1 exposed to H-stearic acid solutions in dry or D_2O-saturated D-toluene (C_{sat}) and upon addition of bulk D_2O

dry D-toluene are very similar to the data obtained when the calcite crystal was characterised in D-toluene only. Replacing the D-acid in dry D-toluene with D-acid in H_2O-saturated D-toluene at $C_{sat}/2$ led to very small changes in reflection and a small change in the level of critical scattering, which may indicate precipitation or dissolution and roughening of the calcite surface. The sample was rerun after realignment to ensure this was not a sample positioning error. Further increase of saturated water to C_{sat}, led to a further drop in the total reflection and addition of a further drop of water led to a very significant change in the reflectivity profile (Figure 7.8 green), particularly a loss of the total reflection intensity. This again suggests either precipitation on or dissolution of the calcite surface.

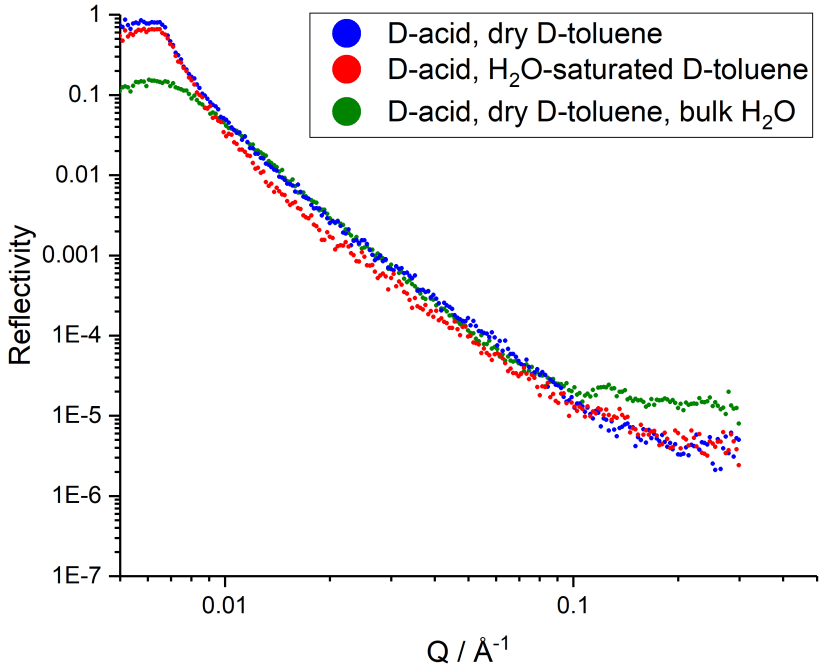

Figure 7.8: NR data from Crystal 2 exposed to D-stearic acid solutions in dry D-toluene, D-toluene saturated with H_2O ($C_{sat}/2$ and C_{sat}), or D-toluene saturated with H_2O with an extra drop of H_2O added (bulk)

7.5 XRR and PXRD

XRR data, shown in Figure 7.9, has been used to characterise calcite crystals before and after the NR experiment, conducted in air. Significantly, the XRR data indicate weak peaks with a periodicity (peaks at 1.7, 3.5 and 5.2 2θ °) typical of the presence of calcium stearate (the pattern from pure calcium stearate is shown in Figure 7.10). Hence, these data suggest that addition of a significant amount of $CaCO_3$ saturated water into stearic acid / toluene solution leads to precipitation of calcium stearate onto the calcite surface. It is this precipitation that leads to the dramatic fall in reflected intensity below the critical angle on adding a drop of water to the toluene.

Calcite dissolution when exposed to $CaCO_3$-saturated or under-saturated water has been previously studied.[193,261] Although pure water rapidly leads to calcite dissolution, $CaCO_3$ pre-saturated water does not dissolve the surface.

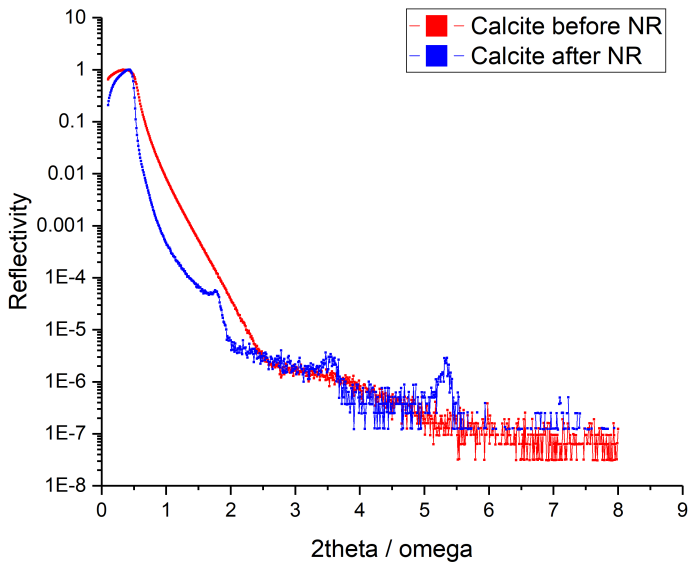

Figure 7.9: XRR measurements on Crystal 1 obtained before (red) and after (blue) the NR experiment. Initial $Ca(OH)_2$ roughness = 12.0 Å, Initial $Ca(OH)_2$ thickness = 30.2 Å; final $Ca(OH)_2$ roughness = 22 Å, $Ca(OH)_2$ thickness = 10 Å. Calcium stearate roughness = 11 Å, Calcium stearate thickness = 7 Å.

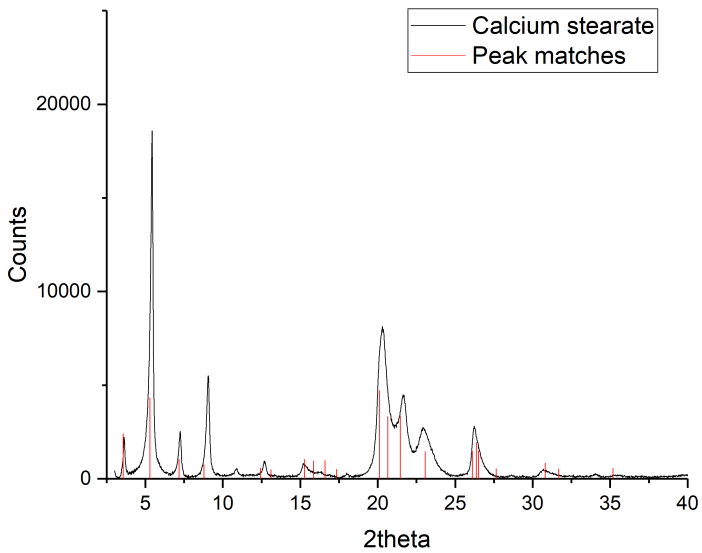

Figure 7.10: Powder X-Ray diffraction of stock calcium stearate (black) and matched calcium stearate peaks from the crystallographic database (red).

7.6 SFG

SFG was run with the assistance of Dr Mike Casford in the Department of Chemistry, University of Cambridge. It is not customary to use birefringent substrates for SFG

due to the complexity of the data and its interpretation. The aim using SFG is to (1) confirm adsorption and (2) deduce conformational disorder.

SFG spectra for stearic acid adsorbed onto a calcite crystal are presented in Figure 7.11. Spectra were collected in the SSP and PPP polarisation combinations over a spectral range of 2800–3000 cm^{-1} to capture the C−H stretching modes. Spectra were recorded both at room temperature and at 60°C in air, the results of which are presented in Figure 7.11 (a) SSP and (b) PPP. The peaks and their assignments are summarised in Table 7.2. Spectral assignments for the methyl and methylene stretches have been aided by comparison with the bands of polymethylene in its IR and Raman spectra.[262,263]

Frequency / cm^{-1}		**Assignment**
PPP	**SSP**	
2846	2848	CH_2 symmetric stretch (d^+)
2870	2876	CH_3 symmetric stretch (r^+)
2910		mixture of CH_2 antisymmetric stretch (d^-) and d^+ Fermi resonance
2958		CH_3 antisymmetric stretch (r^-)
	2934	Fermi resonance of overtone of methyl bending mode with CH_2 symmetric stretch[264,265]

Table 7.2: Summary of SFG peaks in the C−H stretching region.

SSP and PPP spectra were taken at room temperature with the calcite crystal at an initial arbitrary angle of rotation, and then rotated in 15-degree intervals once the scan was completed. The full rotational spectra are given in Figure 7.12.

Assuming a completely all trans well-packed stearic acid monolater, the methylene groups would be locally centrosymmetric and therefore not SFG active. The initial SSP spectrum 7.11 shows a moderate intensity of the CH_2 symmetric stretch (d^+) present at ∼2848 cm^{-1}, which indicates there is some disorder in the alkyl chain, suggesting gauche defects.

Upon rotation of the calcite crystal by 15-degree increments, a marked change in intensity is observed due to the birefringent nature of the calcite crystal. Over the full 360 degree rotation the ratio of the methyl and methylene symmetric stretches, which are used to quantify the degree of conformational disorder as previously described, change very markedly. Due to this, it is not possible to draw firm conclusions as to the degree of conformational disorder present, only that the alkyl chain cannot be in an all trans conformation.

In the SSP both spectra in Figure 7.11 (a) show a moderately strong methylene symmetric stretch at circa 2848 cm^{-1} and a weak methylene symmetric stretch

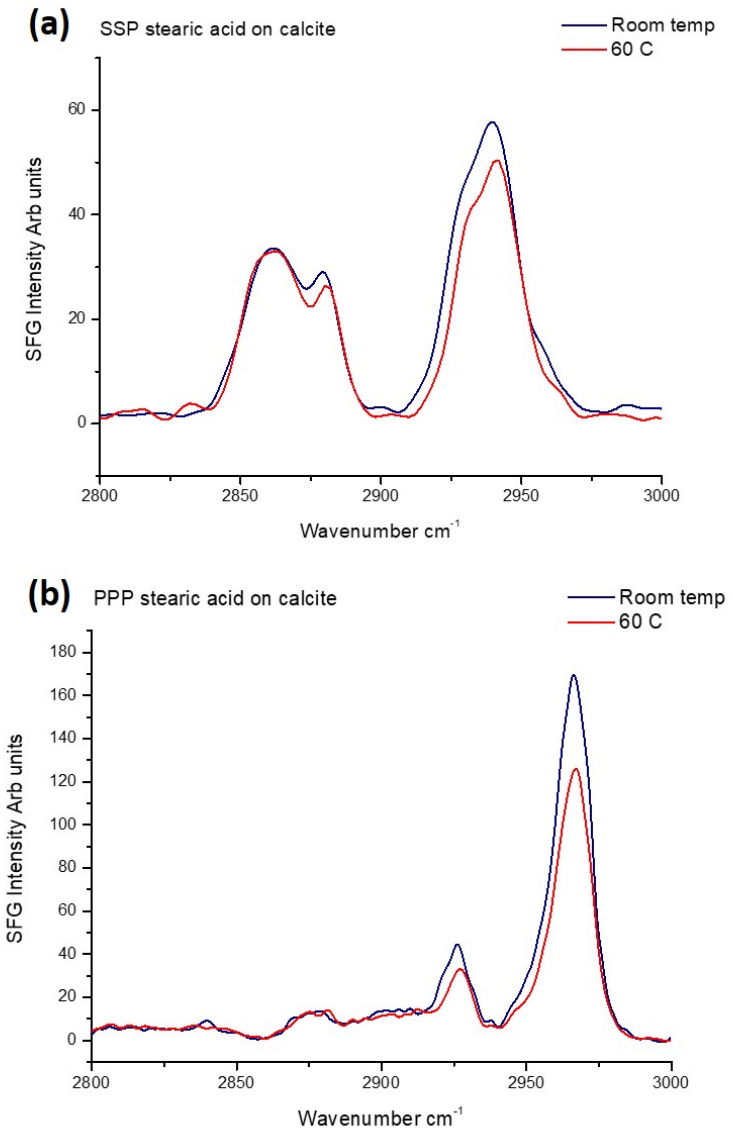

Figure 7.11: SFG of stearic acid on calcite at room temperature and 60 °C. (a) shows SSP polarisation at room temperature (blue) and at 60 °C (red). (b) shows the equivalent PPP polarised spectra.

at circa 2880 cm^{-1} with the methylene mode being marginally weaker in the 60 °C spectra indicating a small decrease in the conformational ordering at higher temperature. In addition, the intensity of the methyl anti symmetric mode at circa 2960 cm^{-1} in the PPP (Figure 7.11 (b)) decreases with increasing temperature suggesting a change in the average methyl tilt angle. On dielectric surfaces the intensity of the methyl anti symmetric mode is at its maximum intensity relative to the methyl symmetric mode at a tilt angle of close to 60 degrees from the surface normal.[266] Taken together this supports a change in orientational ordering with increasing temperature.

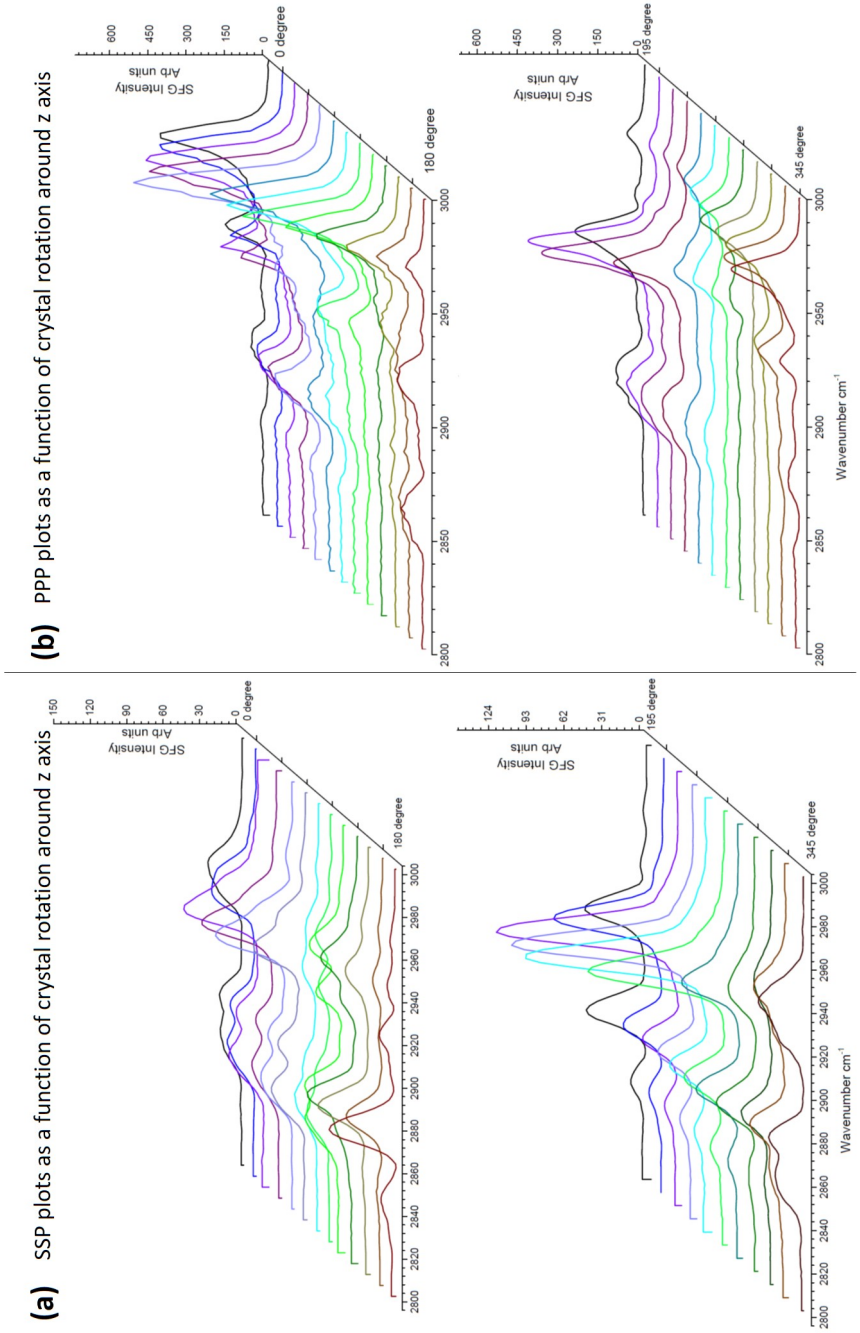

Figure 7.12: SFG spectra of stearic acid on calcite as a function of rotation around the z-axis. (a) SSP polarisation combination and (b) PPP polarisation.

7.7 Conclusions

A combination of depletion isotherms, NR and SFG has been used to probe the adsorption behaviour of stearic acid on calcite from toluene, with and without added water. The stearic acid forms a well-packed monolayer, containing very little toluene and with an all trans conformation, in contrast to the much lower coverages reported when fatty acids adsorb from water on calcite. This difference is particularly interesting when the addition of water to the dry system is also considered. Water-saturated toluene causes very little change in the adsorbed acid, suggesting that, under these conditions, the water does not out-compete the acid to adsorb on the calcite surface. However, once the level of water in the toluene exceeds the saturation concentration, significant surface precipitation of calcium stearate is observed.

The stearic acid monolayer is found to be removable from the calcite surface using pure toluene, and easily reapplied, suggesting physisorption. The adsorption isotherm of stearic acid on calcite in toluene was found to be BET-type and suggests a monolayer is adsorbed and essentially complete at a concentration of 1 mM. Further adsorption occurs at higher concentrations, as the solubility limit of the acid is approached.

The mechanism suggested for this process, illustrated in Figure 7.13, is stearic acid binding to Ca^{2+} ions on the surface, leading to calcium stearate redistributing into the aqueous phase. These results demonstrate that even this essentially close-packed stearic acid monolayer does not protect the calcite surface if it is exposed to free water.

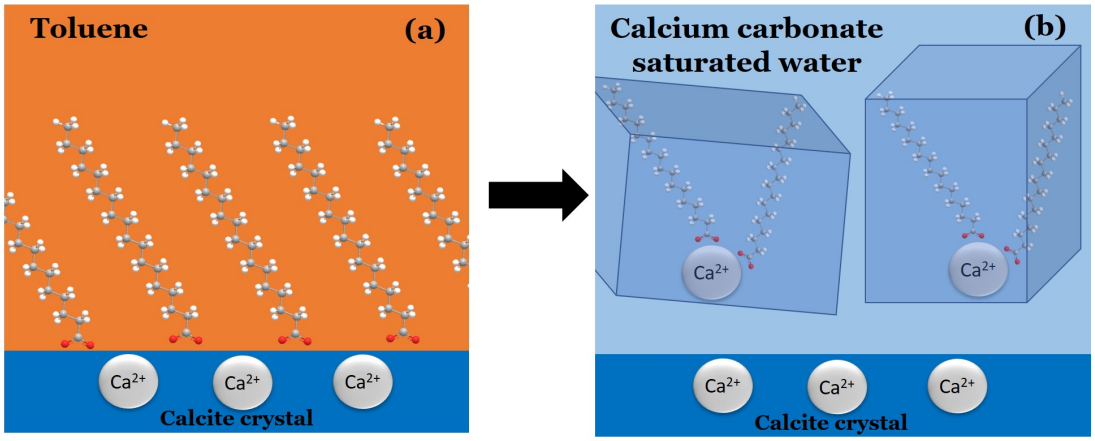

Figure 7.13: Suggested mechanism for the dissolution of the calcite in the presence of stearic acid.

Chapter 8

Conclusions

This thesis has described a range of important aspects that impact oil recovery, particularly adsorption of organics from non-aqueous solutions to mineral surfaces. An approach moving from understanding the complexity of real crude and rock towards a model/single component system has been taken.

1) Characterisation of Real Rock

This stage helped identification of key minerals in reservoir and outcrop core that lined the pore spaces and hence are expected to dominate the rock-fluid interactions. This analysis provided important new insight into the chemical nature of organics adsorbed on the real rock, which could be the foundation for further binding or key to EOR.

Chapter 4 successfully characterised outcrop and reservoir rock samples using a wide range of experimental methods. QEMSCAN was used to assess the underlying mineralogy and importantly distinguishing between bulk and pore-lining mineralogy. This distinction is key to the subsequent work focussing on adsorption. A new image analysis code was developed to help with the analysis that has subsequently been employed by the commercial colleagues. Although QEMSCAN has been utilised by the oil industry before, it has not been used to extract data of pore lining minerals in the way conducted in this thesis. Understanding what minerals line the pores of systems will help choose the correct outcrop with appropriate pore lining minerals to best mimic a reservoir rock during the ageing process.

Data showed that although quartz is the predominant mineral in the bulk of the materials studied here by a significant percentage, the minerals lining pores have

a very different distribution. The number and variety of minerals lining the pores might be important when trying to match an outcrop rock to a reservoir rock prior to an ageing process. This is particularly important as Chapter 5 and 6 (discussed further below) demonstrates different minerals have different adsorption behaviour and would lead to a very different aged product.

Soluble organic molecules were successfully removed using a standard practice Soxhlet extraction. This is shown in an intensity reduction in TOF-SIMS as well as lower carbon content from all pyrolysis techniques. Py-GCMS showed the presence of carbamic acid fragments, which agrees with literature that nitrogen-containing groups as well as acids are present in the irreversibly bound organic layer.

2) Understanding the Ageing Process

After using QEMSCAN to determine the minerals of interest that line the pores of rock, these minerals were independently aged in three different crude oils of varying origin and asphaltene content as well as being pre-treated in DI or brine water or no water.

The most important and novel finding was using HRMS on an aged mica sample: it was found that sulfur containing molecules are most likely the cause of a hydrophobic mica surface when aged in a crude oil with high asphaltene content. Asphaltenes containing sulfur have been detected on mica before but their role in wettability alteration was not clear until now.[267] Understanding what molecules that are native to crude oil can alter wettability on each mineral surface will allow a tunability of wettability within a model rock that could be used for screening EOR methods. The fact that no organics are observed in the powdered materials suggests the organic is binding onto the basal plane rather than edges of mica. Brine appears to form a possible hydrate layer on the mica basal plane, causing organic not to bind in the low asphaltene regime. This finding compliments literature where the combination of clay, brine and asphaltenes are needed for LSEOR.

For untreated powdered quartz, adsorbed nitrogen species are observed via combustion elemental analysis. This correlates with Chapter 4 where nitrogen-containing molecules are detected using Py-GCMS on the quartz-rich reservoir rock. This suggests the irreversibly bound, insoluble and—according to the DSA data—wettability altering molecules on quartz contain nitrogen. This finding is backed up by extensive literature that finds asphaltenes, which contain N, O and S heteroatoms, are the wettability altering molecules on sandstone rock.

Asphaltenes and aromatics are shown to preferentially adsorb onto powdered calcite, observed through SARA analysis of the washing extract and nitrogen content when the organic layer is isolated from dissolving the calcite after ageing. The amount of organic carbon adsorbed is proportional to the amount of asphaltene in the crude oil. Most surprisingly is the loss of carbon when calcite is aged in crude oil from a carbonate well that corresponds to a surface layer of carbonate ions being removed/exchanged. A next step to investigate this system further would be to conduct XPS on the sample, looking at the C 1s and S 2p spectra.

On kaolinite, water inhibits adsorption, irrespective of salt content. Asphaltenes appear to be required for significant adsorption. The delayed adsorption of nitrogen-containing molecules suggest the slow diffusion time for asphaltenic groups when replacing adsorbed smaller aliphatic groups.

Next steps for investigation of all systems should considering utilising HRMS. This powerful technique can begin to deduce molecular groups that are of actually binding onto the mineral surfaces and guide research into model molecules to alter wettability on specific mineral surfaces.

3) Model Systems

A model system was investigated using state of the art techniques in Chapter 7. Stearic acid was adsorbed onto the calcite surface from toluene and characterised using NR, showing a removable and replaceable monolayer of stearic acid layer in pure toluene. The adsorbed stearic acid was removed from the calcite surface upon the addition of wate, forming calcium stearate. The solvent content of the layer was described and even some outline of the conformational order deduced by SFG. These state-of-the-art techniques have not been used for this system before and provide an in-depth understanding of competitive adsorption in binary mixtures.

This study on stearic acid on calcite represents the level of detail now available in favourable cases. Complexity could be increased by investigation of different ions/electrolytes. The interaction between calcite, organics and a brine system should be investigated. Increasing complexity of the system by addition of magnesium, sulfate and chloride ions would allow understanding of the real world system, where these species are common in brine.

Appendix A

QEMSCAN code

Note: The code below works free-standing in Linux or MacOS. For Windows, a CMake method to build the code may be required.

```
/* Program: QEMSCAN code
* Version: 1.0
* Date:    28 September 2018
* Authors: Patrick Welche <prlw1@cam.ac.uk>
*          Belinda Fonseka <bf306@cam.ac.uk>
* Purpose: Calculate fraction of length of void in contact with
*          specific minerals.
*/
#include <array>
#include <cassert>
#include <iostream>
#include <map>
#include <string>

#include <opencv4/highgui.hpp>
#include <opencv4/imgcodecs.hpp>
#include <opencv4/imgproc.hpp>


/* Outcrop rock_2um_phases.png:
* PNG image data, 2356 x 1772, 8-bit/color RGB, non-interlaced
*/
typedef cv::Point3_<uint8_t> Pixel;

std::ostream& operator << (std::ostream& s, uint8_t x) {
   return s << static_cast<unsigned int>(x);
```

```
}

std::ostream& operator << (std::ostream& s, Pixel const& p) {
   return s << '[' << p.x << ' ' << p.y << ' ' << p.z << ']';
}

struct PixelCmp {
   bool operator()(Pixel const& lhs, Pixel const& rhs) const {
      return 10000000*static_cast<uint32_t>(lhs.x)
      + 1000*static_cast<uint32_t>(lhs.y)
      + static_cast<uint32_t>(lhs.z)
      < 10000000*static_cast<uint32_t>(rhs.x)
      + 1000*static_cast<uint32_t>(rhs.y)
      + static_cast<uint32_t>(rhs.z);
   }
};

int main()
{
   std::string const filename("../Outcrop rock_2um_phases.png");
   const char wbefore[] = "before", wafter[] = "after";
   cv::Mat src = cv::imread(filename, cv::IMREAD_COLOR);
   if (src.empty()) {
      std::cerr << "Unable to open \"" << filename << '"'
      << std::endl;
      return 1;
   }

   assert(src.type() == CV_8UC3);

   std::cout << "depth: " << src.depth() << std::endl;
   std::cout << "rows: " << src.rows << std::endl;
   std::cout << "cols: " << src.cols << std::endl;
   std::cout << "channels: " << src.channels() << std::endl;
   std::cout << "type: " << src.type() << std::endl;

   cv::Mat dst; src.copyTo(dst);

   const Pixel space(255,255,255);     /* or border (void) */
   const Pixel quartz(192,192,255);
   const Pixel other(255,255,0);
   const Pixel border(0,0,0);
   const Pixel bulk(128,128,128);      /* bulk void */
   const Pixel quartz_edge(0,0,255);   /* neighbour quartz */
   const Pixel other_edge(255,0,0); /* neighbour other */
```

```

/* - find distribution of pixel values
* - set to "other" pixels which are neither quartz nor space
*/
std::map<Pixel,unsigned int,PixelCmp> hist;
src.forEach<Pixel>([&](const Pixel& p, const int x[]) -> void {
   /* bit of debug
   if (1000 < x[0] && x[0] < 1010 && 1000 < x[1] && x[1] < 1010) {
      std::cout << '(' << x[0] << ',' << x[1] << ") "
      << p << std::endl;
   }
   */
   hist[p] = hist[p] + 1;
   if (!(p == space || p == quartz))
   dst.at<Pixel>(x[0],x[1]) = other;
});

std::cout << "hist size: " << hist.size() << std::endl;
for (auto h : hist)
std::cout << h.first << ": " << h.second << std::endl;

/* get rid of image border */
bool isborder{true};
for (int i = 0; isborder && i < dst.rows; ++i) {
   cv::Mat top = dst.row(i);
   top.forEach<Pixel>([&](const Pixel&p, const int x[]) -> void {
      isborder = isborder && p == space;
   });
   if (isborder) {
      top.forEach<Pixel>([&](Pixel&p, const int x[]) -> void {
         p = border;
      });
   }
}
isborder = true;
for (int i = dst.rows - 1; isborder && i > 0; --i) {
   cv::Mat bottom = dst.row(i);
   bottom.forEach<Pixel>([&](const Pixel&p, const int x[]) -> void {
      isborder = isborder && p == space;
   });
   if (isborder) {
      bottom.forEach<Pixel>([&](Pixel&p, const int x[]) -> void {
         p = border;
      });
   }
```

```
    }
    isborder = true;
    for (int i = 0; isborder && i < dst.cols; ++i) {
        cv::Mat left = dst.col(i);
        left.forEach<Pixel>([&](const Pixel&p, const int x[]) -> void {
            isborder = isborder && (p == space || p == border);
        });
        if (isborder) {
            left.forEach<Pixel>([&](Pixel&p, const int x[]) -> void {
                p = border;
            });
        }
    }
    isborder = true;
    for (int i = dst.cols - 1; isborder && i > 0; --i) {
        cv::Mat right = dst.col(i);
        right.forEach<Pixel>([&](const Pixel&p, const int x[]) -> void {
            isborder = isborder && (p == space || p == border);
        });
        if (isborder) {
            right.forEach<Pixel>([&](Pixel&p, const int x[]) -> void {
                p = border;
            });
        }
    }

    /* set space pixels which are completely surrounded by other
    * space pixels to bulk
    */
    dst.forEach<Pixel>([&](Pixel&p, const int xy[]) -> void {
        int x(xy[0]), y(xy[1]);
        const Pixel& p11 = src.at<Pixel>(x-1,y-1);
        const Pixel& p12 = src.at<Pixel>(x-1,y  );
        const Pixel& p13 = src.at<Pixel>(x-1,y+1);
        const Pixel& p21 = src.at<Pixel>(x  ,y-1);
        const Pixel& p22 = src.at<Pixel>(x  ,y  );
        const Pixel& p23 = src.at<Pixel>(x  ,y+1);
        const Pixel& p31 = src.at<Pixel>(x+1,y-1);
        const Pixel& p32 = src.at<Pixel>(x+1,y  );
        const Pixel& p33 = src.at<Pixel>(x+1,y+1);
        if (p == space) {
            if (p11 == space && p12 == space && p13 == space &&
            p21 == space && p22 == space && p23 == space &&
            p31 == space && p32 == space && p33 == space)
            p = bulk;
```

```
162         }
163     });
164 
165     /* at this point all space pixels are on the edge, so now
166     * count the quartz / not-quartz pixels adjacent to them
167     */
168     unsigned int nquartz{0}, nother{0};
169     dst.forEach<Pixel>([&](Pixel&p, const int xy[]) -> void {
170         if (p == space) {
171             int x(xy[0]), y(xy[1]);
172             std::array<Pixel*, 8> plist;
173             plist[0] = dst.ptr<Pixel>(x-1,y-1);
174             plist[1] = dst.ptr<Pixel>(x-1,y  );
175             plist[2] = dst.ptr<Pixel>(x-1,y+1);
176             plist[3] = dst.ptr<Pixel>(x  ,y-1);
177 
178             plist[4] = dst.ptr<Pixel>(x  ,y+1);
179             plist[5] = dst.ptr<Pixel>(x+1,y-1);
180             plist[6] = dst.ptr<Pixel>(x+1,y  );
181             plist[7] = dst.ptr<Pixel>(x+1,y+1);
182             for (auto pp : plist) {
183                 if (*pp == quartz) {
184                     *pp = quartz_edge;
185                     ++nquartz;
186                 }
187                 if (*pp == other) {
188                     *pp = other_edge;
189                     ++nother;
190                 }
191             }
192         }
193     });
194 
195     /* for display purposes, colour the bulk pixels back to
196     * orginal space colour
197     */
198     dst.forEach<Pixel>([&](Pixel&p, const int xy[]) -> void {
199         if (p == bulk) {
200             p = space;
201         }
202     });
203 
204     std::cout << "nquartz: " << nquartz << std::endl;
205     std::cout << "nother : " << nother  << std::endl;
206     std::cout << "nquartz:nother "
```

```
    << static_cast<double>(nquartz)/(nquartz+nother) << ':'
    << static_cast<double>(nother)/(nquartz+nother)  << std::endl;

    cv::imwrite("outcrop_quartz_analysed.png", dst);

    cv::namedWindow(wbefore, cv::WINDOW_AUTOSIZE);
    cv::imshow(wbefore, src);
    cv::namedWindow(wafter, cv::WINDOW_AUTOSIZE);
    cv::imshow(wafter, dst);
    cv::waitKey(0);

    return 0;
}
```

References

[1] Blok, K., Afanador, A., Van Der Hoorn, I., Berg, T., Edelenbosch, O. Y., Van Vuuren, D. P. Assessment of sectoral greenhouse gas emission reduction potentials for 2030. *Energies* **2020** *13*.

[2] Liu, F., Tait, S., Schellart, A., Mayfield, M., Boxall, J. Reducing carbon emissions by integrating urban water systems and renewable energy sources at a community scale. *Renewable and Sustainable Energy Reviews* **2020** *123*.

[3] Hall, C., Ramírez-Pascualli, C. A. *The First Half of the Age of Oil: An Exploration of the Work of Colin Campbell and Jean Laherrère*. SpringerBriefs in Energy. Springer New York, **2012**.

[4] Morrow, N. R., Mason, G. Recovery of oil by spontaneous imbibition. *Current Opinion in Colloid and Interface Science* **2001** *6*, 321–337.

[5] Reed, R. L., Healy, R. N. Some physiochemical aspects of microemulsion flooding: a review. In *Improved Oil Recovery by Surfactant and Polymer Flooding*. Academic Press, **1977**, pages 383–437.

[6] Babadagli, T. Development of mature oil fields - A review. *Journal of Petroleum Science and Engineering* **2007** *57*, 221–246.

[7] Taber, J., Martin, F., Seright, R. EOR Screening Criteria Revisited - Part 1: Introduction to Screening Criteria and Enhanced Recovery Field Projects. *SPE Reservoir Engineering* **1997** *12*, 189–198.

[8] Bi, Z., Zhang, Z., Xu, F., Qian, Y., Yu, J. Wettability, Oil Recovery, and Interfacial Tension with an SDBS-Dodecane-Kaolin System. *Journal of colloid and interface science* **1999** *214*, 368–372.

[9] Stegemeier, G. L. Relationship of Trapped Oil Saturation to Petrophysical Properties of Porous Media , **1974**.

[10] Dullien, F. A. L., Dhawan, G. K., Gurak, N., Babjak, L. A Relationship

Between Pore Structure and Residual Oil Saturation in Tertiary Surfactant Floods. *Society of Petroleum Engineers Journal* **1972** *12*, 289–296.

[11] Anderson, W. G. Wettability Literature Survey- Part 1: Rock/Oil/Brine Interactions and the Effects of Core Handling on Wettability. *Journal of Petroleum Technology* **1986** *38*, 1125–1144.

[12] Kimbler, O. K., Reed, R. L., Silberberg, I. H. Physical Characteristics of Natural Films Formed at Crude Oil-Water Interfaces. *Society of Petroleum Engineers Journal* **1966** *6*, 153–165.

[13] Bobek, J. E., Mattax, C. C., Denekas, M. O. Reservoir rock wettability—its significance and evaluation. *Trans. AIME* **1958** *213*, 155–160.

[14] Anderson, W. Wettability Literature Survey- Part 2: Wettability Measurement. *Journal of Petroleum Technology* **1986** *38*, 1246–1262.

[15] Anderson, W. G. Wettability Literature Survey-Part 3: The Effects of Wettability on the Electrical Properties of Porous Media. *Journal of Petroleum Technology* **1986** *38*, 1371–1378.

[16] Anderson, W. G. Wettability Literature Survey- Part 4: Effects of Wettability on Capillary Pressure. *Journal of Petroleum Technology* **1987** *39*, 1283–1300.

[17] Anderson, W. G. Wettability Literature Survey Part 5: The Effects of Wettability on Relative Permeability. *Journal of Petroleum Technology* **1987** *39*, 1453–1468.

[18] Anderson, W. G. Wettability Literature Survey-Part 6: The Effects of Wettability on Waterflooding. *Journal of Petroleum Technology* **1987** *39*, 1605–1622.

[19] Rezaeidoust, A., Puntervold, T., Strand, S., Austad, T. Smart water as wettability modifier in carbonate and sandstone: A discussion of similarities/differences in the chemical mechanisms. *Energy and Fuels* **2009** *23*, 4479–4485.

[20] Liu, L., Buckley, J. S. Alteration of wetting of mica surfaces. *Journal of Petroleum Science and Engineering* **1999** *24*, 75–83.

[21] Buckley, J. S. Effective wettability of minerals exposed to crude oil. *Current Opinion in Colloid & Interface Science* **2001** *6*, 191–196.

[22] Ahkami, M., Chakravarty, K. H., Xiarchos, I., Thomsen, K., Fosbøl, P. L.

Determining optimum aging time using novel core flooding equipment. In *Society of Petroleum Engineers - SPE Bergen One Day Seminar*. Society of Petroleum Engineers, **2016**.

[23] Graue, A., Aspenes, E., Bogno, T., Moe, R. W., Ramsdal, J. Alteration of wettability and wettability heterogeneity. *Journal of Petroleum Science and Engineering* **2002** *33*, 3–17.

[24] Jadhunandan, P., Morrow, N. Effect of Wettability on Waterflood Recovery for Crude-Oil/Brine/Rock Systems. *SPE Reservoir Engineering* **1995** *10*, 40–46.

[25] Barclay, S. A., Worden, R. H. Effects of Reservoir Wettability on Quartz Cementation in Oil Fields. In *Quartz Cementation in Sandstones*. Blackwell Publishing Ltd., Oxford, UK, **2009**, pages 103–117.

[26] Van Geet, M., Swennen, R., Wevers, M. Quantitative analysis of reservoir rocks by microfocus X-ray computerised tomography. *Sedimentary Geology* **2000** *132*, 25–36.

[27] Xiao, D., Jiang, S., Thul, D., Lu, S., Zhang, L., Li, B. Impacts of clay on pore structure, storage and percolation of tight sandstones from the Songliao Basin, China: Implications for genetic classification of tight sandstone reservoirs. *Fuel* **2018** *211*, 390–404.

[28] Liu, M., Shabaninejad, M., Mostaghimi, P. Predictions of permeability, surface area and average dissolution rate during reactive transport in multi-mineral rocks. *Journal of Petroleum Science and Engineering* **2018** *170*, 130–138.

[29] Ma, K., Jiang, H., Li, J., Zhao, L. Experimental study on the micro alkali sensitivity damage mechanism in low-permeability reservoirs using QEMSCAN. *Journal of Natural Gas Science and Engineering* **2016** *36*, 1004–1017.

[30] Fang, W., Jiang, H., Li, J., Li, W., Li, J., Zhao, L., Feng, X. A new experimental methodology to investigate formation damage in clay-bearing reservoirs. *Journal of Petroleum Science and Engineering* **2016** *143*, 226–234.

[31] Robin, M., Rosenberg, E., Fassi-Fihri, O. Wettability studies at the pore level: a new approach by use of Cryo-SEM. *SPE Formation Evaluation* **1995** *March*, 11.

[32] Rao, A., Kumar, S., Annink, C., Le-Anh, D., Ayirala, S. C., Alotaibi, M. B., Siretanu, I., Duits, M. H. G., Yousef, A. A., Mugele, F. Mineral Interfaces

and Oil Recovery: A Microscopic View on Surface Reconstruction, Organic Modification, and Wettability Alteration of Carbonates. *Energy & Fuels* **2020** *34*, 5611–5622.

[33] Morrow, N. R. Wettability and Its Effect on Oil Recovery. *Journal of Petroleum Technology* **1990** *42*, 1476–1484.

[34] Pan, C., Feng, J., Tian, Y., Yu, L., Luo, X., Sheng, G., Fu, J. Interaction of oil components and clay minerals in reservoir sandstones. *Organic Geochemistry* **2005** *36*, 633–654.

[35] Gupta, R., Mohanty, K. K. Wettability Alteration Mechanism for Oil Recovery from Fractured Carbonate Rocks. *Transport in Porous Media* **2011** *87*, 635–652.

[36] Andersson, M. P., Dideriksen, K., Sakuma, H., Stipp, S. L. S. Modelling how incorporation of divalent cations affects calcite wettability-implications for biomineralisation and oil recovery. *Scientific reports* **2016** *6*, 28854.

[37] Qi, Z., Wang, Y., He, H., Li, D., Xu, X. Wettability Alteration of the Quartz Surface in the Presence of Metal Cations. *Energy & Fuels* **2013** *27*, 7354–7359.

[38] Hou, B.-f., Wang, Y.-f., Huang, Y. Mechanistic study of wettability alteration of oil-wet sandstone surface using different surfactants. *Applied Surface Science* **2015** *330*, 56–64.

[39] Abdallah, W., Gmira, A. Wettability Assessment and Surface Compositional Analysis of Aged Calcite Treated with Dynamic Water. *Energy & Fuels* **2014** *28*, 1652–1663.

[40] Puntervold, T., Mamonov, A., Aghaeifar, Z., Frafjord, G. O., Moldestad, G. M., Strand, S., Austad, T. Role of Kaolinite Clay Minerals in Enhanced Oil Recovery by Low Salinity Water Injection. *Energy & Fuels* **2018** *32*, 7374–7382.

[41] Song, W., Kovscek, A. R. Functionalization of micromodels with kaolinite for investigation of low salinity oil-recovery processes. *Lab on a Chip* **2015** *15*, 3314–3325.

[42] Al Hadabi, I., Sasaki, K., Sugai, Y. Effect of Kaolinite on Water-in-Oil Emulsion Formed by Steam Injection during Tertiary Oil Recovery: A Case Study of an Omani Heavy Oil Sandstone Reservoir with a High Kaolinite Sludge Content. *Energy & Fuels* **2016** *30*, 10917–10924.

[43] Jalqczuk, B., Biae˜piotrowicz, T. Components of Surface Free Energy of Some Clay Minerals. *Clays and Clay Minerals* **1988** *36*, 243–248.

[44] Myint, P. C., Firoozabadi, A. Thin liquid films in improved oil recovery from low-salinity brine. *Current Opinion in Colloid & Interface Science* **2015** *20*, 105–114.

[45] Haagh, M. E., Schilderink, N., Duits, M. H., Siretanu, I., Krawiec, P., Collins, I. R., Mugele, F. Aging brine-dependent deposition of crude oil components onto mica substrates, and its consequences for wettability. *Fuel* **2020** *274*, 117856.

[46] Yang, S.-Y., Hirasaki, G. J., Basu, S., Vaidya, R. Statistical analysis on parameters that affect wetting for the crude oil/brine/mica system. *Journal of Petroleum Science and Engineering* **2002** *33*, 203–215.

[47] Mugele, F., Siretanu, I., Kumar, N., Bera, B., Wang, L., de Ruiter, R., Maestro, A., Duits, M., van den Ende, D., Collins, I. Insights From Ion Adsorption and Contact-Angle Alteration at Mineral Surfaces for Low-Salinity Waterflooding. *SPE Journal* **2016** *21*, 1204–1213.

[48] Griffin, L. R., Browning, K. L., Lee, S. Y., Skoda, M. W. A., Rogers, S., Clarke, S. M. Multilayering of Calcium Aerosol-OT at the Mica/Water Interface Studied with Neutron Reflection: Formation of a Condensed Lamellar Phase at the CMC. *Langmuir* **2016** *32*, 13054–13064.

[49] Griffin, L. R., Browning, K. L., Truscott, C. L., Clifton, L. A., Clarke, S. M. Complete Bilayer Adsorption of C 16 TAB on the Surface of Mica Using Neutron Reflection. *The Journal of Physical Chemistry B* **2015** *119*, 6457–6461.

[50] Mugele, F., Siretanu, I., Kumar, N., Bera, B., Wang, L., Maestro, A., Duits, M., van den Ende, D., Collins, I. Charge Control And Wettability Alteration At Solid-liquid Interfaces. *SPE Improved Oil Recovery Symposium* **2014** , 12.

[51] Kruge, M. A., Gallego, J. L. R., Lara-Gonzalo, A., Esquinas, N. Chapter 7 - Environmental Forensics Study of Crude Oil and Petroleum Product Spills in Coastal and Oilfield Settings: Combined Insights From Conventional GC–MS, Thermodesorption–GC–MS, and Pyrolysis–GC–MS. Butterworth-Heinemann, **2018**, pages 131–155.

[52] Stoddart, D. P., Hall, P. B., Larter, S. R., Brasher, J., Li, M., Bjorøy, M. The

reservoir geochemistry of the Eldfisk Field, Norwegian North Sea. *Geological Society, London, Special Publications* **1995** *86*, 257–279.

[53] AlRatrout, A., Blunt, M. J., Bijeljic, B. Wettability in complex porous materials, the mixed-wet state, and its relationship to surface roughness. *Proceedings of the National Academy of Sciences* **2018** *115*, 8901 LP – 8906.

[54] Yang, D., Gu, Y., Tontiwachwuthikul, P. Wettability determination of the crude oil-reservoir brine-reservoir rock system with dissolution of CO2 at high pressures and elevated temperatures. *Energy and Fuels* **2008** *22*, 2362–2371.

[55] Zeng, H., Tessarolo, N., Gonzalez, D., Gramin, P., Wicking, C., Pietrobon, M. "Sticky molecules" on rock surface might play an important role in formation damage due to asphaltene deposition. *Fuel* **2020** *277*, 117983.

[56] Wicking, C., Tessarolo, N., Savvoulidi, M., Crouch, J., Collins, I., Couves, J., Kot, E., Banks, N., Hodges, M., Zeng, H. Sequential extraction and characterization of the organic layer on sandstone reservoir rock surface. *Fuel* **2020** *276*, 118062.

[57] Tessarolo, N., Wang, N., Wicking, C., Collins, I., Webb, K., Couves, J., Crouch, J., Durkan, C., Zeng, H. Identification of organic species with "double-sided tape" characteristics on the surface of carbonate reservoir rock. *Fuel* **2020** , 119627.

[58] Buckley, J. S. Asphaltene Precipitation and Crude Oil Wetting. *SPE Advanced Technology Series* **1995** *3*, 53–59.

[59] Buckley, J. S., Liu, Y., Monsterleet, S. Mechanisms of Wetting Alteration by Crude Oils. *SPE Journal* **1998** *3*, 54–61.

[60] Andersen, S. I., Hofsäss, T., Kleinitz, W., Rahimian, I. Organic precipitates in oil production of a Venezuelan oil field. *Petroleum Science and Technology* **2001** *19*, 55–74.

[61] Klein, G. C., Kim, S., Rodgers, R. P., Marshall, A. G., Yen, A., Asomaning, S. Mass Spectral Analysis of Asphaltenes. I. Compositional Differences between Pressure-Drop and Solvent-Drop Asphaltenes Determined by Electrospray Ionization Fourier Transform Ion Cyclotron Resonance Mass Spectrometry. *Energy & Fuels* **2006** *20*, 1965–1972.

[62] Aquino-Olivos, M. A., Andersen, S. I., Lira-Galeana, C. Comparisons Between

Asphaltenes from the Dead and Live-Oil Samples of the Same Crude Oils. *Petroleum Science and Technology* **2003** *21*, 1017–1041.

[63] Subramanian, S., Simon, S., Sjöblom, J. Asphaltene Precipitation Models: A Review. *Journal of Dispersion Science and Technology* **2016** *37*, 1027–1049.

[64] Sjöblom, J., Simon, S., Xu, Z. Model molecules mimicking asphaltenes. *Advances in Colloid and Interface Science* **2015** *218*, 1–16.

[65] Ancheyta, J., Centeno, G., Trejo, F., Marroquín, G., García, J. A., Tenorio, E., Torres, A. Extraction and characterization of asphaltenes from different crude oils and solvents. *Energy and Fuels* **2002** *16*, 1121–1127.

[66] Wilhelms, A., Patience, R., Larter, S., Jørgensen, S. Nitrogen functionality distributions in asphaltenes isolated from several oils from different source rock types. *Geochimica et Cosmochimica Acta* **1992** *56*, 3745–3750.

[67] Subramanian, S., Simon, S., Gao, B., Sjöblom, J. Asphaltene fractionation based on adsorption onto calcium carbonate: Part 1. Characterization of sub-fractions and QCM-D measurements. *Colloids and Surfaces A: Physicochemical and Engineering Aspects* **2016** *495*, 136–148.

[68] Pan, C., Geng, A., Liao, Z., Xiong, Y., Fu, J., Sheng, G. Geochemical characterization of free versus asphaltene-sorbed hydrocarbons in crude oils: Implications for migration-related compositional fractionations. *Marine and Petroleum Geology* **2002** *19*, 619–632.

[69] Deo, M., Parra, M. Characterization of Carbon-Dioxide-Induced Asphaltene Precipitation. *Energy & Fuels* **2012** *26*, 2672–2679.

[70] Cuiec, L. Rock/Crude-Oil Interactions and Wettability: An Attempt To Understand Their Interrelation, **1984**.

[71] Agrawala, M., Yarranton, H. W. An asphaltene association model analogous to linear polymerization. *Industrial & engineering chemistry research* **2001** *40*, 4664–4672.

[72] Kuznicki, T., Masliyah, J. H., Bhattacharjee, S. Molecular Dynamics Study of Model Molecules Resembling Asphaltene-Like Structures in Aqueous Organic Solvent Systems. *Energy & Fuels* **2008** *22*, 2379–2389.

[73] Akbarzadeh, K., Bressler, D. C., Wang, J., Gawrys, K. L., Gray, M. R., Kilpatrick, P. K., Yarranton, H. W. Association Behavior of Pyrene Compounds as Models for Asphaltenes. *Energy & Fuels* **2005** *19*, 1268–1271.

[74] Tan, X., Fenniri, H., Gray, M. R. Pyrene Derivatives of 2,2-Bipyridine as Models for Asphaltenes: Synthesis, Characterization, and Supramolecular Organization. *Energy & Fuels* **2008** *22*, 715–720.

[75] Nordgård, E. L., Landsem, E., Sjöblom, J. Langmuir Films of Asphaltene Model Compounds and Their Fluorescent Properties. *Langmuir* **2008** *24*, 8742–8751.

[76] Andreatta, G., Goncalves, C. C., Buffin, G., Bostrom, N., Quintella, C. M., Arteaga-Larios, F., Pérez, E., Mullins, O. C. Nanoaggregates and Structure-Function Relations in Asphaltenes. *Energy & Fuels* **2005** *19*, 1282–1289.

[77] Zeng, H., Song, Y.-Q., Johnson, D. L., Mullins, O. C. Critical Nanoaggregate Concentration of Asphaltenes by Direct-Current (DC) Electrical Conductivity. *Energy & Fuels* **2009** *23*, 1201–1208.

[78] Simon, S., Jestin, J., Palermo, T., Barré, L. Relation between Solution and Interfacial Properties of Asphaltene Aggregates. *Energy & Fuels* **2009** *23*, 306–313.

[79] Acevedo, S., Ranaudo, M. A., García, C., Castillo, J., Fernández, A. Adsorption of Asphaltenes at the Toluene-Silica Interface: A Kinetic Study. *Energy & Fuels* **2003** *17*, 257–261.

[80] Pan, C., Yang, J., Fu, J., Sheng, G. Molecular correlation of free oil and inclusion oil of reservoir rocks in the Junggar Basin, China. *Organic Geochemistry* **2003** *34*, 357–374.

[81] Jelavić, S., Nielsen, A. R., Blažanović, M., Bovet, N., Bechgaard, K., Stipp, S. L. S. Effects of Cleaning Treatments on the Surface Composition of Porous Materials. *Energy & Fuels* **2018** *32*, 4655–4661.

[82] Adams, J. J. Asphaltene adsorption, a literature review. *Energy and Fuels* **2014** *28*, 2831–2856.

[83] Mitchell, A. G., Hazell, L. B., Webb, K. J. Wettability determination. Pore surface analysis. In *Proceedings - SPE Annual Technical Conference and Exhibition*, volume Gamma. Society of Petroleum Engineers, **1990**, pages 351–360.

[84] Taheri-Shakib, J., Hosseini, S. A., Kazemzadeh, E., Keshavarz, V., Rajabi-Kochi, M., Naderi, H. Experimental and mathematical model

evaluation of asphaltene fractionation based on adsorption in porous media: Dolomite reservoir rock. *Fuel* **2019** *245*, 570–585.

[85] Taheri-Shakib, J., Rajabi-Kochi, M., Kazemzadeh, E., Naderi, H., Salimidelshad, Y., Esfahani, M. R. A comprehensive study of asphaltene fractionation based on adsorption onto calcite, dolomite and sandstone. *Journal of Petroleum Science and Engineering* **2018** *171*, 863–878.

[86] George, S. C., Krieger, F. W., Eadington, P. J., Quezada, R. A., Greenwood, P. F., Eisenberg, L. I., Hamilton, P., Wilson, M. A. Geochemical comparison of oil-bearing fluid inclusions and produced oil from the Toro sandstone, Papua New Guinea. *Organic Geochemistry* **1997** *26*, 155–173.

[87] Schwark, L., Stoddart, D., Keuser, C., Spitthoff, B., Leythaeuser, D. A novel sequential extraction system for whole core plug extraction in a solvent flow-through cell - Application to extraction of residual petroleum from an intact pore-system in secondary migration studies. *Organic Geochemistry* **1997** *26*, 19–31.

[88] López, L., Lo Mónaco, S. Vanadium, nickel and sulfur in crude oils and source rocks and their relationship with biomarkers: Implications for the origin of crude oils in Venezuelan basins. *Organic Geochemistry* **2017** *104*, 53–68.

[89] Subramanian, S., Sørland, G. H., Simon, S., Xu, Z., Sjöblom, J. Asphaltene fractionation based on adsorption onto calcium carbonate: Part 2. Self-association and aggregation properties. *Colloids and Surfaces A: Physicochemical and Engineering Aspects* **2017** *514*, 79–90.

[90] Ganeeva, Y. M., Barskaya, E. E., Yusupova, T. N., Okhotnikova, E. S., Sotnikov, O. S., Remeev, M. M., Khisamov, R. S. Comparative Analysis of Organic Matter of Reservoir Rocks and Domanik Deposits of the Bavly Oil Field. *Petroleum Chemistry* **2020** *60*, 255–263.

[91] Li, M., Larter, S. R., Stoddart, D., Bjorøy, M. Fractionation of pyrrolic nitrogen compounds in petroleum during migration: derivation of migration-related geochemical parameters. *Geological Society, London, Special Publications* **1995** *86*, 103–123.

[92] Abdallah, W. A., Taylor, S. D. Study of asphaltenes adsorption on metallic surface using XPS and TOF-SIMS. *Journal of Physical Chemistry C* **2008** *112*, 18963–18972.

[93] Prado, G. H. C., Rao, Y., de Klerk, A. Nitrogen Removal from Oil: A Review. *Energy & Fuels* **2017** *31*, 14–36.

[94] Collins, I. R., Couves, J. W., Hodges, M., McBride, E. K., Pedersen, C. S., Salino, P. A., Webb, K. J., Wicking, C., Zeng, H. Effect of low salinity waterflooding on the chemistry of the produced crude oil. In *Proceedings - SPE Symposium on Improved Oil Recovery*, volume 2018-April. Society of Petroleum Engineers (SPE), **2018**, pages 14–18.

[95] Martin, J. C. The Effects of Clay on the Displacement of Heavy Oil by Water, **1959**.

[96] Bernard, G. G. Effect of Floodwater Salinity on Recovery Of Oil from Cores Containing Clays, **1967**.

[97] Thomas, B. G., Iliyas, A., Johansen, T. E., Hawboldt, K., Khan, F. Towards Sustainable and Environmentally Friendly Enhanced Oil Recovery in Offshore Newfoundland, Canada, **2010**.

[98] Tang, G. Q., Morrow, N. R. Salinity, Temperature, Oil Composition, and Oil Recovery by Waterflooding. *SPE Reservoir Engineering* **1997** *12*, 269–276.

[99] Ayirala, S. C. C., Yousef, A. A. A. A State-of-the-Art Review To Develop Injection-Water-Chemistry Requirement Guidelines for IOR/EOR Projects. *SPE Production & Operations* **2015** *30*, 26–42.

[100] Buckley, J. S., Wang, J. Crude oil and asphaltene characterization for prediction of wetting alteration. *Journal of Petroleum Science and Engineering* **2002** *33*, 195–202.

[101] Alvarado, V., Garcia-Olvera, G., Hoyer, P., Lehmann, T. E. Impact of Polar Components on Crude Oil-Water interfacial Film Formation: A Mechanisms for Low-Salinity Waterflooding , **2014**.

[102] Morrow, N. R., Tang, G. Q., Valat, M., Xie, X. Prospects of improved oil recovery related to wettability and brine composition. *Journal of Petroleum Science and Engineering* **1998** *20*, 267–276.

[103] Pouryousefy, E., Xie, Q., Saeedi, A. Effect of multi-component ions exchange on low salinity EOR: Coupled geochemical simulation study. *Petroleum* **2016** *2*, 215–224.

[104] Zhang, P., Tweheyo, M. T., Austad, T. Wettability alteration and improved oil recovery by spontaneous imbibition of seawater into chalk: Impact of the

potential determining ions Ca2+, Mg2+, and SO42-. *Colloids and Surfaces A: Physicochemical and Engineering Aspects* **2007** *301*, 199–208.

[105] Yuan, Y., Lee, T. R. Contact Angle and Wetting Properties. In G. Bracco, B. Holst, eds., *Surface Science Techniques*. Springer Berlin Heidelberg, Berlin, Heidelberg, **2013**, pages 3–34.

[106] Joanny, J. F., de Gennes, P. G. A model for contact angle hysteresis. *The Journal of Chemical Physics* **1984** *81*, 552–562.

[107] Vargaftik, N. B., Volkov, B. N., Voljak, L. D. International Tables of the Surface Tension of Water. *Journal of Physical and Chemical Reference Data* **1983** .

[108] Horozov, T. S., Binks, B. P. Colloidal Particles at Liquid Interfaces. In T. S. Horozov, B. P. Binks, eds., *Colloidal Particles at Liquid Interfaces*, chapter Particles. Cambridge University Press, Cambridge, **2006**, 1st edition, pages 1–77.

[109] Lafuma, A., Quéré, D. Superhydrophobic states. *Nature Materials* **2003** *2*, 457–460.

[110] Schwartz, A. M., Minor, F. W. A simplified thermodynamic approach to capillarity. *Journal of Colloid Science* **1959** *14*, 572–583.

[111] Savory, L. D. *Enhanced Oil Recovery by Flooding with Surfactant Solution: A Model Study and Comparison with Theory*. Ph.D. thesis, University of Hull, **2015**.

[112] Galet, L., Patry, S., Dodds, J. Determination of the wettability of powders by the Washburn capillary rise method with bed preparation by a centrifugal packing technique. *Journal of Colloid and Interface Science* **2010** *346*, 470–475.

[113] Kirdponpattara, S., Phisalaphong, M., Newby, B.-m. Z. Applicability of Washburn capillary rise for determining contact angles of powders/porous materials. *Journal of Colloid and Interface Science* **2013** *397*, 169–176.

[114] Susana, L., Campaci, F., Santomaso, A. C. Wettability of mineral and metallic powders: Applicability and limitations of sessile drop method and Washburn's technique. *Powder Technology* **2012** *226*, 68–77.

[115] Thakker, M., Karde, V., Shah, D. O., Shukla, P., Ghoroi, C. Wettability

measurement apparatus for porous material using the modified Washburn method. *Measurement Science and Technology* **2013** *24*, 125902.

[116] Dang-Vu, T., Hupka, J. Characterisation of porous materials by capillary rise method. *Physicochemical Problems of Mineral Processing* **2005** *39*, 47–65.

[117] Mielczarski, J. A. Encyclopedia of Surface and Colloid Science, Second Edition. In A. T. Hubbard, P. Somasundaran, eds., *Encyclopedia of Surface and Colloid Science, Second Edition*, volume 8. Taylor & Francis, New York, **2006**, pages 5965–5978.

[118] Iler, R. K. . The chemistry of silica. Solubility, polymerization, colloid and surface properties, and biochemistry. *Acta Polymerica* **1980** *31*, 406–406.

[119] Peng, L., Qisui, W., Xi, L., Chaocan, Z. Investigation of the states of water and OH groups on the surface of silica. *Colloids and Surfaces A: Physicochemical and Engineering Aspects* **2009** *334*, 112–115.

[120] Young, G. J. Interaction of water vapor with silica surfaces. *Journal of Colloid Science* **1958** *13*, 67–85.

[121] Zhuravlev, L. T. The surface chemistry of amorphous silica. Zhuravlev model. *Colloids and Surfaces A: Physicochemical and Engineering Aspects* **2000** *173*, 1–38.

[122] Howie, R. A. R. J. Reeder, ed. Carbonates: Mineralogy and Chemistry (Reviews in Mineralogy, Volume l 1). Washington, DC (Mineral Society of America), 1983. *Mineralogical Magazine* **1984** *48*, 394.

[123] Lide, D. R. CRC Handbook of Chemistry and Physics: A Ready-Reference of Chemical and Physical Data. In D. R. Lide, ed., *Journal of the American Chemical Society*, 12. American Chemical Society, **2005**, 85 edition, page 4542.

[124] Butler, J. N. *Carbon Dioxide Equilibria and Their Application*. Addison-Wesley, Reading, Massachusetts, **1982**, 1st edition.

[125] Plummer, L., Busenberg, E. The solubilities of calcite, aragonite and vaterite in CO2-H2O solutions between 0 and 90°C, and an evaluation of the aqueous model for the system CaCO3-CO2-H2O. *Geochimica et Cosmochimica Acta* **1982** *46*, 1011–1040.

[126] Somasundaran, P., Zhang, L. Adsorption of surfactants on minerals for wettability control in improved oil recovery processes. *Journal of Petroleum Science and Engineering* **2006** *52*, 198–212.

[127] Moulin, P., Roques, H. Zeta potential measurement of calcium carbonate. *Journal of Colloid and Interface Science* **2003** *261*, 115–126.

[128] Smallwood, P. V. Some aspects of the surface chemistry of calcite and aragonite - Part II: Crystal growth. *Colloid and Polymer Science Kolloid-Zeitschrift & Zeitschrift für Polymere* **1977** *255*, 994–1000.

[129] Somasundaran, P., Agar, G. E. The zero point of charge of calcite. *Journal of Colloid And Interface Science* **1967** *24*, 433–440.

[130] Thompson, D. W., Pownall, P. G. Surface electrical properties of calcite. *Journal of Colloid And Interface Science* **1989** *131*, 74–82.

[131] Vdović, N. Electrokinetic behaviour of calcite - The relation with other calcite properties. *Chemical Geology* **2001** *177*, 241–248.

[132] Fimbel, P., Siffert, B. Interaction of calcium carbonate (calcite) with cellulose fibres in aqueous medium. *Colloids and Surfaces* **1986** *20*, 1–16.

[133] Vdović, N., Kralj, D. Electrokinetic properties of spontaneously precipitated calcium carbonate polymorphs: The influence of organic substances. *Colloids and Surfaces A: Physicochemical and Engineering Aspects* **2000** *161*, 499–505.

[134] Knowles-Van Cappellen, V. L., Van Cappellen, P., Tiller, C. L. Probing the charge of reactive sites at the mineral-water interface: Effect of ionic strength on crystal growth kinetics of fluorite. *Geochimica et Cosmochimica Acta* **1997** *61*, 1871–1877.

[135] Vdović, N., Bišćan, J. Electrokinetics of natural and synthetic calcite suspensions. *Colloids and Surfaces A: Physicochemical and Engineering Aspects* **1998** *137*, 7–14.

[136] Stipp, S. L. Toward a conceptual model of the calcite surface: Hydration, hydrolysis, and surface potential. *Geochimica et Cosmochimica Acta* **1999** *63*, 3121–3131.

[137] van Olphen, H. *An Introduction to Clay Colloid Chemistry.* John Wiley & Sons, Ltd, London, **1977**, 2nd edition.

[138] Meunier, A. Clays. In *Clays.* Springer New York, Berlin, New York, **2005**, page 488.

[139] Civan, F. Overview of Formation Damage. In *Reservoir Formation Damage*, chapter 1. Elsevier Inc., Burlington, **2007**, 2nd edition, pages 1–9.

[140] Grim, R. E. Clay mineralogy. In *Clay mineralogy.* McGraw-Hill, New York, **1968**, page 616.

[141] Gupta, V., Hampton, M. A., Stokes, J. R., Nguyen, A. V., Miller, J. D. Particle interactions in kaolinite suspensions and corresponding aggregate structures. *Journal of Colloid and Interface Science* **2011** *359*, 95–103.

[142] Gupta, V., Miller, J. D. Surface force measurements at the basal planes of ordered kaolinite particles. *Journal of Colloid and Interface Science* **2010** *344*, 362–371.

[143] Grim, R. E. Clay mineralogy. In *Clay mineralogy.* McGraw-Hill, New York, **1953**, page 408.

[144] Wang, Y. H., Siu, W. K. Structure characteristics and mechanical properties of kaolinite soils. I. Surface charges and structural characterizations. *Canadian Geotechnical Journal* **2006** *43*, 587–600.

[145] Zbik, M. S., Smart, R. S., Morris, G. E. Kaolinite flocculation structure. *Journal of Colloid and Interface Science* **2008** *328*, 73–80.

[146] Zbik, M. S., Frost, R. L. Micro-structure differences in kaolinite suspensions. *Journal of Colloid and Interface Science* **2009** *339*, 110–116.

[147] Du, J., Morris, G., Pushkarova, R. A., St. C. Smart, R. Effect of Surface Structure of Kaolinite on Aggregation, Settling Rate, and Bed Density. *Langmuir* **2010** *26*, 13227–13235.

[148] Mungan, N. Permeability Reduction Through Changes in pH and Salinity. *Journal of Petroleum Technology* **1965** *17*, 1449–1453.

[149] de Poel, W., Pintea, S., Drnec, J., Carla, F., Felici, R., Mulder, P., Elemans, J. A. A. W., van Enckevort, W. J. P., Rowan, A. E., Vlieg, E. Muscovite mica: Flatter than a pancake. *Surface Science* **2014** *619*, 19–24.

[150] Schlegel, M. L., Nagy, K. L., Fenter, P., Cheng, L., Sturchio, N. C., Jacobsen, S. D. Cation sorption on the muscovite (0 0 1) surface in chloride solutions using high-resolution X-ray reflectivity. *Geochimica et Cosmochimica Acta* **2006** *70*, 3549–3565.

[151] Nishimura, S., Biggs, S., Scales, P. J., Healy, T. W., Tsunematsu, K., Tateyama, T. Molecular-Scale Structure of the Cation Modified Muscovite Mica Basal Plane. *Langmuir* **1994** *10*, 4554–4559.

[152] Scales, P. J., Grieser, F., Healy, T. W. Electrokinetics of the muscovite mica-aqueous solution interface. *Langmuir* **1990** *6*, 582–589.

[153] Stern, O. Zur theorie der elektrolytischen doppelschicht. *Zeitschrift für Elektrochemie und angewandte physikalische Chemie* **1924** *30*, 508–516.

[154] Wood, M. H. *Adsorption at the metal/liquid interface.* Ph.D. thesis, University of Cambridge, **2015**.

[155] Giles, C. H., Smith, D., Huitson, A. A general treatment and classification of the solute adsorption isotherm. I. Theoretical. *Journal of Colloid and Interface Science* **1974** *47*, 755–765.

[156] Wheeler, D. H., Potente, D., Wittcoff, H. Adsorption of dimer, trimer, stearic, oleic, linoleic, nonanoic and azelaic acids on ferric oxide. *Journal of the American Oil Chemists' Society* **1971** *48*, 125–128.

[157] Jelinek, L., sz Kováts, E. True Surface Areas from Nitrogen Adsorption Experiments. *Langmuir* **1994** *10*, 4225–4231.

[158] Krüss GmbH. Force Tensiometer – K100, **2015**.

[159] Potts, P. J., Webb, P. C. X-ray fluorescence spectrometry. *Journal of Geochemical Exploration* **1992** *44*, 251–296.

[160] Hagan, R. C., Hagan, R. C. X-Ray-Fluorescence Analysis Major Elements in Silicate Minerals. Technical Report September, Los Alamos National Laboratory, **1982**.

[161] Tour, T. E. L. Analysis of rocks using X-Ray Fluorescence. *The Rigaku Journal* **1989** *6*, 3–9.

[162] Gottlieb, P., Wilkie, G., Sutherland, D., Ho-Tun, E., Suthers, S., Perera, K., Jenkins, B., Spencer, S., Butcher, A., Rayner, J. Using quantitative electron microscopy for process mineralogy applications. *JOM* **2000** *52*, 24–25.

[163] Haberlah, D., Strong, C., Pirrie, D., Rollinson, G. K., Gottlieb, P., Botha, P. P., Butcher, A. R. Automated petrography applications in Quaternary Science. *Quaternary Australasia* **2011** *28*, 3–12.

[164] Katzenberg, M. A. Stable Isotope Analysis: A Tool for Studying Past Diet, Demography, and Life History. In *Biological Anthropology of the Human Skeleton: Second Edition.* John Wiley & Sons, Inc., Hoboken, NJ, USA, **2007**, pages 411–441.

[165] Kendall, C., Sklash, C., Bullen, T. D. Isotope tracers on water and solute sources in catchments. In *Solute modelling in catchment systems*. Wiley, New York, **1995**, pages 261–303.

[166] Kendall, C., McDonnell, J. J. Isotope Tracers in Catchment Hydrology. In *Fundamentals of Isotope Geochemistry*, chapter 2. Elsevier Science B.V., Amsterdam, **1998**, pages 51–58.

[167] Binkley, D., Vitousek, P. Plant Physiological Ecology: Field methods and instrumentation. In J. R. Ehleriner, C. B. Osmond, eds., *Plant Physiological Ecology: Field methods and instrumentation*, chapter 13. Springer Netherlands, **1989**, pages 281–300.

[168] Hilton, R. G., Galy, V., Gaillardet, J., Dellinger, M., Bryant, C., O'Regan, M., Gröcke, D. R., Coxall, H., Bouchez, J., Calmels, D. Erosion of organic carbon in the Arctic as a geological carbon dioxide sink. *Nature* **2015** *524*, 84–87.

[169] Taylor, K. G., Gawthorpe, R. L. Basin-scale dolomite cementation of shoreface sandstones in response to sea-level fall. *Bulletin of the Geological Society of America* **2003** *115*, 1218–1229.

[170] Taylor, K. G., Machent, P. G. Systematic sequence-scale controls on carbonate cementation in a siliciclastic sedimentary basin: Examples from Upper Cretaceous shallow marine deposits of Utah and Coloradao, USA. *Marine and Petroleum Geology* **2010** *27*, 1297–1310.

[171] Newport, L. P., Aplin, A. C., Gluyas, J. G., Greenwell, H. C., Gröcke, D. R. Geochemical and lithological controls on a potential shale reservoir: Carboniferous Holywell Shale, Wales. *Marine and Petroleum Geology* **2016** *71*, 198–210.

[172] Pucher, H., Schwaiger, N., Feiner, R., Ellmaier, L., Pucher, P., Chernev, B., Siebenhofer, M. Biofuel production from liquid phase pyrolysis oil: A two-step HDO process. *Green Chemistry* **2015** *17*, 1291–1298.

[173] Xu, X., Zhang, C., Liu, Y., Zhai, Y., Zhang, R. Two-step catalytic hydrodeoxygenation of fast pyrolysis oil to hydrocarbon liquid fuels. *Chemosphere* **2013** *93*, 652–660.

[174] Hammer, N. L., Garrido, R. A., Starcevich, J., Coe, C. G., Satrio, J. A. Two-Step Pyrolysis Process for Producing High Quality Bio-oils. *Industrial & Engineering Chemistry Research* **2015** *54*, 10629–10637.

[175] Rubakhin, S. S., Sweedler, J. V., Springer-Verlag. *Mass spectrometry imaging [electronic resource] : principles and protocols / edited by Stanislav S. Rubakhin, Jonathan V. Sweedler.* . New York : Humana Press, c2010., New York, **2010**.

[176] Oran, U., Ünveren, E., Wirth, T., Unger, W. E. S. Poly-dimethyl-siloxane (PDMS) contamination of polystyrene (PS) oligomers samples: A comparison of time-of-flight static secondary ion mass spectrometry (TOF-SSIMS) and X-ray photoelectron spectroscopy (XPS) results. *Applied Surface Science* **2004** *227*, 318–324.

[177] Rivière, J. C., Myhra, S. *Handbook of Surface and Interface Analysis.* CRC Press, **1998**.

[178] Kamga, A. W., Behar, F., Hatcher, P. G. Quantitative Analysis of Long Chain Fatty Acids Present in a Type I Kerogen Using Electrospray Ionization Fourier Transform Ion Cyclotron Resonance Mass Spectrometry: Compared with BF3/MeOH Methylation/GC-FID. *Journal of the American Society for Mass Spectrometry* **2014** *25*, 880–890.

[179] Cristofolini, L. Synchrotron X-ray techniques for the investigation of structures and dynamics in interfacial systems. *Current Opinion in Colloid & Interface Science* **2014** *19*, 228–241.

[180] Daillant, J., Alba, M. High-resolution x-ray scattering measurements: I. Surfaces. *Reports on Progress in Physics* **2000** *63*, 1725–1777.

[181] Chen, C.-H., Ma´lkova, S., Cho, W., Schlossman, M. L. Configuration of membrane-bound proteins by x-ray reflectivity, **2012**.

[182] Abeles, F. Sur l'itération des matrices carrées a quatre éléments. *Annals of physics* **1950** *5*, 777–782.

[183] Penfold, J., Thomas, R. K. The application of the specular reflection of neutrons to the study of surfaces and interfaces, **1990**.

[184] Daillant, J., Gibaud, A., eds. *X-ray and Neutron Reflectivity*, volume 770 of *Lecture Notes in Physics.* Springer Berlin Heidelberg, Berlin, Heidelberg, **2009**.

[185] Sivia, D. S. *Elementary Scattering Theory: For X-ray and Neutron Users.* Oxford University Press, Oxford, **2011**.

[186] Zemb, T., Lindner, P. *Neutrons, X-rays and Light: Scattering Methods Applied to Soft Condensed Matter*. North-Holland delta series. Elsevier, **2002**.

[187] Roe, R. J., Roe, P. *Methods of X-ray and Neutron Scattering in Polymer Science*. Topics in polymer science : a series of advanced textbooks and monographs. Oxford University Press, **2000**.

[188] Newport, R. J. Neutron scattering at a pulsed source. In R. J. Newport, B. D. Rainford, R. Cywinski, eds., *Neutron scattering at a pulsed source*, volume 24. Adam Hilger, **1988**, pages 304–324.

[189] Hughes, A. RasCAL, https://sourceforge.net/projects/rscl/, **2014**.

[190] Nelson, A. Co-refinement of multiple-contrast neutron/X-ray reflectivity data using MOTOFIT. *Journal of Applied Crystallography* **2006** *39*, 273–276.

[191] Nelson, A. Motofit– integrating neutron reflectometry acquisition, reduction and analysis into one, easy to use, package. *Journal of Physics: Conference Series* **2010** *251*, 12094.

[192] Parratt, L. G. Surface Studies of Solids by Total Reflection of X-Rays. *Physical Review* **1954** *95*, 359–369.

[193] Stocker, I. N., Miller, K. L., Lee, S. Y., Welbourn, R. J., Mannion, A. R., Collins, I. R., Webb, K. J., Wildes, A., Kinane, C. J., Clarke, S. M. Neutron reflection at the calcite-liquid interface. *Progress in Colloid and Polymer Science* **2011** *139*, 91–99.

[194] Houston, S. Email correspondance from BP plc.

[195] Klobes, P., Riesemeier, H., Meyer, K., Goebbels, J., Hellmuth, K.-H. Rock porosity determination by combination of X-ray computerized tomography with mercury porosimetry. *Fresenius' Journal of Analytical Chemistry* **1997** *357*, 543–547.

[196] Zhang, L., Lu, X., Liu, X., Yang, K., Zhou, H. Surface Wettability of Basal Surfaces of Clay Minerals: Insights from Molecular Dynamics Simulation. *Energy & Fuels* **2016** *30*, 149–160.

[197] Breen, C., Clegg, F., Herron, M. M., Hild, G. P., Hillier, S., Hughes, T. L., Jones, T. G. J., Matteson, A., Yarwood, J. Bulk mineralogical characterisation of oilfield reservoir rocks and sandstones using Diffuse Reflectance Infrared Fourier Transform Spectroscopy and Partial Least Squares analysis. *Journal of Petroleum Science and Engineering* **2008** *60*, 1–17.

[198] Karlsen, D. A., Nedkvitne, T., Larter, S. R., Bjørlykke, K. Hydrocarbon composition of authigenic inclusions: Application to elucidation of petroleum reservoir filling history. *Geochimica et Cosmochimica Acta* **1993** *57*, 3641–3659.

[199] Radivojevic, I., Bazzan, G., Burton-Pye, B. P., Ithisuphalap, K., Saleh, R., Durstock, M. F., Francesconi, L. C., Drain, C. M. Zirconium(IV) and hafnium(IV) porphyrin and phthalocyanine complexes as new dyes for solar cell devices. *Journal of Physical Chemistry C* **2012** *116*, 15867–15877.

[200] John Plater, M., Aiken, S., Bourhill, G. Metallated porphyrins containing lead(II), copper(II) or zinc(II). *Tetrahedron* **2002** *58*, 2415–2422.

[201] Treibs, A. Chlorophyll- und Häminderivate in organischen Mineralstoffen. *Angewandte Chemie* **1936** *49*, 682–686.

[202] Http://www.chem.ucalgary.ca/courses/353/laboratory/spec_tables.pdf. Spectroscopic Tables, **2016**.

[203] Https://www.cpp.edu/~lsstarkey/courses/NMR/NMRshifts1H-general.pdf. H-NMR Chemical Shifts, **2017**.

[204] Jennings, K. R. *Spectrometric identification of organic compounds (Fifth Edition)*, volume 26. John Wiley & Sons, Ltd, New York, **1991**, 5th edition.

[205] Simoneit, B. R. T. A review of current applications of mass spectrometry for biomarker/molecular tracer elucidations. *Mass Spectrometry Reviews* **2005** *24*, 719–765.

[206] Pan, C., Liu, D. Molecular correlation of free oil, adsorbed oil and inclusion oil of reservoir rocks in the Tazhong Uplift of the Tarim Basin, China. *Organic Geochemistry* **2009** *40*, 387–399.

[207] Meier, L. P., Menegatti, A. P. A new, efficient, one-step method for the removal of organic matter from clay- containing sediments. *Clay Minerals* **1997** *32*, 557–563.

[208] Allen, F. H., Kennard, O., Watson, D. G., Brammer, L., Orpen, A. G., Taylor, R. Tables of bond lengths determined by X-ray and neutron diffraction. Part 1. Bond lengths in organic compounds. *Journal of the Chemical Society, Perkin Transactions 2* **1987** , S1–S19.

[209] Combes, J. R., White, L. D., Tripp, C. P. Chemical Modification of Metal

Oxide Surfaces in Supercritical CO2. In Situ Infrared Studies of the Adsorption and Reaction of Organosilanes on Silica. *Langmuir* **1999** *15*, 7870–7875.

[210] Ozawa, T. A New Method of Analyzing Thermogravimetric Data. *Bulletin of the Chemical Society of Japan* **1965** *38*, 1881–1886.

[211] Friedman, H. L. Kinetics of thermal degradation of char-forming plastics from thermogravimetry. Application to a phenolic plastic. *Journal of Polymer Science Part C: Polymer Symposia* **2007** *6*, 183–195.

[212] Doyle, C. D. Estimating isothermal life from thermogravimetric data. *Journal of Applied Polymer Science* **1962** *6*, 639–642.

[213] Larsen, J. W., Tepley, L. B. Effect of aqueous alcoholic solvents on counterion-binding to CTAB micelles. *Journal of Colloid and Interface Science* **1974** *49*, 113–118.

[214] 577-11-7 - Dioctyl sulfosuccinate sodium salt, 96% - Docusate sodium - Bis(2-ethylhexyl)sulfosuccinate sodium salt - 44203 - Alfa Aesar.

[215] Walsh, R. Bond dissociation energy values in silicon-containing compounds and some of their implications. *Accounts of Chemical Research* **1981** *14*, 246–252.

[216] Buriak, J. M. Organometallic chemistry on silicon and germanium surfaces. *Chemical Reviews* **2002** *102*, 1271–1308.

[217] Fusi, N., Martinez-Martinez, J. Mercury porosimetry as a tool for improving quality of micro-CT images in low porosity carbonate rocks. *Engineering Geology* **2013** *166*, 272–282.

[218] Moradi, M., Topchiy, E., Lehmann, T. E., Alvarado, V. Impact of ionic strength on partitioning of naphthenic acids in water–crude oil systems – Determination through high-field NMR spectroscopy. *Fuel* **2013** *112*, 236–248.

[219] Al-Mahrooqi, S. H., Grattoni, C. A., Moss, A. K., Jing, X. D. An investigation of the effect of wettability on NMR characteristics of sandstone rock and fluid systems. *Journal of Petroleum Science and Engineering* **2003** *39*, 389–398.

[220] Guan, H., Brougham, D., Sorbie, K., Packer, K. Wettability effects in a sandstone reservoir and outcrop cores from NMR relaxation time distributions. *Journal of Petroleum Science and Engineering* **2002** *34*, 35–54.

[221] Dang, S. T., Sondergeld, C. H., Rai, C. S. Interpretation of

Nuclear-Magnetic-Resonance Response to Hydrocarbons: Application to Miscible Enhanced-Oil-Recovery Experiments in Shales. *SPE Reservoir Evaluation & Engineering* **2018** *22*, 302–309.

[222] Cornwell, C. F. *Sequence stratigraphy and chemostratigraphy of an incised valley fill within the cretaceous blackhawk formation, Book cliffs, Utah.* Ph.D. thesis, Virginia Polytechnic Institute and State University, **2012**.

[223] Qi, Y., Ju, Y., Tan, J., Bowen, L., Cai, C., Yu, K., Zhu, H., Huang, C., Zhang, W. Organic matter provenance and depositional environment of marine-to-continental mudstones and coals in eastern Ordos Basin, China—Evidence from molecular geochemistry and petrology. *International Journal of Coal Geology* **2020** *217*, 103345.

[224] Abdallah, W. A., Taylor, S. D. Surface characterization of adsorbed asphaltene on a stainless steel surface. *Nuclear Instruments and Methods in Physics Research Section B: Beam Interactions with Materials and Atoms* **2007** *258*, 213–217.

[225] Jarrahian, K., Seiedi, O., Sheykhan, M., Sefti, M. V., Ayatollahi, S. Wettability alteration of carbonate rocks by surfactants: A mechanistic study. *Colloids and Surfaces A: Physicochemical and Engineering Aspects* **2012** *410*, 1–10.

[226] Dembicki Jr., H., Horsfield, B., Ho, T. T. Y. Source Rock Evaluation by Pyrolysis-Gas Chromatography. *AAPG Bulletin* **1983** *67*, 1094–1103.

[227] Baraka-Lokmane, S., Main, I. G., Ngwenya, B. T., Elphick, S. C. Application of complementary methods for more robust characterization of sandstone cores. *Marine and Petroleum Geology* **2009** *26*, 39–56.

[228] Lewan, M. D., Maynard, J. B. Factors controlling enrichment of vanadium and nickel in the bitumen of organic sedimentary rocks. *Geochimica et Cosmochimica Acta* **1982** *46*, 2547–2560.

[229] Barwise, A. J. Role of Nickel and Vanadium in Petroleum Classification. *Energy and Fuels* **1990** *4*, 647–652.

[230] Hitchon, B., Filby, R. H. Use of trace elements for classification of crude oils into families - example from Alberta, Canada. *A.A.P.G. Bulletin* **1984** *68*, 838–840.

[231] Peters, C. A., Hallmann, C., George, S. C. Phenolic compounds in oil-bearing

fluid inclusions: Implications for water-washing and oil migration. *Organic Geochemistry* **2018** *118*, 36–46.

[232] Larter, S. R., Aplin, A. C. Reservoir geochemistry: methods, applications and opportunities. *Geological Society, London, Special Publications* **1995** *86*, 5–32.

[233] Badertscher, M., Bischofberger, K., Munk, M. E., Pretsch, E. A Novel Formalism To Characterize the Degree of Unsaturation of Organic Molecules. *Journal of Chemical Information and Computer Sciences* **2001** *41*, 889–893.

[234] Szykuła, K. M., Wicking, C., Whitmarsh, S., Creaser, C. S., Reynolds, J. C. Characterization of Crude Oil and Its Saturate, Aromatic, and Resin Fractions by High-Field Asymmetric Waveform Ion Mobility Spectrometry-High-Resolution Mass Spectrometry. *Energy and Fuels* **2018** *32*, 11310–11316.

[235] Liu, Y., Buckley, J. S. Evolution of wetting alteration by adsorption from crude oil. *SPE Formation Evaluation* **1997** *12*, 5–11.

[236] Rouquerol, F., Rouquerol, J., Sing, K., eds. *Adsorption by powders and porous solids.* 3. Academic Press, London, **1999**, 1st edition.

[237] Ekholm, P., Blomberg, E., Claesson, P., Auflem, I. H., Sjöblom, J., Kornfeldt, A. A Quartz Crystal Microbalance Study of the Adsorption of Asphaltenes and Resins onto a Hydrophilic Surface. *Journal of Colloid and Interface Science* **2002** *247*, 342–350.

[238] De Leeuw, N. H., Parker, S. C. Surface structure and morphology of calcium carbonate polymorphs calcite, aragonite, and vaterite: An atomistic approach. *Journal of Physical Chemistry B* **1998** *102*, 2914–2922.

[239] Parks, G. A. Surface and interfacial free energies of quartz. *Journal of Geophysical Research: Solid Earth* **1984** *89*, 3997–4008.

[240] Al Mahrouqi, D., Vinogradov, J., Jackson, M. D. Zeta potential of artificial and natural calcite in aqueous solution. *Advances in Colloid and Interface Science* **2017** *240*, 60–76.

[241] Snosy, M. F., Abu El Ela, M., El-Banbi, A., Sayyouh, H. Comprehensive investigation of low-salinity waterflooding in sandstone reservoirs. *Journal of Petroleum Exploration and Production Technology* **2020** *10*, 2019–2034.

[242] Katende, A., Sagala, F. A critical review of low salinity water flooding:

Mechanism, laboratory and field application. *Journal of Molecular Liquids* **2019** *278*, 627–649.

[243] Bizaia, N., De Faria, E. H., Ricci, G. P., Calefi, P. S., Nassar, E. J., Castro, K. A., Nakagaki, S., Ciuffi, K. J., Trujillano, R., Vicente, M. A., Gil, A., Korili, S. A. Porphyrin-kaolinite as efficient catalyst for oxidation reactions. *ACS Applied Materials and Interfaces* **2009** *1*, 2667–2678.

[244] Griffin, L. R., Browning, K. L., Truscott, C. L., Clifton, L. A., Webster, J., Clarke, S. M. A comparison of didodecyldimethylammonium bromide adsorbed at mica/water and silica/water interfaces using neutron reflection. *Journal of Colloid and Interface Science* **2016** *478*, 365–373.

[245] Holysz, L., Chibowski, E. Thin-Layer Wicking. *Langmuir* **1992** *8*, 717–721.

[246] González-Martín, M. L., Labajos-Broncano, L., Jańczuk, B., Bruque, J. M. Wettability and surface free energy of zirconia ceramics and their constituents. *Journal of Materials Science* **1999** *34*, 5923–5926.

[247] Neirinck, B., Van Deursen, J., Van der Biest, O., Vleugels, J. Wettability Assessment of Submicrometer Alumina Powder Using a Modified Washburn Method. *Journal of the American Ceramic Society* **2010** *93*, 2515–2518.

[248] Karapanagiotis, I., Manoudis, P. N., Zurba, A., Lampakis, D. From Hydrophobic to Superhydrophobic and Superhydrophilic Siloxanes by Thermal Treatment. *Langmuir* **2014** *30*, 13235–13243.

[249] Cadena-Nava, R. D., Cosultchi, A., Ruiz-Garcia, J. Asphaltene Behavior at Interfaces. *Energy & Fuels* **2007** *21*, 2129–2137.

[250] Hua, R., Wang, J., Kong, H., Liu, J., Lu, X., Xu, G. Analysis of sulfur-containing compounds in crude oil by comprehensive two-dimensional gas chromatography with sulfur chemiluminescence detection. *Journal of Separation Science* **2004** *27*, 691–698.

[251] Stocker, I. N. *Adsorption at the calcite-liquid interface.* Ph.D. thesis, University of Cambridge, **2013**.

[252] Thomas, M. M., Clouse, J. A., Longo, J. M. Adsorption of organic compounds on carbonate minerals: 3. Influence on dissolution rates. *Chemical Geology* **1993** *109*, 227–237.

[253] Lahann, R. W., Campbell, R. C. Adsorption of palmitic acid on calcite. *Geochimica et Cosmochimica Acta* **1980** *44*, 629–634.

[254] Tagavifar, M., Jang, S. H., Sharma, H., Wang, D., Chang, L. Y., Mohanty, K., Pope, G. A. Effect of pH on adsorption of anionic surfactants on limestone: Experimental study and surface complexation modeling. *Colloids and Surfaces A: Physicochemical and Engineering Aspects* **2018** *538*, 549–558.

[255] Zullig, J. J., Morse, J. W. Interaction of organic acids with carbonate mineral surfaces in seawater and related solutions: I. Fatty acid adsorption. *Geochimica et Cosmochimica Acta* **1988** *52*, 1667–1678.

[256] Shi, X., Rosa, R., Lazzeri, A. On the Coating of Precipitated Calcium Carbonate with Stearic Acid in Aqueous Medium. *Langmuir* **2010** *26*, 8474–8482.

[257] Suess, E. Interaction of organic compounds with calcium carbonate-I. Association phenomena and geochemical implications. *Geochimica et Cosmochimica Acta* **1970** *34*, 157–168.

[258] Mihajlović, S. R., Vučinić, D. R., Sekulić, Ž. T., Milićević, S. Z., Kolonja, B. M. Mechanism of stearic acid adsorption to calcite. *Powder Technology* **2013** *245*, 208–216.

[259] Osman, M. A., Suter, U. W. Surface treatment of calcite with fatty acids: Structure and properties of the organic monolayer. *Chemistry of Materials* **2002** *14*, 4408–4415.

[260] Hoerr, C. W., Sedgwick, R. S., Ralston, A. W. The solubilities of the normal saturated fatty acids. III. *Journal of Organic Chemistry* **1946** *11*, 603–609.

[261] Stocker, I. N., Miller, K. L., Welbourn, R. J., Clarke, S. M., Collins, I. R., Kinane, C., Gutfreund, P. Adsorption of Aerosol-OT at the calcite/water interface – Comparison of the sodium and calcium salts. *Journal of Colloid and Interface Science* **2014** *418*, 140–146.

[262] Snyder, R. G., Scherer, J. R. Band structure in the C-H stretching region of the Raman spectrum of the extended polymethylene chain: Influence of Fermi resonance. *The Journal of Chemical Physics* **1979** *71*, 3221–3228.

[263] MacPhail, R. A., Strauss, H. L., Snyder, R. G., Eiliger, C. A. C-H stretching modes and the structure of n-alkyl chains. 2. Long, all-trans chains. *Journal of Physical Chemistry* **1984** *88*, 334–341.

[264] Bain, C. D., Davies, P. B., Ward, R. N. In-Situ Sum-Frequency Spectroscopy of

Sodium Dodecyl Sulfate and Dodecanol Coadsorbed at a Hydrophobic Surface. *Langmuir* **1994** *10*, 2060–2063.

[265] Ward, R. N., Duffy, D. C., Davies, P. B., Bain, C. D. Sum-frequency spectroscopy of surfactants adsorbed at a flat hydrophobie surface. *Journal of Physical Chemistry* **1994** *98*, 8536–8542.

[266] Lu, R., Gan, W., Wu, B.-h., Zhang, Z., Guo, Y., Wang, H.-f. C-H Stretching Vibrations of Methyl, Methylene and Methine Groups at the Vapor/Alcohol (n = 1-8) Interfaces. *The Journal of Physical Chemistry B* **2005** *109*, 14118–14129.

[267] Toulhoat, H., Prayer, C., Rouquet, G. Characterization by atomic force microscopy of adsorbed asphaltenes. *Colloids and Surfaces A: Physicochemical and Engineering Aspects* **1994** *91*, 267–283.